Theoretical Insights into the Molecular Transformations Governing Redox Chemistry

A DISSERTATION

SUBMITTED TO THE FACULTY OF THE

UNIVERSITY OF MINNESOTA

BY

Sagar Balagangadhara Udyavara

IN PARTIAL FULFILLMENT OF THE REQUIREMENTS

FOR THE DEGREE OF

DOCTOR OF PHILOSOPHY

Advised by Professor Matthew Neurock

September 2020

Acknowledgements

First and foremost, I would like to thank my advisor Matt Neurock for his constant support and guidance during my PhD. His constructive, open, and honest feedback over the years has had a profound influence on me in terms of working through research problems, presenting data, and writing manuscripts. The qualities and skills that he has imbibed in me through these years has made me a more thoughtful and analytical person than what I was before I joined his group. I would also like to thank all the collaborators and their PI's with whom I have worked with so far over all these years which has made this PhD journey even more enriching for me and quite a learning experience.

Secondly, I would like to thank all my group members – past and present who have made being in the Neurock group a wonderful and pleasurable experience for me. I owe greatly to the three senior members in my group – Dr. Ashwin Chemburkar, Dr. Tommy Chen, and Dr. Chotitath Sanpitakseree who guided and supported me through the initial phase of my graduation studies and never hesitated to answer any of the doubts that I had regarding my research and about the field. I am equally grateful to the post-docs and other senior members in our group – Dr. Peng Bai, Dr. Stuart Winikoff, and Dr. Erin Fitzharris, from whom I was quite fortunate to gain some wisdom and insights into this field of computational catalysis. My research experience would not have been as much fun without the junior members in the group – Vineet Maliekkal, Rocky Wang, Sahithi Gorthy, Roshan Patel, and Mayank Tanwar, daily "5 pm coffee break conversations" with whom made this research experience quite worthwhile and enjoyable for me.

Outside of work, I would like to thank the three pillars who have inadvertently supported me through my personal and emotional journey here – the members of the lunch squad: Matheus Dorneles de Mello, Pavlos Pachidis, and my roommate for five years, Ashish Jayaraman. Sharing lunch with these guys has been quite a memorable experience for me here during my time here in Minnesota. I also would like to thank my "play buddies" – Mridul Yadav, Ankita Naik, Sahithi Gorthy, Vineet Maliekkal, Paridhi Agrawal, Manjiri Moharir, Shaaz Khaatib, Manish Sachdeva with a special mention of the talented Shashank, who was very open and ever-ready in joining me for whatever activity I proposed to him. Besides this, I would like to thank all the other people as well with whom I have interacted quite closely with over the past five years

and beyond – Pedro, Brandon Foley, Jake Miller, GK, Aditya Bhandari, Kartik Kamat, Pooja Bhalode, Priyanka Biswas, Vineet V, Shreyas Acharya, Mayuresh Chavan, Nilesh Ade, Mohit Phalak, Aditya Salunkhe, Sahil Bhujbal, Tanmay Deshpande, Mihit Parekh, Amala Bhagwat, Shrinath Ghadage, Anuj Patil, Sanjana Kumari, Anurag Kumar, Ashish Sharma, Yan Wang, Aditya Banerji, Nikhil Sethia, Eeshaani Godbole, Supriya Ghosh, Varun, Shilpa, Shamita, Sripal.

Last, but most importantly, I would like to thank my parents and grandparents, to whom I owe a big part of who I am today. Thanks for believing in me and giving me the independence to pursue my wish to do graduate studies and explore my career path. I would also like to thank my brother Roshan Udyavara for being a constant support to me as well as my parents and grandparents in my absence.

Dedicated to my parents

Sudha and Balagangadhara Udyavara

and grandparents

Sunanda and Vithal Thingalaya

Abstract

Redox reactions are one of the most prevalent chemistries and a ubiquitous component in naturally occurring processes as well as in the production of fuels and various chemicals involving pharmaceuticals, agrochemicals, and other industrially relevant chemicals. Research efforts in the past have focused on the development of safe and environmentally benign redox processes using alternative resources to deal with issues pertaining to global warming and depletion of the existing crude oil reserves. In addition, in the area of organic synthesis, new synthesis strategies are being developed to access important redox derived chemical intermediates via use of less toxic and easily available redox reagents. However, as is the case with most newly developed catalytic processes, the fundamental challenges associated with poor reaction selectivity and activity hinder the effectiveness of these new reactive transformations and technologies, making them less desirable compared to the currently used approaches. Understanding the molecular transformations occurring during these processes thus remains the key ingredient in the further development of these new processes. Gaining mechanistic and kinetic insights into the reaction would allow us to identify factors that control the selectivity and activity for the given reaction, which would then guide the development of more active and selective reaction systems. Along these lines, electronic structure calculations based mainly on density functional theory (DFT) has emerged as a powerful tool to model the reaction kinetics and also to gain important perspectives about the chemical reactions that are not observable experimentally. My dissertation thus focuses on using density functional theory (DFT) to gain important molecular level insights into the transformations that control the oxidation and reduction pathways occurring via thermal or electrocatalytic routes for five independent redox chemistries. Further, we also look into the salient features of redox chemistry that come into play during fabrication of electronic devices, particularly for MoS_2 based transistor devices, which ultimately affect its ensuing performance.

The first part of the thesis focuses on *ab-initio* study of three particular systems of interest in oxidation chemistry. Each of these studies separately report on three distinct catalytic features including the nature of the sites, molecularity of the catalyst, and the presence of surface coverages that affect the selectivity towards the desired product. The initial focus is on processes involving partial oxidation of feedstock chemicals

which suffer from issues of low selectivity since the processes of over-oxidation is thermodynamically more favorable. One such example of a system that suffers from over-oxidation is sulfur oxidative coupling of methane (SOCM), which involves selective production of ethylene from methane using sulfur as an oxidant. Herein, we report a detailed kinetic and mechanistic study for SOCM reaction done over a sulfided Fe_3O_4 catalyst (FeS_2). Experimental mechanistic analysis involving Delplot and contact time studies reveal a reaction network for SOCM that is different compared to the traditional OCM. Further computational analysis done for this reaction network suggests a site-specific formation of the selective C_2 products and unselective carbon-di-sulfide, allowing for potential tuning of the reaction selectivity. The second system of interest that displays challenges with over-oxidation is the dehydrogenation of cyclohexanone. In this study, we examine the role of the homogeneity of the catalyst ($Pd(DMSO)_2(TFA)_2$) in selective control of the dehydrogenation reaction of cyclohexanone. Our DFT calculations indicate that the dehydrogenation proceeds via a rate determining intermolecular deprotonation step, activating the C-H bond at the alpha position. Using distortion-interaction analysis, the further activation of the cyclohexenone intermediate formed is shown to be inhibited due to its higher C-H bond strengths as well as due to its weaker interactions with the hydrogen abstracting entity, TFA^- compared to cyclohexanone. Besides issues pertaining to over-oxidation affecting the selectivity, for reacting species with multiple reaction centres or functionalities, multiple parallel reaction pathways can emerge which could also lead to lowering of selectivity towards the desired intermediate. Primary electro-oxidation of glycerol over Pt catalyst is one such example wherein the product distribution is dependent on the carbon center that is being activated (primary versus secondary). Using DFT calculations, we hereby report the influence of coverages on directing the oxidation of the C-H bond at the primary versus the secondary position. We show that under high coverage conditions, oxidation at the primary C-H bond to form glyceraldehyde is preferred despite the stronger C-H bond strengths whereas under low coverage conditions, the weaker secondary C-H bond is preferentially activated to form dihydroxyacetone. We further examine the influence of the reaction conditions such as the pH, metal surface, and the operating potentials on the resultant product distribution for electrocatalytic glycerol oxidation over Pt.

The second part of the thesis involves a mechanistic investigation of some important reduction chemistries, in particular - the hydrogen evolution reaction (HER) and the electrochemical Birch reduction. In the HER, we hereby examine MoS_2 as a non-precious catalyst for use in fuel cells for production of hydrogen from water, and report enhancements in its electrocatalytic activity via application of an external electric field normal to the MoS_2 electrode surface (back-gating). DFT studies aimed to understand the mechanistic nuances of the observed increased activity show that the excess electron densities induced via back-gating increase the binding energies of the hydrogen on the MoS_2 surface, which in turn lead to improvements in the electrocatalytic activity of MoS_2 for HER. In the next topic, we look at the Birch reduction process wherein we report a practical, safe, and scalable electrosynthetic strategy for the reduction of the arenes to dienes and for other similar reductive transformations and subsequently determine the mechanistic nuances of the reaction in the presence of various reagents and additives. Through electroanalytical and computational investigations, we have shown the reaction pathway to proceed via the reduction of the substrate near the electrode surface with the protonation step as the rate limiting step of the reaction. Further, we have deciphered the unique role of each of the reagents used in the study – electrolyte, lithium bromide (LiBr); solvent, tetrahydrofuran (THF); proton source, dimethyl urea (DMU); and the additive, tris(pyrrolidino)phosphoramide (TPPA), to understand how these components co-operatively aid in promoting the desired transformations towards higher reaction yields.

In the final part of the thesis, diverging from the theme of redox reactions in chemical production, we investigate the influence of the redox reactions in device fabrication processes with the aim to mitigate some of the issues concerning the contact problem typically observed at the interface. We study here a system of MoS_2-metal contacts, which have applications in development of sub-nanometric transistors. Via our "single-atom addition" approach used here, we show that the nature of the metal deposited strongly influences the resulting structural and electronic properties of the MoS_2-metal interface. In conjunction with analytical scanning tunnelling electron microscopy (STEM) studies, we screen and characterize the interfacial properties for different metal contacts including Sc, Ti, Cu, In, and Au, with the aim to design systems that minimize the contact resistance at these interfaces.

Table of Contents

List of Figures

List of Tables

List of Schemes

Chapter 1 – Introduction

Redox (oxidation-reduction) reaction, a type of chemical reaction which involves a change in the oxidation state of the reacting elements are ubiquitous in nature, a prime example being the reductive photosynthesis ($6CO_2 + 6H_2O \rightarrow C_6H_{12}O_6 + 6O_2$) and the oxidative respiration processes ($C_6H_{12}O_6 + 6O_2 \rightarrow 6CO_2 + 6H_2O$) that occur in plants. Redox chemistry also plays a central role in various industrially relevant chemical transformations for synthesis of fuels, chemicals, medicines, as well as biomass upgradation.[1–10] These reactions can be carried out thermally wherein they are aided by a co-reactant which acts as an oxidizing (O_2,[5,11,12] S_2[13–15], CO_2[16–19]) or reducing agent (Pt/H_2,[20–22] $LiAlH_4$[23,24]). Another way to effect these transformations is using electrochemistry wherein by applying a negative or positive potential at the electrode surface, the reduction or the oxidation reactions can be mediated respectively.[1,4,7,13,25–30]

Reactions such as oxidation of methane to different fuels and chemicals such as CO[31] and CH_3OH [32], CO oxidation to CO_2,[33,34] dehydrogenation of alkanes to alkenes,[35–39] alcohol oxidation,[40–42] are a few examples of oxidation reactions. Reactions which involve partial oxidation of the reactants, for example methane oxidation to methanol,[43] however, are difficult to control and are known to output a multitude of products, which negatively affects the selectivity towards the product of interest. Thus, understanding and gaining molecular level insights into the pathways controlling the oxidation chemistry becomes crucial in order to obtain selective oxidation towards the desired product. The first part of the thesis, **Chapters 2-4** deals with looking specifically at three different oxidation chemistries which are characterized by the formation of multitude of products through multiple parallel or sequential pathways. Through experimental mechanistic studies and DFT calculations, in these chapters, we evaluate the energetics of the different pathways prevalent in the reaction network, and gain insights into the factors which govern selectivity towards a product of interest with the aim to design more selective catalysts.

In **Chapter 2**, we focus on the sulfur oxidative coupling of methane (SOCM) reaction which involves the direct conversion of methane to ethylene using sulfur as an oxidant, a softer alternative to oxygen. The discovery of shale gas reserves has accelerated the search for direct methane conversion technologies to value added products. OCM is

one such technology which can be used to directly upgrade methane to ethylene.[44–47] This reaction however leads to over-oxidized products such as CO_2, leading to low ethylene selectivities. With use of sulfur as a softer oxidant, we aim to reduce this thermodynamic driving force for over-oxidation so as to selectively produce ethylene.[13,14] While OCM is well studied, the field of SOCM is relatively new and relevant mechanistic and kinetic studies on the SOCM reaction are quite few.[13] Thus, in this study, we aim to understand the kinetics and mechanisms that govern the SOCM reaction over sulfided Fe_3O_4 catalyst which has been shown to afford high ethylene selectivities.[14] We show that the relevant mechanisms in SOCM are vastly different than the traditional OCM. Delplot analysis done to decipher the SOCM reaction network reveal that, unlike OCM, ethylene as well as CS_2 formation in SOCM is shown to be formed directly from methane. Using DFT calculations, we further show that the iron-sulfur site pairs (Fe-S_{brid}) present on the sulfided Fe_3O_4 (FeS_2) surface selectively lead to the generation of gas phase methyl radicals, which couple to form ethane, with ethylene likely formed via successive fast dehydrogenation of ethane. The adsorbed sulfur sites (S_{dim}), on the other hand, predominantly catalyse the unselective process of the formation of the over-oxidized product CS_2. Further kinetic studies done show a first order dependence with respect to both sulfur as well as methane. Also, an overall apparent barrier of 66 kJ/mol was determined experimentally, which is shown to be an ensemble average of the apparent barriers of two parallel reaction pathways – one leading to ethylene formation over Fe-S_{brid} sites with apparent computed barrier of 163 kJ/mol and other leading to predominant CS_2 formation over adsorbed sulfur sites with an apparent barrier of 44 kJ/mol.

Chapter 3 deals with looking into cyclohexanone dehydrogenation reaction over a homogeneous $Pd(TFA)_2(DMSO)_2$ catalyst. The dehydrogenation of cyclohexanone can afford either a singly dehydrogenated product, cyclohexenone or a doubly dehydrogenated product, phenol, both of which have varied applications in synthesis of pharmaceutical intermediates and fine chemicals. Recent studies by Stahl et al.[5,48–52] have shown that selective dehydrogenation of cyclohexanone to cyclohexenone can be driven by use and stabilization of homogeneous catalyst $Pd(TFA)_2$ in presence of the DMSO ligand. In this chapter, we thus aim to first understand the mechanisms that govern the dehydrogenation of cyclohexanone over the homogeneous $Pd(DMSO)_2(TFA)_2$ catalyst, post which we then further dwell into the factors that

control the selectivity towards cyclohexenone versus phenol using DFT calculations. We show that the dehydrogenation of cyclohexanone over $Pd(DMSO)_2(TFA)_2$ proceeds via a rate determining step of alpha C-H activation which occurs via a proton abstraction by the dissociated TFA^- ligand. This proton abstraction step is hindered for the cyclohexenone species due to the stronger C-H bond strengths of C-H bond at C_2 position and weaker orbital interactions of the attacking TFA^- anion with the C_4 C-H bond, thus inhibiting its further dehydrogenation to phenol. Through our computational analysis, we further show that use of a more basic covalent ligand such as acetate (OAc) could aid in further improvements in the catalytic activity for the specific reaction.

While in **Chapters 2 and 3**, the reactions are driven thermally with use of oxidizing reagents (S_2 and O_2 respectively), recent advances in renewable energy technologies have prompted the use of electricity to drive chemical reactions.[1,10,25,27–30] By simple tuning of the redox potentials, one can either catalyze oxidation or reduction reactions. **Chapter 4**, in particular, deals with looking at the electrocatalytic oxidation of glycerol molecule over single crystal Pt (111) surface. Glycerol is a polyol species containing multiple functional groups which can undergo a wide range of reactions and hence afford different reaction products. In this chapter, we primarily focus on the primary oxidation reaction involving the conversion of glycerol to dihydroxyacetone (DHA), a product of oxidation of its secondary alcohol group and glyceraldehyde (GALD), a product of oxidation of its primary alcohol group. Previous studies on glycerol electro-oxidation have shown that over Pt (111) surfaces, glycerol electro-oxidation primarily proceeds towards GALD formation over DHA,[53] reasons for which remain elusive. Using DFT calculations, through model propanol (1-propanol and 2-propanol) systems, we show that CO coverages in acidic media and OH coverages in alkaline media present on the Pt (111) surface sterically hinder the selectivity and rate determining C-H activation step of the secondary alcohol group, leading to the dominant formation of GALD. Overlaying of Pt atoms over a Bi or Cu surface has been shown to lower the C-C bond dissociation energies (BDEs), which would likely lower the CO coverages in acidic media and aid in the selective activation of the weaker secondary C-H bond to form DHA.

Chapters 5 and 6 deal with understanding the mechanistic details of the electrocatalytic reductive transformations. Electrocatalytic reduction has recently gained traction for synthesis of fuels and chemicals from exhaust streams such as CO_2

and H_2O to produce chemicals such as CO,[54,55] HCOOH,[55,56] or C_{2+} alcohols,[57] and for fixation of N_2 to produce NH_3.[58,59] New reduction technologies such as those involving CO_2 conversion however typically suffer from lower activities, higher cost, and lower efficiency. Hence, continual efforts need to be made to improve these technologies in terms of its activity, efficiency, and cost. These efforts can be supplemented by the theoretical understanding of the various factors underpinning its performance such as the catalyst and its reaction environment, aiding in the development of the new technologies.

Of the prevalent electrocatalytic reduction technologies, Hydrogen evolution reaction (HER) is one of the key electrocatalytic reduction reactions, which involves H_2 production from water for use in fuel cell. Previous studies have shown precious metal catalyst Pt to be optimal for HER reaction. MoS_2, a non-precious material has also shown great promise as a catalyst for HER and can be a potential alternative to the more expensive Pt.[60,61] However, the catalytic activity of this catalyst for HER is inferior to that of Pt with overpotentials of 294 mV compared to an overpotential of 70 mV seen for Pt, thus putting the focus towards lowering the overpotentials for HER over MoS_2. **Chapter 5** thus deals with optimizing the electrocatalytic properties of MoS_2 wherein we show that by applying an external electric field normal to the catalyst surface, the overpotentials for HER over MoS_2 can be brought down by 140 mV, thus increasing its electrocatalytic activity for HER. Using DFT calculations, we show that the excess electron density induced due to the field-effect over the active S-vacancy sites increase the adsorption strength of the hydrogen, which in turn promotes the HER. We further predict that switching the dielectric used in the electrochemical setup from SiO_2 to a high-κ dielectric, HfO_2 can lead to further substantial improvements in the electrocatalytic activity, with calculations suggesting a ten-fold increase in the hydrogen binding energies.

In addition to well-known electrocatalytic reactions such as HER, a new foray of electrolysis has evolved wherein it is currently being explored for use in synthesis of pharmaceutical intermediates and other fine chemicals.[1,25,30] Electrochemistry allows one to access new modes of reactivity and transformations to produce intermediates and chemicals which typically are either inaccessible or quite laborious to access via use of chemical reagents.[30] In **Chapter 6**, we explore the application of electrocatalysis for one such reduction chemistry prevalent in synthesis of pharmaceutical drug

candidates, namely the Birch reduction. Birch reduction involves the conversion of aromatics to dienes and involves electron transfer and proton transfer steps to afford the product from the reactant. This reaction previously was carried out in presence of Li^0 in liquid ammonia with alcohols such as tert-butanol as the proton source and the solvated electrons from Li^0 in liquid ammonia as the electron source and thus the reducing agent.[62–65] The technical difficulties involved in handling of chemicals such as Li and liquid NH_3, however, made this process difficult to scale. In this study, we propose a safe and scalable strategy in order to reduce aromatics to dienes which involves use of electrolysis with lithium bromide (LiBr) as the electrolyte, dimethylurea (DMU) as the proton source, and tris(pyrrolidino)phosphoramide (TPPA) as an additive which acts as a charge protection agent. Through our DFT studies in conjunction with electroanalytical experiments, we show that the mechanism for the Birch reduction progresses on the electrode surface rather than through the Li^0 species wherein the electron transfer to the substrate occurs via the electrode and LiBr is shown to promote this electron transfer process by stabilizing the bound negatively charged intermediate. Further, using potential dependent DFT calculations, we see a potential dependent change in the kinetics of the reaction, wherein at less reductive potentials, the first protonation step is rate-determining, but as the conditions become more reductive and the potential drops down to more negative values, the second protonation step starts becoming rate-determining. Using DFT calculations, we further characterize the properties of the proton source, solvent, and the additive used in the reaction which lead to such high yielding transformations.

In addition to the prevalence of redox reactions in chemical transformations for fuels and chemicals production, redox chemistries are also quite commonly observed during fabrication of nanoscale devices such as transistors, and memory-chips as well. Thus, in the final thesis chapter, **Chapter 7**, we transition from the theme of redox reactions in chemical systems and look at how similar concepts also play a role in the field of electronics wherein the redox chemistry of the material choice used in the fabrication of sub-nanometric devices dictates its subsequent performance. We herein take the example of metal-MoS_2 contacts which are prevalent in MoS_2-based transistor devices.[66–68] The interface that develops in these contacts plays a crucial role in its performance.[69–72] However, the structure of the interface in this case depends on the redox chemistry that occurs when the metal comes in contact with the MoS_2. Through

our computational screening studies, we have been able to identify that highly reducing metals (M) with high binding energies to MoS_2 such as Ti and Sc tend to disrupt the interface of MoS_2 forming M_xS_y clusters, which degrades the performance characteristics of the device. Hence, metals with moderate binding energies and lower reducing capabilities such as In, Ga, and Cu are more suited to function as optimal metal contacts to MoS_2, and have been shown to lead to formation of clean and pristine interfaces with improved device performance seen in case of In.

Chapter 2 - "Soft" Oxidative Coupling of Methane to Ethylene. Mechanistic Insights from Combined Experiment and Theory

Adapted from Liu, S., Udyavara S., Peter, M., Lohr T.L., Neurock M., Marks, T.J., "Soft" Oxidative Coupling of Methane to Ethylene. Mechanistic Insights from Combined Experiment and Theory, *to be submitted.*

Theoretical results presented herein were performed by SU under the supervision of MN

2.1. Synopsis

The oxidative coupling of methane to ethylene using gaseous disulfur ($2CH_4 + S_2 \rightarrow C_2H_4 + 2H_2S$) as an oxidant (SOCM) proceeds with promising selectivity. Here we report detailed experimental and theoretical studies that examine the mechanism for the conversion of CH_4 to C_2H_4 over an Fe_3O_4-derived catalyst (FeS_2) which achieves a promising ethylene selectivity of 33%. We compare and contrast these results with those for the classic, highly exothermic oxidative coupling of methane using O_2 (OCM; $2CH_4 + O_2 \rightarrow C_2H_4 + 2H_2O$). Kinetic/mechanistic analysis of SOCM along with density functional theory analysis show that ethylene is produced as a primary product of methane activation that proceeds via the coupling of CH_2 intermediates largely over Fe-S_{brid} sites that bridge Fe surface sites, as well as the adsorbed sulfur sites to some extent on the heavily sulfided Fe_3O_4 surface. In contrast, and unlike OCM, the overoxidized CS_2 by-product forms predominantly via CH_4 oxidation, rather than from the C_2 products, via a series of C-H activation and S-addition steps at adsorbed sulfur sites on the FeS_2 surface. The experimental rate law for methane conversion is first-order in both CH_4 and S_2, consistent with the involvement of two S sites in the rate-determining methane C-H activation, with a CD_4/CH_4 kinetic isotope effect of 1.78±0.18. The experimental apparent activation energy for methane conversion is 66 ± 8 kJ/mol,

which is significantly lower than those reported for CH_4 oxidative coupling with O_2. All evidence argues that SOCM proceeds via a very different pathway than OCM.

2.2. Introduction

The oxidative coupling of methane (OCM) with O_2 would seem to be an attractive, direct route to convert methane, one of the most earth-abundant carbon sources,[44] to ethylene ($2CH_4 + O_2 \rightarrow C_2H_4 + 2H_2O$), a key chemical building block,[73,74] and this process has been investigated extensively[75–88] since pioneering studies in 1982.[47] Nevertheless, despite the significant research efforts, the widespread implementation of OCM has been challenged by the severe over-oxidation of methane to CO_2 and other undesired oxygenates. Alternatively, CH_4 can be converted to C_2H_4 via non-oxidative pathways,[73,89–95] however the severe reaction conditions required typically result in extensive carbon deposition and catalyst deactivation. In preliminary studies, we reported a direct $2CH_4 + S_2 \rightarrow C_2H_4 + 2H_2S$ coupling process that moderates the driving force for methane over-oxidation by using gaseous disulfur (S_2) as a soft oxidant ("SOCM"; Figure 2.1a).[13] S_2 is isoelectronic with O_2 and the major species in sulfur vapor in the temperature range 700 – 925 °C.[96–98] It is a far less aggressive oxidant than O_2.[13,99,100] In this oxidative methane coupling scenario, the elemental sulfur would be regenerated from the H_2S co-product using the established Claus process (Figure 2.1b),[96] in a closed cycle in which sulfur essentially mediates/moderates the high non-selective reactivity of O_2. Results to date indicate that SOCM can yield higher ethylene selectivities than conventional OCM, raising intriguing questions about the mechanism as well as the possibility of greater selectivity. Very early studies of S_2 as a hydrocarbon oxidant focused on coal or hydrocarbon conversion to CS_2.[101,102] This laboratory first showed that methane + $S_{2(g)}$ yields ethylene over a PdS/ZrO_2 catalyst, with selectivities as high as ~20 %.[13] Subsequent work with metal oxide precatalysts afforded C_2H_4 selectivities as high as 33 %.[14]

Nevertheless, in contrast to extensive OCM[45,86,103–106] and nonoxidative CH_4 coupling studies,[107] far less is known about SOCM phenomenology, and very little about the actual reaction mechanism. Post-SOCM X-ray photoelectron spectroscopy (XPS), X-ray diffraction (XRD), and elemental analysis suggest that the metal oxide catalysts are sulfided under SOCM conditions. Earlier DFT analyses for layered MoS_2 catalysts suggest that methane is activated at M-S or S-S sites to form surface-bound CH_3^*

species which undergo dehydrogenation to form surface-bound CH_2^* species that then couple to produce C_2H_4. It was proposed that CH_3* species can also desorb as methyl radicals which subsequently couple to form ethane. The over-oxidation product, CS_2, was tentatively suggested to form via sulfur addition to surface methylidene intermediates.[13]

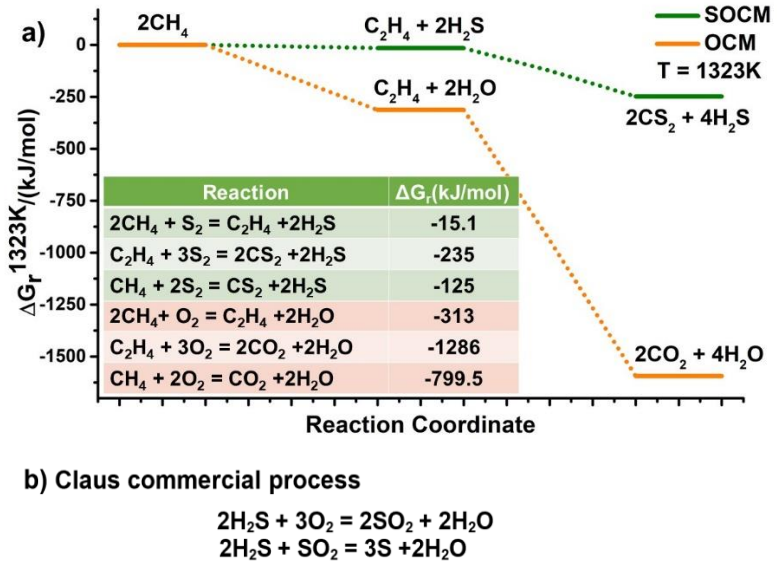

b) Claus commercial process

$$2H_2S + 3O_2 = 2SO_2 + 2H_2O$$
$$2H_2S + SO_2 = 3S + 2H_2O$$

Figure 2.1: Energetic comparison between SOCM and OCM, and the commercial pathway to recover elemental sulfur from H_2S: (a) Gibbs free energy of the indicated desired and over-oxidation reactions in OCM and SOCM processes at T= 1323K. (b) Catalytic Claus process used to recover elemental sulfur from H_2S.

At this stage in SOCM development, experimental kinetic/mechanistic and theoretical analyses are needed to better understand the pathways for CH_4 conversion to C_2H_4 and other products (C_2H_6, C_2H_2, CS_2). As shown in Figure 2.2, the first step may involve methane activation to form a surface-bound methyl intermediate that can follow one of two paths to products. The first proceeds through a series of H abstraction reactions to form methylene (CH_2) and methylidyne surface (CH) intermediates that can either couple to form C_2 products or undergo complete oxidation to CS_2. The second path involves the formation of methyl intermediates that first couple on the surface or in the gas phase to form ethane which can subsequently undergo successive dehydrogenation to ethylene, acetylene, and finally oxidation to CS_2. CS_2 which is the major byproduct in the oxidative conversion of methane is thus formed by different steps in pathway A vs pathway B. Therefore, it is crucial to understand the predominant pathways as well

as the active sites for C_2 and CS_2 formation. Such insights should aid in elucidating the nature of the active sites, kinetics and mechanisms and identifying optimum reaction conditions and catalyst structural/compositional features for targeted catalyst design.

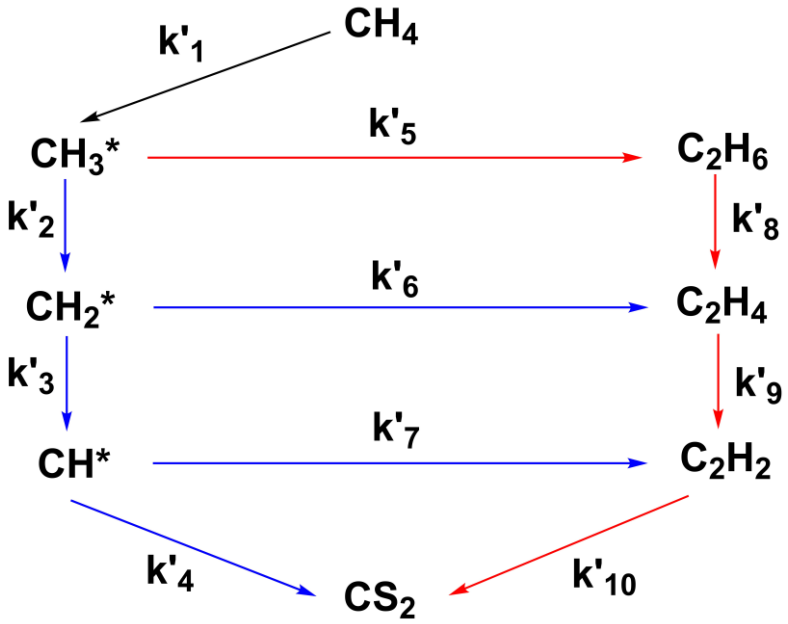

Figure 2.2: Possible reaction pathways for SOCM. Blue: Pathway A - methyl, methylene and methylidyne intermediates couple to form C_2 products and eventually get fully oxidized to CS_2. Red: Pathway B - Methyl radicals form ethane, and other C_2 products and CS_2 are formed via stepwise dehydrogenation.

This study examines the mechanism of SOCM on a sulfided Fe_3O_4 catalyst that affords C_2H_4 selectivities up to 33 %.[14] We begin with a brief summary of SOCM phenomenology, followed by a structural analysis of how the iron phases evolve during sulfurization and SOCM. Next, detailed kinetic and mechanistic studies are presented to determine reaction orders with respect to methane and S_2, activation energetics, and kinetic isotope effects, and to provide insights into the reaction pathways and mechanisms governing C_2 vs CS_2 formation. Complementary first-principles density functional theory (DFT) calculations are discussed to analyze SOCM reaction pathways and mechanisms, the nature of the active sites, and their role in forming the observed products. Finally, the SOCM and OCM processes are compared in detail, revealing that they follow distinctly different reaction pathways, and that the data and analyses can aid in future catalyst and reaction design.

2.3. Results

2.3.1. Sulfur Oxidative Coupling of Methane. General Phenomenology

The methodology for all catalytic runs begins by first exposing the Fe_3O_4 precatalyst to flowing H_2S (sulfurization) for several hours to produce the active catalyst; see the SI for details and below for catalyst characterization. Catalytic experiments utilize a flowing Ar + methane + S_2 vapor stream in the plug-flow reactor described previously (see SI for details).[13,14] The gaseous products and unreacted methane are quantified by gas chromatography (GC) using flame FID and TC detection. The primary SOCM reaction products are ethylene and CS_2, with minor amounts of ethane and acetylene. Methane conversion and ethylene selectivity are quantified as a function of catalyst and reaction temperature. Under the operating conditions, the Fe catalysts exhibit stable selectivity and conversion for the duration of kinetic measurements (SI Figure S2.1). Methane conversion increases linearly with increasing contact time for all contact times examined here (SI Figure S2.14). A detailed discussion of conversion as a function of contact time using a plug flow reactor model is provided in the SI. The effects of altering the feedstock flow rate, contact time are also examined. Detailed carbon balance data are summarized in SI Table S2.9. The spent catalyst is characterized by X-ray diffraction and X-ray photoelectron spectroscopy as discussed below.

2.3.2. Characterization of Fresh and Spent Fe Based Catalysts

Powder X-ray diffraction (pXRD), XPS and Raman spectra were employed to monitor the transformations of the Fe_3O_4 precatalyst under sulfurization and SOCM reaction conditions (see SI for experimental details). After Fe_3O_4 precatalyst sulfurization, the only phase observed by pXRD is the known FeS phase (Figure 2.3a).[108,109] Note that these XRD data differ somewhat from those reported previously since the sensitivity was increased significantly using improved instrumentation (Scintag XDS2300, see SI). However, the Fe 2p XPS of the catalyst surface (Figure 2.3b) contains both an intense Fe 2p3 peak at BE= 707.19 eV, assignable to FeS_2 (literature, 707.25 eV[110]), along with weaker 2p3 peak at BE = 710.37 eV assignable to FeS (literature, 710.3 eV[111]). Raman spectrum of sulfurized Fe catalysts (Figure 2.3c) confirmed crystalline phases of FeS(ν= 319cm^{-1})[112] and FeS_2(ν= 338, 373, and 425cm^{-1}).[113] Note that compared with literature values, Raman peaks of FeS_2 shifted for as large as 5 cm^{-1}, suggesting a small crystal size.[114–116] The fact that FeS_2 is not visible in the pXRD scans,

paired with shifted FeS_2 signals in Raman spectroscopy argues that any FeS_2 present in this S-rich environment is small crystals, or only as a thin crystalline layer on the Fe catalyst surface. To further confirm the presence of FeS_2 and investigate its morphology and composition, we performed Transmission Electron Microscopy (TEM) on the Fe catalysts after sulfurization for 6 hours without any SOCM reactions. The FeS_2 powders were observed as shown in Figure S2.2a. Selected area diffraction patterns of the particle along the [001], [102] and [012] zone axes were obtained as shown in Figure S2.2b-d. All the diffraction patterns can be indexed with FeS_2 (space group $Pa\bar{3}$). In addition, energy-dispersive X-ray spectroscopy (EDS) was also performed on the same particle, which confirms the composition of FeS_2 (Figure S2.3). Figure 3d indicated the Fe and S signals in the EDS spectrum, and the ratio of Fe:S is around 1:2. We therefore conclude that the two principal phases of interest for catalysis are FeS_2 and FeS. Further analysis of the reactivity of these phases is discussed in the Theoretical Discussion section below.

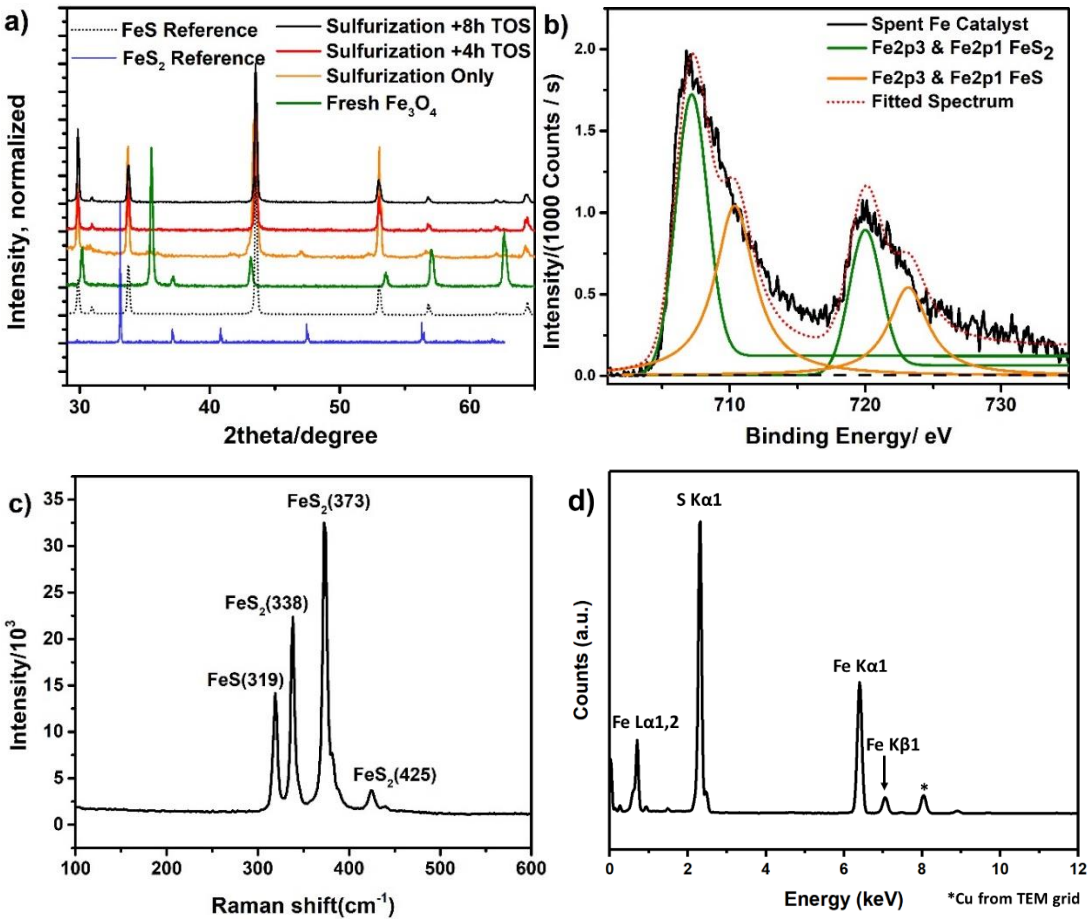

Figure 2.3: Surface characterization of fresh and spent catalysts: (a) pXRD spectra of fresh Fe_3O_4 precatalysts (green), sulfurized Fe catalyst (orange), sulfurized Fe catalyst collected after TOS of 4 h under kinetic measurement condition (red), and sulfurized Fe catalyst after TOS of 8 h (black) under kinetic measurement condition. Reference peak: FeS (black dotted line), FeS_2 (blue solid line) (b) XPS spectrum of spent Fe catalysts after TOS of 8h. Reaction condition: at 865°C, WHSV of 0.785 h^{-1} and CH_4:S_2 ratio = 1.099. (c) Raman spectrum of sulfurized Fe catalyst. Excitation wavelength: 532nm. Sulfurization condition: 4 hours at 865°C, WHSV of 0.785 h^{-1} and H_2S partial pressure = 3.3%, S_2 partial pressure = 3.0%. (d) EDS spectrum of a selected area on a particle in the sample of Fe catalysts after sulfurization for 6 hours without any SOCM reactions.

It is not surprising that precatalysts can undergo *in situ* changes in structure and composition of the phases present under the conditions employed for the reaction. For SOCM, previously we reported that several precatalysts are readily sulfurized in the presence of elemental sulfur at 950°C.[13,14] In OCM too, a recent study by Kwapien at al.[117] showed that volatilization of Li species in Li-doped MgO OCM catalysts creates defects on the MgO catalyst surface that are active in the oxidative activation of methane. Similar defects are created in Li-free MgO under OCM reaction conditions, leading to time-dependent changes in activity. In the present studies, we find that the Fe_3O_4 precatalyst undergoes sulfurization *in situ* to generate bulk FeS and likely surface FeS_2. The catalyst structure, however, remains stable and independent of the time on stream post sulfurization, consistent with the essentially constant catalytic performance with times on stream up to 40 hours.[117]

2.3.3. Kinetics. Determination of Optimum Temperature Range for Data Collection

As shown in Figure S2.13, the slope of the SOCM Arrhenius plot for methane conversion has a discontinuity above ~900°C, implying a change in reaction mechanism. A plausible explanation is that the reaction becomes diffusion-limited/non-catalytic above ~900°C.[118] Such catalytic phenomena are not unprecedented and typically become more common at higher temperatures. For SOCM, because the apparent activation energy is lower than in typical OCM reports (see more below), it is possible the overall reaction becomes diffusion-limited above ~900°C. Therefore, the

present SOCM kinetic measurements were conducted well below 900°C. Note that previously, 33% C_2H_4 selectivity at 9% CH_4 conversion were reported at 950 ºC over an Fe catalyst[14] -- different temperatures than in the present mechanistic study.

2.3.4. Kinetics. Reaction Order

The gaseous sulfur and methane reaction orders were calculated by measuring the changes in the rate of methane conversion as a function of the sulfur and methane pressures, respectively. The rate orders measured here are overall apparent rate orders and represent a measured average over the different parallel pathways occurring in the reaction network, details of which are discussed further below. The sulfur reaction order was determined using excess CH_4 under pseudo-first order conditions with sulfur flow rates ranging from 5.08 to 30.5 μmol/min at 865°C (see SI for details). The measured rates of reaction under these conditions were found to be directly proportional to $[S_2]$ (Figure 2.4a). Plotting the natural logarithm of the rate of methane conversion versus the natural logarithm of $[S_2]$ yields a slope of 1.05 ($R^2 = 0.96$), indicating that the overall reaction is first-order with respect to $[S_2]$.

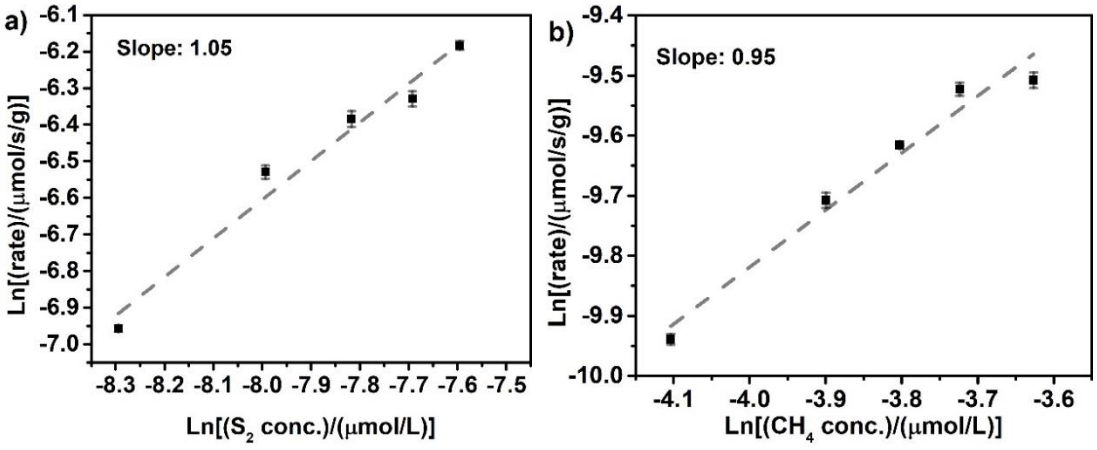

Figure 2.4: Influence of sulfur and methane concentrations on SOCM reaction rate: (a) natural logarithm of reaction rate vs. natural logarithm of S_2 concentration ($[S_2]$), and (b) the natural logarithm of the reaction rate vs. the natural logarithm of CH_4 concentration. Reaction condition: WHSV = 0.785h^{-1}, 865°C.

A similar approach was used to experimentally establish the reaction order for methane. The methane flowrate was varied to establish methane concentrations between 78.7 to 280 μmol/min with excess S_2. Figure 2.4b shows the natural logarithm of the rate of methane conversion versus the natural logarithm of the CH_4 concentration for four

different total flow rates. The results exhibit direct linear dependence on [CH_4] with a slope of 0.95 (R^2 =0.96), thus indicating that the overall reaction is first-order with respect to CH_4.

Potential product inhibition effects on the rates were measured using the same approach, but in the presence of added CS_2 and H_2S. The H_2S and CS_2 reaction orders were determined using excess CH_4 at an S_2 flow rate of 52.0 μmol/min at 865 °C. The approximately zero-order plots (see SI Figure S2.4) indicate that the rate of methane conversion is zero-order in both CS_2 and H_2S, which indicates that CS_2 and H_2S do not play a significant inhibitory mechanistic role under the present reaction conditions.

2.3.4. Kinetics. Apparent Activation Energy

The SOCM activation energy (E_{act}) was determined by constructing Arrhenius plots over the temperature range of 835-865 °C (See SI Figures S2.7-S2.9 for Arrhenius plots of methane consumption, ethylene formation, and CS_2 formation). CH_4 conversions were held between 5-8 % for a CH_4/S_2 ratio of 1.099 (see SI for details). The temperature dependence of the CH_4 conversion rate from seven experimental runs yields an activation energy (E_{act}) of 66±8 kJ/mol. Similar to the rate orders, the apparent activation barriers measured here are a measured average over the different parallel CH_4 activation paths involved in the reaction network. This can be validated by examining the differences in apparent activation energy for the formation of ethylene and CS_2 which are measured to be 85±2kJ/mol and 39±4kJ/mol, respectively, from the measured formation rate of ethylene and CS_2 (See SI Table S2.2). As discussed in the theoretical analysis section below, the apparent activation barriers reflect the heat of adsorption to form the active sulfur sites on the surface along with the intrinsic barrier for the rate-limiting C-H bond activation step. While the formation of ethylene and CS_2 both involve the initial C-H activation of methane in the rate-determining step, they proceed over different surface sites that require different energetic costs to form and thus result in different measured apparent barriers. While the large differences in the apparent barriers for CS_2 vs C_2H_4 formation might suggest that CS_2 formation dominates the product distribution, there are significantly higher entropic costs involved in the formation of CS_2 as it requires the adsorption of gas phase sulfur to form the active sulfur site pairs that lead to the formation CS_2 (see in Theoretical Discussion below). Appropriately accounting for the entropic loss for the adsorption of S_2 and Boltzmann-

weighting the free energies over the different metal and sulfur site pairs that lead to C_2H_4 and CS_2 provides a product distribution that is in good agreement with the experimental results.

2.3.5. Kinetic Isotope Effect

Kinetic isotope effect (KIE) data were acquired by comparing the rate of consumption of CH_4 versus CD_4, as detailed in SI. According to the four trials listed in SI Table S2.3, at 865 °C with WHSV = 0.628 h^{-1}, the SOCM CH_4/CD_4 kinetic isotope effect is measured to be 1.78±0.18, arguing that C-H bond cleavage is involved in the rate-limiting step. This value is similar to reported OCM values over various oxides (Li/MgO, $SrCO_3$, Sm_2O_3, $Na/MnO_x/SiO_2$ and $Mn/Na_2WO_4/SiO_2$) which range between 1.2 - 1.8.[106,119–121] More comparative data for SOCM versus OCM are provided below in the Section Comparison with Conventional OCM.

2.3.6. Reaction Pathways and Networks

Rigorous quantitative kinetic analyses are often challenging for complex reaction systems with multiple reaction paths. The Delplot analysis developed by Bhore et al.[122] plots selectivity or yield for a particular product (y) divided by the reaction conversion (x) versus conversion and subsequently extrapolates the plot back to zero conversion $\left(\lim_{x\to 0}\frac{y}{x}\right)$, enabling determination of the primary products (those with non-zero positive intercepts) and non-primary products (those with intercepts approaching zero). A Delplot analysis was carried out here to determine the product ranks and to construct an approximate reaction network. Figure 2.5 shows the first (a), second (b), and third (c) rank Delplots for methane under SOCM conditions. Note that the sum of all gaseous product selectivities is somewhat lower than 100 % because of minor coke formation which was reported and quantified previously.[14] The intercepts for C_2H_6, C_2H_4, and CS_2 all appear to be non-zero in the first-rank Delplot, while the intercept for C_2H_2 is zero. In the second-rank Delplot, the intercepts of all products diverge except for C_2H_2. In the third-rank Delplot, the intercepts of all products diverge. These results suggest that methane reacts directly to form ethane, ethylene, and carbon disulfide (pathway A), whereas acetylene is produced as a secondary reaction product and is not directly formed from methane (pathway B).

Similarly, the first and second rank Delplot reported in Figure S2.10 indicate that ethane almost exclusively reacts to form ethylene, while CS_2 is a higher-rank product of ethane. The first rank ethylene Delplot (Figure S2.11a, b) shows that the C_2H_2 is the primary product of ethylene, whereas the first rank acetylene Delplot (Figure S2.12a) shows that acetylene primarily forms CS_2. For acetylene, as the conversion decreases, the carbon balance strays further from 100%. This is likely due to the formation of coke.

Note that the Delplot analysis only provides the shortest route in a reaction network. From the data presented in Figure 2.5, it is likely that methane undergoes a series of C-H activation steps to directly form C_2H_6, C_2H_4, and CS_2 and therefore confirms the occurrence of pathway A (Reactions 1, 2, 3, 4, 5, and 6 in Figure 2.2). The C_2H_2 is likely formed via the dehydrogenation of C_2H_4 (Reaction 9). A path involving the stepwise dehydrogenation from C_2H_6 to C_2H_4 and then to C_2H_2 (pathway B) however, cannot be ruled out. The Delplots of ethylene and acetyene suggest that such pathways are possible. Whether or not they are predominant is explored further below.

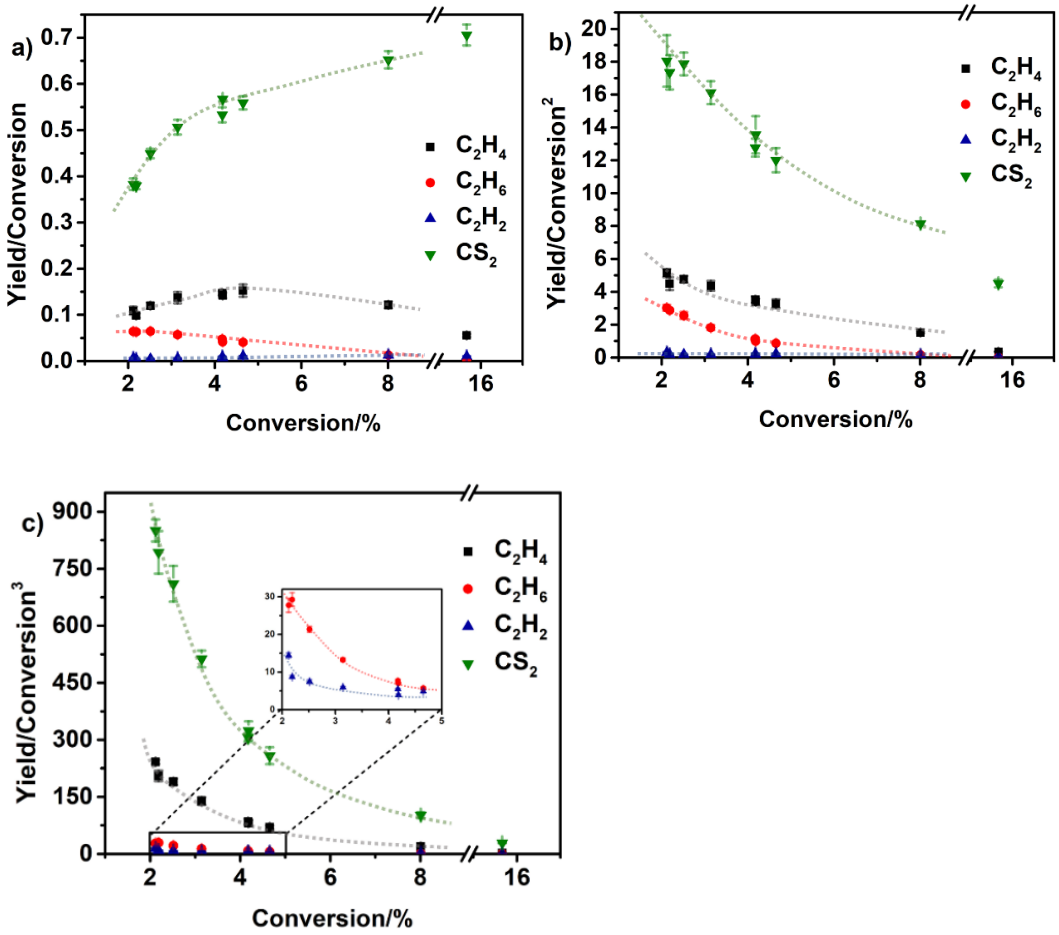

Figure 2.5: Delplots for methane: first-rank Delplot (a), second-rank Delplot (b), and third-rank Delplot (c) for the SOCM reaction over an Fe_3O_4–based catalyst. Reaction condition: 865°C, CH_4:S_2 = 1.099, WHSV range: $0.13h^{-1}$ ~ $0.98h^{-1}$.

2.3.7. SOCM Reaction Sequence

Insights into SOCM reaction sequences are further obtained by examining product distributions as a function of contact time (t_c). All CH_4 experiments are carried out in the low conversion regime as verified by the linear relation between CH_4 conversion and t_c (Figure S2.14). The SOCM C_2 product yields to C_2H_6, C_2H_4, and C_2H_2 versus t_c are shown in Figure 2.6a. The C_2H_6 yield peaks early ($t_c \approx 0.1$ s) and rapidly decays with increasing t_c, while the C_2H_4 and C_2H_2 yields exhibit maxima at after $t_c \approx 0.4$ s and after $t_c \approx 0.6$ s, respectively. C_2H_4 yield then decays rapidly whereas C_2H_2 yield remains constant for an extended period before decaying. The relative evolution of the C_2H_6, C_2H_4, and C_2H_2 yield with t_c suggests consecutive dehydrogenations as in the sequence (pathway b):

$$CH_4 \rightarrow C_2H_6 \rightarrow C_2H_4 \rightarrow C_2H_2$$

Figure 2.6b plots total C_2 and CS_2 yields versus t_c. CS_2 yield increases linearly with increasing t_c between t_c = 0.07s and t_c = 0.66s from 1% to 11%. CS_2 yield increases more gradually after t_c = 0.7s, reaching 14% at t_c = 1.33s. Note that C_2 yield does not decay during the initial rise of CS_2 yield, but falls during the more gradual increase of the CS_2 yield at t_c >0.2 s. This suggests that the major fraction of CS_2 evolved at low t_c likely arises from direct $CH_4 \rightarrow CS_2$ conversion, whereas the increased CS_2 selectivity at t_c >0.2 s likely reflects the conversion of C_2 intermediates to CS_2.

To examine the extent that C_2 products undergo conversion to CS_2 under SOCM conditions, the oxidation of C_2H_6 with S_2 was studied at a C_2/S_2 ratio ≈ 1.1 at 865 °C. Note that the relative product concentrations do not correspond to the ones under SOCM conditions. Ekstrom *et al.*[123] reported that CH_4 OCM conversion is strongly compromised by the addition of C_2 species due to competition for active sites. In the present study, the measured C_2H_6 conversions are > 50% at all WHSV values. Figure 2.6c shows the yield to CH_4, C_2H_4, C_2H_2, and CS_2. It is evident from Figure 2.6b and Figure 2.6c that at similar t_c = 0.66 s, CS_2 yield reaches 11% and 5% for methane and ethane, respectively, indicating that $C_2 \rightarrow CS_2$ oxidation is significantly slower than

$CH_4 \rightarrow CS_2$. This agrees with the Delplot analysis indicating that CS_2 is a first rank product. The increased CS_2 yield in Figure 2.6c is accompanied by a concomitant fall in C_2H_4 yield, which may reflect a $C_2H_4 \rightarrow CS_2$ process. The oxidation of C_2H_2 with S_2 was also studied at a C_2H_2/S_2 ratio of ≈ 1.1 at 865 °C (Figure S2.15). Similar to C_2H_6 oxidation, CS_2 selectivity increases gradually from 30% to 60%, within t_c = 0.088-0.500s, correlating with direct oxidation of C_2H_2 to CS_2.

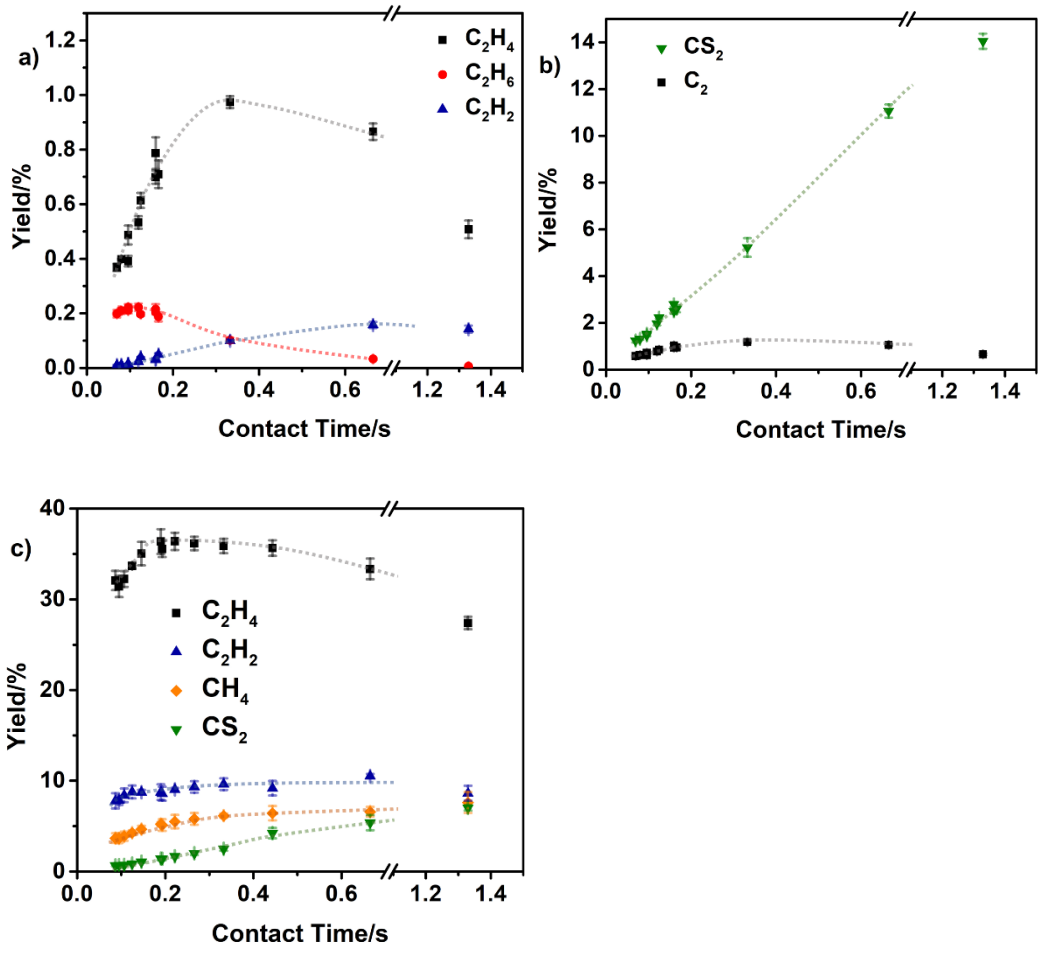

Figure 2.6: SOCM product distribution as function of contact time using methane and ethane as feed: (a) Methane: yield to C_2H_6 (red), C_2H_4 (black) and C_2H_2 (blue), (b) Methane: yield to the combined C_2 products (black) and CS_2 (green) in SOCM as a function of the contact time. (c) Ethane: yield towards C_2H_4 (black), C_2H_2 (blue), CH_4 (orange), and CS_2 (green). Reaction condition: 865°C, WHSV range: $0.13h^{-1} \sim 0.98h^{-1}$, $CH_4:S_2$ = 1.099 (a&b), $C_2H_6:S_2$ = 1.099(c)

2.4. Discussion of Experimental Results

The surface characterization discussed above confirms that the catalyst consists of two phases – FeS and FeS_2, with the latter likely the catalytically active surface. Further discussion of the active phase is provided below in the theoretical analysis. The changes in CH_4 conversion rate with changes in S_2 and CH_4 concentrations shown in Figure 2.4 indicate that the SOCM reaction, under the conditions examined here is essentially first-order in both CH_4 and S_2 partial pressures. The present first-order dependence on S_2 partial pressure suggests that the surface-bound S_2* species may be the dominant participant in the rate-limiting step and may account for the lower 66±8 kJ/mol activation energy versus the >100 kJ/mol typically reported for OCM.[106,121,124,125] The higher OCM activation energy may be due to fact that the C-H activation in OCM involves only a single oxygen site (where $r_{OCM} = k_{O2}^{1/2}P_{O2}^{1/2}$) whereas the apparent activation in SOCM is carried out over the S_2* ($r_{SOCM} = k'_{S2}P_{S2}$) and in addition may reflect the more energetically demanding dissociative adsorption of O_2 versus molecular adsorption of S_2.[99] This is analyzed in more detail in the Theoretical Discussion Section below.

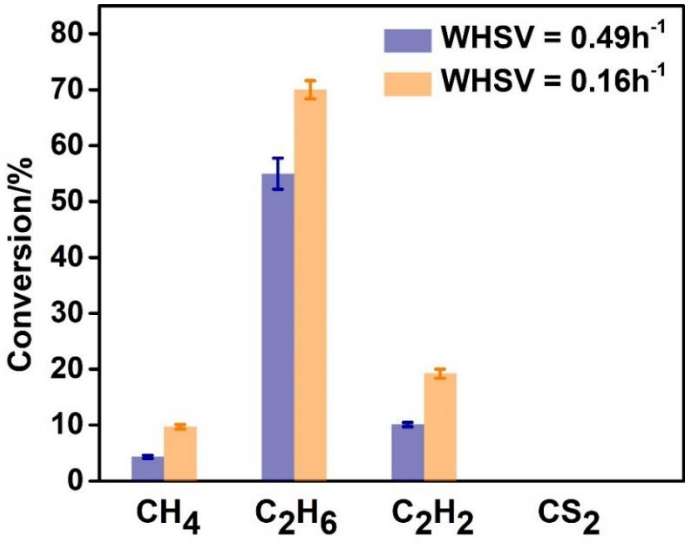

Figure 2.7: Comparative SOCM conversions of CH_4, C_2H_6, C_2H_2 and CS_2 at WHSV = 0.16h^{-1} and WHSV = 0.49h^{-1}. Reaction condition: at 865°C, CH_4:S_2 = 1.099, C_2H_6:S_2 = 1.099, C_2H_2:S_2 = 1.099, CS_2:S_2 = 1.099.

As shown in Figure 2.5, methane can be directly converted to C_2H_6, C_2H_4, and CS_2. Since the observed KIE is 1.78±0.18, the rate-determining step in SOCM reasonably involves methane C-H bond cleavage, in agreement with the first order dependence on

methane as well as previous studies of OCM.[106,119–121,126–128] This argues that the rate-limiting step in both SOCM and OCM is the cleavage of a methane C-H bond, irrespective of the oxidant.

Detailed analysis of the methane Delplot extrapolated intercepts of Figure 2.5 shows that C_2H_6, C_2H4, and CS_2 are directly formed from methane with the CS_2 formation rate being significantly faster than that of C_2H_6 and C_2H_4 formation. The direct formation of C_2H_4 from methane confirms the occurrence of the primary pathway involving the hydrogen abstraction of methyl radicals to form methylene intermediates and their subsequent coupling in SOCM under the present experimental conditions. C_2H_4 can also form via secondary paths involving the dehydrogenation of ethane. C_2H_2, however, cannot be formed directly from methane. The fact that CS_2 is readily formed from methane, while acetylene formation is prohibited, strongly suggests that the CH intermediate, if formed, has a much higher tendency for complete oxidation than coupling. Furthermore, Delplots of ethylene (Figure S2.11) confirm the dehydrogenation of ethylene primarily to form acetylene. Therefore, from the Delplots, reaction 7 in Figure 2.2 is ruled out as being significant, while the others are confirmed.

As shown in Figure 2.6, the SOCM product distribution varies with contact time t_c. Figure 6a shows that for SOCM C_2H_6 selectivity is highest at the lowest contact time whereas the maxima of the C_2H_4 and the C_2H_2 selectivity are at $t_c \approx 0.15$ s and $t_c \approx 0.36$ s, respectively. This strongly suggests that C_2H_4 and C_2H_2 are formed via C_2H_6 and C_2H_4 dehydrogenation, respectively. This seemingly contradictory finding can be explained by the characteristics of Delplots. As noted above, Delplots always provide the shortest reaction route. Consider the following reaction network: A → B → C, A → C, A being the reactant and B, C being the products. Then according to the first and second rank Delplots of A as the feed, B and C will both be found to be first rank products of A.

The reaction sequence results indicate that the predominant pathways for the formation of ethylene and CS_2 are different. CS_2 is primarily formed directly from CH_4, as evident in Figure 2.6, as the CS_2 selectivity increases with the C_2 selectivity at low contact time. In contrast, ethylene is likely formed via a primary pathway (evident from the Delplot) as well as a secondary path via ethane dehydrogenation. Early OCM studies by Hutchings[129] over Li/MgO and Lunsford[130] over $Mn/Na_2WO_4/SiO_2$ and

$Mn/Na_2WO_4/MgO$ reported that small amounts of C_2H_4 are formed directly from CH_4 at short contact times, but the majority of C_2H_4 is formed via C_2H_6 dehydrogenation. Analogous to the present results, at 830 °C Baerns[131] reported an OCM C_2H_6 selectivity maximum at shorter contact times than C_2H_4, providing further evidence for step-wise dehydrogenation. These issues are taken up further in the theory discussion below.

The dehydrogenation pathway is also supported by comparing relative reactivity of methane and C_2 species. Figure 2.7 shows the conversions of CH_4, C_2H_6, C_2H_2, and CS_2 at two different space velocities at 865 °C. The CS_2 conversion is zero, the CH_4 conversion is less than that of C_2H_2, while that of C_2H_6 is the highest at both contact times. Taking into account that for all t_c values, C_2H_4 selectivity is greater than that of both C_2H_2 and C_2H_6, and that C_2H_4 selectivity is always greater than C_2H_6 under the present kinetic measurement conditions, it is concluded that SOCM hydrocarbon reactivity increases in the order:

$$\mathbf{CH_4 < C_2H_4 < C_2H_2 < C_2H_6}$$

The greater reactivity of C_2H_6 versus C_2H_4 leads to the rapid oxidation of C_2H_6 to C_2H_4. This is reflected in the high C_2H_4/C_2H_6 selectivity ratio of 9-12 and has been observed previously in this Laboratory for other SOCM catalysts at t_c = 0.16 s. However, a significant fraction of C_2H_4 is also formed directly from CH_4 via coupling of CH_2 intermediates as argued by the Delplot analysis, and the theoretical analysis below.

2.5. Theoretical Analysis of the SOCM Reaction Mechanism

Complementary first principles density functional theory (DFT) calculations were carried out to elucidate the SOCM elementary reaction pathways, the nature of the active sites, and plausible mechanisms that govern the direct conversion of methane to C_2H_6, C_2H_4 and CS_2 over sulfided Fe_3O_4 as discussed above. The experimental studies discussed above indicate that the CH_x pathway (Pathway A in Figure 2.2) is the critical path in the activation of methane and in the formation of C_2 products and CS_2. As such, theory was used to examine the mechanism and the active sites for the activation of CH_4 and the formation of the desired C_2H_4 and undesired CS_2 products via the CH_x pathway. Such insights may aid in the design of more active and selective SOCM catalysts. Ab initio thermodynamic simulations were carried out to determine the lowest energy FeS_x surface structures and the nature of the active surface sites. The reaction energies and activation barriers for the adsorption and activation of S_2 and CH_4 and the

subsequent reactions to form C_xH_y and CS_2 products were calculated at 0 K. These energies were then used with Arrhenius expressions and kinetic models to establish the effects of temperature, the apparent activation barriers and the rate orders. Frequency calculations were carried out to determine the zero-point energy (ZPE), the thermal corrections to the energy and the entropies which were subsequently used to compute free energies. The details of the calculations are reported in the Methods section.

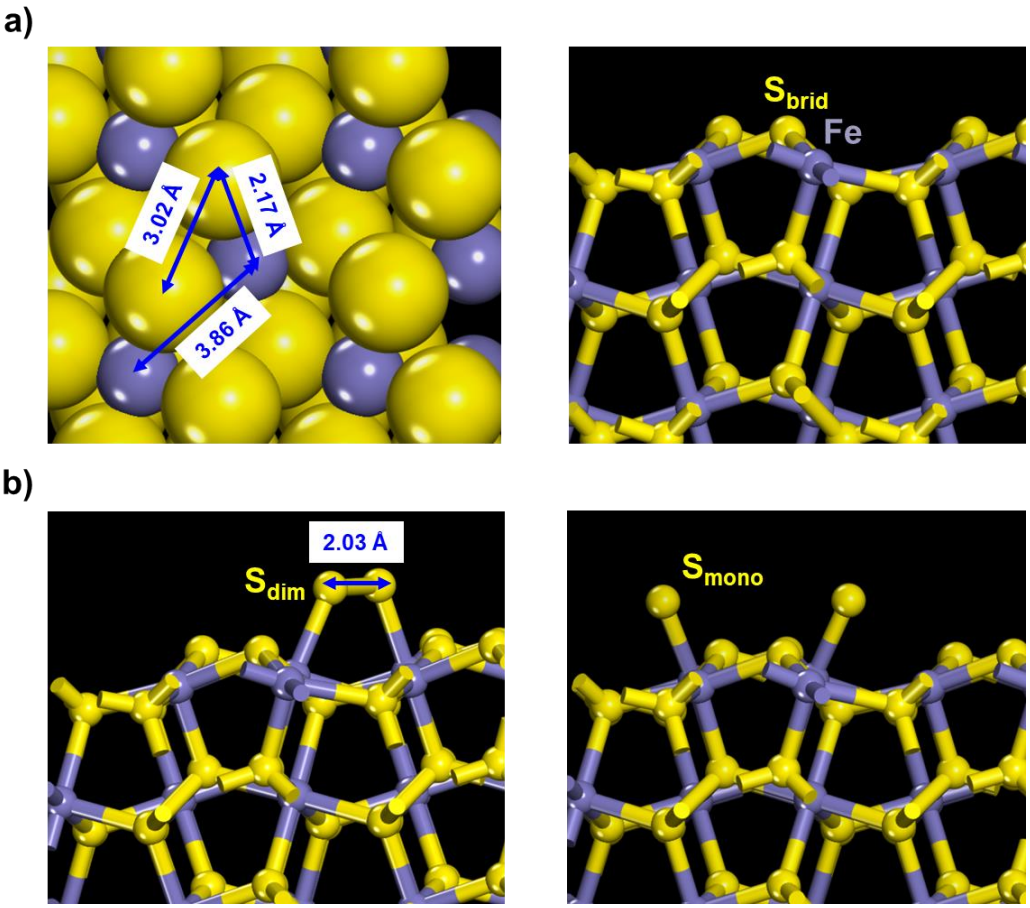

Figure 2.8: Different SOCM active sites on FeS_2: (a) Top (left) and side view (right) of the model sulfur terminated-001S FeS_2 surface that is used to model SOCM over a sulfided Fe_3O_4 catalyst. (b) Adsorbed sulfur dimer sites (S_{dim}) (left) and adsorbed monomeric sulfur sites (S_{mono}) (right) formed on the FeS_2 surface. As the disulfur is adsorbed over the FeS_2 surface, the S-S bond distance elongates from its gas phase distance of 1.91 Å to 2.03 Å. Sulfur atoms are shown in yellow whereas the iron atoms are shown in purple.

The pXRD and XPS analyses of the spent catalysts discussed above identify FeS to be the dominant phase with FeS_2 only found near the surface, in an amorphous phase or as a thin layer. Our theoretical analyses thus focused on both the FeS and FeS_2 phases.

Detailed DFT calculations show that while FeS is the dominant phase, the electronic energy barriers to activate methane at the exposed sulfur sites on the FeS surface are > 300 kJ/mol, and as such, the FeS surface and phase is catalytically inactive. A more detailed discussion of the theoretical analysis of the SOCM reaction over the model FeS surface is included in the SI. Overall, the computational and characterization studies indicate that the sulfur-terminated 001-S FeS_2 surface is the active surface for methane conversion and hence was used to model the working sulfided Fe_3O_4 surface and to examine the surface chemistry (see SI for additional details on modeling the catalyst surface).

The sulfur-terminated 001-S FeS_2 surface is comprised of exposed Fe and S_{brid} atoms that bridge the Fe surface sites (Figure 2.8a). This surface thus contains S_{brid}-S_{brid}, Fe-S_{brid}, and Fe-Fe site pairs that could all potentially carry out C-H bond activation. Methane activation was therefore examined at all three of these site pairs. The transition state for methane C-H activation over the Fe-Fe site pair could not be isolated, likely due to the very long 3.86 Å Fe···Fe distance which impedes concerted C-H activation over these pairs. However, activation barriers of 261 and 163 kJ/mol (ΔG_{act} = 362 and 254 kJ/mol respectively) were calculated for methane C-H activation over the S_{brid}-S_{brid} and Fe-S_{brid} sites, respectively. The lower Fe-S_{brid} site pair barrier suggests that such sites are favored for the initial activation of methane over the activation on the S_{brid}-S_{brid} sites.

In addition to these atomic site pairs, molecular S_2 can adsorb from the gas phase onto the exposed Fe sites on the catalyst surface, yielding chemisorbed S_2*. The two sulfur atoms on the bound S_2* can also be catalytically active. Similar molecularly adsorbed O_2* intermediates are thought to dissociate to form the active O* species responsible for OCM C-H activation.[75,132–134] Here we examine the adsorption and reactivity of gaseous S_2 on the FeS_2 surface. Molecular S_2 is found to adsorb most favorably in a di-σ configuration forming σ-bonds to two neighboring, exposed Fe sites (Figure 2.8b). The calculated adsorption energy of this S_2^* dimer (S_{dim}) is rather large, -215 kJ/mol. The favorable formation of these bound sulfur dimers in SOCM suggests that such sites may play a role in methane activation. These molecularly bound S_2* species can also dissociate over two vicinal Fe sites to yield monoatomic terminal sulfur site pairs (S_{mono}-S_{mono}; Figure 2.8b). While the direct activation of the S_2 dimer to form these monomeric species (S_{mono}) is much less exothermic (ΔE_{rxn} = -25 kJ/mol, ΔG_{rxn} = 78

kJ/mol) than S_2 adsorption (ΔE_{ads}= -215 kJ/mol, ΔG_{ads}= -104 kJ/mol), the barrier for the subsequent activation of the C-H bond of methane is significantly lower over S_{mono} site pairs than over the S_{dim} site as discussed below. Further details regarding the adsorbed S_{dim} and S_{mono} site formation are given in the SI.

The active catalytic surfaces present under working conditions are likely extensively covered with sulfur at the higher pressures of S_2 or H_2S used in the experiments discussed above. Exposed metal sites, however, can readily form at the present high SOCM CH_4/S_2 ratios (~1.099) and temperatures, as was observed over PdS. As such, the Fe-S_{brid}, S_{dim} (S_2*) and S_{mono}-S_{mono} site pairs are all likely present on the surface under reaction conditions and can participate in the surface chemistry.

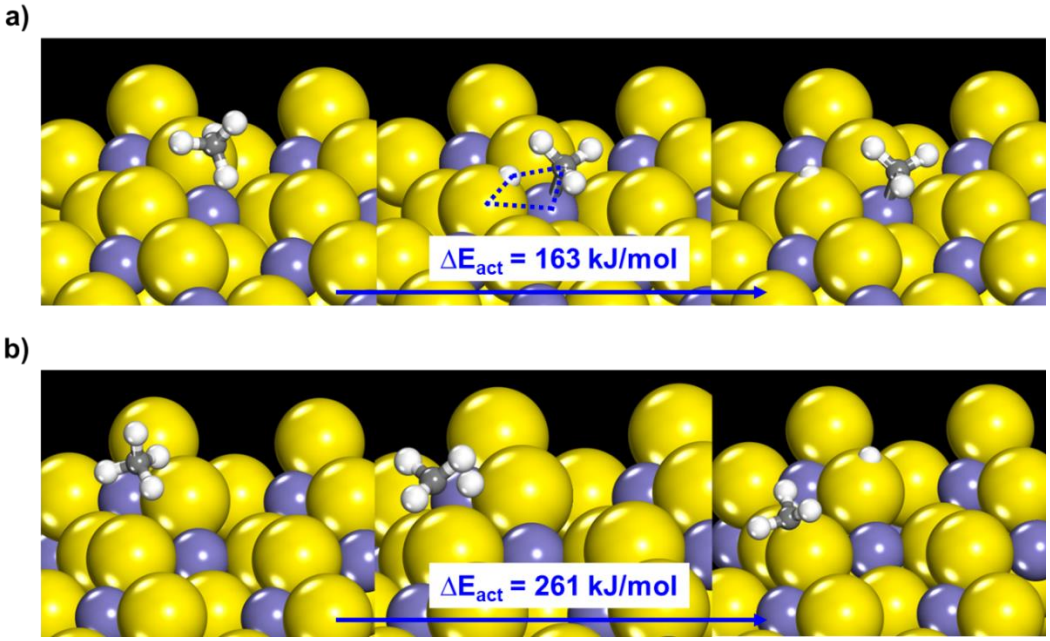

Figure 2.9: SOCM methane C-H activation over the surface sites of sulfided Fe_3O_4 catalyst (FeS_2)**:** Optimized reactant, transition state, and product structures for initial methane C-H bond activation over (a) Fe-S_{brid} site pairs and the (b) bridged sulfur site pairs (S_{brid}-S_{brid}). Methane activation over the Fe-S_{brid} proceeds via a four centered transition state (shown via dotted blue lines), whereas activation over S_{brid}-S_{brid} sites proceeds via a radical like mechanim. Yellow, sulfur; purple, Fe; white, H; grey, C.

Methane activation over the Fe-S_{brid} surface site pairs proceeds with a barrier of 163 kJ/mol (ΔG_{act} = 254 kJ/mol) via C-H bond scission which involves Fe surface atom insertion into the C-H bond of methane, together with a simultaneous H-abstraction by the neighboring S_{brid} site via a four-centered transition state as in Figure 2.9a. This

ligand-assisted C-H activation is similar to that found in σ-bond metathesis.[135–137] A Bader charge analysis[138] for this reaction shows an increase of 0.23 e^- on the CH_3 group and a loss of 0.18 e^- on the H atom in proceeding from the initial state to the transition state, suggesting heterolytic C-H bond activation. The transition state structure is very similar to those obtained for methane C-H activation over partially reduced PdS,[13] PdO,[11] CuO,[139] and MgO[117] surfaces.

In contrast to the above scenario, methane C-H bond activation over the bridging sulfur sites (S_{brid}-S_{brid}) proceeds via a homolytic mechanism with a barrier of 261 kJ/mol (ΔG_{act} = 362 kJ/mol) whereby the CH_3 and H take on free radical character as the C-H bond is activated (Figure 2.9b). The transition state for this initial C-H bond activation involves a H atom that is nearly fully bound to the surface S and a free CH_3 radical which weakly interacts with the surface. Bader TS charge analyses show a gain of 0.07 e^- for the CH_3 group, indicating radical-like character. Very similar, radical-like H-abstraction transition states are reported for oxygen-covered metal surfaces,[11,31,139] reducible metal oxides,[35,140] and sulfur-covered metal sulfides.[13] The present results are also consistent with recent studies on the oxidative coupling of methane over Li-doped MgO which indicate that CH_3 radical formation only proceeds in the presence of O_2.[117]

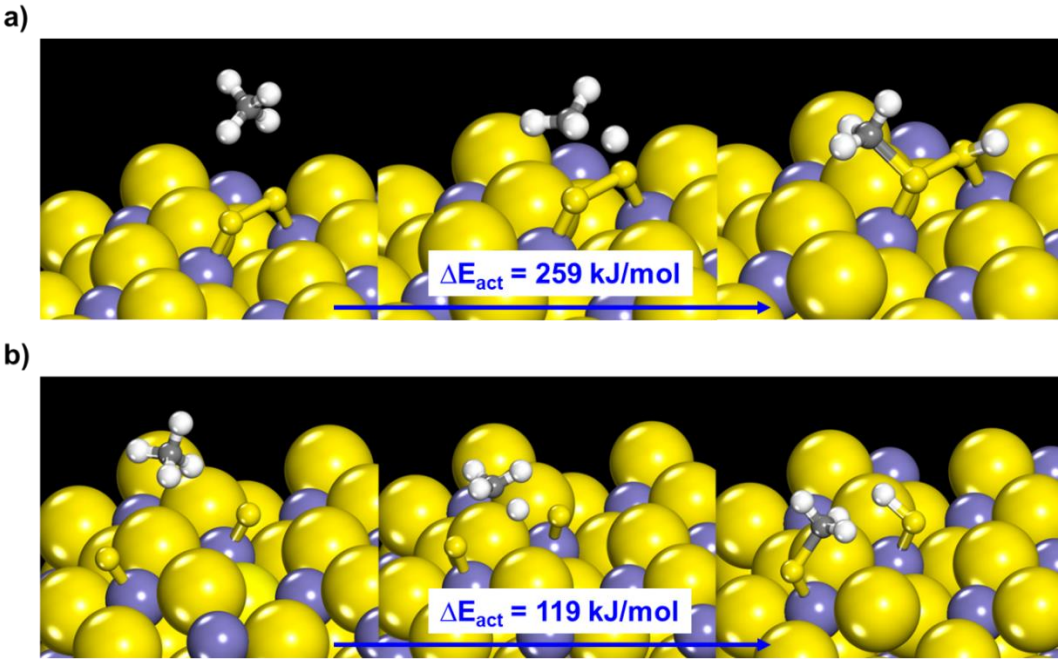

Figure 2.10: SOCM methane C-H activation over the adsorbed sulfur sites of sulfided Fe_3O_4 catalyst (FeS_2)**:** Optimized reactant, transition state, and product structures for initial methane C-H bond activation over adsorbed (a) S_{dim} site, and (b) S_{mono}-S_{mono} site

pairs. Methane activation over both S_{dim} as well as S_{mono}-S_{mono} site pairs proceed via radical like mechanism. Yellow, sulfur; purple, Fe; white, H; grey, C.

Methane activation over the S_{dim} dimeric and the terminal monomeric S_{mono}-S_{mono} sites which can also be present on the surface proceeds via a similar homolytic C-H activation mechanism (Figure 2.10a, Figure 2.10b). The intrinsic electronic energy barriers over the S_{dim} and S_{mono}-S_{mono} sites are computed to be lower than that over S_{brid}-S_{brid} sites discussed above (261 kJ/mol), with energies of 259 (ΔG_{act} = 343 kJ/mol) and 119 kJ/mol (ΔG_{act} = 204 kJ/mol), respectively. While the intrinsic C-H activation barrier over the two monomeric S_{mono} sites is significantly lower than over the S_{dim} sites, there is a higher energetic cost required to activate S_2^* (S_{dim}) to form these reactive S_{mono} sites. The higher energy cost thus limits the concentration of the S_{mono} sites, and in turn limits methane activation over these sites. The activation of methane over S_{dim} sites, on the other hand, is preceded by an exothermic adsorption step that lowers the overall apparent reaction barrier (see below for further discussion) and thus makes it equally probable to catalyze the C-H activation of methane as that over the Fe-S_{brid} sites.

The CH_3^* species produced in the aforementioned processes can subsequently react to form ethane, ethylene, and/or CS_2, the selectivities of which are governed by competition between the C-C coupling rates and those for C-H activation. C-C coupling steps to form C_2 products can either occur through the surface intermediates or through gas phase radicals which are generated via desorption of the adsorbed CH_x* intermediates from the catalyst surface. As noted above, since methane is found here to be most favorably activated over the Fe-S_{brid} and S_{dim} sites, we next examined the subsequent C-H activation, C-C bond formation, and desorption steps for the CH_3^*, CH_2^*, and CH^* intermediates adsorbed over the S_{dim} and Fe-S_{brid} site pairs to examine the selectivity towards different observed products. The results reported in Table 2.1 show that the free energy barriers for C-H activation are less than those for both the C-C coupling for CH_x^* intermediates as well as the desorption free energies on the S_{dim} sites. As such, the resulting CH_x^* intermediates formed on these surface sulfur sites preferentially undergo subsequent C-H activation steps as opposed to CH_x^* coupling or desorption. Methane, thus, would preferentially fully oxidize at these sites to form CS_2 via C-H activation, suggesting that while the adsorbed S_{dim} sites readily activate methane, they may also catalyze direct CS_2 formation as a primary product (Similar

results also hold for S_{mono}-S_{mono} site pairs. See Table S2.6). This is similar to the role of adsorbed O species which are thought to be responsible for methane over-oxidation to CO_2 in OCM over MgO.[75] This is also consistent with the present experimental data showing that CS_2 is produced as a primary product from CH_4. It is important, however, to note two things here – While the free energy barrier for desorption of CH_3* intermediate (127 kJ/mol) is higher than that for further activation to form CH_2* (115 kJ/mol), the difference is minimal enough to suggest that a significant proportion (~20%) of CH_3* intermediates adsorbed over the S_{dim} sites can also desorb as methyl radicals, which can then couple to form ethane in gas phase. Secondly, by comparing the free energy barrier for C-H activation of CH_2* (26 kJ/mol shown in Table 2.1) with that for coupling of CH_2* (64 kJ/mol), it can similarly be postulated that CH_2* coupling over these adsorbed sulfur sites to form ethylene can still proceed but does so to a much lower extent than that for C-H activation of CH_2* to form CS_2, thus accounting for the first-order Delplot observed experimentally for formation of ethylene.

Table 2.1: Computed SOCM C-H activation, C-C coupling free energy barriers, and desorption free energies over the Fe-S and S_{dim} catalytic sites of the FeS_2 surface.

Species	***C-H activation free energy barrier (kJ/mol)***		***C-C coupling free energy barrier (kJ/mol)***		***Desorption free energies (kJ/mol)***	
	Fe-S_{brid} site	S_{dim} site	Fe-S_{brid} site	S_{dim} site	Fe-S_{brid} site	S_{dim} site
CH_3	189	115	209	285	81	127
CH_2	188	26	48	64	234	292
CH	189	175	83	412	321	558

Similar analysis done over Fe-S_{brid} sites, comparing the free energy barrier for C-H activation of the adsorbed methyl intermediate (CH_3*) (see SI Figure S2.16a) with its desorption free energy, on the other hand, show a large difference in free energy barrier of 108 kJ/mol. As such, the large difference in the barriers suggest that desorption of the adsorbed methyl intermediates to form radicals significantly favored over further C-H bond activation at the Fe sites. Hence, over the Fe-S_{brid} sites of the FeS_2 surface, there is exclusive formation of methyl radicals occurring, which can then couple in the

gas phase to selectively form ethane, as is typically reported in OCM reactions.[76,141,142] The ethane formed can then likely undergo fast dehydrogenation to form ethylene rapidly as discussed previously, leading to the high observed ethylene selectivities.

The present results reveal that in SOCM, methane can be activated over dimeric and monomeric adsorbed sulfur site pairs to primarily form CS_2 as well as output C_2 products (ethane and ethylene) in smaller proportions compared to CS_2. In addition, over Fe-S_{brid} site pairs, methane activates to exclusively yield ethane as a primary product, which can then undergo rapid dehydrogenation to form ethylene. The active sites identified here have similarities to the active sites proposed for OCM with the dissociated O* sites proposed over La_2O_3 catalysts[134] and lattice Mg^{+2}-O^{-2} sites recently proposed for MgO based catalysts.[117] Thus, based on the different identified active sites, we can write an overall rate expression for methane conversion as the sum of methane activation rates over the different proposed sites as follows:

$$r = k_{C-H\_FeS}[CH_4][Fe][S_{brid}]\frac{z}{(L_1+L_2)} + k_{C-H\_Sdim}[CH_4][S_{dim}] + k_{C-H\_Smono}[CH_4][S_{mono}]^2\frac{z}{2L_1} \quad (2.1)$$

where L_1 and L_2 correspond to the total concentration of Fe and S_{brid} sites respectively, and z is the coordination number of the respective site with the z/L ratios thus corresponding to the probability of finding the two sites adjacent to each other. The terms $k_{C\text{-}HFeS}$, $k_{C\text{-}HSdim}$, and $k_{C\text{-}HSmono}$ refer to the rate constants for C-H bond activation of methane over the Fe-S_{brid}, S_{dim} and S_{mono}-S_{mono} sites respectively.

Equation 2.1 can be simplified further by noting the experimental results shown in Figure 2.6b reveal that >50 % of the reacted methane is converted directly to CS_2 via a primary pathway. Our computational studies have shown primary CS_2 formation to occur via methane activation over the adsorbed sulfur sites. As such, the measured activation barriers may be initially approximated as those for the direct methane activation occurring over the S_{dim} or S_{mono} sulfur sites, forming CS_2. Thus, the above rate order can further be approximated as follows:

$$r = k_{C-H\_Sdim}[CH_4][S_{dim}] + k_{C-H\_Smono}[CH_4][S_{mono}]^2\frac{z}{2L_1} \quad (2.2)$$

Now, assuming that the surfaces are fully equilibrated with the gas phase reactants under reaction conditions, we would expect the reaction to yield an equilibrium

distribution of S_{dim} or S_{mono} sites (derivation in SI). At low or moderate surface sulfur coverages, the rate law in eq. 2.2 reduces to the following:

$$r' = k_{app}[CH_4][S_2] \quad (2.3)$$

where r' is the surface rate, k_{app}, apparent rate constant for methane activation over the S_{dim} site is calculated to be $k_{C\text{-}H\_Sdim}K_{Sdim}z/2$ while that over the S_{mono} site is calculated to be $k_{C\text{-}H\_Smono}K_{Smono}z/2$ ($k_{C\text{-}H}$ and K refer to the intrinsic rate constant for C-H activation and the equilibrium constant for the formation of the adsorbed sulfur sites). The experimental barrier of +66 kJ/mol over FeS_2 reported above is significantly lower than barriers reported for OCM.[106,125,143] To better understand what leads to the unusually low apparent SOCM barriers, we used the DFT-calculated intrinsic activation barriers along with the heats of adsorption and the dissociative heats of adsorption of S_2, and the rate expressions derived from the elementary steps (see SI) to compute the apparent activation barriers at the S_{dim} and S_{mono}-S_{mono} sites to compare with the measured activation barrier.

The apparent activation barriers, $\Delta E_{app,}$ over the S_{dim} and S_{mono} sites were calculated to be 44 and 94 kJ/mol respectively. Assuming that the activation entropies for methane activation over the S_{dim} and S_{mono}-S_{mono} sites are equal due to the similar nature of the sites, it can be seen that the S_{dim} sites are likely the predominant sites for methane activation to form CS_2 and S_{mono}-S_{mono} sites are likely irrelevant. The calculated barrier for methane activation over S_{dim} sites, however are 20 kJ/mol lower than the overall apparent barrier for methane conversion of 66±8 kJ/mol measured experimentally. It is important to note that the experimentally determined activation barriers represent an average barrier over the different sites to form the different products (C_2 as well as CS_2). For simplicity, the computational apparent activation barriers here were derived by approximating the rate expression only in terms of methane activation over S_{dim} sites that lead to predominant CS_2 formation. A parallel methane activation pathway occurring over the Fe-S_{brid} sites, which lead to ethane formation, which also contributes to the overall apparent methane activation barrier, was neglected in the above analysis as it was not found to be dominant. A more appropriate Boltzmann weight-averaged barrier for overall methane conversion over the Fe-S_{brid}, and the S_{dim} sites would lead to a barrier that is much closer to the experimentally measured overall barrier of 66

kJ/mol. Hence, micro-kinetic modeling of the overall pathway considering parallel methane activation routes over the S_{dim} and Fe-S_{brid} sites results was done which results in overall apparent barriers of 57 kJ/mol for methane activation. (see SI for further information). In addition to the barriers, the micro-kinetic model reveals rate orders of 0.89 and 1 with respect to the partial pressures of CH_4 and S_2, in close agreement with experimentally determined rate orders.

The SOCM pathways established here are summarized in Figure 2.11. For the detailed energetics of reaction pathways over Fe-S_{brid}, S_{dim} and S_{mono} sites see SI Figure S2.31. Methane can be activated heterolytically over the Fe-S_{brid} site pairs and homolytically over adsorbed sulfur sites (primarily S_{dim}). The resulting CH_3^* surface species then react via two parallel pathways to yield C_1 intermediates that ultimately form CS_2 or C_2 intermediates and products. The CH_3^* intermediates desorb to form methyl radicals which then couple in the gas phase to form C_2H_6 which can further dehydrogenate rapidly to form C_2H_4, C_2H_2, and finally, fully oxidized CS_2. The CH_3^* surface intermediates can also undergo subsequent C-H activation steps to form CH_2^*, CH^*, C^* or CS_2 over the adsorbed sulfur sites. C_2H_4 is also formed via the coupling of CH_2^* intermediates over S_{dim} sites to some extent. The relative rate for each transformation is labelled as fast or slow in Figure 2.11. At short contact times, the low selectivity to the C_2 products vs. that for CS_2 formation shows that the rate C_2 products formation is slow versus the rate of CS_2 formation. The high C_2H_4 selectivity in the C_2H_6 conversion experiments and the lower C_2H_2 selectivity indicate that C_2H_6 dehydrogenation to C_2H_4 is significantly faster than C_2H_4 to C_2H_2 dehydrogenation. Finally, the gradual increase in CS_2 selectivity with increasing contact time for C_2H_6 and C_2H_2 oxidation shows that CS_2 formation rates from C_2 hydrocarbons are comparatively slow.

2.6. Comparison with conventional OCM

As discussed earlier, a first-order rate dependence is observed with respect to both methane as well as S_2 for SOCM. This rate dependence on CH_4 in SOCM is not unexpected since the first C-H bond activation is rate-limiting, and OCM exhibits similar behavior with a similar KIE.[131,143,144] However, the present first-order dependence on S_2 partial pressure is noteworthy since most OCM studies report half-order dependence on O_2 partial pressure, where rapid O_2 dissociation and subsequent CH_4 activation by chemisorbed O^* or lattice O^-/O^{-2} sites are generally proposed, with

the exact nature of active sites still debated. Recent investigations by Kwapien et al.[117] however indicate that the O^{-2} sites are the active sites for methane activation rather than the O^- sites originally proposed by Lunsford for Li-MgO catalysts.[45]

Further, the apparent SOCM activation energy obtained (66 kJ/mol) is significantly lower than reported OCM barriers which range from 113-172 kJ/mol over doped lanthanide and alkaline earth oxides[125,143] to ≥ 200 kJ/mol over Mn/Na_2WO_4 as well as other transition metal catalysts.[106,143] A good portion of the difference in the barriers is likely due to differences in what is measured in apparent barrier. In the Fe-S SOCM system discussed herein the apparent rate constant is proportional to $k_{C\text{-}H}K_{S2}$. In OCM systems where the rate is half order in oxygen, the apparent rate constant is likely proportional to $k_{C\text{-}H}K_{O2}^{1/2}$. The lower apparent activation energy for CS_2, suggests that CS_2 formation is kinetically more favorable than that of ethylene. In contrast, the source of over-oxidation product CO_2 in OCM is largely attributed to C_2 products oxidation.[130,145] OCM kinetic studies over several catalysts show that the CO_x formation rate for the oxidative conversion of C_2H_4 or C_2H_6 is up to 6.5x greater than that from the direct oxidation of CH_4.[145] As such, the intercept of CO_2 is zero in a first-rank Delplot for methane OCM over 16% Li/TiO_2, 9% $Li/NiTiO_3$, and 17% Li/La_2O_3 catalysts,[146] whereas a non-zero intercept is observed here for CS_2. The different Delplot ranks of CO_2 and CS_2, as well as the rate laws, thus indicate that the SOCM mechanism is significantly different from that of OCM, with the over-oxidation products formed predominantly via different pathways. Furthermore, the OCM literature describes non-zero intercepts for C_2H_6 and C_2H_4 in first-rank Delplots over the aforementioned catalysts.[146] Similar non-zero SOCM intercepts are seen here in Figure 2.5a which can be partially attributed to the relatively rapid rate of activating the weaker ethane C-H bond versus that of the stronger methane C-H bond in addition to direct ethylene formation via CH_2* coupling.[99]

The C_2 selectivity in this work stands in contrast to OCM where nearly all reported C_2H_4/C_2H_6 product ratios are << 1.[86,104,143,147–149] Considering the lower C-H bond dissociation energy of C_2H_6 (420 kJ/mol) versus C_2H_4 (463 kJ/mol),[150] a higher reactivity of C_2H_6 over C_2H_4 is, all other things being equal, expected for both OCM and SOCM. Note however that gas phase reactivity data, indicate that the C-H bond cleavage for hydrocarbons also depends on the H affinity of the H abstractant.[151,152] Previous OCM studies showed that the relative activation energies for C_2H_6 and C_2H_4

strongly depend on the activating species (see SI Table S2.5).[153] Thus, surface OCM O* species are likely to have different relative activation energies and give different product distributions than surface SOCM S_2* species, plausibly affording the higher SOCM C_2H_4/C_2H_6 ratios. Also, the direct formation of ethylene via coupling of CH_2* intermediates observed here can in addition account for the higher C_2H_4/C_2H_6 ratios. In OCM, the selectivity to acetylene is usually negligible[128] since any acetylene formed is immediately oxidized to CO_2 over metal oxide surfaces.[154] In contrast, acetylene readily forms in the present SOCM and is more stable because of the thermodynamically weaker S_2 oxidizing power versus O_2, limiting acetylene over-oxidation and affording selectivity of 2%.

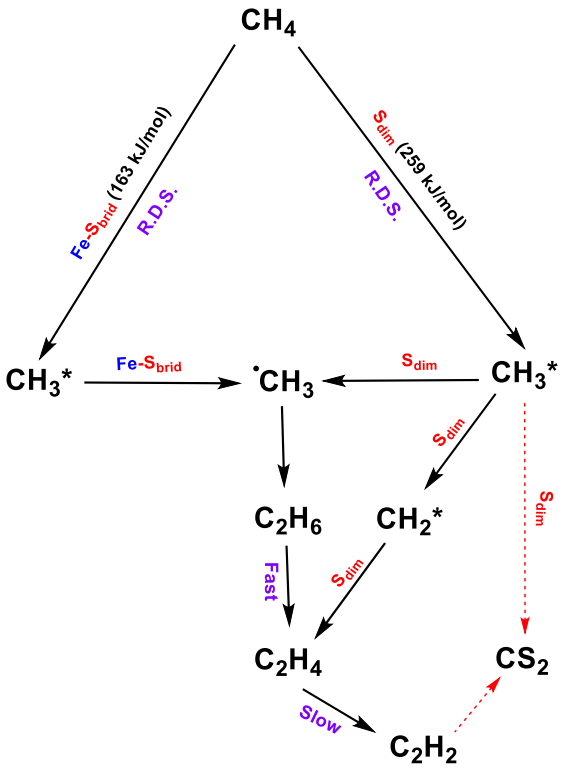

Figure 2.11: SOCM reaction scheme, summarizing the pathways for the reactions of CH_4 with S_2 at 865 °C. CH_4 is activated predominantly over S_{dim} or Fe-S sites, with the radical recombination, surface coupling, and dehydrogenation yielding C_2 products. CS_2 is largely formed directly from CH_4. The numbers in the brackets correspond to the activation energies (in kJ/mol) for methane activation (w.r.t gas phase methane) over the respective sites.

Note also an OCM study by Iglesia[155] where it was reported that H_2O generates ·OH radicals which enhance rate and selectivity. While SOCM studies of whether analogous

·SH radicals are important and similarly impact the reaction rate and C_2 yield, have not been conducted, the zero-order dependence on H_2S concentration does not currently support such a picture.

Table 2.2: Comparison of OCM vs. SOCM mechanism and catalytic performance

	OCM	SOCM (this work)
Conversion/Selectivity	CH_4 conversions: 40-50% C_2 selectivities: 60-70 %[45,46,103,143]	CH_4 conversions: 7-10% C_2 selectivities: 20-37%[14]
C_2H_4/C_2H_6 product ratio	Usually smaller than 1[104,143,149,156]	9 - 12[14]
Catalyst stability	Poor for many catalysts[46,143,157]	Negligible deactivation observed[14]
Over-oxidation	CO_2 formed via C_2 product oxidation[130,145]	CS_2 formed directly from CH_4
Apparent E_a	113 – 200 kJ/mol[106,143]	66 ± 8 kJ/mol
C_2H_2 formation	Not observed or not detectable[128]	1-2%
Rate law	Rate ~ $[CH_4]^1$ $[O_2]^{1/2}$ [106,130,131]	Rate ~ $[CH_4]^1$ $[S_2]^1$
KIE (CD_4/CH_4)	1.2 – 1.8[106,119–121]	1.78±0.18

2.7. Conclusions

S_2 vapor can serve as a "soft" alternative oxidant in the catalytic conversion of methane to C_2 products over sulfided Fe_3O_4 catalysts with selectivities as high as 33%, as reported previously.[14] Kinetic/mechanistic analysis of SOCM show that ethane and ethylene both are produced as a primary product of methane activation. DFT analysis suggest that ethane formation proceeds via coupling of gas phase methyl radicals

formed via desorption of the methyl intermediates from the Fe-S_{brid} and S_{dim} sites. Primary ethylene, on the other hand, is formed via coupling of CH_2 intermediates over the adsorbed sulfur sites (primarily S_{dim}) on the heavily sulfided Fe_3O_4 surface. C_2H_4 yields are limited by the direct conversion of CH_4 to CS_2 and by C_2H_4 over-oxidation. These C-H activation processes appear to proceed over the adsorbed sulfur sites which are highly active for C-H cleavage. This is a rather different scenario than that of OCM in which CO_x is predominantly formed via the oxidation of C_2 products. In addition to primary ethylene product formation, rapid dehydrogenation of C_2H_6 vs C_2H_4 leads to C_2H_4/C_2H_6 ratios >> 1 in SOCM, typical OCM processes yield C_2H_4/C_2H_6 ratios of <<1. In contrast to typical OCM kinetic studies which report methane conversion rates that are half-order in O_2, the SOCM reaction order is first-order in S_2. First-order behavior is consistent with the involvement of two sulfur sites in the rate-determining C-H activation of methane over the adsorbed S_2* sites (S_{dim}). A summary of reaction pathways over Fe-S, S_{dim} and S_{mono} sites is provided in Figure S2.31. The experimental apparent activation energy for SOCM of 66±8 kJ/mol is significantly lower than the 109-259 kJ/mol reported in OCM studies. The DFT results indicate that the lower barrier is the result of the strong heat of adsorption of sulfur on the surface which significantly lowers the apparent activation energy. A detailed comparison of SOCM versus OCM is presented in Table 2.2. The fundamental insights that result from this work should help to aid in the design of more active and selective catalysts for direct ethylene formation from methane.

2.8. Methods

Experimental

Fe_3O_4 nanopowder (≥97 % metals purity) was purchased from Alfa Aesar. Reactor measurements were carried out in the custom packed bed reactor which has been described previously.[13] The quartz reactor tube was charged with 200 mg of Fe_3O_4 catalyst with a particle size of 180-300 μm before each experiment. The catalyst was heated to 950 °C and held for 4 h in the presence of a gas stream that contained 0.28 wt. % S_2 and 0.33 wt. % H_2S before exposure to the reaction gases. The flow rates of the hydrocarbon gases and the Ar and He balance gases were controlled with Brooks Model 5850E mass flow controllers. The following hydrocarbon reactants were used in the reactor studies: 10.01% CH_4/He, 4.970% C_2H_6/He, 5.002% C_2H_2/He, 98% CD_4,

99.99% CH_4. The S_2 flow rate was adjusted by changing the temperature of the S_2 evaporator and subsequently measured gravimetrically as a function of temperature. The effluent distribution was continuously monitored by gas chromatography (Agilent 7890A, equipped with FID, TCD, and FPD detectors).

SOCM reactions were carried out at 865°C while varying the partial pressures of S_2 and CH_4 to determine the reaction orders and for studies varying the conversion to determine the product rankings and the reaction sequence in Delplot analyses. The apparent activation energy was calculated by plotting ln rate versus 1/T for temperatures ranging from 835 to 865 °C. Kinetic isotope studies were carried out at 865 °C. The Arrhenius plot shown in Figure S2.13 shows a slight change in the slope that occurs at ~ 900 °C, which is likely indicative of a change in the rate-limiting step. This may be the result of non-catalytic mass transfer (diffusion) effects or the result of other competing processes.[118] Considering that the accuracy of the kinetic isotope effect and activation parameters would be compromised if diffusion became rate-limiting, the data were collected at a lower temperature where the observed microkinetics would be controlled solely by the reaction of interest.[118]

Computational

As discussed in the main section, XRD and XPS studies carried out on the spent catalyst show presence of two phases in the catalyst, namely FeS and FeS_2. Thus, we used both FeS as well as FeS_2 surfaces as models for our computations examining SOCM reaction over the sulfided Fe_3O_4 surface. The detailed analysis outlying the models used for FeS and examination of the subsequent methane activation reactions occurring over the FeS surface is given in the SI. For the FeS_2 surface, Scanning Tunneling Microscopy (STM), Ultraviolet Photoelectron Spectroscopy (UPS), Low Energy Electron Diffraction (LEED) studies,[158–160] and theoretical calculations[161,162] suggest that the stoichiometric sulfur terminated 001-S surface of FeS_2 is the most stable. As such, the 001-S terminated surface of FeS_2 was used herein as a model surface for FeS_2 and to explore its catalytic reactivity.

The results reported herein were determined using plane-wave density functional theory calculations implemented in the Vienna ab initio simulation package (VASP).[163–166] The exchange and correlation gradient corrections were determined using the generalized gradient approximation (GGA) by Perdew-Burke-Ernzerhof (PBE).[167]

Plane waves were constructed using an energy cut-off of 396 eV with projector augmented wave potentials (PAW) used to describe the interaction between the core and valence electrons.[168] A 2x2x1 unit cell consisting of 12 atomic layers with 15 Å of free vacuum space was used for all the calculations. The bottom three layers of the slab were held fixed to the bulk structure. A 3x3x1 Gamma-centered k-point grid was used to model the first Brillouin zone. The k-point grid and energy cut-off were determined based upon the convergence calculations. Dispersive forces were accounted for by using the D2 method of Grimme.[170] Spin polarized calculations were performed considering the ferromagnetic nature of iron.[171] The electronic energies were converged to within a tolerance of 10^{-6} eV. All of the structures were optimized until the maximum force on each atom was calculated to be less than 0.05 eV/Å.

Initial transition states were isolated using the climbing image nudged elastic band (Cl-NEB) method.[172,173] These initial transition states were further refined using the dimer method.[174] In the Cl-NEB method, a reaction path is described by interpolating a series of images along the reaction coordinate joining reactants to products. The structures for each of these images were subsequently optimized until the tangential and normal forces were less than 0.3 eV/Å. The highest energy structures determined from the Cl-NEB method were then used in the dimer method and optimized until the forces converged to less than 0.05 eV/Å.

In order to determine the thermal corrections to the ground state electronic energies, the free energies (ΔG) of the elementary steps were determined using the formula,

$$\Delta G = \Delta E + \Delta E_{vib} + \Delta ZPE - T\Delta S \qquad (2.4)$$

where, ΔE is the ground state electronic energy determined from DFT calculations, ΔE_{vib} is the thermal corrections to the energy due to the molecular vibrations, ΔZPE is the zero-point energy corrections to the ground-state energy, ΔS is the entropy difference composed of the vibrational entropy (ΔS_{vib}) and translational entropy (ΔS_{trans}). All the thermal corrections to the electronic energies defined above are determined from the computed frequencies using statistical mechanics formulae. The loss in entropy (ΔS) for adsorption/dissociative adsorption reactions for molecular species are determined by using the formula put forth by Campbell and Sellers.[175]

2.9. Acknowledgments

The authors thank the Minnesota Supercomputing Institute (MSI) at the U. of Minnesota and the Pacific Northwest National Laboratory (PNNL) for use of computing resources.

2.10. Supporting Information

2.10.1. Catalytic Studies

Experimental Setup

Detailed information on the experimental setup was given in previous work.[13] The packed-bed reactor is situated in an oven, which contains a sulfur vapor generator, a preheat furnace and a reactor furnace. Elemental sulfur is generated by heating the oven to a temperature of 470 K and passing a constant argon stream through the sulfur vapor generator. To convert gaseous S_x into S_2, the preheat furnace is set to a temperature of 923 K. Subsequently, CH_4 and a trace of H_2S are added to the S_2/Ar effluent and the educt mixture is directed through the reactor furnace containing 200 mg of catalyst. After exiting the reactor region, the product stream is directed through an S_2 condenser to trap unreacted sulfur and the products are analyzed by GC (Agilent 7890 GC). The GC is equipped with Agilent HP- PLOT/Q column, flame ionization detector(FID), and thermal conductivity detector(TCD).

Experimental Procedure

The Fe_3O_4 nanopowder used in the current experiments was purchased from Alfa Aesar and has a purity of ≥97%. After pressing the oxides into pellets and grinding, particles with a diameter of 180 μm-300 μm were loaded into the reactor tube. After calibration of the hydrocarbon flow, the oven, preheat furnace and reactor furnace temperatures were set to their respective reaction temperatures in a flow of S_2/H_2S/Ar. After 4 h at the reaction temperature, the hydrocarbon flow was introduced. By using argon as a balance gas, the educt concentrations were held constant.

Determination of the Experimental Quantities

The selectivity of C_2 products, conversion of methane and yield of C_2 products are calculated as:

$$Selectivity = \frac{formed\ product\ of\ interest}{converted\ educt} \quad (2.5)$$

$$Conversion = \frac{converted\ educt}{supplied\ educt} \quad (2.6)$$

$$Yield = \frac{formed\ product\ of\ interest}{supplied\ educt} \quad (2.7)$$

This method (henceforth referred to as method A) of calculation was also used in previous works describing the SOCM reactions.[14] It is worth pointing out that this method is the technically rigorous method to calculate the selectivities and conversions. While this method takes all the gaseous products into consideration, the carbon deposit formed on the catalyst is not accounted for. Specifically, when the conversion is under differential condition(<5%), the numerator in equation 2.6 is quite small. As the numerator in equation 2.6 is also the denominator in equation 2.5, this could lead to significant deviations in the results calculated from equation 2.5. To take the carbon formation into consideration, we can calculate the carbon deposit selectivity by assuming all the carbon loss is due to the formation of coke. However it should be noted that, the estimated carbon deposit selectivity can be too high compared to the "true" carbon deposit selectivity, as not necessarily all the carbon loss is due to coke formation; the carbon loss could also be due to the formation of heavier hydrocarbons that are not detected in the GC, or due to random analytical errors. The conversions and selectivities to gaseous product and carbon deposit are calculated using method A and are listed in Table S2.1.

Table S2.1: Selectivity and conversion calculated using method A. Experimental condition: at 865°C, WHSV range: $0.13h^{-1}$ ~ $0.98h^{-1}$, CH_4:S_2 =1.099

Method A												
Contact time/s	C_2H_4 Selectivity /%		C_2H_6 Selectivity/%		C_2H_2 Selectivity/%		CS_2 Selectivity /%		CH_4 Conversion/%		CH_4 Conversion/%	
	μ	σ	μ	σ	μ	μ	σ	σ	μ	σ	μ	Σ
0.069	6.870	0.250	3.705	0.229	0.197	5.363	0.009	0.476	66.056	1.420	5.363	0.009

0.080	8.344	0.391	4.385	0.245	0.235	4.777	0.711	2.405	59.495	1.868	4.777	0.711
0.096	11.976	0.663	6.430	0.292	0.469	3.268	0.003	2.524	36.203	2.541	3.268	0.003
0.096	11.228	0.270	5.115	0.317	0.315	4.340	0.247	1.026	48.074	2.478	4.34	0.247
0.120	13.706	0.616	5.711	0.266	0.583	3.890	0.102	4.992	29.372	1.045	3.89	0.102
0.125	14.702	0.592	4.721	0.264	0.951	4.175	0.686	5.265	26.323	0.774	4.175	0.686
0.160	14.196	0.583	4.155	0.277	0.673	4.924	0.445	2.277	24.278	1.286	4.924	0.445
0.160	14.882	0.697	4.062	0.121	0.562	5.289	1.137	3.388	33.271	0.950	5.289	1.137
0.166	15.250	0.768	4.032	0.273	1.055	4.654	0.089	4.296	23.761	0.511	4.654	0.089
0.333	12.158	0.672	1.271	0.097	1.248	8.011	0.944	3.823	20.096	0.928	8.011	0.944
0.665	5.527	0.304	0.208	0.008	1.005	0.098	70.602	1.992	15.665	1.539	15.665	1.539
1.330	2.083	0.119	0.023	0.001	0.583	0.015	57.623	4.057	24.377	0.281	24.377	0.281

*μ: mean value, σ: standard deviation

Methane Conversion vs Time on Stream

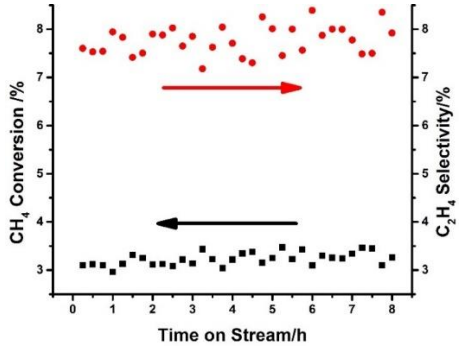

Figure S2.1: CH_4 Conversion and C_2H_4 selectivity versus Time on Stream. At 865 °C, WHSV = 0.628 h^{-1}, CH_4/S_2 ratio of 1.099.

The conversion of methane and selectivity towards ethylene were plotted versus the time on stream. As evident by Figure S2.1, the conversion and selectivity are stable at 3% and 8%, respectively for 8 h.

2.10.2. Characterization Studies

X-ray Diffraction of Fresh and Spent Catalysts

The X-ray diffraction studies of fresh, sulfurized, and spent catalysts were performed on Scintag XDS2300 Automated diffraction system, with four-circle pole-figure and residual stress device, thin film diffraction attachment and solid-state detector. This diffractometer is different from our previous (Rigaku Ultima), because the Scintag XDS2300 is not prone to Fe fluorescence and therefore provides a higher signal to noise ratio. The samples analyzed here are: fresh Fe_3O_4 precatalysts, sulfurized Fe catalyst, sulfurized Fe catalyst collected after TOS of 4h under kinetic measurement condition, and sulfurized Fe catalyst after TOS of 8h under kinetic measurement condition. The sulfurization condition used in this work is: 4 hours at 865°C, WHSV of 0.785 h^{-1} and H_2S partial pressure = 3.3%, S_2 partial pressure = 3.0%. The kinetic measurement condition is defined as: at 865°C, WHSV of 0.785 h^{-1} and CH_4:S_2 ratio = 1.099.

After the sulfurization, we observed that the only crystalline phase in spent Fe catalyst is FeS. The FeS phase is stable independent of the time on stream for the first 8 hours. We concluded that the bulk of the catalysts are a crystalline FeS phase.[108]

XPS Spectra of Spent Catalysts

The XPS of spent Fe catalysts were performed on The XPS (Thermo Scientific ESCALAB 250Xi), which is equipped with an electron flood gun and a scanning ion gun. The sample analyzed here is: the sulfurized Fe catalyst collected after TOS of 4h under kinetic measurement condition. The kinetic measurement condition is defined as: at 865 °C, WHSV of 0.785 h^{-1} and CH_4:S_2 ratio = 1.099.

It is evident from XPS spectrum that, on the surface of spent Fe catalysts after TOS = 4 h two iron sulfide species coexist. The 2p3 peak at BE= 707.19 eV corresponds to FeS_2 (literature 707.25eV[110])and the 2p3 peak at BE= 710.37 eV corresponds to FeS (literature 710.3eV[111]). The FeS_2 phase is not visible in pXRD experiment, and we hypothesized that either the FeS_2 exists in an amorphous phase, or exists exclusively on the surface of spent Fe catalysts as a thin layer. We therefore concluded that the two phases of interest for catalysis are FeS_2 and FeS.

Raman Spectrum of Sulfurized Catalysts

The Raman spectra were collected using a HORIBA LabRAM HR Evolution Confocal RAMAN system with multi-laser capability, using 532nm excitation wavelength. The sample analyzed here is Fe catalysts that were sulfurized but not used in SOCM reactions, the sulfurization condition used in this work is: 4 hours at 865°C, WHSV of 0.785 h^{-1} and H_2S partial pressure = 3.3%, S_2 partial pressure = 3.0%. We also attempted to collect Raman spectra on the spent Fe catalysts after SOCM reactions, however, only carbon peaks could be identified. We suspect the thick carbon layer prevented the catalysts underneath it from being probed.

The peaks observed in the Raman spectrum of the sulfurized Fe catalysts can be assigned to FeS and FeS_2. The peak with wavenumber ν= 319cm^{-1} can be assigned to FeS.[112] The peaks with wavenumber ν= 338, 373, and 425cm^{-1} can be assigned to FeS_2.[113] Note that compared with the literature value for the peaks corresponding to FeS_2, peaks observed in this work have shifted for as large as 5 cm^{-1}. It is well known that as the crystal size decreases, the Raman spectroscopy is susceptible to shifts in peaks.[114–116] Therefore, the shifts in peaks for FeS_2, paired with the fact that FeS_2 peaks did not appear in pXRD spectra, strongly suggest that FeS_2 exist in a crystalline phase, with rather small crystal sizes.

Scanning and Transmission Electron Microscopy on Sulfurized Catalysts

Transmission Electron Microscopy (TEM) was performed on the Fe catalysts after sulfurization for 6 hours without any SOCM reactions. The powders were dropped on lacey ultrathin C-coated Cu grids. Selected area electron diffraction (SAED) patterns and energy-dispersive X-ray spectroscopy (EDS) were obtained using a JEOL Grand ARM operated at 300 kV. The FeS_2 powders were observed as shown in Figure S2.2. SAED patterns of the particle along the [001], [102] and [012] zone axes were obtained as shown in Figure S2.2b-d All the diffraction patterns can be indexed with FeS_2 (space group $Pa\bar{3}$). In addition, energy-dispersive X-ray spectroscopy (EDS) was also performed on the same particle. Figure S2.3 shows the EDS spectrum, quantitative analysis shows the ratio of Fe:S is around 1:2. We therefore conclude that the two principal phases of interest for catalysis are FeS_2 and FeS.

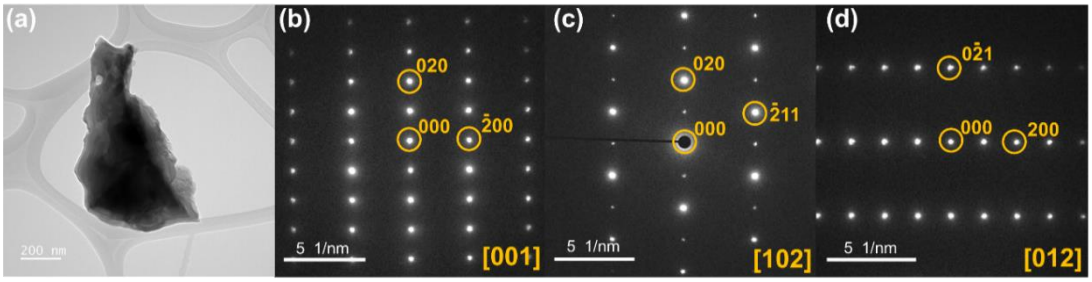

Figure S2.2: (a) Typical TEM image of FeS2 particle in the sample of Fe catalysts after sulfurization for 6 hours without any SOCM reactions. SAED pattens of the (b) [001], (c) [102] and (d) [012] zone axes respectively. All the diffraction patterns can be indexed with FeS2 (space group $Pa\bar{3}$).

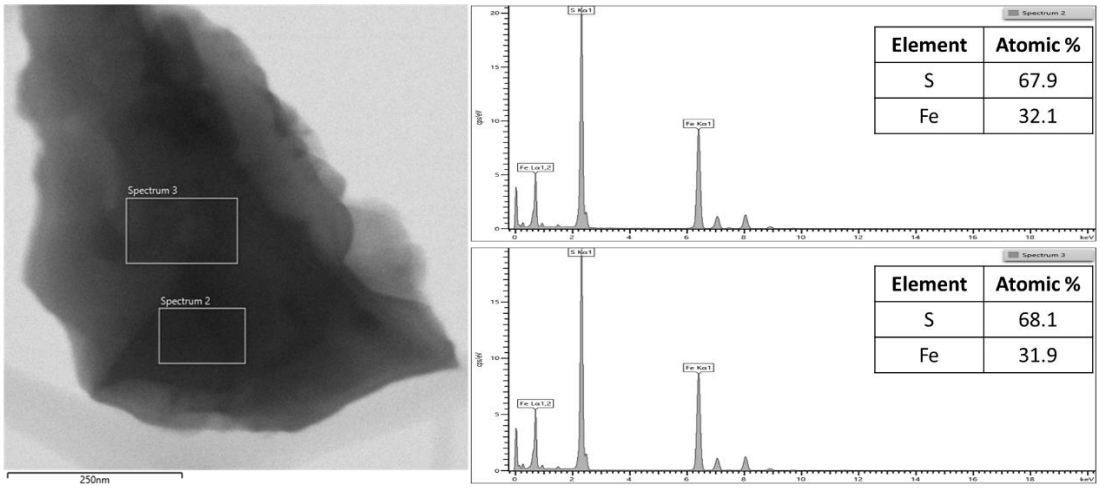

Figure S2.3: Bright-field scanning transmission electron microscope image and EDS spectra of the selected areas on a particle in the sample of Fe catalysts after sulfurization for 6 hours without any SOCM reactions. The peaks of Fe and S are indexed in the spectra. The quantitative analysis shows the ratio of Fe:S is around 1:2.

2.10.3. Rate order determination

Determination of the Reaction Order in CH_4

In order to reduce the S_2 conversion (closer to differential regimes), we systematically increased the weight hourly space velocity (WHSV, defined as CH_4 mass flow/catalyst mass) by increasing the mass flow rate of CH_4. At the WHSV values of 0.785 h^{-1}, 0.942 h^{-1} and 1.099 h^{-1}, the S_2 conversion decreased to 10-13 %, 12-15 %, and 13-15 % respectively. In order to determine the kinetic order, the reaction rate was divided by the arithmetic mean between the initial and the exit S_2 concentration (C_{S2}) to take into account the variation of the S_2 concentration within the catalyst bed. The reaction rate is calculated in a similar manner in the activation energy section.

Determination of the Reaction Order in S_2

In order to reduce the CH_4 conversion (closer to differential regimes), we systematically increased the weight hourly space velocity (WHSV, defined as CH_4 mass flow/catalyst mass) by increasing the mass flow rate of CH_4. At the WHSV values of 0.785 h^{-1}, 0.942 h^{-1} and 1.099 h^{-1}, the CH_4 conversion are well below 6%. Since the conversion is low, the rate is calculated by assuming a differential condition.

SOCM Reaction Rate Law: Influence of H_2S and CS_2, and apparent rate of formation for ethylene and CS_2

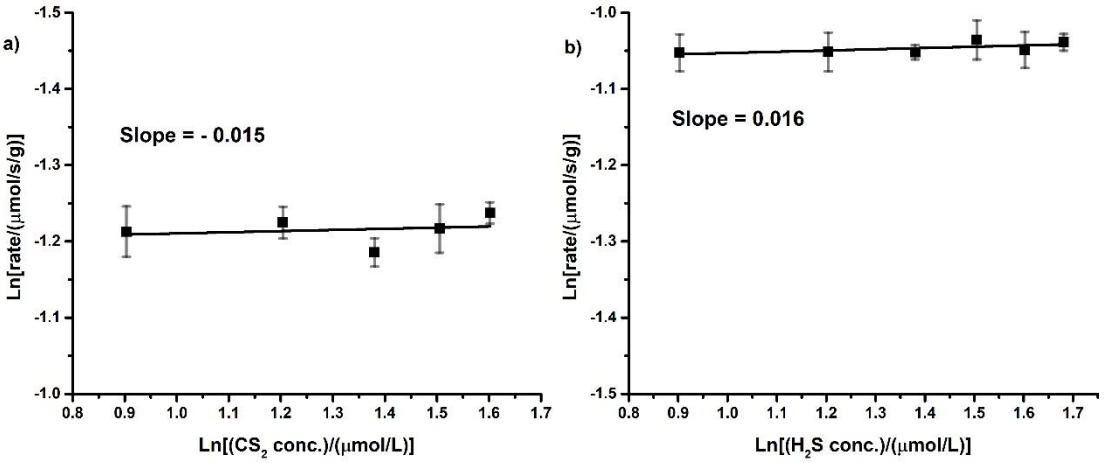

Figure S2.4. Influence of H_2S and CS_2 concentrations on the SOCM reaction rate: (a) natural logarithm of reaction rate vs. natural logarithm of CS_2 concentration and (b) the natural logarithm of the reaction rate vs. the natural logarithm of H_2S concentration. Experiment conditions: WHSV = 0.785h^{-1}, 865°C.

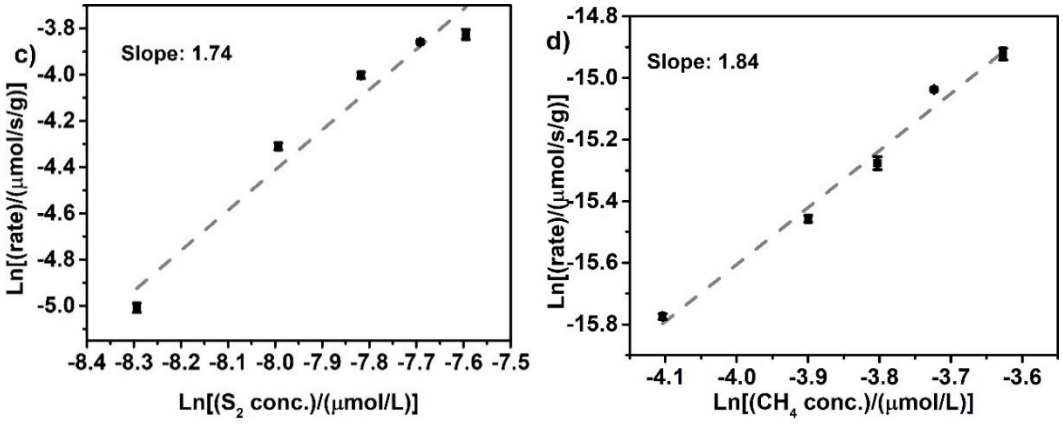

Figure S2.5. Influence of S_2 and CH_4 concentrations on the apparent formation rate of ethylene: (a) natural logarithm of apparent formation rate of ethylene vs. natural logarithm of S_2 concentration and (b) the natural logarithm of apparent formation rate of ethylene vs. the natural logarithm of CH_4 concentration. Experiment conditions: WHSV = 0.785h^{-1}, 865°C.

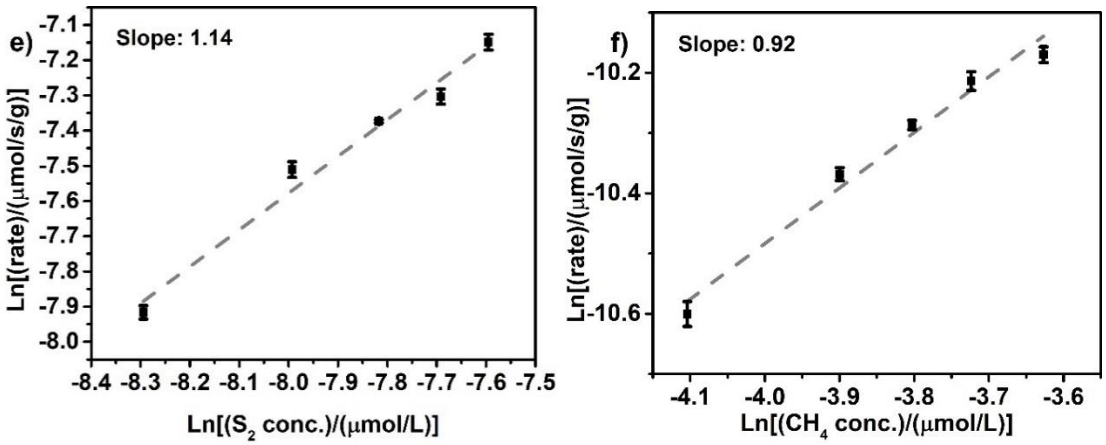

Figure S2.6. Influence of S_2 and CH_4 concentrations on the apparent formation rate of CS_2: (a) natural logarithm of apparent formation rate of CS_2 vs. natural logarithm of S_2 concentration and (b) the natural logarithm of apparent formation rate of CS_2 vs. the natural logarithm of CH_4 concentration. Experiment conditions: WHSV = 0.785h^{-1}, 865°C.

As shown in Figure S6 and S7, the apparent rate of formation of ethylene is r = $k[CH_4]^{1.84}[S2]^{1.74}$, while the apparent rate of formation of CS_2 is r' = k'$[CH_4]^{0.92}[S2]^{1.14}$. Considering the calculation results presented below and in the main text, it is not surprising that the apparent rate of formation of ethylene has a rate expression that is closer to second order in methane and S_2 while the apparent rate of formation of CS_2 is more reminiscent of the observed overall rate expression, which is first order in both methane and S_2.

2.10.4. Determination of the Activation Energy

To determine the activation energy of CH_4, an Arrhenius plot was employed. Since for all reactions taken into account, the conversion of CH_4 was lower than 10% and did not change with TOS, it is reasonable to apply the steady-state approximation and to assume that the reaction is under differential conditions.

Thus, the reaction rate can be simply given by Eq. 2.8:

$$Reaction\ rate \quad r_{CH_4} = c_{CH_4} f_{CH_4} v, \tag{2.8}$$

where c_{CH_4} is the concentration of methane, f_{CH_4} is the conversion of methane and v is total flow rate.

And the reaction rate constant is then given by Eq. 2.9:

$$Reaction\ rate\ constant\ k = \frac{vf_{CH_4}}{c_S}, \quad (2.9)$$

where c_S is the concentration of sulfur.

With Eq. (2.9) and the Arrhenius equation $\ln(k) = -\frac{E_a}{R}\left(\frac{1}{T}\right) + \ln(A)$, the apparent activation energy (E_a) can be determined by measuring the conversion of methane. Similarly, by calculating the rate of formation of CS_2 and C_2H_4 from methane, the apparent activation energies for the formation of CS_2 and C_2H_4, respectively, was calculated. Figures S2.7-S2.9 show the Arrhenius plots for these trials, and Table S2.2 shows activation energies acquired from separate runs in the temperature range of 835°C to 865°C:

Table S2.2: Measured apparent activation energy for SOCM in the temperature range of 835°C to 865°C.

Trial	Activation Energy (CH_4 conversion)/ (kJ/mol)	Activation Energy (CS_2 Formation)/ (kJ/mol)	Activation Energy (C_2H_4 formation)/ (kJ/mol)
#1	67.0 ± 1.70	38.8 ± 3.34	82.8 ± 2.22
#2	69.9 ± 2.42	34.4 ± 4.30	82.9 ± 4.02
#3	63.6 ± 2.23	44.4 ± 4.57	88.3 ± 2.79
#4	50.7 ± 3.55	39.1 ± 4.49	84.7 ± 2.47
#5	58.9 ± 1.67		
#6	75.9 ± 1.91		
#7	67.8 ± 1.83		

By taking the average of the second column of the apparent activation energy for methane conversion shown in Table S2.5, the activation energy is concluded to be 65.9 ± 8.2 kJ/mol or 15.74 ± 1.98 kcal/mol.

According to the DFT calculations, CH_4 is adsorbed and then activated on the surface adsorbed sulfur sites, or the Fe-S_{brid} sites. At the transition state, the KIE can be written

as a ratio of the rate of CH_4 vs. CD_4. And because the reaction conditions are kept strictly the same:

$$KIE = \frac{r_{CH4}}{r_{CD4}} = \frac{k_{CH4}}{k_{CD4}} = \frac{(\frac{Q_{TS,CH4}}{Q_{CH4}Q_{active\ sties}})}{(\frac{Q_{TS,CD4}}{Q_{CD4}Q_{active\ sties}})} = \frac{Q_{TS,CH4}}{Q_{TS,CD4}} \times \frac{Q_{CD4}}{Q_{CH4}} \quad (2.10)$$

where Q is the partition function. Considering that Q can be further divided into translational, rotational, vibrational, and electronic partition functions:

$$Q = Q_{trans}Q_{rot}Q_{vib}Q_{elec} \quad (2.11)$$

We can now consider the separate contribution from each partition function. Note that for transition state, because it is adsorbed, the translational and vibrational energy contribution should be negligible. Therefore, for the first two terms in equation 2.11, only gaseous molecules are considered:

$$\frac{Q_{trans,CD4}}{Q_{trans,CH4}} = (\frac{m_{CD4}}{m_{CH4}})^{3/2} \quad (2.12)$$

$$\frac{Q_{rot,CD4}}{Q_{rot,CH4}} = (\frac{I_{CD4}}{I_{CH4}})^{3/2} \quad (2.13)$$

where I is the moment of inertia of the molecule.

Because $Q_{vib} = \frac{1}{1-e^{-\theta_v}}$ where $\theta_v = \frac{h}{2\pi k_b}\sqrt{\frac{k}{\mu}}$, $\frac{Q_{vib,CD4}}{Q_{vib,CH4}} \approx 1$ and $\frac{Q_{vib,TS,CH4}}{Q_{vib,TS,CD4}} \approx 1$

And lastly, since electronic separation from ground state is usually very large, $Q_{elec} \approx g_0$

$$\frac{Q_{elec,CD4}}{Q_{elec,CH4}} = e^{\frac{(E_{CH4}-E_{CD4})}{RT}} \quad (2.14)$$

$$\frac{Q_{elec,TS,CH4}}{Q_{elec,TS,CD4}} = e^{\frac{(E_{TS,CD4}-E_{TS,CH4})}{RT}} \quad (2.15)$$

$$KIE = \frac{Q_{TS,CH4}}{Q_{TS,CD4}} \times \frac{Q_{CD4}}{Q_{CH4}} = (\frac{m_{CD4}}{m_{CH4}})^{3/2}(\frac{I_{CD4}}{I_{CH4}})^{3/2}\ e^{\frac{(E_{TS,CD4}-E_{CD4}+E_{CH4}-E_{TS,CH4})}{RT}}$$

$$= 3.96e^{\frac{(E_{TS,CD4}-E_{CD4}+E_{CH4}-E_{TS,CH4})}{RT}} \quad (2.16)$$

where E is the zero-point energy of corresponding species. In particular,

$$E_{TS,CD4} - E_{CD4} + E_{CH4} - E_{TS,CH4} = \Delta E_{CD4} - \Delta E_{CH4} \quad (2.17)$$

where ΔE is the zero-point energy difference between the gaseous molecule and transition state.

Assuming a methyl radical-like transition state structure, then $\Delta E_{CD4} - \Delta E_{CH4} \approx 0$,[106] and thus the KIE is calculated to be 1.67 at 835°C.

In our current experiment of the KIE is determined to be 1.78 ± 0.18. This is in good agreement with the calculated KIE assuming a radical-like transition state. Indeed, over S_{dim} sites, the transition state for the initial C-H bond activation involves a H atom that is nearly fully bound to the surface S and a free CH_3 radical which weakly interacts with the surface. Bader TS charge analyses show a gain of 0.07 e^- for the CH_3 group, indicating radical-like character(see main text). Very similar, radical-like H-abstraction transition states are reported for oxygen-covered metal surfaces,[11,31,139] reducible metal oxides,[35,140] and sulfur-covered metal sulfides.[13] The present results are also consistent with recent studies on the oxidative coupling of methane over Li-doped MgO which indicate that CH_3 radical formation only proceeds in the presence of O_2.[117] Therefore it is reasonable to conclude that, a radical-like, weakly-bound, late transition state structure would indeed be in agreement with the measured KIE.

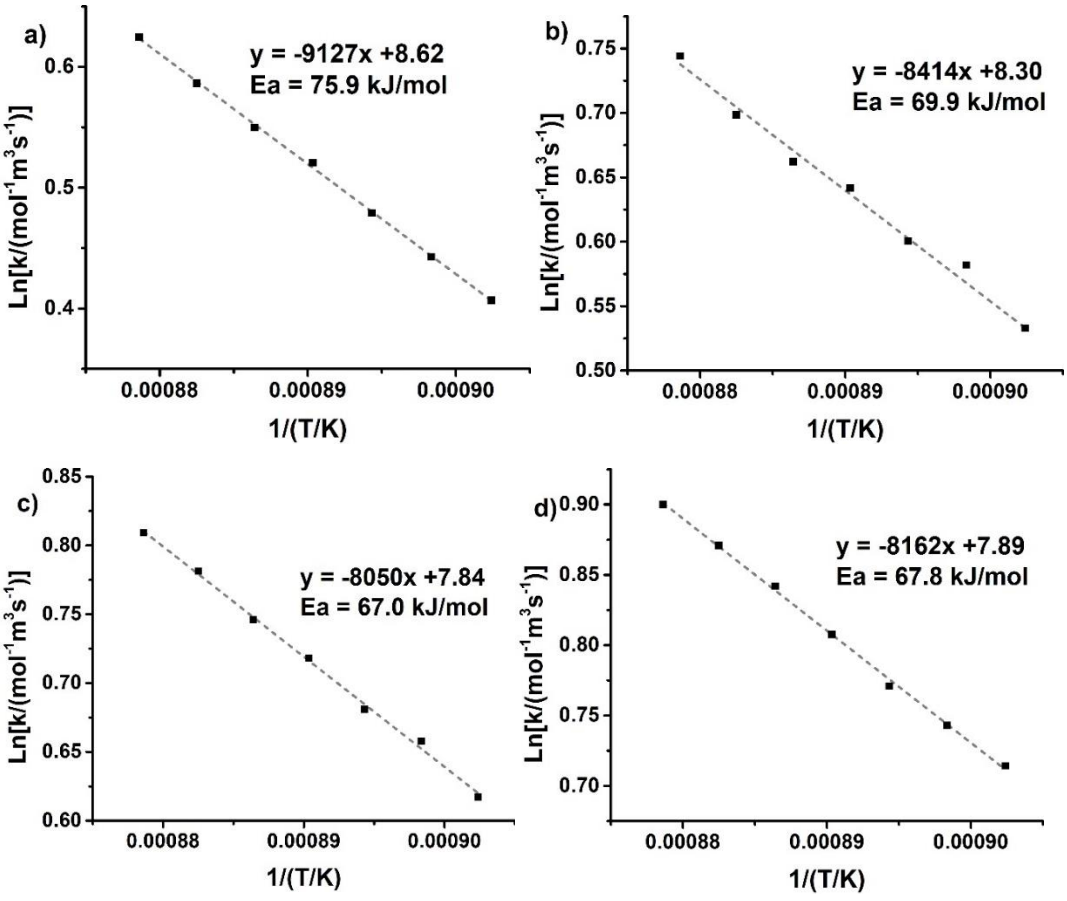

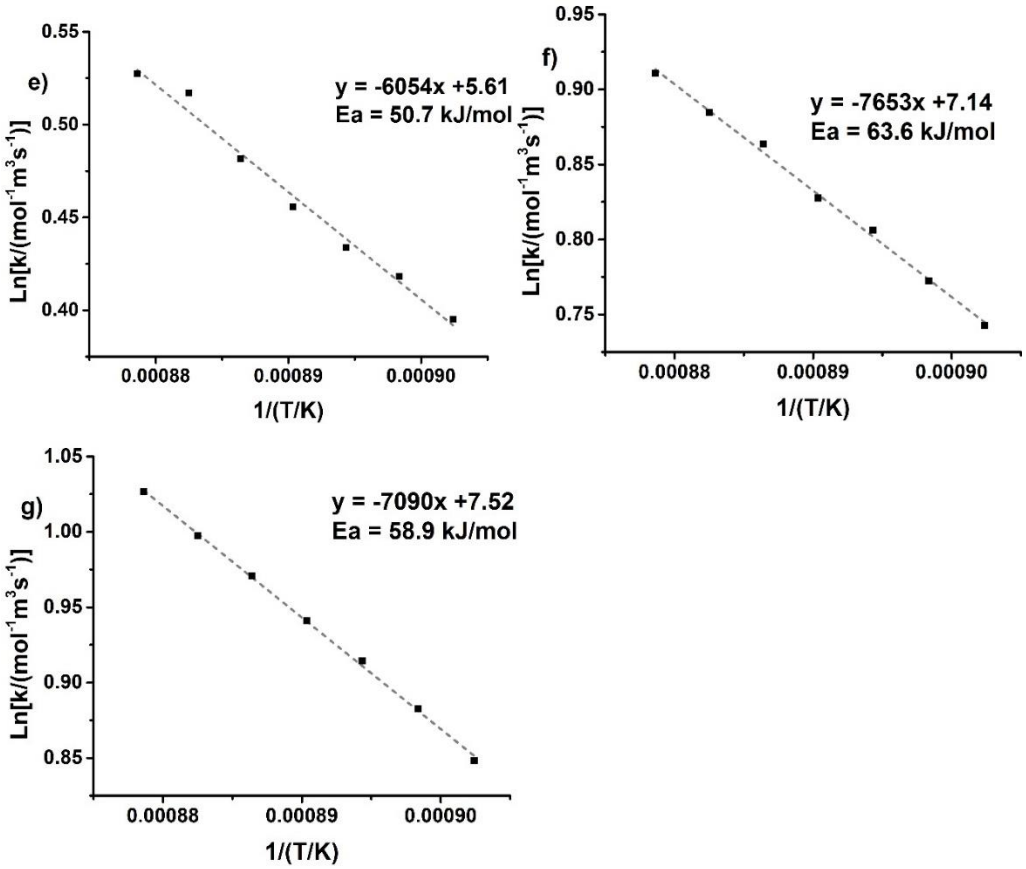

Figure S2.7. Arrhenius plots of the rate of methane consumption. Experiment conditions: WHSV = 0.785h^{-1}, 835 - 865°C.

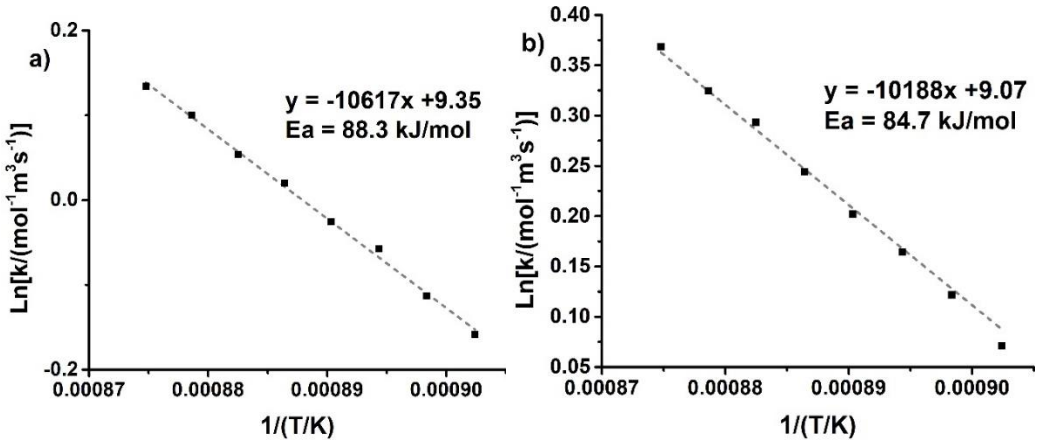

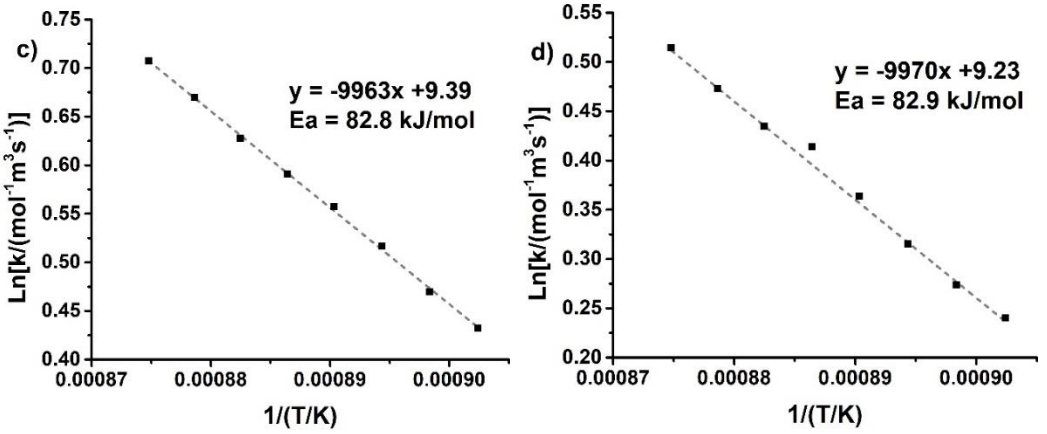

Figure S2.8. Arrhenius plots of the rate of ethane formation. Experiment conditions: WHSV = 0.785h^{-1}, 835 - 865°C.

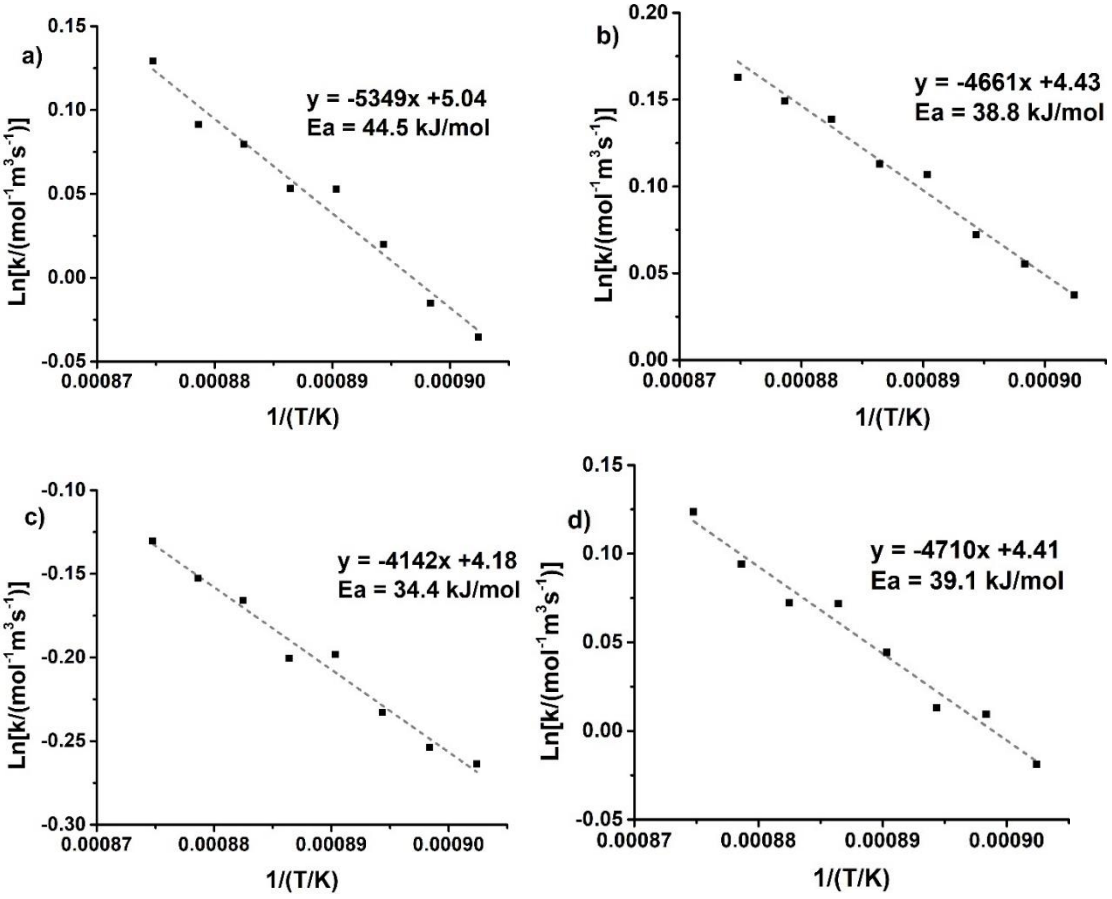

Figure S2.9. Arrhenius plots of the rate of CS_2 formation. Experiment conditions: WHSV = 0.785h^{-1}, 835 - 865°C.

2.10.5. Determination of the Kinetic Isotope Effect

The kinetic isotope effect (KIE) was investigated to compare the reaction constant for CD_4 and CH_4. A 2-way valve was employed to switch between non-isotope labelled and isotope labelled feed gas. All conversions and selectivities were collected only after the equilibrium was reached. By applying aforementioned assumption, the reaction constant could be acquired in a similar manner (Eq. 2.18).

$$Reaction\ rate\ r_{CD_4} = c_{CD_4} f_{CD_4} v \tag{2.18}$$

And the KIE is given by the ratio between the reaction rates for CH_4 and CD_4:

$$KIE = \frac{r_{CH_4}}{r_{CD_4}} \tag{2.19}$$

which can be further simplified to eq. 2.19 if the total space velocity and concentration remain the same for CD_4 and CH_4:

$KIE = \frac{f_{CH_4}}{f_{CD_4}}$,where f_{CH4} and f_{CD4} are conversions of CH_4 and CD_4, respectively.(2.20)

Table S2.3 shows the results of 4 independent trials of KIE measurements.

Table S2.3: Measured KIE at 865 °C and the WHSV 0.628 h^{-1}

Trial	CH_4 Conversion /100%	CD_4 Conversion /100%	KIE
#1	0.026	0.015	1.73
#2	0.027	0.015	1.80
#3	0.030	0.016	1.81
#4	0.030	0.014	2.14

The average KIE of 4 trials is 1.78 ± 0.18.

Ethylene is an intermediate, formed from methane and can react to form acetylene. Both pathways have been confirmed by the mechanistic studies. However, it is also noteworthy that, in our current model, ethylene and CS_2 are formed at different active sites, both directly formed from methane (see below). In this case, if the consumption of ethylene is only a small fraction of the total amount of ethylene generated at steady

state, we can still consider ethylene formation a parallel reaction with the formation of CS_2, rather than an intermediate step as in ethylene → acetylene reaction.

Under the conditions for the measurement activation energy, the temperature was varied between 835°C to 865°C. Methane and sulfur are fed at a 1.099 ratio, and total flowrate is 120mL/min, ensuring a t_c = 0.096s. Under this condition, we listed the ratio of ethylene and acetylene yield in Table S2.4.

Table S2.4: Ratio of ethylene yield to acetylene yield in the measurements of activation energy. T = 835°C -865°C, WHSV = 0.98h^{-1}, CH_4:S_2 = 1.099

T/°C		835	840	845	850	855	860	865
X_{C2H4}:X_{C2H2}	μ	20.473	21.870	22.048	22.848	22.890	23.172	23.472
	σ	0.108	0.164	0.098	0.300	0.273	0.300	0.136

*μ: mean, σ: standard deviation

As can be seen in Table S2.4, under this condition only a very small fraction (<5%) of ethylene is converted to form acetylene (tc = 0.166s). Indeed, even at the lowest contact time(t_c = 0.07s) tested in this work, the ratio of ethylene yield to acetylene yield to is greater than 10. As t_c is increased, this ratio increases. Therefore, it is conceivable that the measurement of apparent activation of ethylene reflects the reaction of methane → ethylene, rather than in the reaction of ethylene → acetylene.

2.10.6. Delplots

The Delplot method developed by Bhore et al.[122] plots the yield of a particular product (y) divided by the reaction conversion (x) versus conversion. Extrapolating the curves back to zero conversion $\left(\lim_{x\to 0}\frac{y}{x}\right)$ allows one to discern the primary products which have non-zero positive intercepts and the non-primary products which approach zero. This is known as the first order Delplot. Similar, higher-ranked Delplots can be constructed by plotting y/x^r where r is the product rank (primary =1, secondary = 2, tertiary =3, etc.) vs. conversion to determine the secondary, tertiary, and extended products. The same analyses can also be used to identify the minimum number of slow steps between the reactant and the product of interest in a reaction network.

The first order and second order Delplots were plotted to determine the smallest number of slow steps between CH_4 and C_2H_6, C_2H_4, C_2H_2 and CS_2. The experiment was carried out in the aforementioned reactor and at 865°C . The different conversions were achieved by varying the total flow rate with the CH_4:S_2 ratio = 1.099.

The following Delplots of C_2H_2 show that most acetylene is converted to CS_2 directly, as the intercept is non-zero in first-rank Delplot but diverges in second rank Delplot. The same trend is observed for C_2H_4 and CH_4.

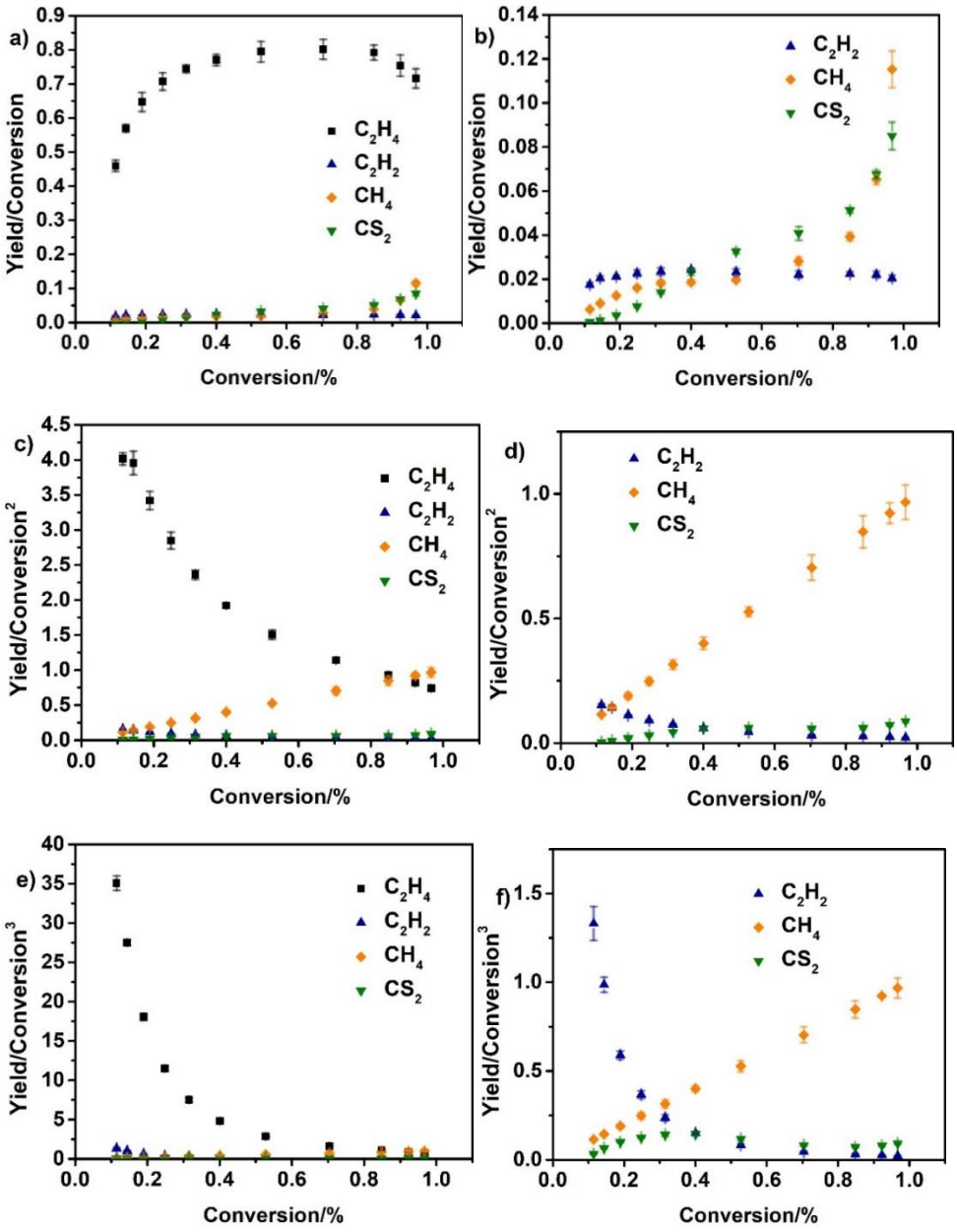

Figure S2.10. First-rank(a), first-rank without ethylene(b), second-rank(c), second-rank without ethylene(d), third-rank(e) and third-rank without ethylene(f) Delplot for ethane.

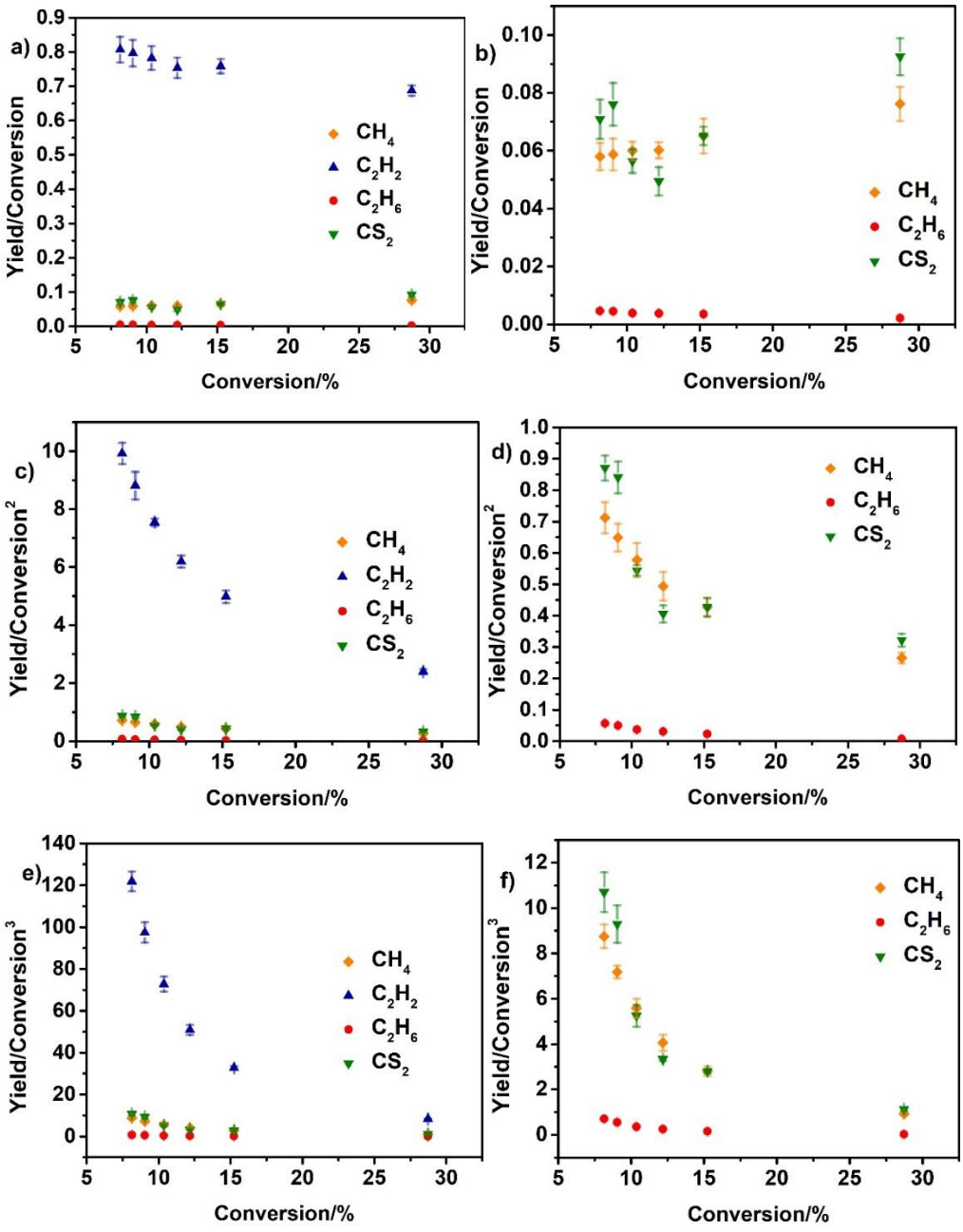

Figure S2.11. First-rank(a), first-rank without acetylene(b), second-rank(c), second-rank without acetylene(d), third-rank(e) and third-rank with only ethane(f) Delplot for ethylene.

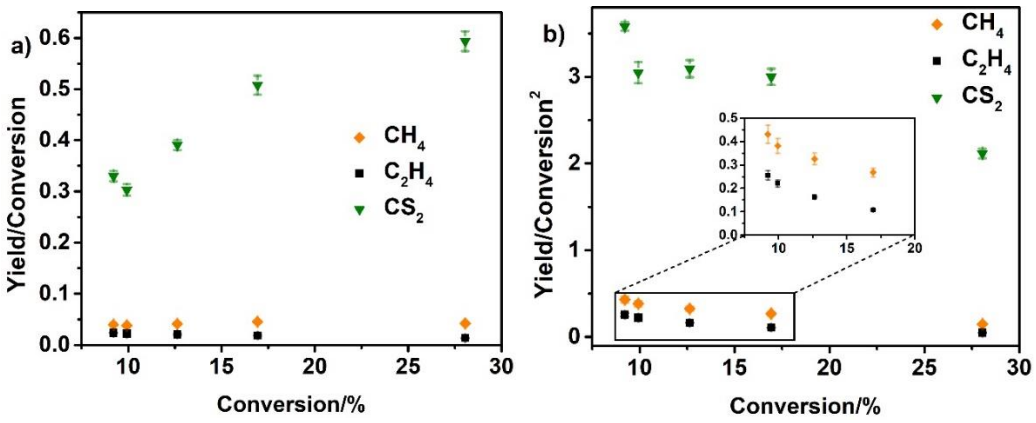

Figure S2.12: First-rank(a) and second-rank(b) Delplot for acetylene.

2.10.7. Determination of Temperature Range for Kinetic Measurements

The reaction rate of methane (µmol/mL/s) was measured in the temperature range from 780°C to 960°C with the CH_4:S_2 ratio = 3.07. As can be seen from Figure S2.13, the slope changes at around 880°C , which indicates a change in the rate determining step. It has been observed in many heterogeneous catalytic systems that at higher temperatures, where the diffusion rate is lower than the reaction rate, a change of slope is observed in the Arrhenius plot.

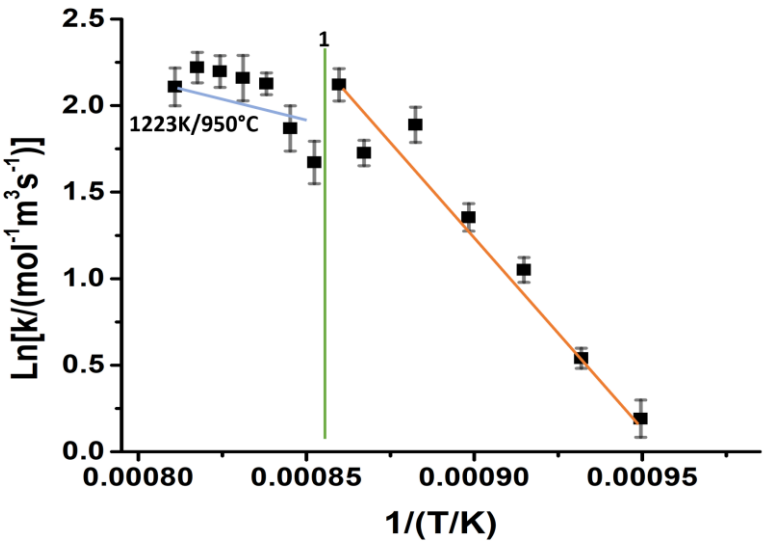

Figure S2.13: Natural logarithm of overall rate of SOCM methane consumption as a function of temperature over the temperature range of 780°C to 960°C

2.10.8. Product Selectivities vs Contact Time

The contact time has been calculated by dividing the catalyst volume after reaction by the flow rate. The catalyst volume after the reaction was ≈ 4 mL.

2.10.9. Conversion of Methane vs. Contact Time

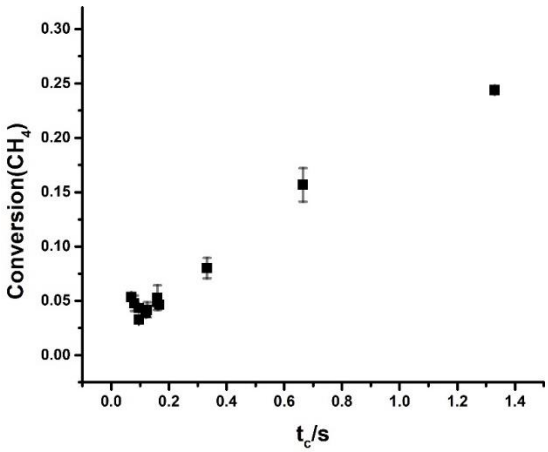

Figure S2.14: SOCM methane conversion increases with increasing contact time.

2.10.10. Literature Activation Energy of Gas Phase Reactions for OCM

The activation energies for various gas phase reactions has been extracted from the extensive literature summary of Baulch et al.[151,152] The CH_4 activation energies reported in previous OCM studies vary widely depending upon the catalyst and catalytic conditions. Apparent activation energies ≥ 200 kJ/mol were found using Mn/Na_2WO_4 as well as other transition metal catalysts[106,143] whereas the apparent barriers over doped lanthanide and alkaline earth oxides are lower and in the range of 113-172 kJ/mol.[125,143] Previous reports on CH_4 to CS_2 conversion using various sulfur oxidants gave activation energies in the range 131-160 kJ/mol,[176–179] similar to those of the lanthanide and alkaline earth oxide OCM catalysts. Note however, that the corresponding reaction conditions are rather different than the ones in the present work (CH_4/S ratios of <1, temperatures of 500-700 °C over silica gel catalysts).

Table S2.5: Literature apparent reported activation energies for gas phase reactions in OCM. Data from the literature summary of Baulch et al.

Reaction	Temp Range/°C	Intercept	Slope	Oxidant	Prefactor (cm^3 $molecule^{-1}$ s^{-1})	E_{act} (kJ/mol)	Rate constant at 950°C (cm^3 $molecule^{-1}$ s^{-1})
$O+C_2H_2$	880-950	22.54	-2710	O	1.63E-10	22.53	1.77E-11
$O+C_2H_4$	880-950	23.63	-1809	O	5.47E-11	15.04	1.25E-11
$O+C_2H_6$	880-950	22.30	-4291	O	2.07E-10	35.68	6.19E-12
$O+CH_4$	880-950	22.16	-5696	O	2.38E-10	47.36	2.26E-12
$O_2+C_2H_6$	880-950	-23.03	-26100	O_2	1.00E-10	217.01	5.39E-20
O_2+CH_4	880-950	-23.44	-28630	O_2	6.60E-11	238.04	4.50E-21
$H+C_2H_2$	880-950	-23.03	-14000	H	1.00E-10	116.40	9.89E-11
$H+C_2H_4$	880-950	-20.83	-7500	H	9.00E-10	62.36	8.94E-10
$H+C_2H_6$	880-950	-21.95	-5110	H	2.93E-10	42.49	2.92E-10

H+C H_4	880-950	-21.81	-6788	H	3.37E-10	56.44	3.35E-10
OH+ C_2H_2	880-950	-23.03	-6500	OH	1.00E-10	54.04	9.95E-11
OH+ C_2H_4	880-950	-24.10	-2990	OH	3.40E-11	24.86	3.39E-11
OH+ C_2H_6	880-950	-23.32	-2263	OH	7.45E-11	18.82	7.44E-11
OH+ CH_4	880-950	-23.89	-3083	OH	4.21E-11	25.63	4.20E-11

2.10.11. SOCM Product Distribution as a Function of Contact Time (Feed: C_2H_2)

The contact time has been calculated by dividing the catalyst volume after reaction by the flow rate. The catalyst volume after the reaction was ≈ 4 mL.

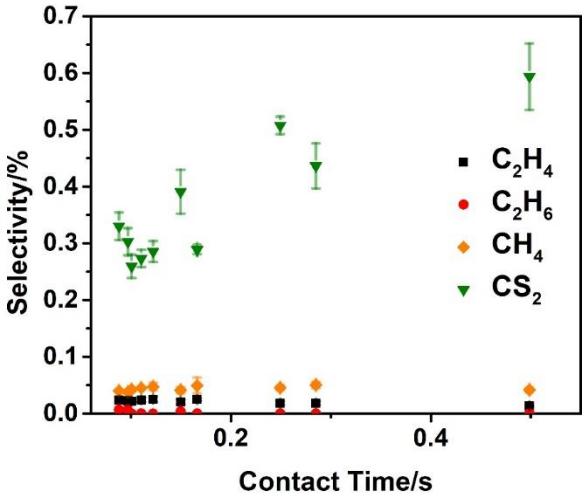

Figure S2.15: The distribution of SOCM products as a function of contact time t_c for C_2H_2 as the feed gas

2.10.12. C-H Bond Activations

i) Fe-S_{brid} site

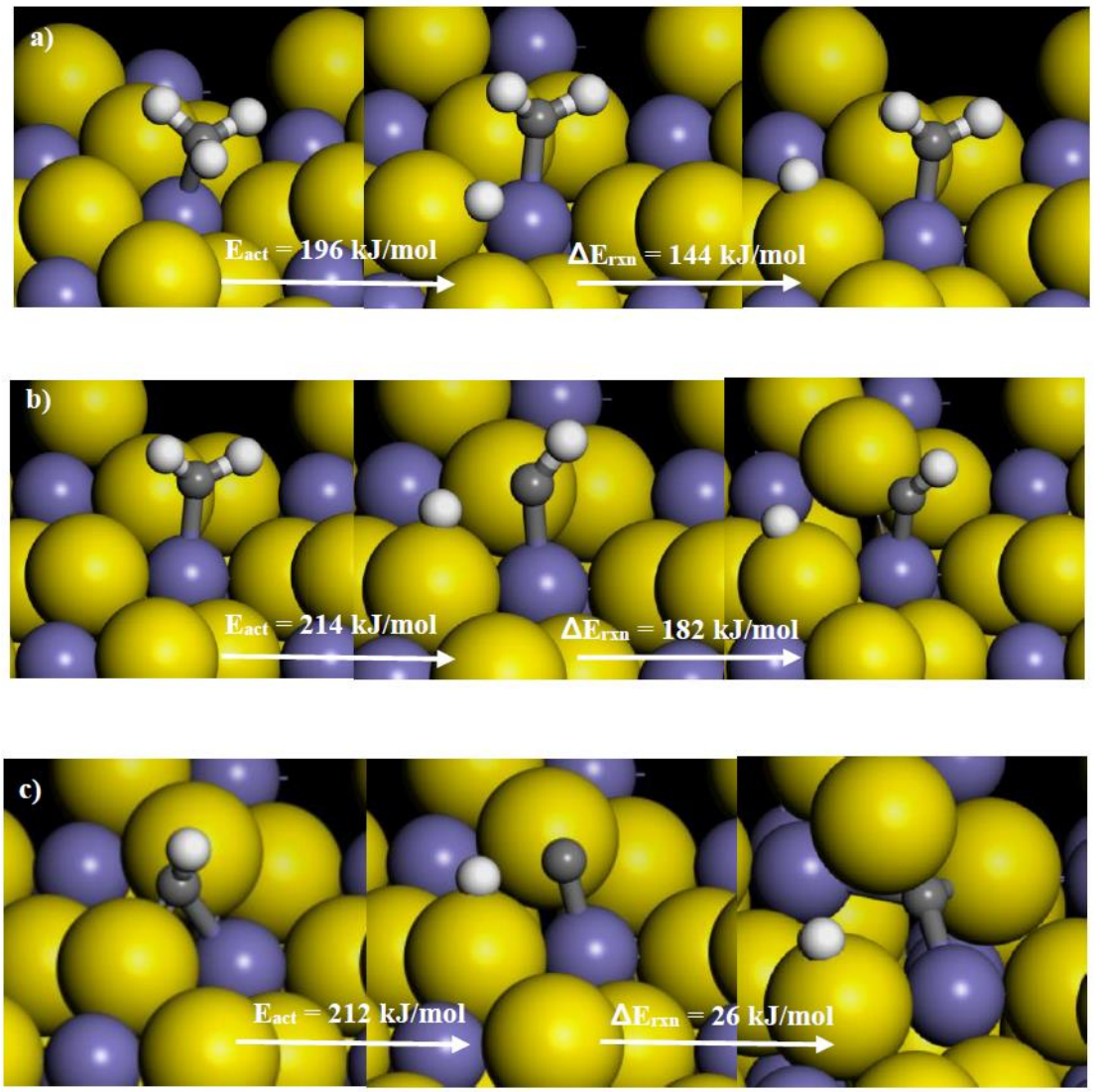

Figure S2.16: Optimized reactant, transition state and product structures for C-H bond activation of: a) CH_3^* b) CH_2^* and c) CH* respectively on the model sulfided Fe_3O_4 surface over Fe-S_{brid} site.

ii) S_{dim} site

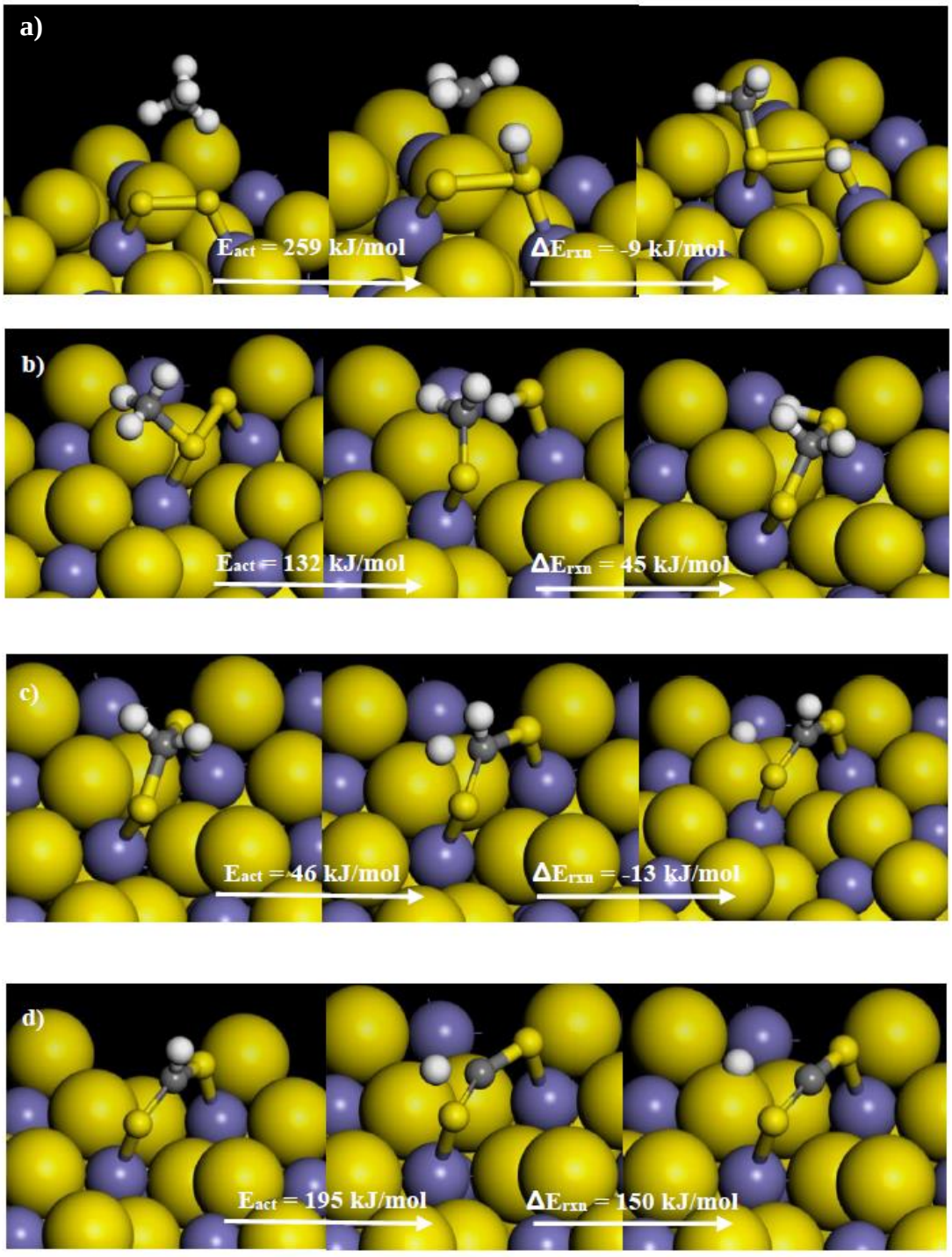

Figure S2.17: Optimized reactant, transition state and product structures for C-H bond activation of: a) CH_4 b) CH_3^* c) CH_2^* and d) CH* respectively over the adsorbed sulfur dimer site (S_{dim}) on the model sulfided Fe_3O_4 surface

iii) S_{mono}-S_{mono} site

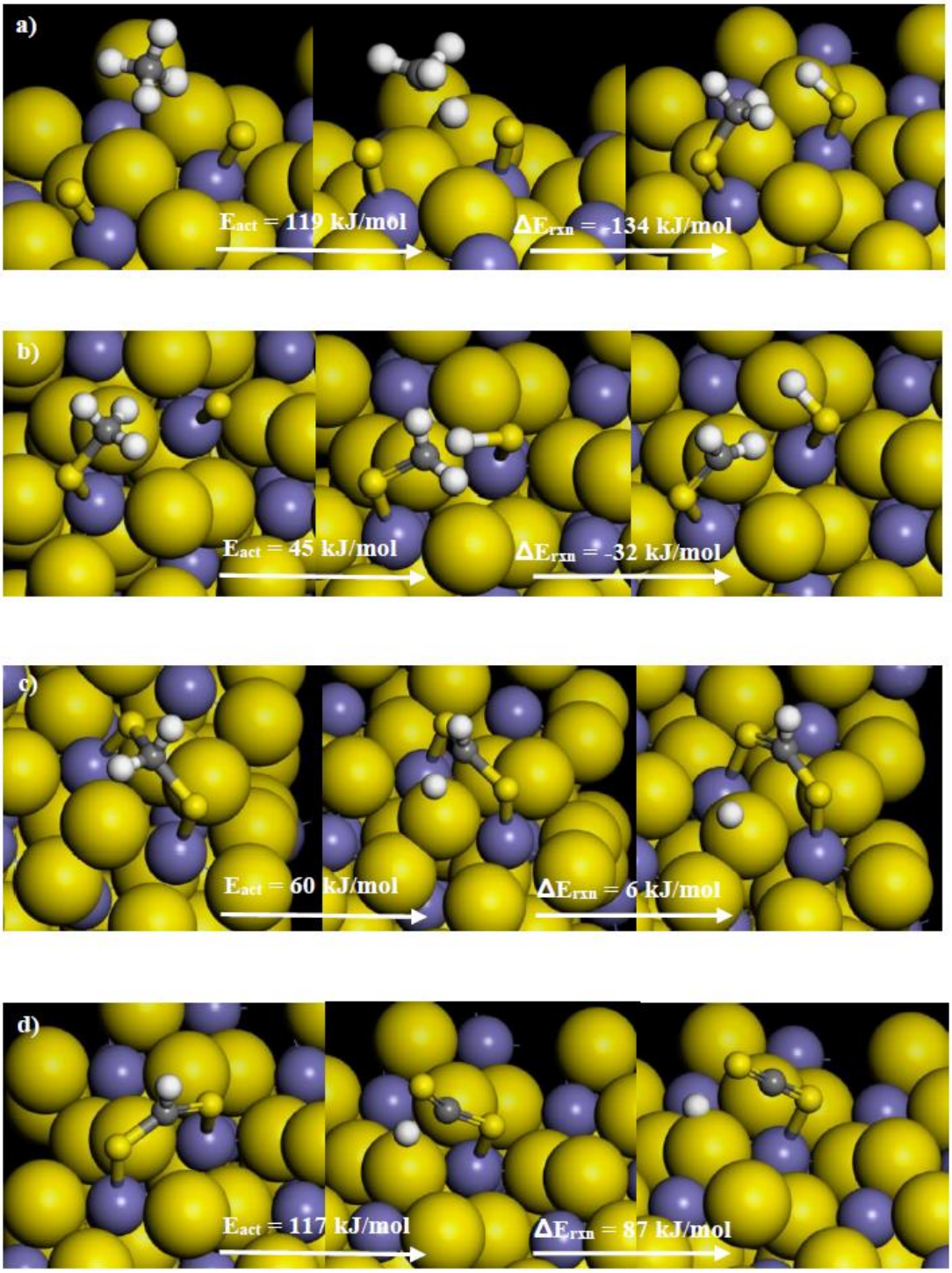

Figure S2.18: Optimized reactant, transition state and product structures for C-H bond activation of: a) CH_4 b) CH_3^* c) CH_2^* and d) CH^* respectively over the adsorbed sulfur monomer sites (S_{mono}) on the model sulfided Fe_3O_4 surface

2.10.13. Coupling reactions

i) Fe-S_{brid} site

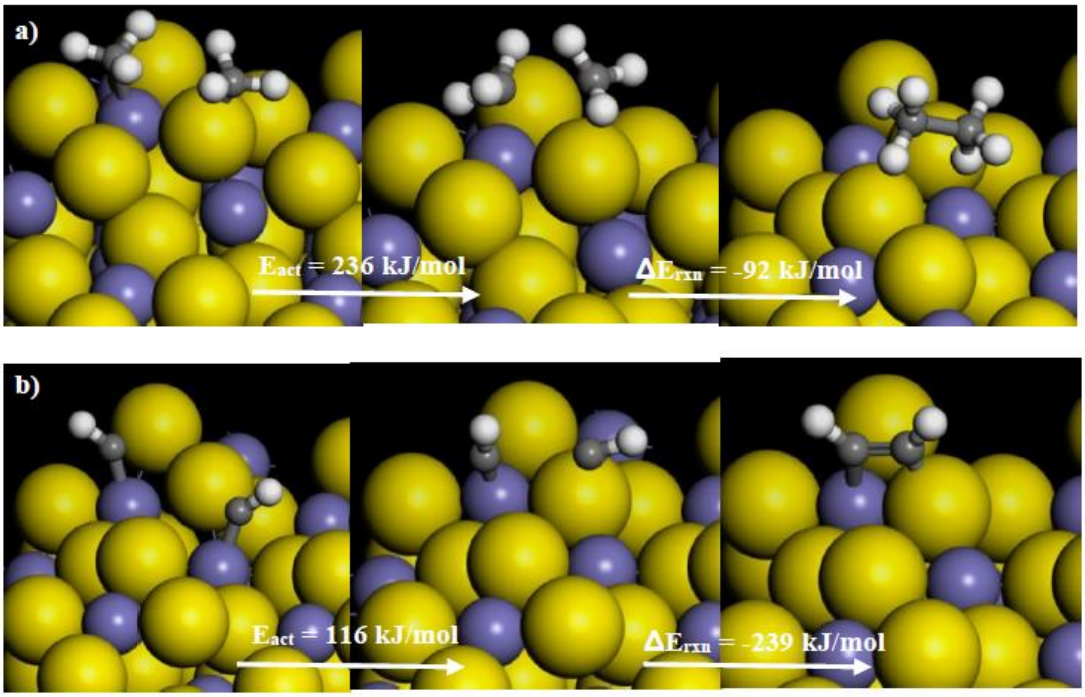

Figure S2.19: Optimized reactant, transition state and product structures for coupling reaction of a) CH_3^* b) CH_2^* and c) CH* respectively over the Fe-S_{brid} sites on the model sulfided Fe_3O_4 surface

ii) S_{dim} site

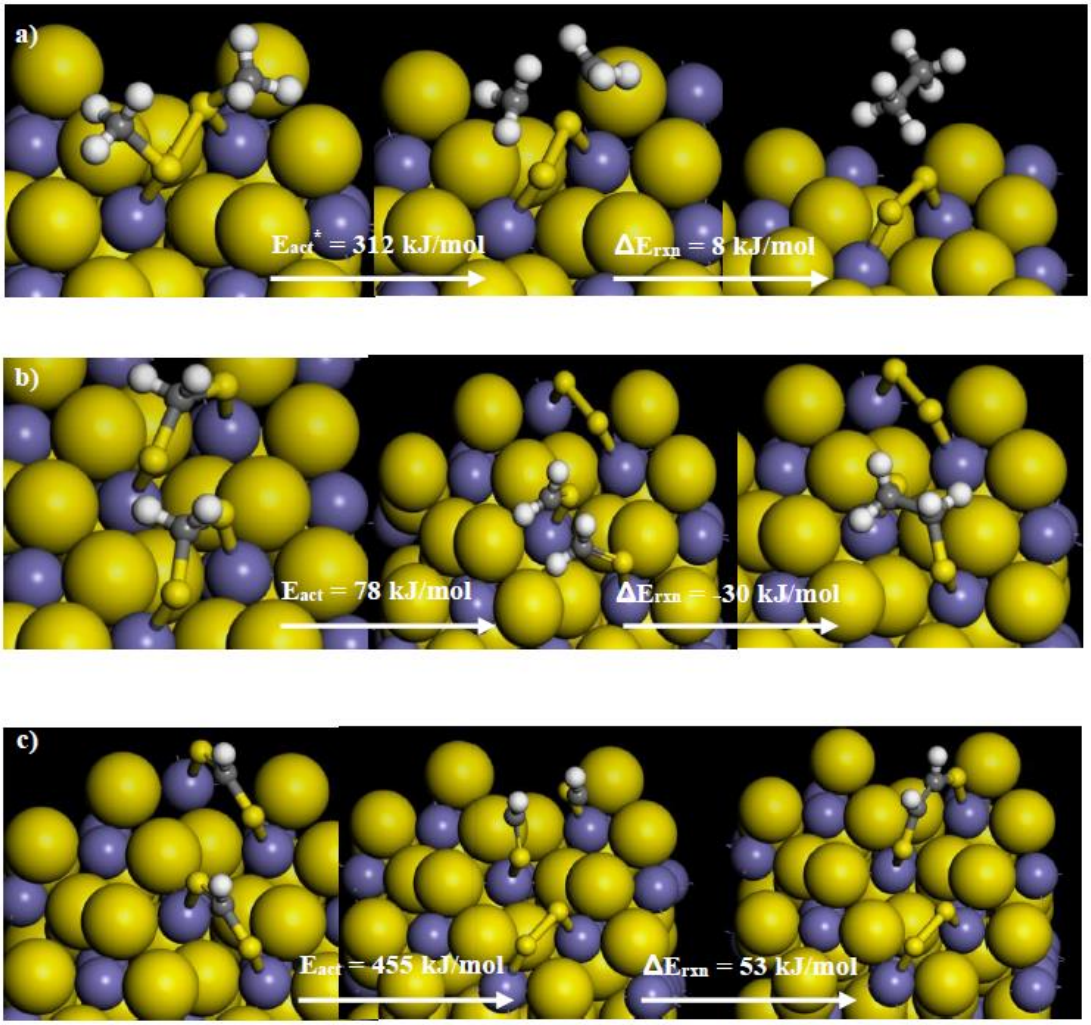

Figure S2.20: Optimized reactant, transition state and product structures for coupling reaction of a) CH_3^* b) CH_2^* and c) CH^* respectively over the adsorbed sulfur dimer sites (S_{dim}) on the model sulfided Fe_3O_4 surface

(*Dimer calculations converged until a force of 0.1 eV/Å)

iii) S_{mono}-S_{mono} site

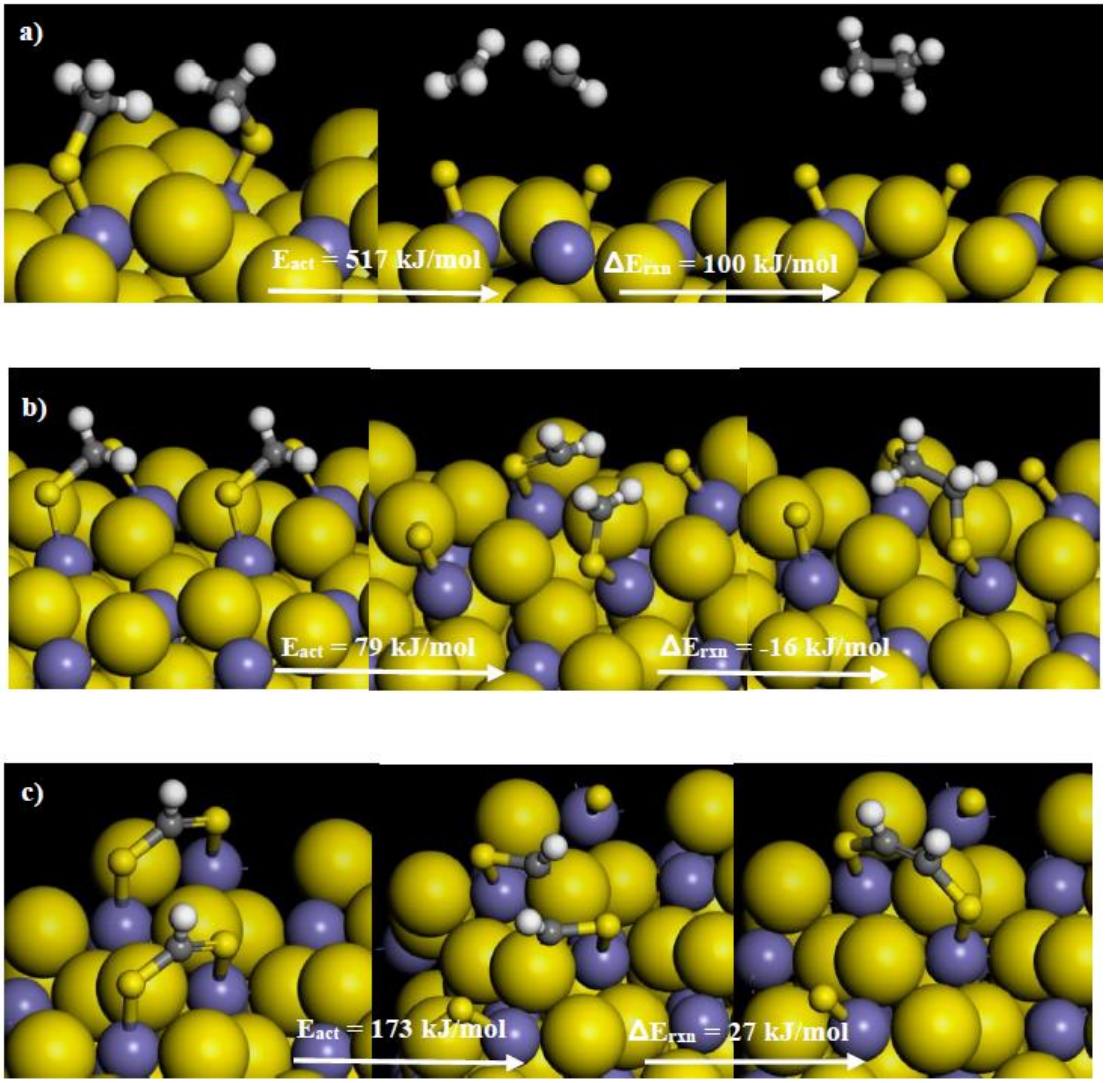

Figure S2.21: Optimized reactant, transition state and product structures for coupling reaction of: a) CH_3^* b) CH_2^* and c) CH^* respectively over the adsorbed sulfur monomer sites (S_{mono}) on the model sulfided Fe_3O_4 surface

2.10.14. Formation of S_{mono} and S_{dim} site

The most favorable site for S_2 adsorption on the FeS_2 surface was that for two Fe sites in side-on adsorption which led to an adsorption energy of -215 kJ/mol. Adsorption on the sulfur sites was found to be unfavorable unlike the case for La_2O_3, where O_2 adsorption over the oxygen sites was the most favorable.[180] These results are in accordance with the studies done on FeS_2 surface for O_2 adsorption where side-on adsorption on Fe metal sites was found to be the most favourable followed by on-top adsorption on a single Fe site.[181] The side-on adsorption leads to generation of sulfur

dimer (S_{dim}) sites. Another possible active site is sulfur monomer site (S_{mono}) which can be generated by dissociation of S-S bond in the adsorbed sulfur and binding of the sulfur on another Fe site. An energy diagram showing the pathway for formation of S_{mono} sites from the S_{dim} sites has been shown in Figure S2.21. Upon Bader charge analysis[138] of the S_{mono} species adsorbed on the surface, it is seen that net charge accumulation on both the sulfur species is 0.61 e^- with respect to the gas phase sulfur which is equally distributed among both the sulfur sites. The overall reaction energy for generation of S_{mono} sites with respect to the gas phase S_2 is -25 kJ/mol. Hence, generation of S_{dim} sites is more favourable than the generation of S_{mono} sites. However, under the reaction conditions, both types of active sites can exist in equilibrium because of the high operating temperatures with the S_{dim} sites being more dominant than the S_{mono} sites.

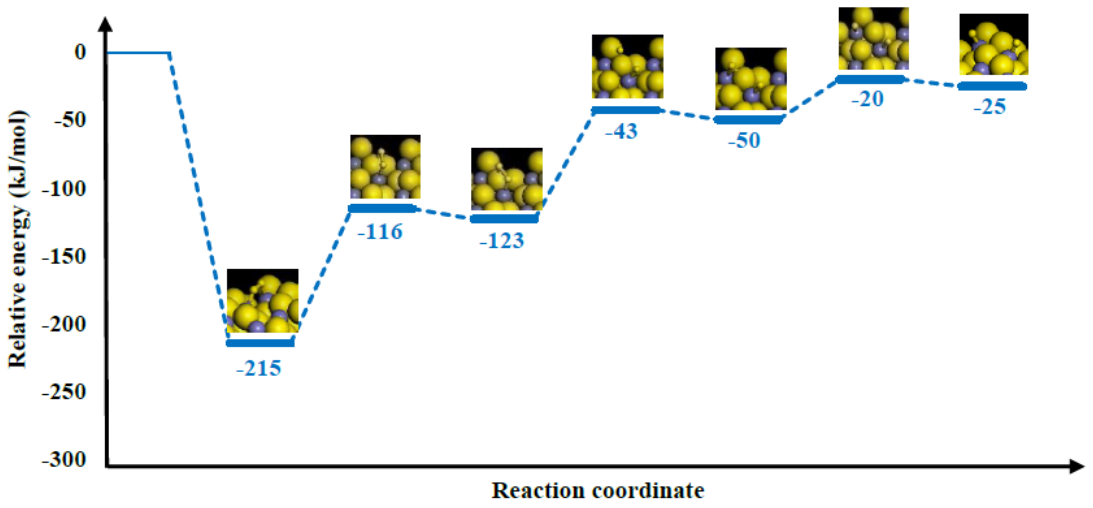

Figure S2.22: Potential energy diagram representing the formation of S_{mono} sites from S_{dim} sites

2.10.15. Comparison of C-H Activation and C-C Coupling Barriers for S_{mono}-S_{mono} Site Pairs

Table S2.6: Comparison of the C-H activation, C-C coupling free energy barriers, and desorption free energies over S_{mono}-S_{mono} site pairs adsorbed over the FeS_2 surface

Species	*C-H activation free energy barrier (kJ/mol)*	*C-C coupling free energy barrier (kJ/mol)*	*Desorption free energies (kJ/mol)*
CH_3	29	464	201
CH_2	42	61	404
CH	95	169	638

2.10.16. Derivation of Rate Law

Table S2.7: Proposed mechanism for SOCM reaction over sulfided Fe_3O_4 catalyst

Site	**Elementary steps**	**ΔH_{rxn} (kJ/mol)**	**ΔH_{act} (kJ/mol)**
Fe-S_{brid}	$CH_{4(g)} + S_{dim} \rightarrow CH_3 - S_{dim} - H$ (2.21)	95	163
S_{dim}	$S_{2(g)} + 2Fe \rightarrow S_{dim}$ (2.22)	-215	-
	$CH_{4(g)} + S_{dim} \rightarrow CH_3 - S_{dim} - H$ (2.23)	-9	259
S_{mono} - S_{mono}	$S_{2(g)} + 2Fe \rightarrow 2S_{mono}$ (2.24)	-25	-
	$CH_{4(g)} + 2S_{mono} \rightarrow CH_3 - S_{mono} + H - S_{mono}$ (2.25)	-134	119

As previously described in eq. (2.1) in the main text, using eqs. (2.21), (2.23), and (2.25), the overall rate of methane activation can be written as follows:

$$r = k_{C-H\_FeS}[CH_4][Fe][S_{brid}]\frac{z}{(L_1+L_2)} + k_{C-H\_Sdim}[CH_4][S_{dim}] + k_{C-H\_Smono}[CH_4][S_{mono}]^2\frac{z}{2L_1} \quad (2.26)$$

However, as discussed previously in the main section, since the CS_2 formation is the dominating pathway which occurs over the adsorbed sulfur sites, the barriers measured most closely represent barriers for the rate determining initial C-H activation over these adsorbed sulfur sites. Thus, while methane activation partially occurs over the Fe-S_{brid} sites as well to give rise to ethylene, for simplification, kinetic modeling herein is done by considering the methane activation occurring dominantly over the adsorbed sulfur sites.

Thus, considering the methane activation over the adsorbed sulfur dimer sites, the first step of formation of adsorbed sulfur dimer sites is assumed to be quasi-equilibrated. Thus, from eq. (2.22), we get,

$$[S_{dim}] = K_{Sdim}[Fe]^2[S_2]\frac{z}{2L_1}, \quad (2.27)$$

$$\text{where, } K_{Sdim} = A_{Sdim}\exp\left(\frac{-\Delta H_{rxn}}{RT}\right) \text{ and } \Delta H_{rxn} = -215 \text{ kJ/mol}, \quad (2.28)$$

L_1 is the total number of Fe sites, and z is the co-ordination number of the Fe site

The second step (eq. (2.23)) which involves the C-H activation is rate determining. Thus, the rate law can be written as:

$$r = k_{C-HSdim}[CH_4][S_{dim}] = k_{C-HSdim}K_{Sdim}[CH_4][Fe]^2[S_2]\frac{z}{2L_1}, \quad (2.29)$$

$$\text{where, } k_{C-HSdim} = A_{C-HSdim}\exp\left(\frac{-\Delta H_{act}}{RT}\right), \Delta E_{act} = 259 \text{ kJ/mol} \quad (2.30)$$

At high CH_4/S_2 ratios i.e. low sulfur (S_2) pressures and high temperatures, the Most Abundant Surface Intermediate (MASI) will be the metal sites where $L_1 = [Fe]$.

As such the rate can be written as:

$$\frac{r}{L_1} = r' = k_{app}[CH_4][S_2] \quad (2.31)$$

$$\text{where, } k_{app} = A_{Sdim}A_{C-HSdim}\frac{z}{2}\exp\left(\frac{-(\Delta H_{rxn}+\Delta H_{act})}{RT}\right) = A_{app}\exp\left(\frac{-\Delta H_{app}}{RT}\right) \quad (2.32)$$

It should be noted that herein, we use ΔE_{rxn} and ΔE_{act} as approximate values of ΔH_{rxn} and ΔH_{act}. This leads to,

$$\Delta E_{app} = \Delta E_{rxn} + \Delta E_{act} = -215 + 259 = 44\ kJ/mol \quad (2.33)$$

Similarly, for S_{mono} sites as well, we would get

$$r' = k_{app}[CH_4][S_2]$$

$$\text{where, } k_{app} = A_{Smono}A_{C-HSmono}\frac{z}{2}\exp\left(\frac{-(\Delta H_{rxn}+\Delta H_{act})}{RT}\right) = A_{app}\exp\left(\frac{-\Delta H_{app}}{RT}\right) \quad (2.34)$$

$$\Delta E_{app} = \Delta E_{rxn} + \Delta E_{act} = -25 + 119 = 96\ kJ/mol \quad (2.35)$$

2.10.17. Micro-kinetic modeling of the SOCM reaction

Micro-kinetic modeling was done for the SOCM reaction network in order to determine the ensemble averaged methane activation barriers considering methane activation over Fe-S_{brid} and S_{dim} sites as well as to compute the ethylene formation barriers and CS_2 formation barriers using computationally determined parameters.

Elementary reaction steps involving subsequent surface reactions, desorption, and adsorption steps were included in the kinetic modeling. The elementary reactions considered in the model along with their DFT determined activation energies and free energy barriers are summarized in Table S2.8. DFT estimated electronic energy barriers were used for the different elementary reaction steps involved in the model, with the exception of the desorption of methyl radicals, wherein the desorption energy was adjusted to 209 kJ/mol from its DFT determined value of 199 kJ/mol, within the range of DFT error.[182] The pre-exponentials for sulfur adsorption were adjusted by using optimized entropy values of 1.75 times that estimated via Campbell-Seller's theory. The higher entropic loss herein can likely be attributed to the strong binding of sulfur to the surface which further hinders its translation degree of freedom parallel to the plane, in addition to loss along the direction perpendicular to the plane. Similar entropic losses were also observed for the exothermic oxygen dissociation over Pt surface wherein the experimentally determined entropic loss was found to be 1.65 times higher than the entropic loss derived via Campbell-Sellers theory (ΔS_{exp} = -125.5 J/molK, ΔS_{est} = -76 J/molK).[31] For methane activation over S_{dim} sites, which occur via a homolytic pathway wherein the transition state involves a methyl radical like state, the entropic

losses are assumed to be negligible, assuming similar translation and rotational degrees of freedom between the reactant and the transition state, which is also in line with the experimental KIEs observed. For methane activation over Fe-S_{brid} sites involving heterolytic activation of methane, the entropy is assumed to be 1.7 times the estimated entropy using Campbell-Seller's formula. Similar entropy was also determined experimentally for methane activation over PdO surfaces showing entropic losses to be approximately 1.6 times than the estimates from Campbell Sellers theory (ΔS_{exp} = -134 J/molK, ΔS_{est} = -83 J/molK).[11] The adjustment described herein were done so as to have the C_2/CS_2 selectivities close to the experimental value of 2 observed at the lowest contact times.

Table S2.8: Summary of the elementary reactions considered in the micro-kinetic model and their subsequent electronic energies, entropies, and free energies used in the model. The energies are given in kJ/mol and the entropies are given in J/molK.

No.	Reaction	ΔE_{act}	ΔS_{act}	ΔG_{act}	ΔE_{rxn}	ΔS_{rxn}	ΔG_{rxn}
1	$S_2 + 2Fe \leftrightarrow S_{dim}$	0	0	0	-215	-172	-20
2	$CH_4 + S_{dim} \leftrightarrow CH_3\text{-}S_{dim}\text{-}H$	259	0	259	-10	-104	104
3	$CH_3\text{-}S_{dim}\text{-}H + S_{brid} \leftrightarrow CH_3\text{-}S_{dim} + H\text{-}S_{brid}$	70	9	55	30	-3	32
4	$CH_3\text{-}S_{dim} \leftrightarrow CH_2\text{-}S_{dim}\text{-}H$	132	6	115	45	-12	54
5	$CH_2\text{-}S_{dim}\text{-}H + S_{brid} \leftrightarrow CH_2\text{-}S_{dim} + H\text{-}S_{brid}$	70	9	55	30	-3	32
6	$CH_2\text{-}S_{dim} + S_{brid} \leftrightarrow CHS_{dim} + H\text{-}S_{brid}$	46	10	26	-13	1	-18
7	$CHS_{dim} + S_{brid} \leftrightarrow CS_2^* + H\text{-}S_{brid}$	195	11	175	150	4	141
8	$CS_2^* \leftrightarrow CS_2 + 2Fe$	46	99	-66	46	97	-64
9	$CH_3\text{-}S_{dim} \rightarrow CH_3^{\cdot} + S_{dim}$	209	63	135	209	63	135
10	$CH_4 + Fe + S_{brid} \leftrightarrow CH_3^* + H\text{-}S_{brid}$	163	-149	324	95	-165	277

11	$CH_3^* \rightarrow CH_3^{\cdot} + Fe$	153	63	81	153	63	81
12	$CH_3^{\cdot} + CH_3^{\cdot} \rightarrow C_2H_6$	0	0	0	-392	-6	-379
13	$C_2H_6 + S_{dim} \leftrightarrow C_2H_4 + H\text{-}S_{dim}\text{-}H$	143	8	117	110	18	82
14	$H\text{-}S_{dim}\text{-}H \leftrightarrow H_2\text{-}S_{dim}$	80	9	71	80	9	71
15	$2H\text{-}S_{dim} \leftrightarrow H_2\text{-}S_{dim} + S_{dim}$	80	9	71	80	9	71
16	$H_2\text{-}S_{dim} \leftrightarrow H_2S + Fe + S_{mono}$	85	89	-15	85	89	-15
17	$2H\text{-}S_{brid} \leftrightarrow H_2 + 2S_{brid}$	16	9	5	-121	95	-225
18	$H\text{-}S_{brid} + S_{mono} \leftrightarrow S_{brid} + H\text{-}S_{mono}$	9	11	-6	-120	10	-131
19	$H\text{-}S_{brid} + S_{dim} \leftrightarrow S_{brid} + H\text{-}S_{dim}$	41	12	23	-30	3	-32
20	$2H\text{-}S_{mono} \leftrightarrow H_2S^* + S_{mono}$	93	-7	96	29	-13	44
21	$H_2S^* \leftrightarrow H_2S + Fe$	94	89	-7	94	89	-7

The micro-kinetic model was run in a batch mode for differential CH_4 conversions (upto 1%). The forward rate constants ($k_{i,f}$) and backward rate constant ($k_{i,b}$) for each elementary step i was determined from the Gibbs free energy of activation ($\Delta G_{act,i}$) and Gibbs free energy of reaction ($\Delta G_{rxn,i}$) using transition state theory as follows:

$$k_{i,f} = \frac{k_B T}{h} \exp\left(\frac{-\Delta Gact,i}{RT}\right), \tag{2.36}$$

$$k_{i,b} = \frac{k_B T}{h} \exp\left(\frac{-(\Delta Gact,i - \Delta Grxn,i)}{RT}\right), \tag{2.37}$$

Using these rate constants (k_i), the rate of each elementary step i (r_i) is defined as,

$$r_i = k_i \prod_{j=1}^{N} C_j^{n_{j,i}} \tag{2.38}$$

where C_j is the concentration of species j, $n_{j,i}$ is the stoichiometry of species j in reaction i. N is the total number of species = 27.

The differential equations defining the rate of change of concentrations for species j is then defined as:

$$\frac{dC_j}{dt} = \sum_{i=0}^{Nr} n_{j,i} r_i \qquad (2.39)$$

N_r defined is the total number of elementary reactions in the model, which is 21.

The differential equations for 21 chemical reactions involving 27 species were solved using ode23s solver in MATLAB. The initial concentrations of CH_4 and S_2 were each taken as 0.001 mol/L with a temperature of 1138 K. For apparent rate order determination, the concentrations of the input gas phase species were varied from 0.0008 mol/L to 0.001 mol/L. The simulations were run until a time of 0.15 s, yielding low differential methane conversions of ~0.85 %. The methane and sulfur rate orders obtained from the simulations were determined to be 1 and 0.89 respectively, plots for which are shown in Figure S2.23 and S2.24 respectively.

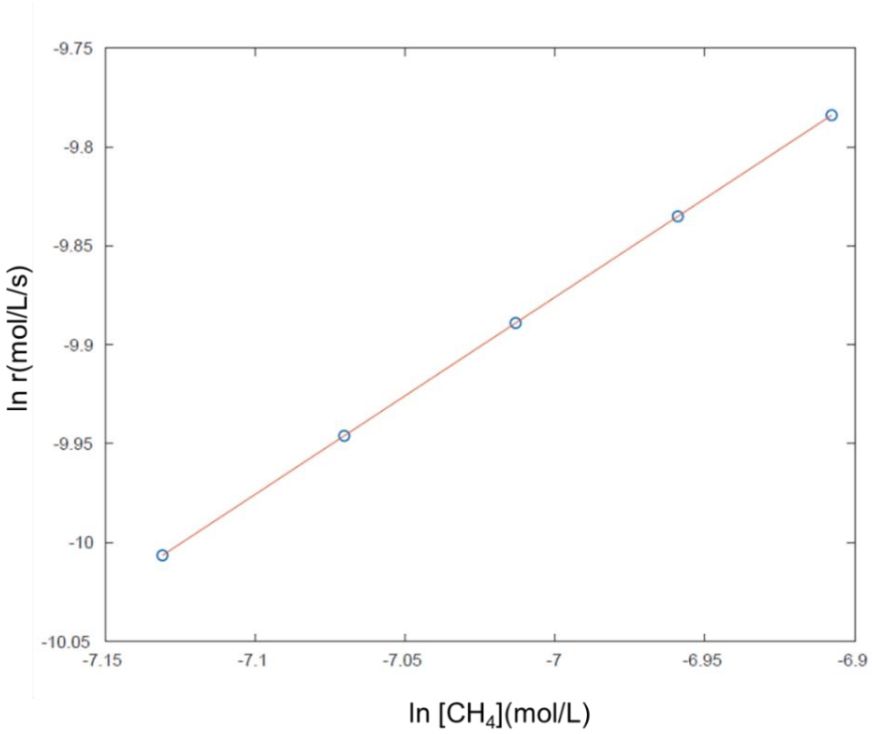

Figure S2.23: Natural logarithm of simulated reaction rate in mol/L/s versus natural logarithm of initial methane concentration in mol/L

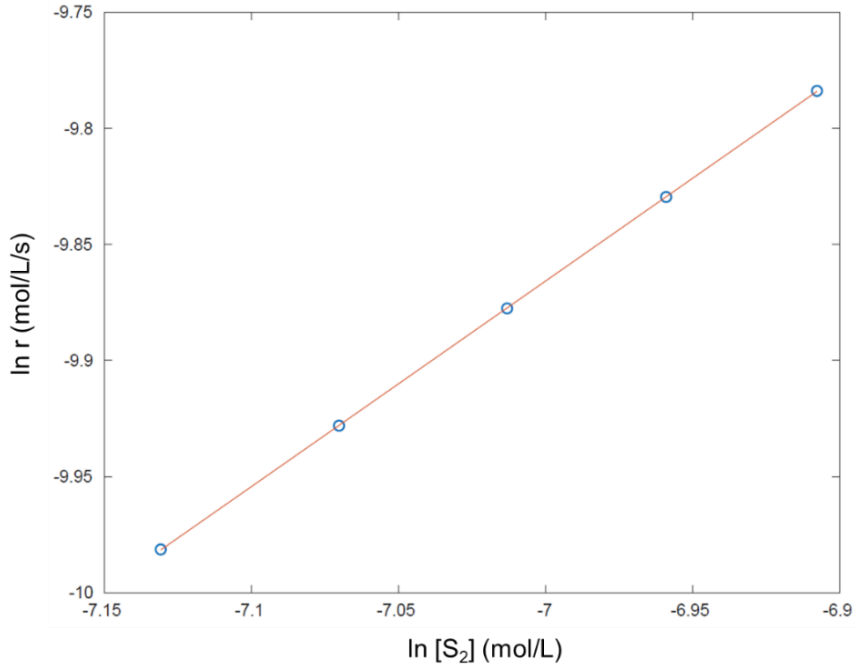

Figure S2.24: Natural logarithm of simulated reaction rate in mol/L/s versus natural logarithm of initial sulfur concentration in mol/L

The methane activation barrier was determined by simulation of the established SOCM micro-kinetic model at different temperatures varying from 1136 to 1138 K in steps of 0.5 K. The rate constants at these different temperatures for methane activation were then determined assuming first order dependence of rates on CH_4 and S_2. Plotting the simulated rate constants at different temperatures, the activation barrier of 57 kJ/mol for methane activation was determined. The Arrenhius plots obtained from the simulation is shown in Figures S2.25.

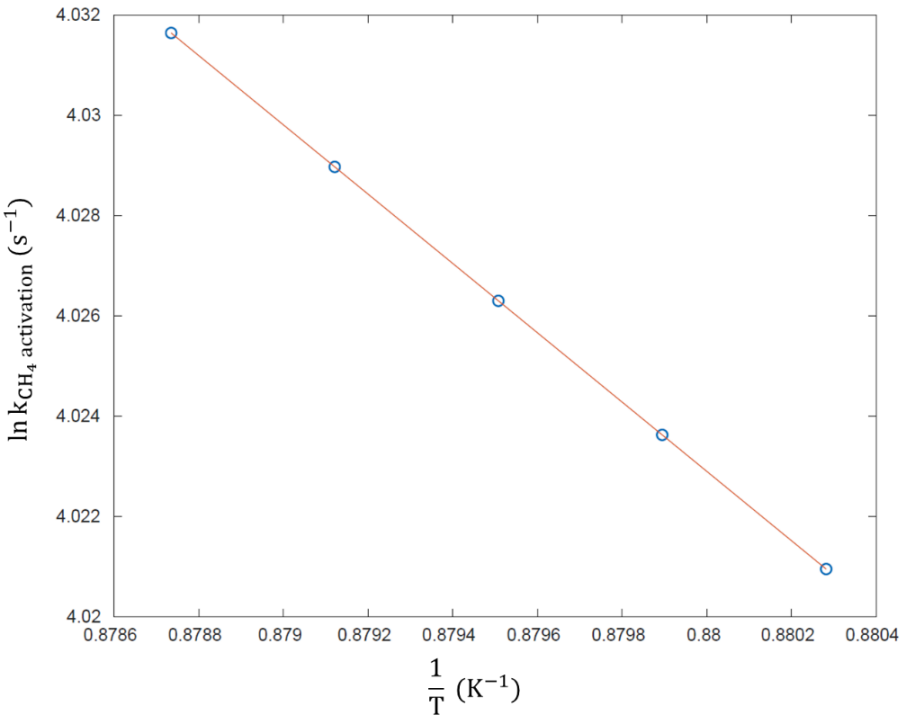

Figure S2.25: Simulated Arrenhius plot for determination of activation barrier of CH_4 activation

2.10.18. Calculations on FeS Surface

Surface Models

pXRD analysis done indicated the presence of a hexagonal phase of FeS crystal under the reaction conditions used for the kinetic study of the SOCM reaction. The hexagonal FeS crystal formed was modelled based on the crystallographic data provided by Fasiska,[183] the structure of which is shown in Figure S2.26. The crystallographic lattice can be seen as a stacking of close packed iron and sulfur planes with iron atoms filling in the octahedral interstices between the two adjacent sulfur layers. In order to then determine the most stable surface termination for this FeS crystal under the different sulfur pressures/chemical potentials, we conducted an ab-initio thermodynamic study as described by Scheffler et al.[184] for the different possible surface terminations. The FeS structure can be decomposed into two FeS layers - the sulfur terminated surface (001-S) surface and the iron terminated surface (001-Fe) surface along the [001] direction and three FeS layers - the 010-S, 010-2S, and the 010-Fe surfaces along the [010] direction. The surface slab constructed from the (001) terminated surface was represented by a 3x3 supercell while those constructed from the (010) terminated

surface was represented by an 2x3 supercell. Each of these surface slabs were then separated by a vacuum layer of 15 Å to avoid spurious interactions between the neighbouring supercells. The parameters used for electronic and geometric minimization are same as that described before in the Computational Methods Section. The resultant optimized surface slab structures of each of the different surface terminations examined are shown in Figure S2.27.

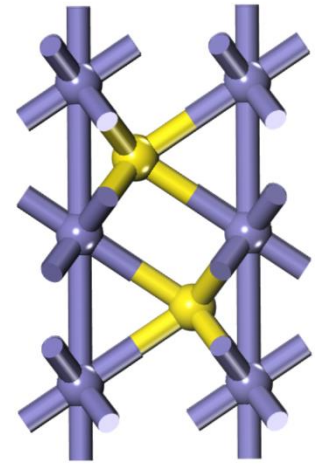

Figure S2.26. Bulk crystal structure of the hexagonal FeS phase

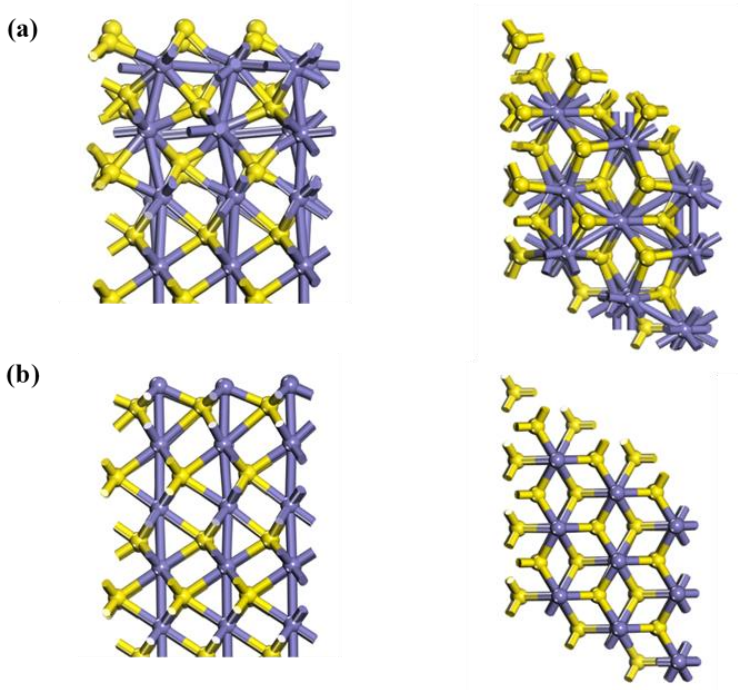

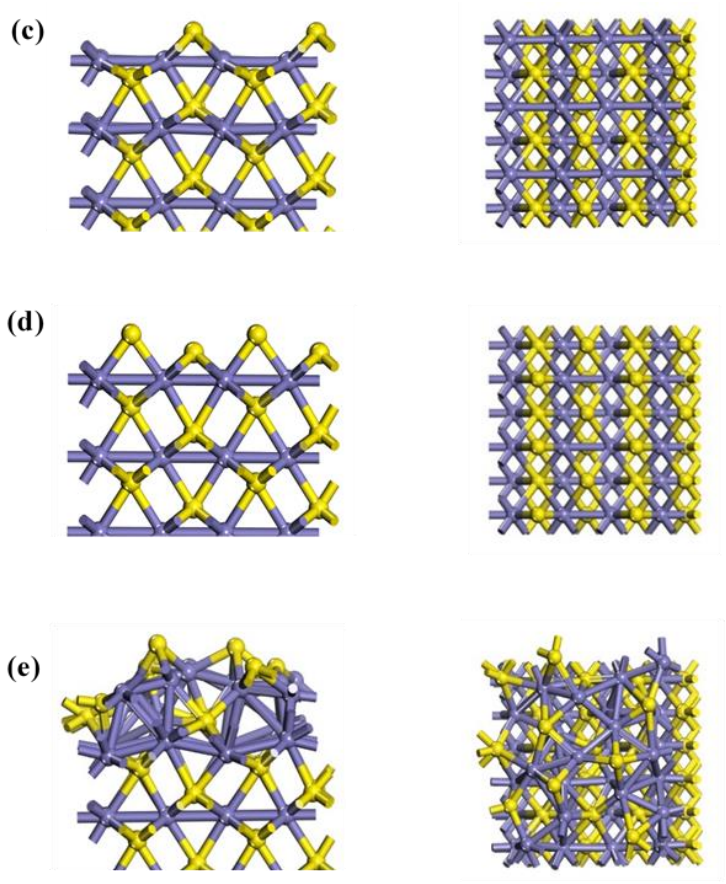

Figure S2.27. Side view (left) and top view (right) of the optimized surface slab models for the different terminated surfaces of FeS examined for ab-initio thermodynamic studies (a) 001S (b) 001Fe (c) 010S (d) 0102S (e) 010Fe

The surface energies of the above optimized structures were then plotted as a function of the chemical potential using the formula given in eq. 2.40.

$$\gamma(T,P) = \frac{1}{2A}[E_{surface} - N_{Fe}E_{FeS} + (N_{Fe} - N_S)\mu_S(T,P)] \quad (2.40)$$

where $\gamma(T,P)$ is the surface energy of the surface at sulfur pressure P and temperature T,

A is the surface area of the supercell used,

$E_{surface}$ is the electronic energy of the surface determined from DFT calculations

N_{Fe} is the number of Fe atoms present in the surface unit cell

N_S is the number of S atoms present in the surface unit cell

E_{FeS} is the electronic energy of the bulk FeS per formula unit as determined from DFT calculations

μ_S is the chemical potential of sulfur which is determined as,

$$\mu_S(T,P) = \frac{1}{2}(E_{S_2} + \tilde{\mu}_{S_2} + kTln\left(\frac{P}{P_0}\right)) \quad (2.41)$$

Where E_{S_2} is the DFT energy of the disulfur molecule,

P_0 is the reference pressure (taken as 1 atm here)

$\tilde{\mu}_{S_2}$ contains the temperature dependent enthalpic and entropic contributions for the disulfur molecule which are tabulated in the JANAF thermodynamic table.[100]

The results of this study are shown in Figure S2.28 wherein from the plot of surface energy vs the chemical potential, the 001-S terminated surface was identified as the most stable surface at the operating sulfur pressures of ~0.01 atm at a temperature of 1100 K. Thus, further calculations to examine the SOCM reaction over the FeS surface were done using the 001-S terminated surface of FeS as our model surface as shown in Figure S2.27a

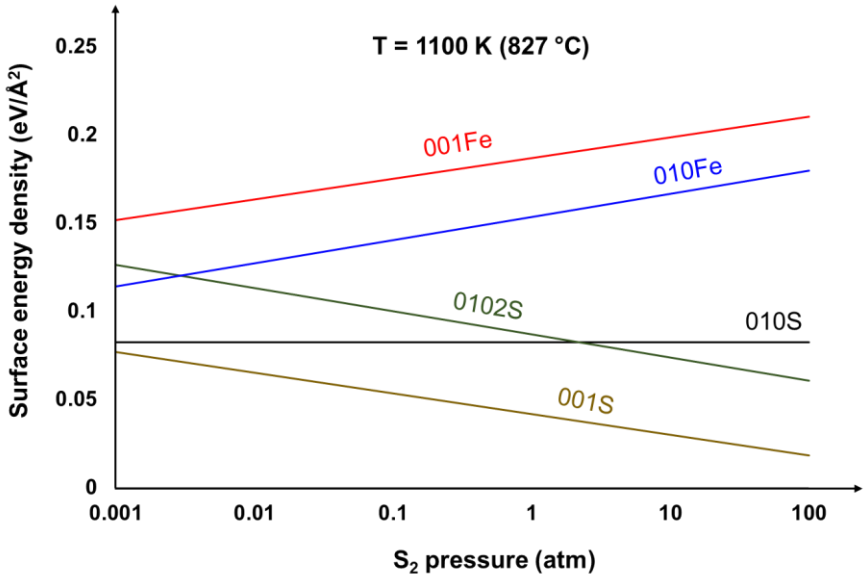

Figure S2.28. Ab-initio thermodynamic studies showing the variation of surface energy with the chemical potential (pressures) of sulfur for different examined terminated surfaces. The calculations are done for a temperature of 1100 K corresponding approximately to the reaction temperature of 875° C.

Methane Activation over FeS Surface

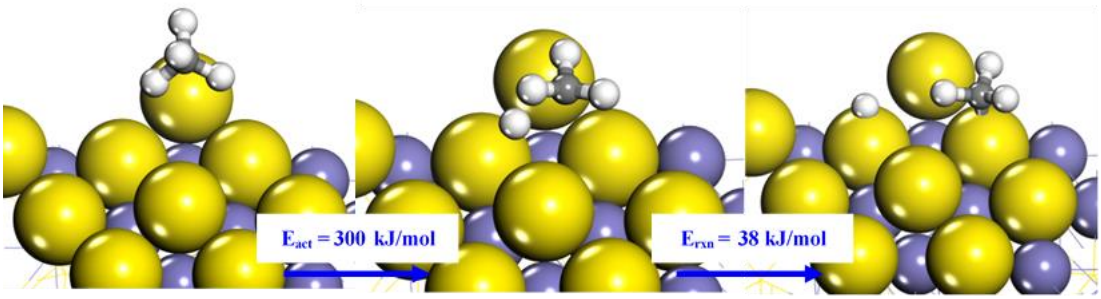

Figure S2.29. Reactant, transition and product states for methane activation over the S-S site pairs present on the 001- S terminated FeS surface

From Figure S2.27a, we can identify that there are only sulfur sites that are present on the 001-S terminated FeS surface. Hence, methane can be activated only over these S-S site pairs. Examination of methane activation over these sites show an activation barrier of 300 kJ/mol and a reaction energy of 38 kJ/mol. The reactant, product and transition state structures of methane activation over the S-S sites are shown in Figure S2.29. Such high barriers thus suggest that FeS surface isn't active enough for methane activation compared to FeS_2 surface, wherein low activation barriers of 163 kJ/mol was determined as discussed in the main text. Hence, the role of FeS surface sites in methane activation can be ruled out.

Disulfur Adsorption

We have seen in the case of FeS_2 that the sulfur adsorbs strongly on the surface over the exposed Fe sites generating adsorbed sulfur sites, either in monomeric (S_{mono}) or dimeric form (S_{dim}), which are active for methane activation. Hence, we also looked at sulfur adsorption on FeS surface which can possibly function as active sites. Sulfur can adsorb either molecularly or dissociatively over the S-S site pairs. However, the adsorption of sulfur over these sites was found to be endothermic with an adsorption energy of 18 kJ/mol and 58 kJ/mol respectively for molecular and dissociative adsorption (Figure S2.30). Such endothermic energies coupled with the high entropic penalty of adsorbing sulfur on the surface at the high operating temperatures of 875 ºC suggest that the formation of catalytic adsorbed sulfur sites over the FeS surface is unlikely to occur and hence are not formed on the FeS surface.

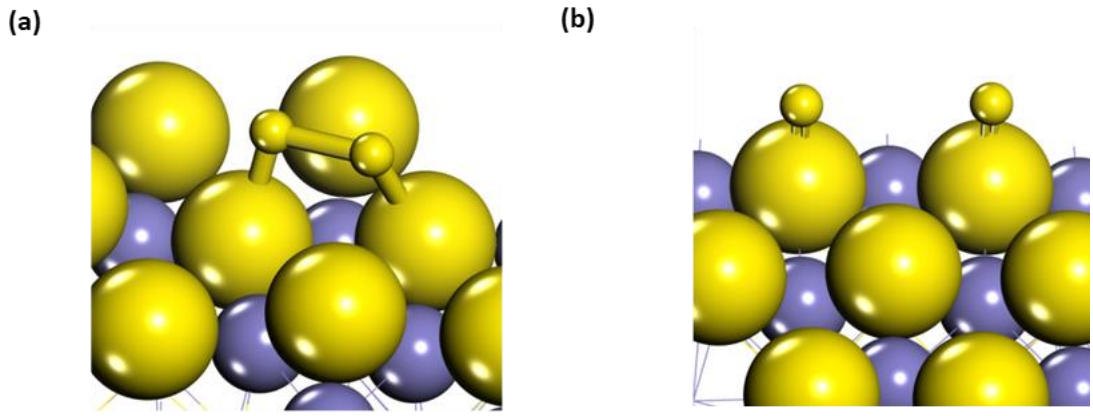

Figure S2.30. (a) Molecular adsorption and (b) Dissociative adsorption of disulfur over the exposed S-S sites present on the FeS surface

Thus overall, methane activation and sulfur adsorption studies done over the FeS surface suggest the FeS phase to be unreactive for methane activation indicating that it is likely the FeS_2 surface that catalyzes the reaction, which has been proven to be quite active via computational studies as discussed in the main text.

2.10.19. Summary of primary reaction pathways of SOCM occurring over the Fe-S_{brid}, S_{dim} and S_{mono} sites present on the sulfided Fe_3O_4 surface and their energetics

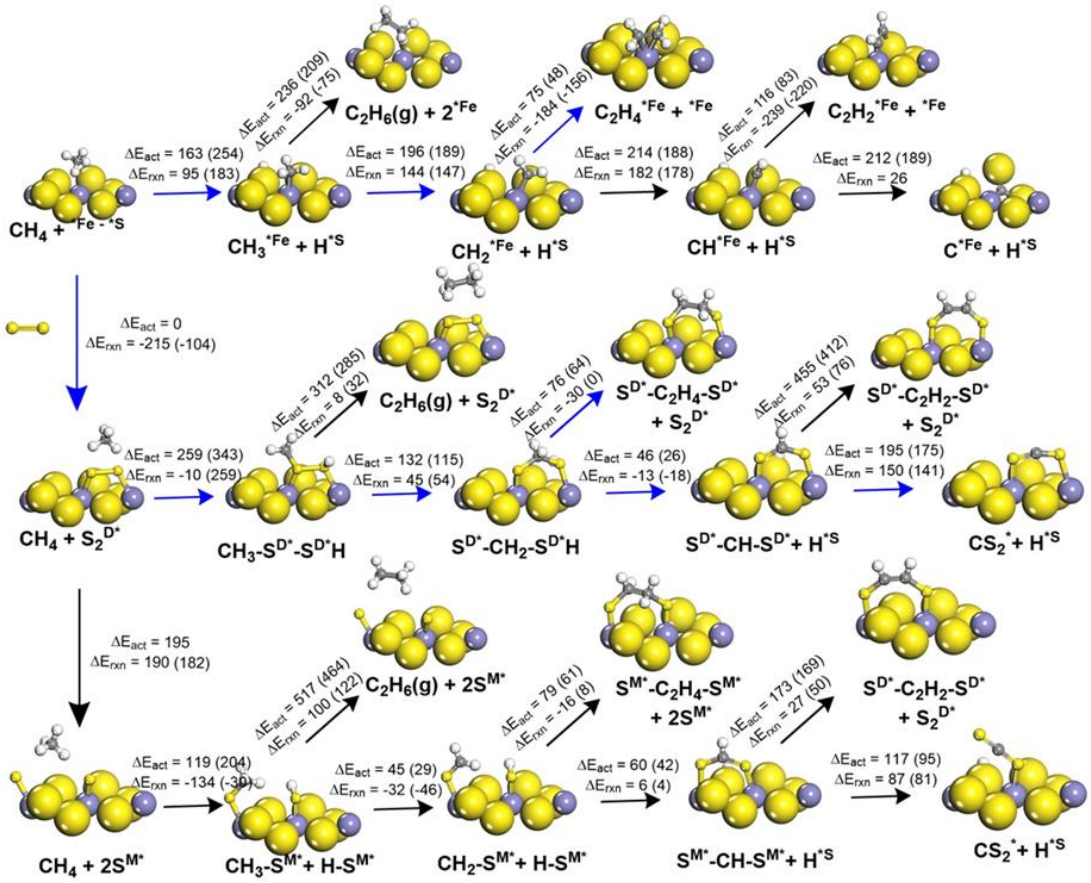

Figure S2.31. Summarized primary reaction pathways over different active sites and the respective enthalpy of activation and enthalpy of reactions: a) over Fe-S_{brid} sites; b) over S_{dim} (S_2^{D*}) sites; c) over S_{mono} (S_M*) sites. Arrows in blue denote the dominant pathways in the reaction network as summarized in Figure 2.11 in main text. The numbers in brackets represent the free energy values of the reaction.

2.10.20. SOCM Carbon Balance

Here we report the carbon balance of all the reactions in Table S2.9 using the following equation:

$$Carbon\ Balance = \frac{Carbon_{outlet}}{Carbon_{inlet}} = \frac{\sum x C_x H_y S_{z\ outlet}}{\sum x C_x H_y S_{z\ inlet}} \quad (2.42)$$

Table S2.9. Carbon balance in SOCM reactions

Experiment		Carbon Balance
Reaction Order Determination	S_2	97.6%
	CH_4	98.9%
	H_2S	97.4%
	CS_2	94.2%
Delplot	Feed: CH_4	97.9%
	Feed: C_2H_6	98.9%
	Feed: C_2H_4	94.1%
	Feed: C_2H_2	91.8%
Product distribution vs. contact time	Feed: CH_4	97.8%
	Feed: C_2H_6	98.4%
	Feed: C_2H_2	93.1%
Apparent activation energy		98.4%

Note that previously, 12 wt% coke formation was reported over Fe_3O_4 at 950°C with a WHSV of 0.785h^{-1} and a CH_4 : S_2 of 3.01 after TOS = 6hr. It was also concluded that coke formation does not deactivate the catalysts in SOCM. In the present study,10 wt% coke formation on Fe_3O_4 is observed at 865°C with a WHSV of 0.785h^{-1} and a CH_4 : S_2 of 3.01 after TOS = 20hr. Additionally, as shown above, when operated at a lower temperature, the carbon loss is lower than 10% for all experiments. Therefore carbon formation is insignificant and does not deactivates the Fe catalysts.

Chapter 3 - Computational study of the dehydrogenation of cyclohexanone over $Pd(DMSO)_2(TFA)_2$ catalyst and origins of selectivity towards cyclohexenone versus phenol

Adapted from Udyavara, S., Ryan, M. C., Stahl, S.S., and Neurock, M., Computational study of the dehydrogenation of cyclohexanone over $Pd(DMSO)_2(TFA)_2$ catalyst and origins of selectivity towards cyclohexenone versus phenol, *under preparation*

Theoretical calculations were performed by SU under the supervision of MN

3.1. Synopsis

Pd^{II} based catalyst systems stabilized by the presence of ancillary dimethyl sulfoxide (DMSO) ligand have been shown to yield high chemoselectivity towards cyclohexenone in the dehydrogenation of cyclohexanone. Density functional theory (DFT) calculations are used herein to elucidate the elementary kinetics and mechanisms that control the selective dehydrogenation of cyclohexanone to cyclohexenone as well as to phenol over $Pd(DMSO)_2(TFA)_2$. The computational results suggest that the mechanism for dehydrogenation over $Pd(DMSO)_2(TFA)_2$ proceeds via: i) substitution of trifluoroacetate ligand (TFA) with cyclohexanone which binds via its carbonyl oxygen to the Pd^{II} metal center, ii) intermolecular deprotonation of the oxygen bound cyclohexanone via the dissociated TFA anion, iii) dissociation of DMSO leading to isomerization of the Pd bound O-enolate species to an η^2-enolate bound to the metal via its oxygen and carbon atoms and iv) reductive β-hydride elimination to produce cyclohexenone. The initial activation of the alpha C-H bond was found to be the rate determining step with an overall apparent free energy barrier of 123 kJ/mol which is consistent with published kinetic isotope effects and experimentally obtained rate orders. Subsequent calculations comparing the apparent free energy barriers of the rate determining initial C-H activation step between cyclohexanone and cyclohexenone dehydrogenation show higher barriers towards the latter for C-H activation occurring at both, its C_2 (carbon atom ortho to the carbonyl carbon) and C_4 (carbon atom para to the carbonyl carbon) positions. A detailed analysis of the distortions and interactions suggests that the higher free energy barrier for C-H activation at the C_2 position is due to the stronger C_2 C-H bond of cyclohexenone relative to cyclohexanone, whereas the higher free energy barrier for C-H activation at the C_4 position is due to weaker orbital interaction of the attacking TFA^- with the C_4 end of cyclohexenone. The higher free

energy barriers for subsequent C-H activation thus limit the further dehydrogenation of cyclohexenone over homogeneous $Pd(DMSO)_2(TFA)_2$ catalyst which in turn increases the selectivity of the cyclohexanone dehydrogenation reaction towards cyclohexenone. Further screening studies suggest that increased dehydrogenation rates can be obtained by designing catalytic systems with more basic covalent ligands such as OAc in place of TFA since its greater proton affinity would promote the activation of the acidic C-H bond.

3.2. Introduction

Transition metal catalyzed C-H functionalization reactions are critical transformations used in synthesis of pharmaceuticals, agrochemicals, natural products, and industrial materials.[8,185–190] The formation of unsaturated C-C bonds from saturated C-C bonds is often the first step in C-H functionalization reactions.[191–194] Numerous studies have been carried out to establish metal-ligand complexes to selectively carry out C-H activation and dehydrogenations involving iridium/PCP-pincer and ruthenium-hydride complexes,[195–198] and palladium salts such as $PdCl_2$ or $Pd(OAc)_2$,[199–202] These reactions, however, typically require the use of costly and toxic reagents or co-catalysts[199,201] and multiple step processes which makes it hard to scale up.[202] Recently, there has been a surge in the field of Pd^{II}-catalyzed aerobic oxidation catalysis as an atom efficient and environmentally safe alternative to these processes to carry out similar catalytic transformations.[5,42,49,203–206] Stahl et al. recently advanced the utility of the Pd^{II} oxidase catalysis for dehydrogenation reactions of cyclohexanone and other carbonyl compounds to form phenols, cyclohexenone and other unsaturated cyclic enones.[5,48,49,51,207,208]

However, controlling the chemoselectivity for the dehydrogenation reaction poses a significant challenge, given the multitude of products that can be obtained through sequential oxidation pathways. An approach to control the chemoselectivity for the dehydrogenation reaction of cyclohexanone was recently reported in studies by Stahl et al. who have reported preferential tuning of the reaction selectivity by modulating the ligand environment around the $Pd(TFA)_2$ catalyst (Scheme 3.1).[48,51] Subsequent experimental mechanistic investigations showed that DMSO ligands, in particular, stabilize the homogeneous system that selectively catalyzes the first dehydrogenation step over the second dehydrogenation step, leading to the higher observed

cyclohexenone yields of ~91% and low phenol yields of ~8%.[52] The use of 2-Me_2Npy and diazafluorenone ligands along with Pd^{II}, on the other hand, catalyzes the first dehydrogenation step to form cyclohexenone. However, the Pd^{II} species were shown to evolve into soluble Pd nanoparticles which catalyze the further dehydrogenation of cyclohexanone to form phenol with yields as high as 79%.[50]

Scheme 3.1: Ligand dependent $Pd(TFA)_2$-catalyzed selective dehydrogenation of cyclohexanone

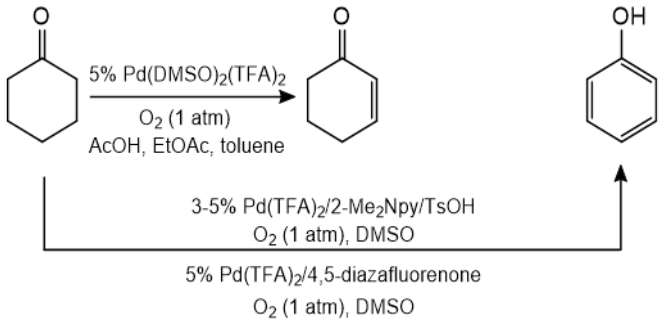

The mechanistic investigation is rather insightful but still limited in terms of the specific elementary steps and the specific sites that carry out these steps. In addition, there are a few unanswered questions as to how the stability of the homogeneous catalyst controls the selectivity of the reaction. Specifically, what are the factors that prevent cyclohexenone from dehydrogenating further like cyclohexanone over the homogeneous catalyst? It was hypothesized that cyclohexenone likely binds to the metal center as an alkene adduct unlike cyclohexanone, which may block access to succeeding C-H activation routes.[52] However, computational studies that go into the details of this phenomena are still rather elusive. Detailed analysis and understanding of the elementary reaction steps and the effect of catalyst homogeneity on the reaction selectivity requires a thorough computational investigation. Thus, to gain further insights into this intriguing experimental strategy to control the selectivity, herein, we sought to ab-initio quantum chemical calculations, to elucidate the sites and the mechanisms that drive the selective dehydrogenation of cyclohexanone to cyclohexanone over $Pd(TFA)_2(DMSO)_2$ catalyst.

We initially examine the elementary reaction steps involved in the cyclohexanone dehydrogenation reaction over $Pd(TFA)_2(DMSO)_2$. Based on previous mechanistic studies,[52] the mechanism is thought to proceed by an initial formation of Pd^{II}–

cyclohexanone adduct followed by concerted cleavage of C-H bond and dissociation of the TFAH ligand, and a β-hydride elimination to afford the cyclohexenone product as shown in Scheme 3.2. The catalyst is then re-oxidized back to its initial state, in presence of oxygen, in the second part of the redox cycle. The authors propose a five co-ordinate transition state for the initial rate determining C-H activation step resembling closely to the computationally and experimentally validated five co-ordinate transition state structure proposed for $Pd(py)_2(OAc)_2$ catalyzed aerobic oxidation of alcohols involving O-H bond activation.[207]Steinoff However, there is no reported computational evidence yet for existence of such a transition state for C-H activation reactions. Further, besides the mechanism proposed by the authors, the reaction can also be envisioned to proceed via displacement of either of the DMSO or TFA ligand to form a four co-ordinate intermediate, through which the alpha C-H activation step can proceed. C-H activation that proceeds via such four co-ordinate structures are much more common and widely reported for Pd^{II}-catalyzed alkane and arene C-H functionalization reactions.[209–212] While the minimal effect of DMSO concentration on the reaction rate suggests that DMSO likely does not dissociate prior to the rate limiting alpha C-H activation step, the studies however still don't rule out the possibility of the mechanism proceeding via a TFA dissociation step.

Scheme 3.2: Proposed mechanism for $Pd(DMSO)_2(TFA)_2$-catalyzed dehydrogenation of cyclohexanone[52]

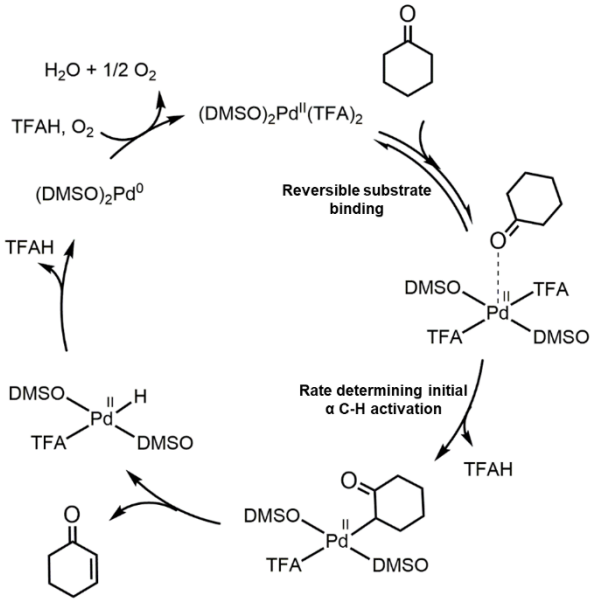

Therefore, in this study, we begin with a thorough investigation of several possible mechanisms for the initial alpha C-H activation step proceeding through five co-ordinate complex (Pathway A) or four co-ordinate complexes formed via displacement of either the DMSO (Pathway B) or TFA ligand (Pathway C) as shown in Scheme 3.3 and then subsequently examine the β-hydride elimination paths for the activation of the second C-H bond. We further then explore the origins of the higher selectivity obtained for cyclohexenone over phenol by determining the kinetics of the cyclohexenone dehydrogenation reaction and comparing it with that of cyclohexanone dehydrogenation reaction. Finally, insights gained from these studies were subsequently used to screen different catalysts to identify the properties of the covalent ligands that could effectively lead to more active dehydrogenation catalysts. Overall, we hope that the molecular level insights gained from these studies would aid in the development of selectivity control strategies for other oxidation chemistries.

Scheme 3.3: Mechanistic routes involving three distinct intermediate Pd complexes preceding the initial alpha C-H activation step considered in the computational study

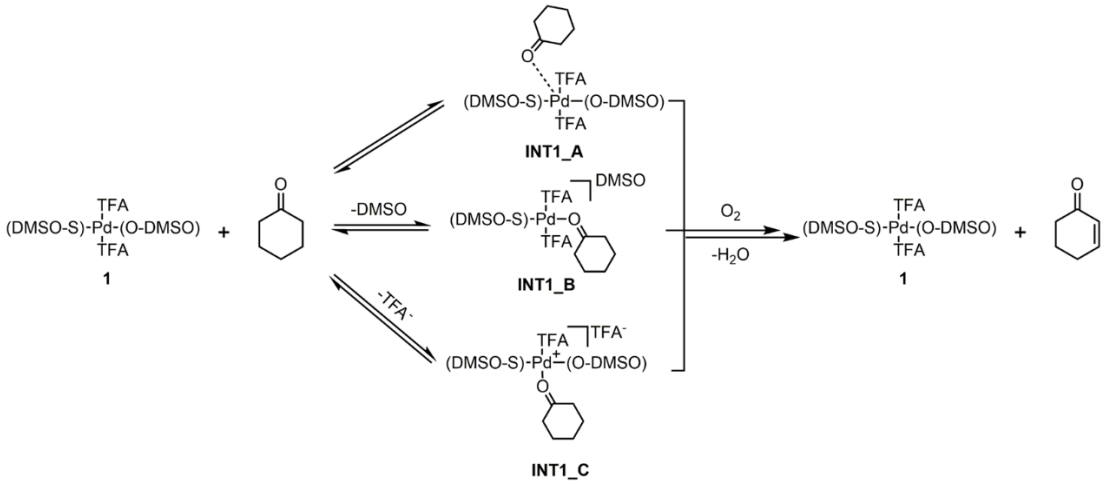

3.3. Computational methods

The calculations reported herein were all carried out using the Gaussian 09 software.[213] Structural optimizations and transition state searches were done using the M06L density functional.[214] The SDD basis set[215] and the 6-311++G(d,p) basis set [216–218] were used to describe the Pd atom, and all other atoms , respectively. Frequency calculations were carried out at the same level of theory to validate the stationary minima (no imaginary frequencies) and isolated transition state structures (single imaginary frequency). The frequencies were also used to determine the entropic and zero-point

energies (ZPE) for all reactant, intermediate, transition state and product structures. The calculated entropies and ZPE corrections determined at a temperature of 333 K (60 °C) and 1 atm pressure were then used together with the electronic energies to determine free energies. Solvent effects on the resultant energetics were calculated by carrying out single point energy calculations on the gas phase optimized structures using the implicit SMD solvation model[219] wherein ethyl acetate was used as the solvent. The absolute free energies of the species in the solvent were then computed as,

$$G_{sol} = G_{gas} + (E_{sol} - E_{gas}) + RTln(24.7), \quad (3.1)$$

where E_{sol} and E_{gas} are the electronic energies of the species in the solvent and the gas phase respectively, G_{gas} is the computed free energy in the gas phase and RTln(24.7) is the correction term added to correct for the standard state concentration of 1 M in solution phase.

3.4. Results and Discussion

3.4.1. Cyclohexanone dehydrogenation mechanistic analysis - First C-H activation step

3.4.1.1. Five coordinate complex (Pathway A): With Pd(S-DMSO)(O-DMSO)$(TFA)_2$ determined as the resting state of the catalyst (see SI for further details), the initial C-H activation step via the five coordinate Pd intermediate (**INT1_A**) proceeds in a concerted fashion forming a five-centered transition state (**TS1_A**) with the oxygen of cyclohexanone bound to the metal center and the C-H bond being activated by the TFA ligand as shown in Scheme 3.4. However, such a five coordinate transition state could not be isolated and the transition state search optimizations resulted in structures corresponding to a 4 coordinate TS with either the DMSO or the TFA dissociated (see SI for further details). Similar attempts reported by Goddard et al. to isolate a five coordinate C-H activation transition state for secondary alcohol oxidation reactions catalyzed by (-)-sparteine-Pd^{II} complexes also resulted in dissociation of the associated chlorine (Cl) ligand, thus resulting in a four coordinate transition state.[220] In addition, other studies on isolating a five-centered Pd intermediate for oxidative addition of aryl halides to Pd(0) complexes also showed similar ligand displacements yielding more stable four coordinate intermediates.[221–223] The results herein in conjunct with previously reported studies thus indicate that the formation of

a five coordinate transition state in a C-H activation step is unprecedented and hence is unlikely to occur.

Scheme 3.4: Five coordinate TS pathway (Pathway A) for $Pd(TFA)_2(DMSO)_2$-catalyzed dehydrogenation of cyclohexanone

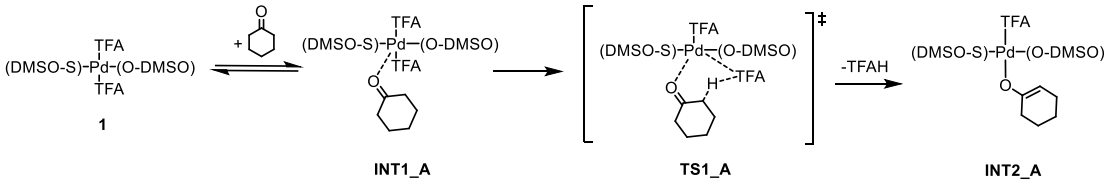

3.4.1.2. Four co-ordinate complex via DMSO Ligand Displacement (Pathway B): The DMSO ligand displacement by cyclohexanone proceeds with an energetic penalty of 17 kJ/mol to form **INT1_B** wherein the more labile O-bound DMSO gets substituted by the cyclohexanone substrate (see SI for further information). Upon the displacement of the DMSO ligand by cyclohexanone, the C-H bond of cyclohexanone can then be activated via commonly reported base assisted C-H activation routes including concerted metalation deprotonation (CMD) and sigma-bond metathesis (SBM).[187,189,209,212] Oxidative addition (OA) also presents another alternative for the activation of the C-H bond. However, previous reports have suggested such routes to be less accessible in presence of a basic ligand such and hence is not considered herein.[210,224] In addition, an intramolecular deprotonation route which proceeds through the oxygen adsorbed cyclohexanone intermediate is also considered. The above elementary mechanistic initial C-H activation steps have been outlined in Scheme 3.5, the energetics for which are summarized in the free energy diagram shown in Figure 3.1.

a) **Concerted Metalation Deprotonation (CMD):** In the CMD route, the cyclohexanone which is initially bound via oxygen rotates in order to allow the formation of Pd C-H adduct intermediate **INT2_B**. The formation of this intermediate has an overall reaction free energy of 84 kJ/mol. The carbonyl oxygen acts as a better Lewis base than the C-H adduct and binds more strongly to the electrophilic metal center. This results in energetic penalty to form the less stable C-H adduct. The C-H bond of the adduct is subsequently activated via a concerted insertion of the electrophilic metal to the C-H bond together with the abstraction of the proton via the oxygen of the unbound acetate to form a six-member ring

transition state (**TS1_B**) that goes on to form **INT3_B** involving the binding of enolate (at the C_1) and TFAH to Pd center. Similar pathways were previously shown to be dominant for arene and alkane C-H activation in cross-coupling and functionalization reactions.[209,210,225] In this case however, this pathway proceeds with a high overall apparent free energy barrier of 182 kJ/mol and an overall reaction free energy of 72 kJ/mol, thus making this pathway unlikely to occur under the operating reaction temperature of 60 ºC.

Scheme 3.5: Proposed mechanistic pathways for $Pd(DMSO)_2(TFA)_2$-catalyzed cyclohexanone dehydrogenation proceeding via cyclohexanone displacement of DMSO (Pathway B)

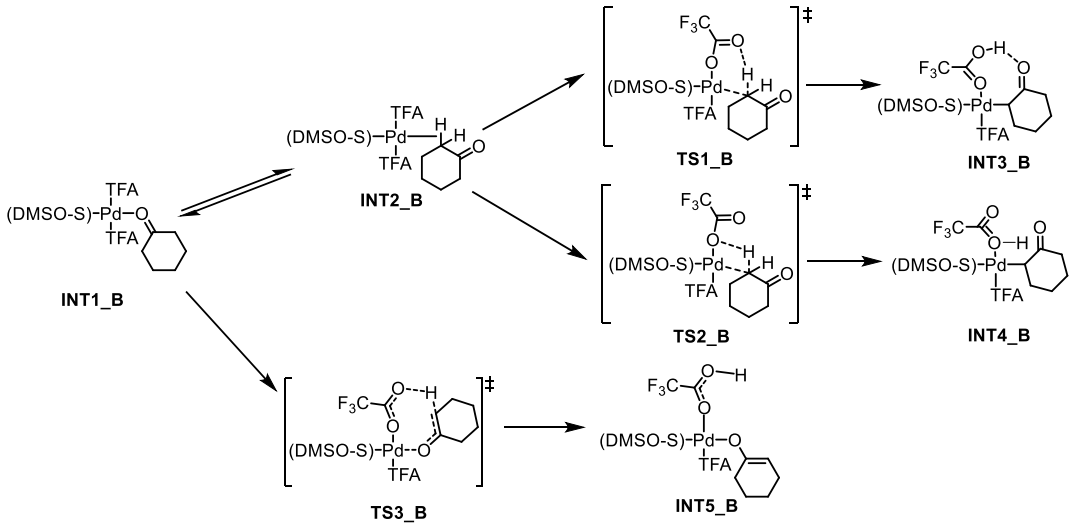

b) Sigma Bond Metathesis (SBM): The SBM pathway proceeds similarly to that for the CMD path in that cyclohexanone binds to form the C-H adduct (**INT2_B**). In the SBM path, however, the hydrogen is abstracted by the bound oxygen of the acetate rather than the unbound oxygen via the four center transition state (**TS2_B**) to form **INT4_B**. This mechanism proceeds with a free energy barrier of 238 kJ/mol and an overall reaction free energy of 154 kJ/mol which are significantly higher than the energies reported for the formation of **TS1_B** and **INT3_B** in the CMD path. The bound acetate oxygen is significantly less basic than that of the unbound oxygen and has a much lower proton affinity, thus leading to the much higher free energy barrier to abstract the acidic proton. Similar results have also been reported for C-H olefinations of toluene derivates wherein it has been shown that the CMD pathway

is favored over the SBM pathway as a result of the higher basicity of the hydrogen abstracting oxygen.[210,212,224]

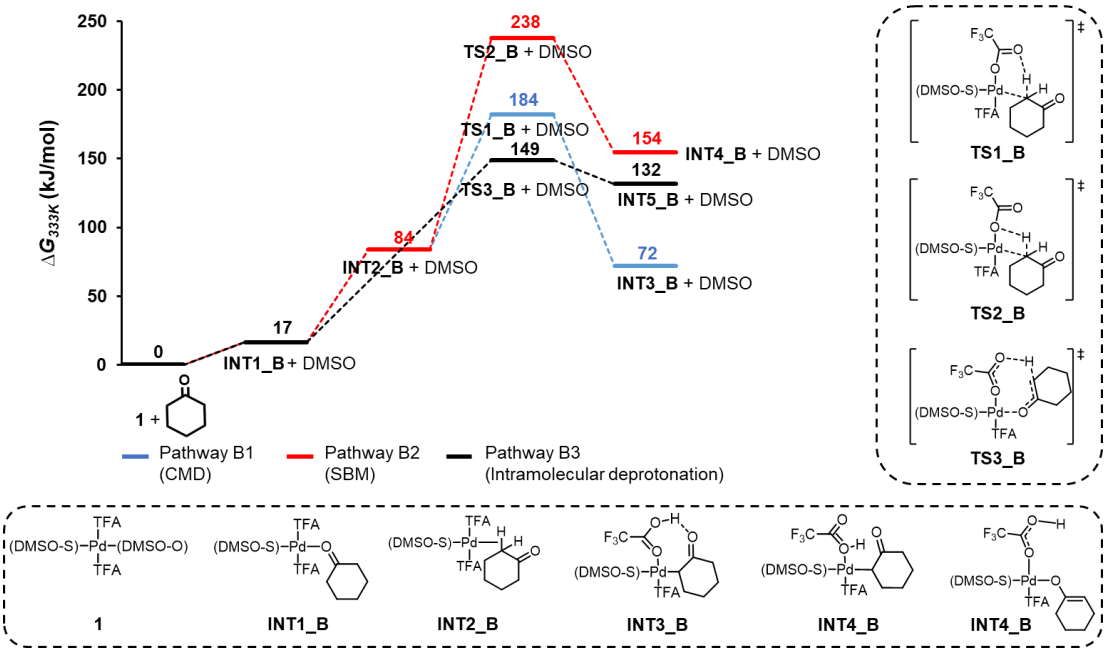

Figure 3.1: Free energy profile of the different considered mechanistic pathways for the initial alpha C-H activation of cyclohexanone proceeding via elimination of the neutral DMSO ligand (Pathway B). All energies are relative to *trans*-$Pd(DMSO)_2(TFA)_2$ (**1**) + cyclohexanone.

c) Intramolecular Deprotonation: In this path, unlike that of the CMD and SBM pathways, the reaction proceeds directly via the abstraction of hydrogen from the O-bound cyclohexanone by the oxygen of the bound TFA moiety to form an O-bound Pd-enolate (**INT5_B**). Hydrogen abstraction is only considered herein by the unbound oxygen as the results presented in 3.2.1.2b as well as in previous studies[210,212,224] show that it is more basic and more reactive for hydrogen abstraction. This path proceeds via a concerted C_2-H activation by the free oxygen of the acetate and a keto-enol tautomerization of the (Pd^{II})-bound enolate via a six member-ring transition state (**TS3_B**) to form **INT5_B**. The apparent free energy barrier and the overall reaction free energy for this reaction are 149 kJ/mol[226] and 132 kJ/mol, respectively. Figure 3.1 which compares all the possible pathways proceeding via displacement of the DMSO ligand examined herein shows that the intramolecular deprotonation pathway has the lowest overall apparent free energy barrier of 149 kJ/mol. This pathway, as mentioned above, eliminates the need to

form the higher energy C-H adduct intermediate. The electrophilic Pd^{II} Lewis acid center instead stays bonded to the basic carbonyl oxygen. This stabilizes the transition state for the C-H activation, thus lowering the overall free energy barrier over that for the CMD and SMD paths. In addition, the Pd^{II} withdraws electron density from bound enolate which increases the acidity of the C_2 hydrogen, thus facilitating hydrogen abstraction by the vicinal bound TFA. The stabilization of the bound cyclohexanone and the enhanced acidity of the bound enolate both act to lower the apparent free energy barrier observed for the intramolecular deprotonation path.

3.4.1.3. Four co-ordinate complex via TFA Ligand Displacement (Pathway C): The displacement of the TFA ligand by cyclohexanone leads to the formation of an ionic system involving a cationic Pd complex (**INT1_C** in Scheme 3.6) along with the displaced TFA anion. This results in a significantly higher energetic penalty of 89 kJ/mol for this step compared to the 17 kJ/mol required to displace the DMSO ligand. The oxygen bound cyclohexanone can then undergo C-H activation at the α-C via the concerted metalation deprotonation (CMD) or the intramolecular deprotonation discussed in the previous section. In addition, the availability of the free TFA anion also opens up the possibility for an intermolecular deprotonation pathway wherein the dissociated TFA anion (TFA^-), rather than the Pd-bound TFA, abstracts the hydrogen. The various elementary C-H activation routes proceeding via the cationic Pd complex have been outlined in Scheme 3.6, with the resulting energetics for these paths are summarized in Figure 3.2.

a) **Concerted Metalation Deprotonation (CMD):** The CMD pathway, as discussed previously in section 3.2.1.2, proceeds initially through the formation of a C-H adduct. The overall reaction free energy required to form this C-H adduct intermediate (**INT3_C**) via **INT2_C**, the cis-form of the catalyst, was calculated to be 160 kJ/mol. The subsequent activation of the C-H bond via **TS1_C** to form the Pd-C enolate **INT4_C** results in an apparent free energy barrier of 264 kJ/mol and an overall reaction free energy of 197 kJ/mol. The high overall free energy barrier in this case eliminates the likelihood of observing the CMD pathway via the cationic Pd complex. The SBM pathway examined in Pathway B which proceeds via DMSO elimination had a significantly higher apparent free energy barrier (238 kJ/mol) than that for the CMD pathway (182 kJ/mol). The free energy barrier for the SBM path

in the present TFA elimination system is also likely higher than that for the CMD path and as such was considered to be unlikely to occur in the TFA elimination system examined here that requires the formation of the cationic Pd complex.

Scheme 3.6: Proposed mechanistic pathways for $Pd(DMSO)_2(TFA)_2$–catalyzed cyclohexanone dehydrogenation proceeding via cyclohexanone displacement of TFA (Pathway C)

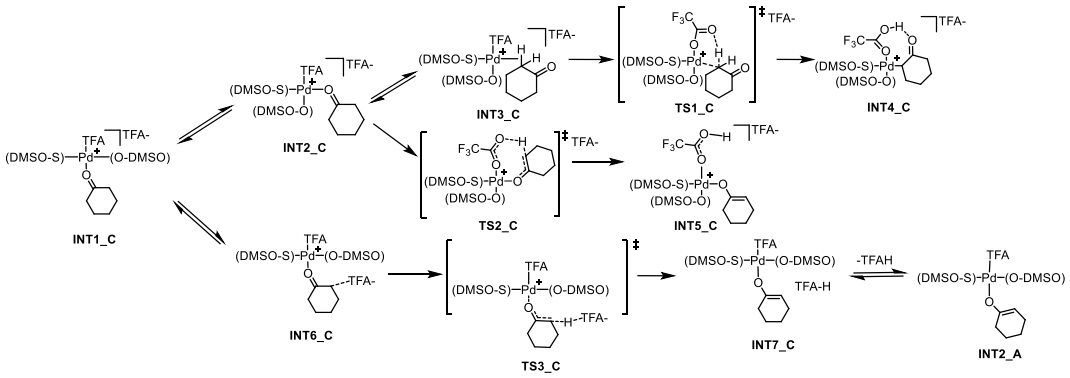

b) **Intramolecular deprotonation:** As seen previously in section 3.4.1.2a, C-H bond activation which proceeds via the O-bound cyclohexanone intermediate give lower apparent free energy barriers. A similar lower free energy barrier of 214 kJ/mol was found herein as well wherein the bound cyclohexanone that forms is deprotonated by the bound TFA molecule to form **INT5_C** via the transition state shown in **TS2_C**. However, the high computed free energy barrier of 214 kJ/mol suggest that despite the lowering of the apparent free energy barriers, the occurrence of the intramolecular deprotonation pathway for this cationic complex is still unlikely.

c) **Intermolecular deprotonation:** While the Pd-associated TFA anion was acting as the base to abstract the proton, the dissociated TFA anion is significantly more basic than the bound TFA and as such may be more reactive. This abstraction of the proton at the C_2 position by the TFA anion, known as the intermolecular deprotonation pathway, proceeds via **TS3_C** transition state shown in Figure 3.3 resulting in the formation of Pd bound O-enolate **INT7_C**. The apparent free energy barrier and the overall reaction free energy for this path were calculated to be 123 kJ/mol and 113 kJ/mol, respectively. Similar transition states have been reported for Ru(II) catalyzed C-H bond activation of functionalized arenes and Pd(II) catalyzed arylation.[227,228]

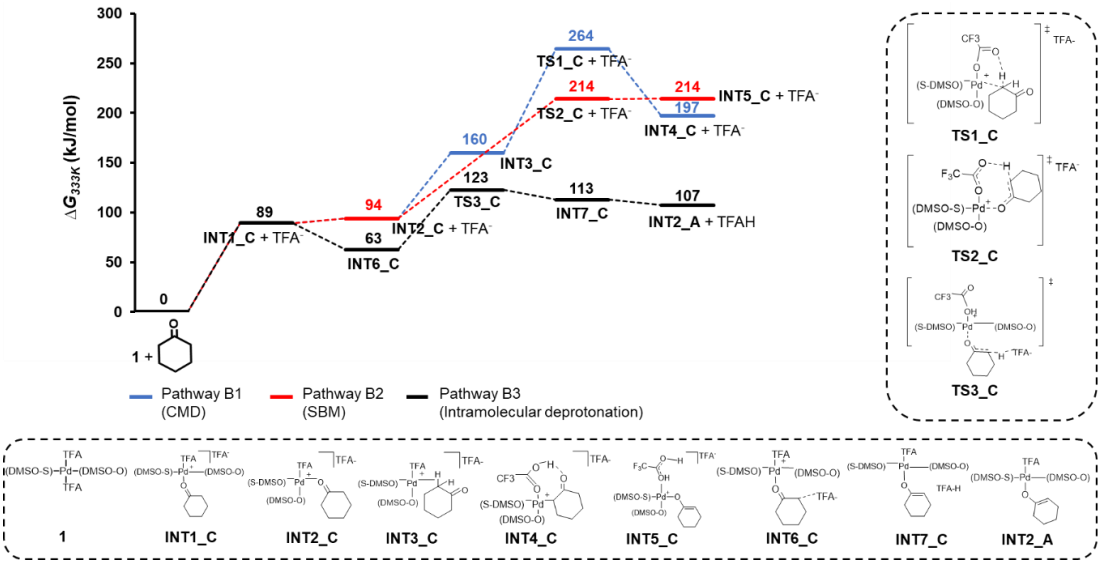

Figure 3.2: Free energy profile for the different mechanistic pathways considered for the initial alpha C-H activation of cyclohexanone proceeding via elimination of the anionic TFA ligand (Pathway C). All energies are relative to *trans*-Pd(DMSO)$_2$(TFA)$_2$ (**1**) + cyclohexanone.

Thus, among the different mechanistic routes proceeding via substitution of the TFA ligand with cyclohexanone, the *intermolecular deprotonation* path was found to be the most favored with the lowest overall apparent free energy barrier of 123 kJ/mol. Comparing this route with the intramolecular deprotonation pathway that proceeds via displacement of the DMSO ligand with an apparent free energy barrier of 149 kJ/mol, we can infer the intermolecular deprotonation route to be the most likely route for the initial alpha C-H activation step. The successive steps for this lowest free energy barrier route were then subsequently examined in the following section.

3.4.2. Cyclohexanone dehydrogenation mechanistic analysis - Second C-H activation step

The Pd-bound enolate intermediate that forms via the initial C-H activation of the cyclohexanone can subsequently react via the activation of neighboring C-H bond to complete the dehydrogenation of cyclohexanone to cyclohexenone. The two paths considered here and highlighted in Scheme 3.7 include the conventional β-hydride elimination and the reductive β-hydride elimination. While the conventional β-hydride elimination is the most common route reported for Pd^{II} catalyzed oxidation reactions involving alcohol oxidation[42,229,230] and alkane dehydrogenation,[193] the reductive β-

hydride elimination route is however less common, but has been shown to be prevalent in case of Pd-NHC catalyzed alcohol oxidation.[231] We thus examine both these pathways here to determine the most likely route involved in activation of the second C-H bond. The detailed elementary steps for both of these pathways are described below with the overall energetics summarized in Figure 3.4.

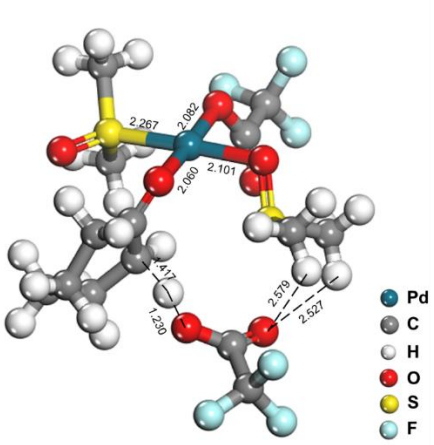

Figure 3.3: Ball-and-stick model of the optimized transition state structure for the intermolecular deprotonation of cyclohexanone (**TS3_C**). The bond length metrics are given in Å.

a) **β-hydride elimination:** β-hydride elimination requires a free coordination site on the Pd complex in order to cleave the C-H bond and abstract the hydrogen. This proceeds via the dissociation of the O-bound DMSO from the metal center and is subsequently followed by the isomerization of the Pd-O enolate (**INT2_A**) to its η^2-enolate form (**INT1_D**) wherein both the oxygen and the carbon atoms of the enolate moiety bind to the metal center. This dissociation reaction proceeds with an intrinsic reaction free energy of -43 kJ/mol. The β-hydrogen can now be activated in order to generate the Pd-hydride intermediate (**INT2_D**). This reaction proceeds with an apparent free energy barrier of 114 kJ/mol[232] via **TS1_D** to form **INT2_D** with a similar reaction free energy of 114 kJ/mol. The cyclohexenone that forms subsequently desorbs to yield **INT3_D** and generate the free cyclohexenone product. The overall reaction free energy for this step was calculated to be 96 kJ/mol. The hydride intermediate that formed subsequently reacts with the bound TFA via a reductive elimination as shown in **TS2_D** in Scheme 3.7 to form TFAH bound to the reduced Pd^0 catalyst (**INT4_D**). This reaction occurs with an overall apparent

free energy barrier and reaction free energy of 135 and 111 kJ/mol respectively. The bound TFAH in the intermediate **INT4_D** is ultimately eliminated via substitution with DMSO to form **INT7_D**.

Scheme 3.7: Proposed mechanistic pathways for the β-hydride elimination step in $Pd(TFA)_2(DMSO)_2$-catalyzed dehydrogenation of cyclohexanone

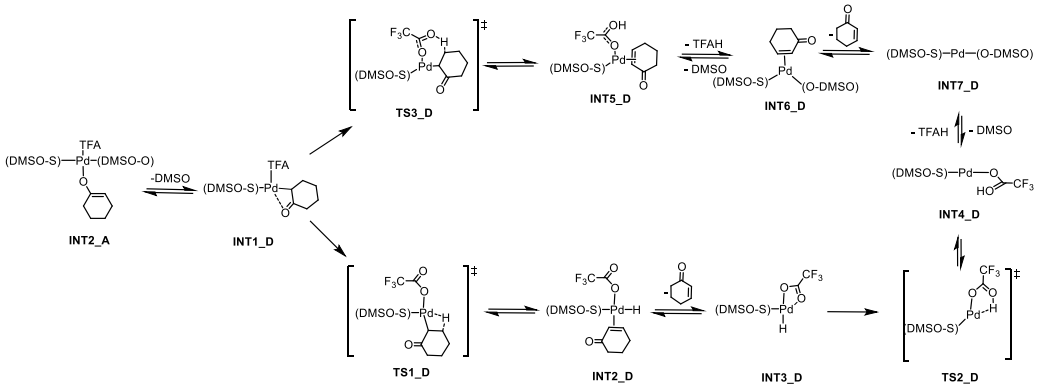

b) **Reductive β-hydride elimination:** The β-hydride elimination reaction discussed above in 3.2.2a can also proceed in a concerted mechanism whereby the β-hydride elimination and the reductive elimination steps occur together. In this mechanism, the β-hydrogen is directly abstracted by the TFA ligand to form the TFAH and cyclohexenone product without the need to form the β-hydride. The cyclohexenone that forms binds to the Pd center as alkene adduct (**INT5_D**), which can subsequently desorb to form the cyclohexenone product and **INT6_D**. The calculated transition state for the reductive β-hydride elimination **TS3_D** which is shown in Figure 3.5 results in an overall apparent free energy barrier of 107 kJ/mol, which is considerably lower than the activation free energy barrier of 135 kJ/mol computed for the stepwise β-hydride elimination path.

Thus, based on the computed free energy barriers for the second C-H activation step, the second C-H activation likely proceeds via a reductive β-hydride elimination pathway. The overall apparent free energy barrier for this second C-H activation step (107 kJ/mol) is also considerably lower than the apparent free energy barrier for the initial alpha C-H activation step (123 kJ/mol). Thus, the initial alpha C-H activation step which proceeds via an intermolecular deprotonation pathway like TS is the rate limiting step for this reaction. These results agree with the experimental studies reported previously[52] which show a kinetic isotope effect (KIE) of 2.9 for the activation at the

alpha C-H position. Furthermore, the free energy barrier of 102 kJ/mol[52] extracted from the experimental kinetic data agrees with the DFT computed free energy barrier presented above (123 kJ/mol) within typical DFT errors of ~20 kJ/mol.[182] Also, the derivation of the rate orders for the intermolecular deprotonation mechanism (see SI for further details) suggest a first order dependence on both cyclohexanone as well as the catalyst, which agrees with the experimentally derived rate orders.

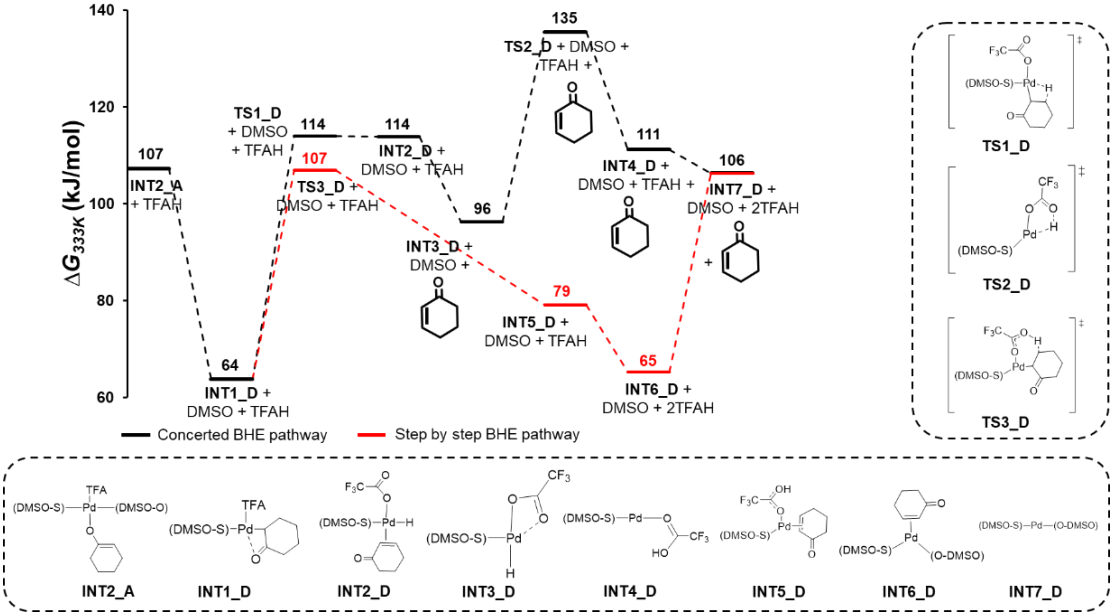

Figure 3.4: Free energy profile of the different considered mechanistic pathways for the second C-H activation step. All energies are relative to *trans*-Pd(DMSO)$_2$(TFA)$_2$ (**1**) + cyclohexanone.

Overall, the congruence observed between the experimental data[52] and the interpretations made from the computationally determined mechanism confirms that the dehydrogenation of cyclohexanone occurs through the pathway summarized in Scheme 3.8. The reduced Pd^0 catalyst which is formed upon oxidation of the cyclohexanone then gets re-oxidized in presence of the oxygen back to the resting state to regenerate the Pd(TFA)$_2$(DMSO)$_2$ (**1**) catalyst. Examination of the catalyst re-oxidation cycle is beyond the scope of this work and readers can refer to work by several other research groups for studies related to Pd^0 catalyst re-oxidation in presence of DMSO[230] as well as other ligands[233–235].

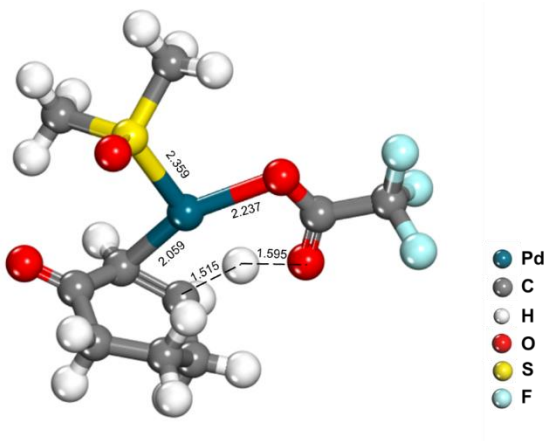

Figure 3.5: Ball-and-stick model of the optimized transition state structure for the concerted reductive β-hydride elimination of cyclohexanone (**TS3_D**). The bond length metrics are given in Å.

3.4.3. Cyclohexanone versus cyclohexenone dehydrogenation

Cyclohexanone is shown to initially bind to the Pd center via its carbonyl oxygen atom before the rate determining activation of the alpha C-H bond. Cyclohexenone, on the other hand, has both a carbonyl as well as a C=C moiety that can bind to the metal center. Thus, in order to probe the most favored mechanistic path for cyclohexenone dehydrogenation, we initially examined the binding of cyclohexanone to the metal center. We subsequently analyzed the possible pathways and mechanism for cyclohexenone dehydrogenation and compared the lowest energy path with the lowest energy path for cyclohexanone dehydrogenation. Further analysis of the difference in the free energy barriers between the two pathways was then carried out elucidate the reasons for the higher selectivity to form cyclohexenone over phenol.

3.4.3.1. Binding mode of cyclohexenone: The reaction energies required to displace off the TFA ligand by cyclohexenone was examined. Both adsorption modes, including cyclohexenone binding via carbonyl oxygen and alkene adduct, were examined so as to determine its most favorable binding mode. The calculations (see SI) indicate binding via the carbonyl oxygen to be more favorable than the alkene adduct by 30 kJ/mol. As such cyclohexenone binds via its carbonyl oxygen atom in a similar manner to that of cyclohexanone. The similar binding of both cyclohexanone and cyclohexenone thus rules out the notion that the different binding modes lead to the observed differences in selectivity, as was hypothesized previously.[52]

Scheme 3.8: Proposed detailed catalytic mechanism for $Pd(DMSO)_2(TFA)_2$-catalyzed dehydrogenation of cyclohexanone in EtOAc solvent

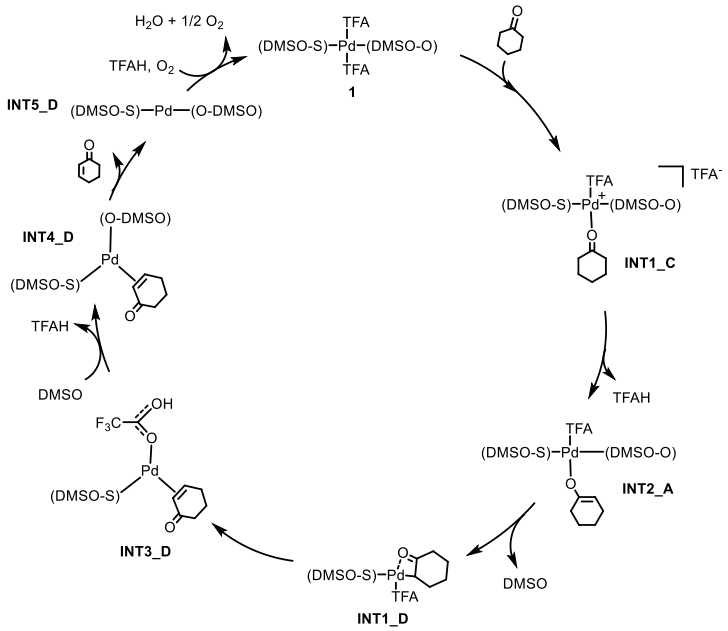

3.4.5.2. Cyclohexenone dehydrogenation mechanistic cycle: As cyclohexanone and cyclohexenone both bind to the Pd via their carbonyl oxygen atoms, we assume that the mechanistic paths for cyclohexanone and cyclohexenone dehydrogenation are similar. In cyclohexenone dehydrogenation, however, there are two C-H bonds that can be activated. The first involves the alpha (C_2) C-H bond analogous to the alpha C-H activation for cyclohexanone dehydrogenation, while the second involves the gamma (C_4) C-H bond. Cyclohexenone, can be dehydrogenated via initial C-H activation of either of these C-H bonds as shown in Scheme 3.9. Hence, both these resultant dehydrogenation paths were examined, results of which are shown in the energy diagram in Figure 3.6**.** Herein we specifically focus on the initial C-H activation step as this is the step that controls the rates for both cyclohexanone and cyclohexanone.

Similar to the mechanism proposed for cyclohexanone dehydrogenation (Scheme 3.8), the first step in the dehydrogenation of cyclohexanone involves the displacement of the anionic TFA ligand by the cyclohexenone moiety, which proceeds with a reaction free energy of 86 kJ/mol, 3 kJ/mol lower than that of cyclohexanone. The lower energetic penalty for substitution of the TFA ligand with cyclohexenone is associated with the higher basicity of cyclohexenone (Proton affinity = -581 kJ/mol) compared to

cyclohexanone (Proton affinity = -557 kJ/mol). This is due to the presence of the electron-rich alkene moiety which enables an increased electron donation from the bound oxygen to the electrophilic metal center.

Scheme 3.9: Modes of C-H activation involved in the initial rate determining intermolecular deprotonation step for dehydrogenation of cyclohexenone

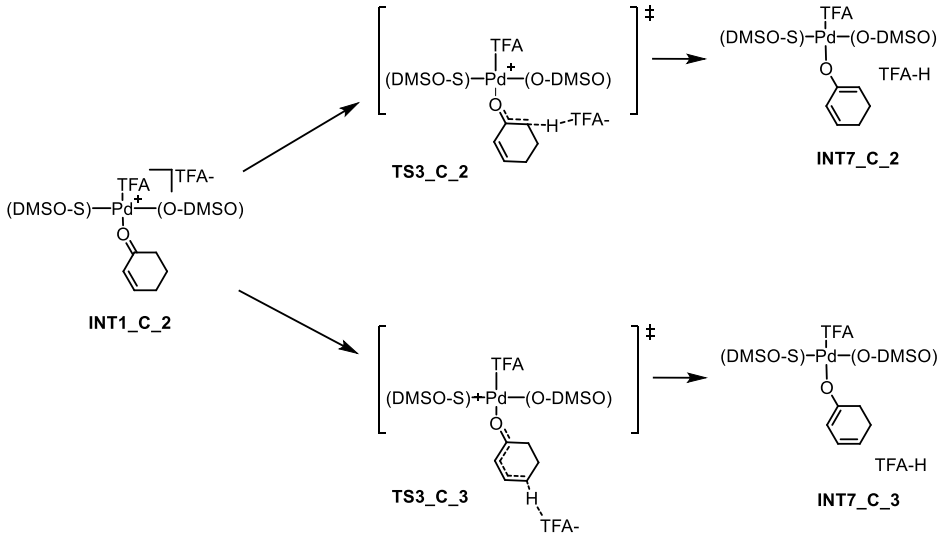

The dissociated TFA ligand can then attack the C-H bond of the bound cyclohexenone, abstracting the hydrogen as a proton either from the alpha (C_2) carbon or the gamma (C_4) carbon. Comparing the C_2 C-H activations for cyclohexanone and cyclohexenone shown in Figure 3.6, we can see that the overall apparent free energy barriers for the initial rate-determining C-H activation for cyclohexanone and cyclohexenone at the C_2 position are 123 and 141 kJ/mol respectively (Figure 3 and 7a respectively). This thus suggests that the C-H activation at the C_2 position of cyclohexenone is less favored than that of cyclohexanone which is consistent with the higher cyclohexenone selectivity observed experimentally. This difference in the free energy barriers also follows the calculated deprotonation energies of the C_2 C-H bonds for cyclohexenone and cyclohexanone which have values of 681 kJ/mol and 657 kJ/mol respectively. The stronger C-H bond at C_2 position for cyclohexenone versus cyclohexanone limits its C-H activation. The higher deprotonation energies for cyclohexenone can be attributed to the electron-rich alkene group present in the molecule which makes the C_2 hydrogen less acidic via stabilization of the partial positive charge that is developed on the carbonyl carbon.

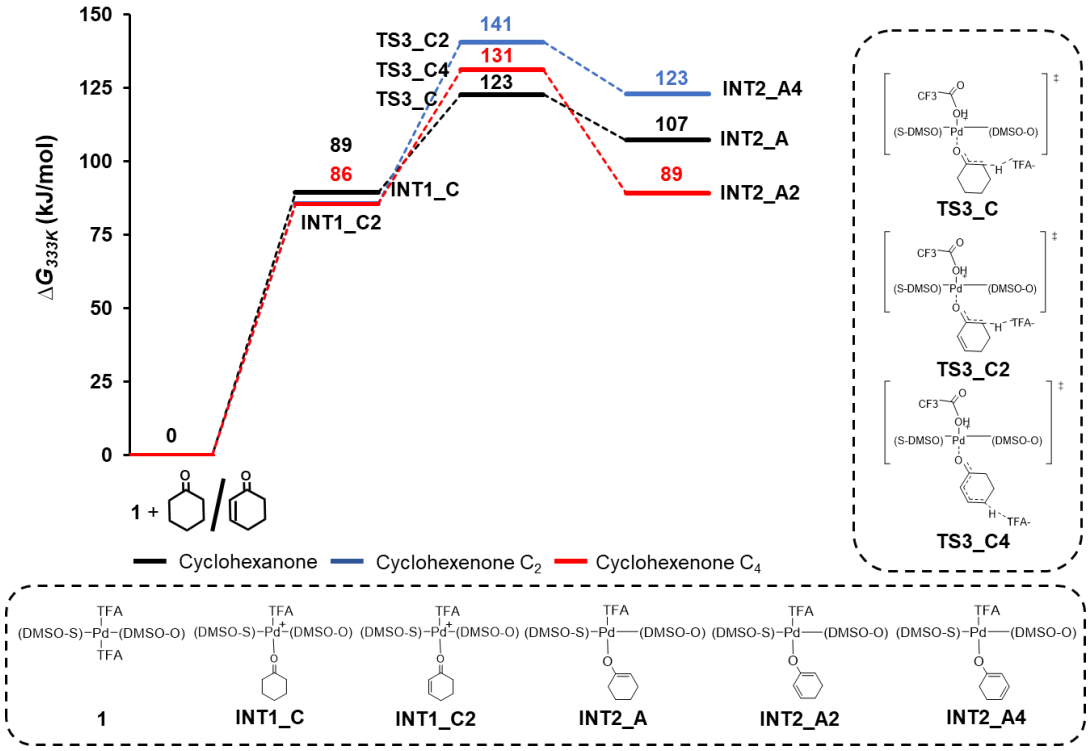

Figure 3.6: Abbreviated free energy profile comparing the initial alpha C-H activation of cyclohexanone versus that of cyclohexenone proceeding via elimination of the anionic TFA ligand (Pathway C). All energies are relative to *trans*-Pd(DMSO)$_2$(TFA)$_2$ (**1**) + cyclohexanone/cyclohexenone.

In addition to C-H bond activation at the C_2 position, the dissociated TFA anion can also attack the adsorbed cyclohexenone molecule at the C_4 C-H position as was discussed. The overall apparent free energy barrier to activate the C_4 C-H bond was calculated to be 131 kJ/mol (Figure 3.7b), which is 8 kJ/mol higher than the free energy barrier to activate the C_2 C-H bond of cyclohexanone (123 kJ/mol). Hence, while the C-H bond activation at the C_4 position is more feasible than that at C_2 position for cyclohexenone, it is still energetically more difficult to activate cyclohexenone than cyclohexanone. The deprotonation energies of C_2 C-H bond of cyclohexanone and C_4 C-H bond of cyclohexenone, however, were calculated to be equivalent at 657 kJ/mol and, as such, are unable to explain the trends seen in the free energy barriers. In order to understand the features that lead to the higher free energy barrier to activate C_4 position of cyclohexenone, we carried out a detailed distortion-interaction analysis[209,236,237] which allows us to separate out the distortion effects to the transition state (TS) from the interaction effects of the reacting species**.**

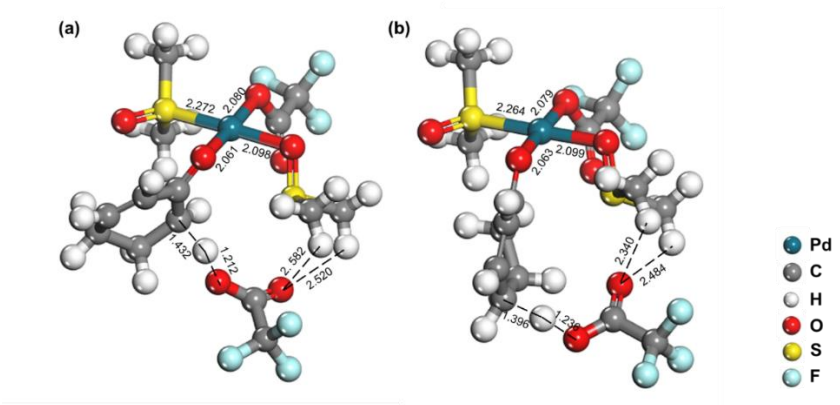

Figure 3.7: Ball-and-stick model of the optimized transition state structure for the intermolecular deprotonation of cyclohexenone via a) attack at C_2 C-H bond (**TS3_C2**) and b) attack at C_4 C-H bond (**TS3_C4**). The bond length metrics are given in Å.

3.4.5.3. Distortion-Interaction analysis: To determine the distortion effects of the TS, we evaluated single point energies of the TS structure by freezing the TS without the interacting TFA^-. The resultant calculations analyzing the distortion effects on the TS for the activation of the C_2 C-H bond of cyclohexanone activation and the activation of the C_4 C-H bond of cyclohexenone are summarized in Figure 3.8. It is to be noted that since the intrinsic activation barrier calculations are carried out with reference to the separated reactant (TFA^- and Pd-complex) states, the calculated intrinsic barrier herein is negative due to the interaction effects between the reactant species in TS which are absent in the reference state. From this analysis, we see that the distortion energy for both the transition states involving cyclohexanone C-H activation at the C_2 position and cyclohexenone C-H activation at the C_4 position are almost equivalent with the cyclohexenone C_4 TS being slightly more distorted with a distortion energy of 128 kJ/mol compared to the cyclohexanone C_2 C-H activation TS which has a slightly lower distortion energy of 126 kJ/mol. The main contributing factor to the differences in the apparent free energy barriers is the interaction energies. The interaction energy for TFA^- interacting with cyclohexanone at the C_2 carbon was found out to be -146 kJ/mol and that for TFA^- interacting with cyclohexenone via its C_4 carbon was determined to be -129 kJ/mol. This difference in the interaction energy can be attributed to the difference in the LUMO energy levels of the species being activated with the cyclohexanone C_2 moiety having lower LUMO level (-439 kJ/mol) compared to cyclohexenone C_4 moiety (-427 kJ/mol), which thus favors a facile electron transfer from the HOMO of the

attacking TFA^-. A distortion-interaction analysis was also carried out to examine the transition state of C-H activation of cyclohexenone at C_2 position and the major contributing factor for the higher overall apparent free energy barrier in this case was the distortion energy (126 kJ/mol for cyclohexanone vs 156 kJ/mol for cyclohexenone C_2) caused due to the stronger C-H bond as mentioned before. The interaction energies in this case were almost similar (-146 kJ/mol for cyclohexanone and -147 kJ/mol for cyclohexenone C_2).

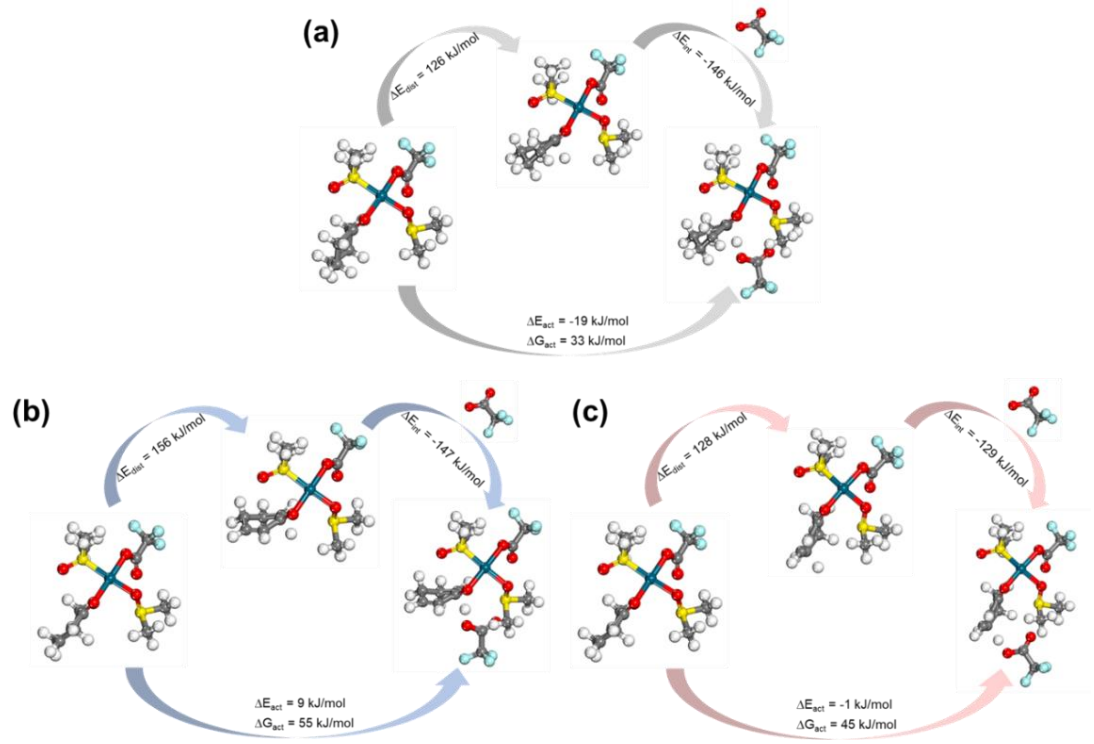

Figure 3.8: Distortion-interaction analysis for the three transition states of the intermolecular deprotonation reaction of (a) cyclohexanone and cyclohexenone via attack at the (b) C_2 and (c) C_4 C-H bond

Thus, through the analysis of the mechanistic pathways and the distortion-interaction analysis, we see that while the stronger C-H bond disfavors C-H activation at the C_2 position of the cyclohexenone, the weaker interactions with the TFA^- that result from the higher LUMO levels disfavors C-H activation at the C_4 position. These factors contribute to the higher selectivity to form cyclohexenone over the homogeneous catalyst. Thus, from these results, we can see as to why maintaining the homogeneity of the catalyst and isolating the single metal center is important in driving higher selectivities to the primary dehydrogenation product i.e. cyclohexenone. Thus, the role

of DMSO in preventing nucleation of the homogeneous catalyst is important in obtaining higher selectivities towards cyclohexenone. The presence of additional metal sites would likely facilitate the binding of the dehydrogenated products and stabilize the product as well as the transition states favoring further dehydrogenation as observed experimentally. Studies along these lines are currently being conducted in our group.

3.4.6. Catalyst screening

The mechanistic results presented herein were subsequently used to aid in screening different ligands that may enhance the activity and selectivity. Since DMSO was found to be crucial for catalyst stabilization, we did not screen the coordinated L-type ligands. We instead examined the covalent X-type ligands. The electronic structure of the metal center can be tuned by modifying the ligand environment to help promote catalytic activity. For example, for Pd-catalyzed oxidative biaryl coupling, use of $Cu(OTf)_2$ as co-catalyst along with $Pd(OAc)_2$ showed 45-fold higher rates.[238] NMR analysis coupled with DFT studies suggest that the increased rates are the result of the replacement of OAc ligand with OTf ligand. Thus, along similar lines, we conducted a screening study to examine the influence of different X-type ligands (listed in Table 3.1) on the catalytic activity for cyclohexanone dehydrogenation.

Table 3.1: DFT computed ligand dissociation energies and protonation energies of different screened basic X-type ligands

Ligands	Dissociation energy (kJ/mol)	Protonation energies (kJ/mol)
TFA	94	-1218
OAc	131	-1303
Cl	76	-1176
Br	96	-1193
OTf	41	-1135

The mechanistic analyses discussed above showed that the intermolecular deprotonation of cyclohexanone was the rate controlling step and that the apparent free energy barrier for the dehydrogenation consisted of the reaction free energy for the initial substitution reaction along with the intrinsic free energy barrier for the abstraction of the proton by the dissociated ligand. As such, two factors that control the

activity of the ligand are its: i) Dissociation energy from the Pd complex and ii) Protonation energy by the cyclohexanone substrate. These two factors, however, tend to oppose one another since the ligands which readily dissociate will bind the proton more weakly. Hence, we expect that the ideal ligand would be one that would equally favor the dissociation as well as the proton abstraction step. We thus examined the energies for ligand dissociation (leading to substitution with cyclohexanone) as well as the protonation energies for different basic X-type ligands shown in Table 3.1. The ligand dissociation energies were found to correlate with the protonation energies of the ligands (see SI for further details). However, the relative change in the dissociation energies versus that for protonation energies was lower, suggesting the protonation energies to be the dominant factor dictating catalytic reactivity. From this analysis, we would expect that the ligand with the highest absolute value of the protonation energies or the most basic ligand to be a more active catalyst. From Table 3.1, we see that OAc ligand has the most favorable protonation energies and hence is expected to be the more active ligand. The other ligands examined all have protonation energies that are less than that of TFA, thus making them ineffective to lead to further improvements in the activity. We thus examined the overall apparent free energy barriers for our reaction with the $Pd(OAc)_2(DMSO)_2$ catalyst for the alpha C-H activation of cyclohexanone and determined an apparent free energy barrier of 85 kJ/mol (see Figure S3.6) which is 38 kJ/mol lower than that for $Pd(TFA)_2(DMSO)_2$. Previous experiments carried out using $Pd(OAc)_2(DMSO)_2$ catalyst however showed a lower rate of reaction compared to that over $Pd(TFA)_2(DMSO)_2$.[52] This can be attributed to the different resting states in both cases. NMR analysis of the resting state of OAc ligated Pd center show formation of acetate bridged linear trimer Pd complexes as shown in Figure S3.7.[239] Hence, the extra energetic penalty needed to separate the trimeric Pd complex into monomeric ligand likely contributes to the experimentally observed lower reaction rates. Hence, future efforts in order to maximize the reactivity should be aimed at isolating monomeric Pd complexes using more basic X-type ligands compared to TFA such as OAc mentioned here.

3.5. Conclusion

In summary, the cyclohexanone dehydrogenation pathway over the homogeneous Pd catalyst was found to proceed via the following pathway: Substitution of TFA ligand with cyclohexanone, Intermolecular deprotonation of the bound cyclohexanone by the

displaced free TFA anion, dissociation of DMSO leading to isomerization of Pd-O enolate to its η^2-enolate form binding via carbon and oxygen to the metal center, subsequent reductive β-hydride elimination to form bound cyclohexenone which then undergoes dissociation to generate cyclohexenone. The initial alpha C-H activation was found to be the rate determining step for this reaction which proceeds with an apparent free energy barrier of 123 kJ/mol, in good agreement with the previously determined experimental kinetics. Comparison of the cyclohexanone and both modes of cyclohexenone pathway (via C_2 as well as C_4) show higher free energy barriers for cyclohexenone dehydrogenation compared to cyclohexanone dehydrogenation. The roots of lower cyclohexenone dehydrogenation rates and hence higher selectivity towards cyclohexenone were traced to two reasons: i) the higher energy of deprotonation of alpha (C_2) C-H bond of cyclohexenone versus that of cyclohexanone and ii) the weaker interaction of the attacking TFA^- moiety when attacking the C-H bond at the cyclohexenone C_4 position, which prevents the further dehydrogenation of cyclohexenone over the homogeneous Pd catalyst. Further, screening studies of different X-type ligands suggest protonation energies to be a dominating factor dictating the overall apparent free energy barrier and thus activity of the reaction, with use of more basic ligands such as OAc predicted to promote catalytic activity. The results of this study can be extended to selectively carry out similar dehydrogenation or oxidation chemistries of other cyclic ketones such as cyclopentanone.

3.6. Acknowledgements

The authors thank the Minnesota Supercomputing Institute (MSI) at the U. of Minnesota and the Pacific Northwest National Laboratory (PNNL) for use of computing resources.

3.7. Supplementary Information

3.7.1. Determination of catalyst resting state

In order to determine the resting state for our catalytic system, we initially examined the energetics of the different catalyst configurations in presence of the solvent and the substrate. The thermodynamics for ligand substitution and dissociation reactions of the starting catalyst $Pd(DMSO)_2(TFA)_2$ with the substrate and the solvent are presented below in Scheme S3.1 and S3.2. The results of these calculations indicate that the $Pd(DMSO)_2(TFA)_2$ (Figure S3.1) is the most stable catalyst configuration with the

ligands bound to the metal center where the TFA ligands and the DMSO ligands lie in a *trans*-configuration. The results also indicate that the binding configuration of the two bound DMSO's are different from each other where one of the DMSO's binds via its sulfur (S) atom to the metal center and the other binds via its oxygen atom (O). While binding via sulfur is electronically favored, steric effects of the neighboring methyl groups prohibit the binding of both the DMSO's via their sulfur atoms, thus leading to the S+O bound state as the most stable configuration. These results are further validated via experimental NMR studies done by Diao et al. which suggest similar catalyst configuration namely Pd(S-DMSO)(O-DMSO)$(TFA)_2$ to be present in the reaction mixture containing ethyl acetate as the solvent.[239] Thus based on the above discussion, the Pd(S-DMSO)(O-DMSO)$(TFA)_2$ catalyst was chosen as the starting structure for subsequent mechanistic studies.

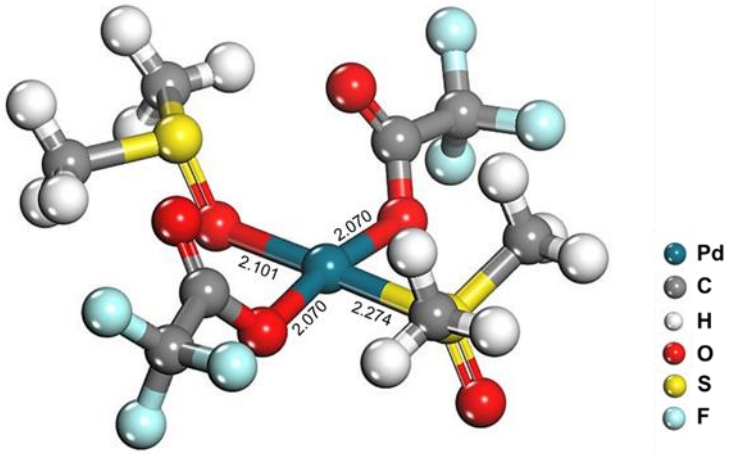

Figure S3.1: Ball-and-stick model of the optimized structure of the resting state of the catalyst, *trans*-$Pd(DMSO)_2(TFA)_2$ (**1**). The bond-length metrics are given in Å.

Scheme S3.1: Thermodynamics for the different configurations of the starting catalyst $Pd(TFA)_2(DMSO)_2$. The reaction energies and free energies shown are given in kJ/mol.

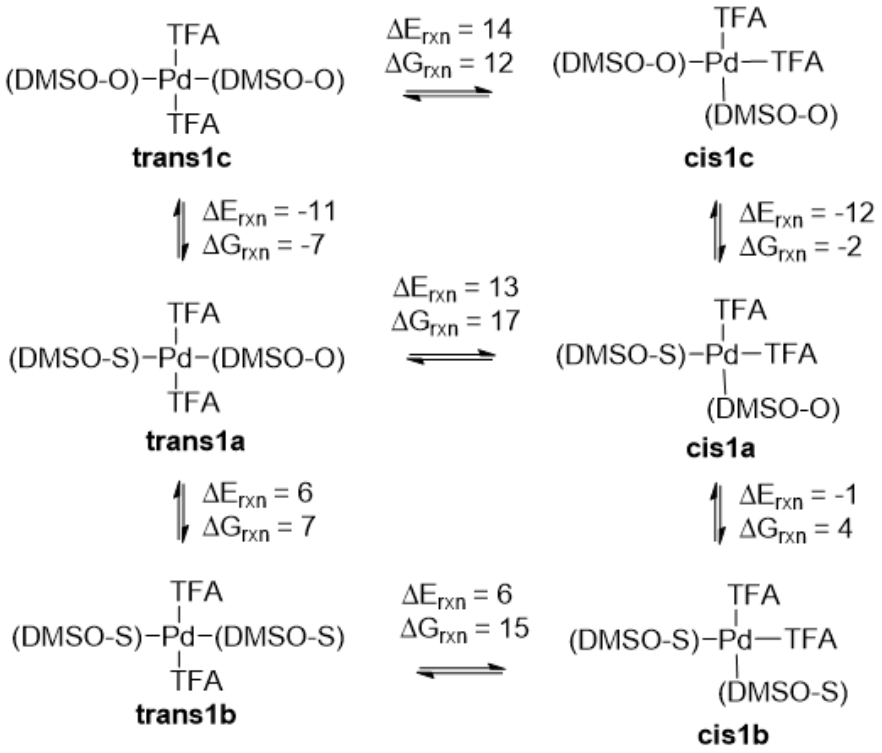

Scheme S3.2: Thermodynamics for the ligand substitution reactions of the catalyst $Pd(DMSO)_2(TFA)_2$ with the reaction mixture components. The reaction energies and free energies shown are given in kJ/mol.

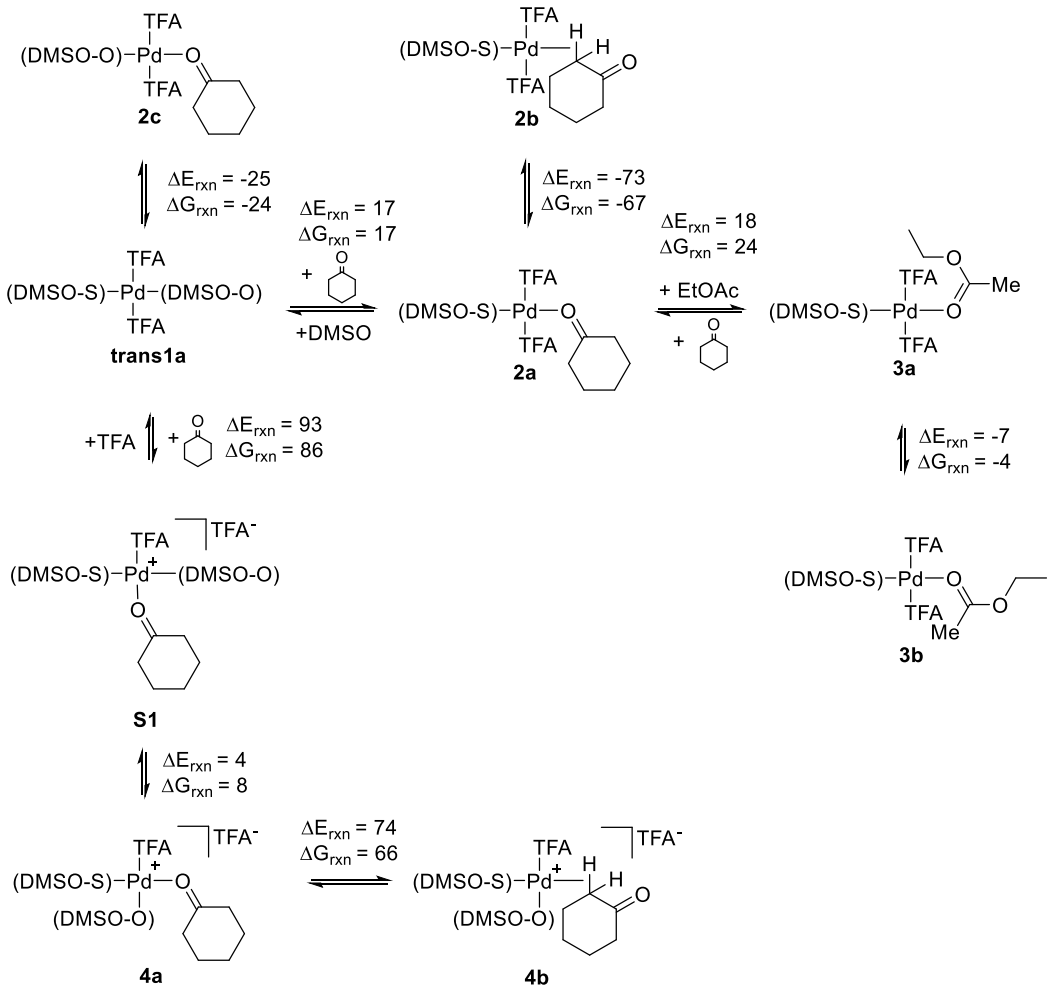

3.7.2. Five co-ordinate transition state optimization attempts

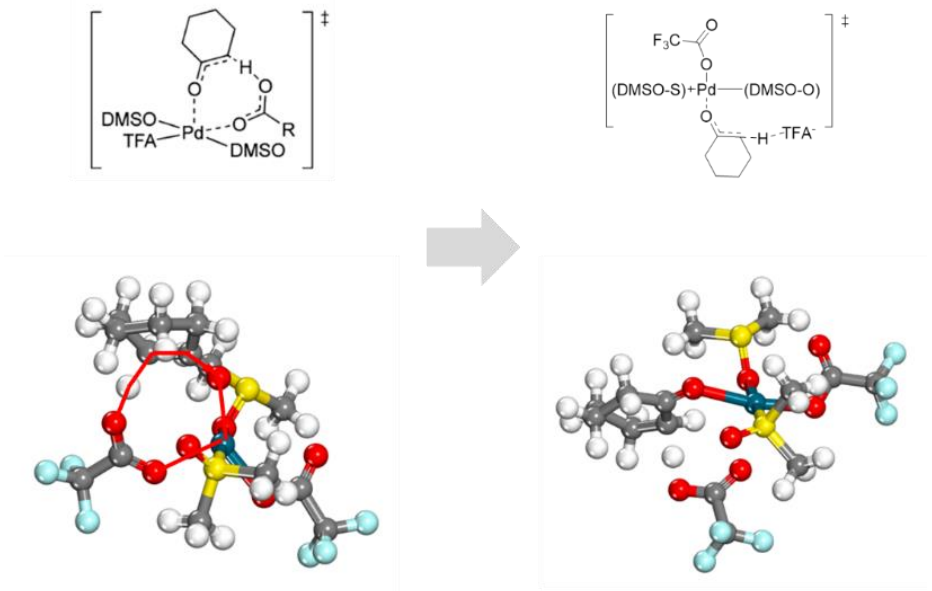

Figure S3.2: Guess structure for the five co-ordinate transition state isolation (left) and optimized structure of the transition state search (right) showing optimization to a four co-ordinate transition state with the TFA ligand dissociated

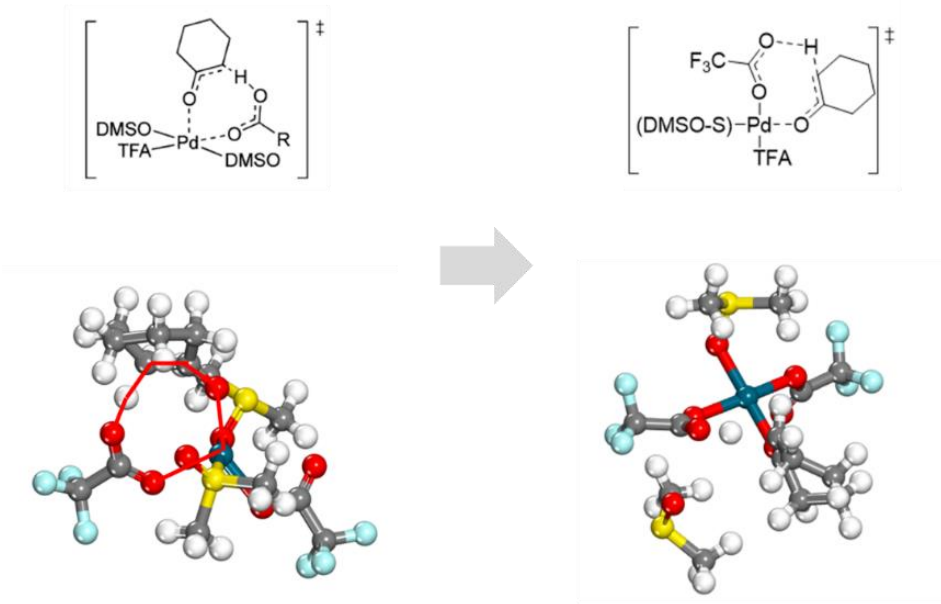

Figure S3.3: Guess structure for the five co-ordinate transition state isolation (left) and resultant structure of the transition state search after 99 optimization cycles (right) showing the optimization progressing towards a four co-ordinate transition state with the DMSO ligand dissociated

3.7.3. Rate order derivation

The computationally determined mechanism as well as the experimental kinetics suggest the alpha C-H activation to be the rate determining step (RDS). Thus, looking at the mechanism schematic in Scheme 3.8, we can write the rate expression as follows:

$$r = k_2[\boldsymbol{INT1\_C}][TFA^-] \tag{3.2}$$

where k_2 is the rate constant for the alpha C-H activation step

INT1_C is formed by ligand substitution of TFA^- in **1** with cyclohexanone and assumed to be equilibrated. Hence the expression of [**INT1_C**] can be written as:

$$[\boldsymbol{INT1\_C}] = \frac{K_1[\mathbf{1}][cyclohexanone]}{[TFA^-]} \tag{3.3}$$

where K_1 is the equilibrium constant for the ligand substitution step

Thus, we get the rate expression from equations (1) and (2) as,

$$r = k_2 \frac{K_1[\mathbf{1}][cyclohexanone]}{[TFA^-]}[TFA^-] \tag{3.4}$$

$$\text{Thus, } r = k_2 K_1[\mathbf{1}][cyclohexanone] \tag{3.5}$$

indicating a first order dependence with respect to the catalyst (**1**) and cyclohexanone in agreement with the experimental kinetic studies.

3.7.4. Cyclohexenone binding on Pd^{II} catalyst

Cyclohexenone as discussed in the main text can bind either via an alkene adduct (Figure S3.3a) or via its carbonyl oxygen atom similar to cyclohexanone (Figure S3.3b). Comparison of the reaction energies for substitution of TFA ligand with cyclohexanone bound via either of the two modes discussed above suggest the oxygen bound cyclohexenone to be more stable. Hence, cyclohexenone, like cyclohexanone also binds via its carbonyl oxygen rather than through the alkene adduct.

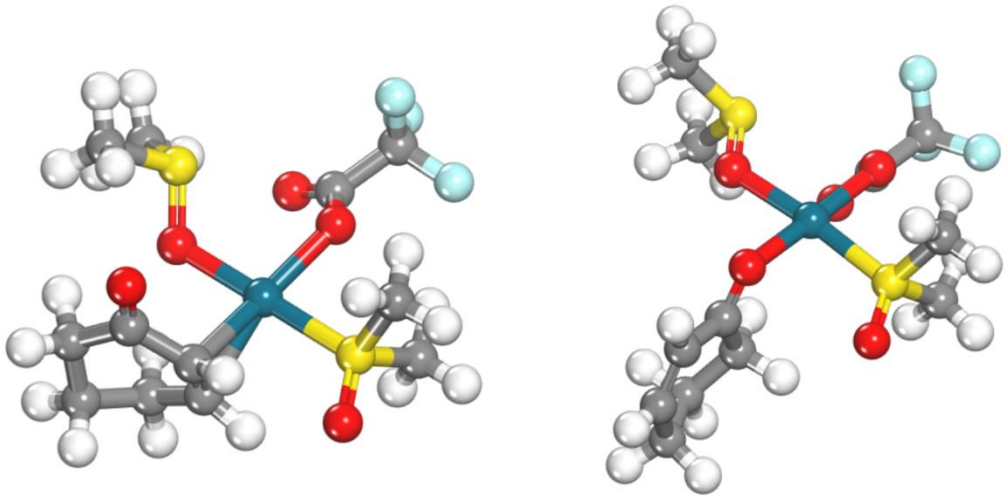

ΔE_{rxn} = 116 kJ/mol **ΔE_{rxn} = 86 kJ/mol**

Figure S3.4: DFT optimized structure of cyclohexenone binding via the alkene adduct (left), and carbonyl oxygen atom (right) to the Pd center after displacement of the TFA ligand

3.7.5. Ligand dissociation energy dependence on protonation energy

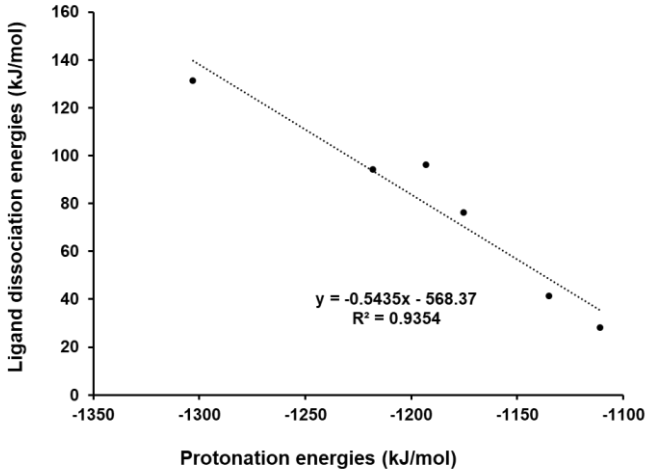

Figure S3.5: Correlation between the ligand dissociation energies and the protonation energies for different screened ligands. The graph suggests a linear fit between the dissociation energies and the protonation energies. The slope of -0.5435 however suggests that the ligand dissociation energies do not scale equally as protonation energies for different ligands suggesting the protonation energies of the ligands to be the dominant factor controlling the reactivity of the catalyst

3.7.6. Transition state calculations for alpha C-H activation of cyclohexanone over $Pd(OAc)_2(DMSO)_2$ catalyst

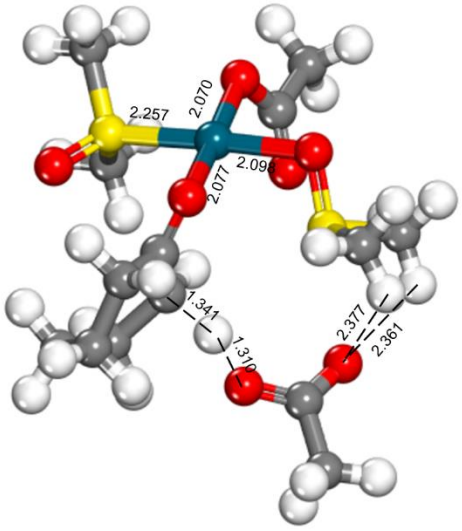

Figure S3.6: Ball-and-stick model of the optimized transition state structure for the intermolecular deprotonation of cyclohexanone over $Pd(OAc)_2(DMSO)_2$ catalyst. The bond length metrics are given in Å.

3.7.7. Acetate bridged linear trimer Pd complex structure

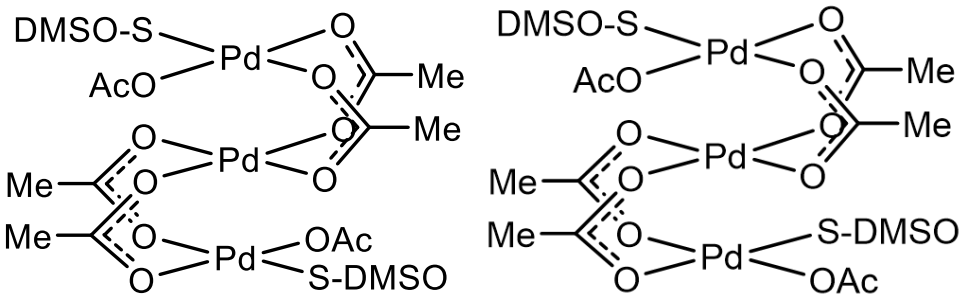

Figure S3.7: Structures of the acetate-bridged trimer Pd complex reported to be observed for $Pd(OAc)_2$ complexes with DMSO ligands present in EtOAc solution[239]

Chapter 4 - Theoretical insights into the factors governing selectivity in electro-oxidation of alcohols (glycerol) over Pt catalyst

Adapted from Udyavara, S. and Neurock M., Theoretical insights into the factors governing selectivity in electro-oxidation of alcohols (glycerol) over Pt catalyst, *under preparation*

Theoretical calculations were done by SU under the supervision of MN

4.1. Synopsis

Glycerol, a by-product of biodiesel production is highly versatile in that it carries multiple functionalities and can be used in the production of various chemical intermediates including glyceric acid, dihydroxyacetone, acrolein, among others. Herein, we examine some of the factors that control the selectivity in the electro-oxidation of glycerol over Pt (111) in acidic and alkaline media through detailed density functional theory (DFT) studies using 1- and 2-propanol as a model substrate. We show that the presence and coverage of surface intermediates such as CO and OH on the Pt (111) surface in acidic and alkaline media, respectively hinder the activation of the secondary C-H bond over the primary C-H bond, thus favoring the formation of glyceraldehyde (GALD) over dihydroxyacetone (DHA) in glycerol electro-oxidation reaction (GEOR). The inherent presence of OH^- ions in the solution phase in alkaline media prevents the removal of the OH groups from the surface. Reactions, however that occur in acidic media, can take advantage of overlaying Pt atoms onto a Bi or Cu surface to limit the coverages of CO that form on the surface, thus providing the unhindered activation of the weaker secondary C-H bond to selectively form DHA.

4.2. Introduction

The electro-oxidation of small alcohol molecules has generated significant interest due to their potential use in direct alcohol fuel cells (DAFC) and also for the selective production of chemical intermediates.[4,41,240–245] In particular, glycerol, which is a by-product formed during the production of biodiesel has gained interest due to its surplus availability given the steady increase in biodiesel production during the past few years.[41,242,243,246–250] The excess glycerol produced has been considered as a feed for fuel cell applications since it is non-toxic, inflammable, and has low volatility.[251] In

addition to its application in fuel cells, glycerol is also of considerable interest in production of chemicals as it's different functionalities allow it to be converted by reforming, hydrogenolysis, and oxidation into various industrially-relevant chemical intermediates including acrolein, syngas, propane-diols, glyceric acid, and others.[242,243,247,248,250,252] In particular, glycerol oxidation can result in a variety of products ranging from primary oxidation products such as glyceraldehyde and dihydroxyacetone to secondary and tertiary oxidation products such as glyceric acid, formic acid, and others as shown in Figure 4.1.[242,246,249] Among the various oxidation products that can be obtained, dihydroxyacetone (DHA) poses significant economic value compared to other products due to its applications in cosmetic industry as a tanning agent and as a building block for organic synthesis of other fine chemicals.[41,247,253,254]

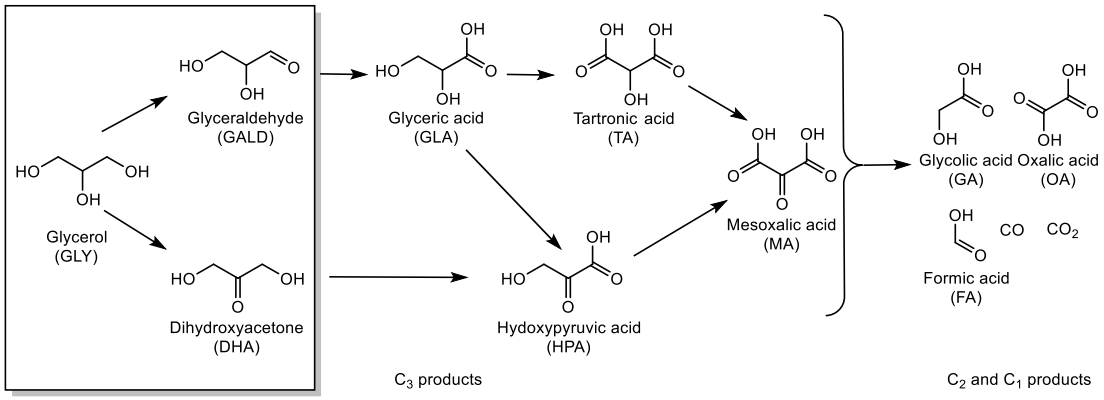

Figure 4.1: Schematic of the reaction pathways and products for the glycerol oxidation reaction. The reaction of interest in this study is boxed.

Previous experimental studies on glycerol electro-oxidation (GEOR) show that the resultant product distribution and the activity of the reaction depend upon the pH, catalyst, as well as operating potentials.[53,251,255–258] While metals such as Au,[53,259,260] Pd,[261–263] and Ni[264,265] catalysts have been shown to be active for GEOR in alkaline media, Pt is the most widely studied catalyst owing to its high activity and excellent stability in both acidic as well as alkaline media.[53,266–268] Glycerol electro-oxidation over Pt in acidic media (pH < 7) at potentials less than 0.6 V produces glyceraldehyde (GALD) as the major product with reaction selectivities of 80-100 %. Glyceraldehyde is formed by the oxidation of the primary alcohol group.[53] At potentials > 0.6 V, the reactive glyceraldehyde intermediate oxidizes further to form glyceric acid. In alkaline

media (pH > 7), a twenty-fold increase in the current density for the glycerol electro-oxidation reaction is observed with glyceric acid (GLA) being formed as the major product of the reaction (Selectivity = 40-100 % at 0.6-1.1 V) with GALD (Selectivity = 10 % at 0.8 V) also formed as a reactive intermediate. The formation of dihydroxyacetone (DHA), which is the product for the oxidation of the secondary alcohol group is negligible in both acidic as well as alkaline media, with maximum selectivities of ~10 %. While monometallic Pt catalysts are unselective towards DHA formation, GEOR in acidic media over Bi,[269–273] and Sb[267,273,274] modified Pt catalysts or over bimetallic catalysts such as PtRu[266] demonstrated significant increases in the selectivity to DHA with up to 90%. Similar studies carried out over Bi-modified Pt in alkaline media, however, failed to show any improvements in DHA selectivity, with GLA still being the dominant product.[275,276]

While there have been significant advances in the experimental optimization of the catalyst and reaction conditions to improve selective GEOR with higher current densities, there have been very few computational studies aimed at understanding the peculiar differences in the selectivities that are observed across different metal systems, pH, and potentials. Herein we carry out first-principles density functional theory (DFT) calculations to examine and help determine the factors that govern the selectivity of electro-oxidation of glycerol towards glyceraldehyde versus dihydroxyacetone in both acidic as well as alkaline media to help potentially guide future efforts aimed at the design of new and improved catalysts for selective GEOR.

Modeling the pathways and the kinetics of glycerol oxidation, is rather challenging which likely explains the limited number of computational studies that have been done on this system.[277–280] Glycerol, a three functional group polyol can adopt up to 100 different conformations on the surface or in the solution phase.[281] As such, it is very challenging to model the pathways for electro-oxidation of glycerol in solution media since the various conformations of the glycerol molecule and its subsequent intermediates need to be examined and optimized to find a reasonable minimum structure. To help overcome some of these challenges and provide guidance, we examined propanol (1-propanol and 2-propanol) as a model system to elucidate the effects of electronics and sterics of the different carbon centers present in glycerol on its oxidation kinetics. Table 4.1**Table 3.1** lists the known C-H and O-H bond energies of 1-propanol and 2-propanol[282] and compares them with DFT calculated bond energies

of primary and secondary C-H and O-H bond of glycerol. From the table, we see that the relative strengths in the C-H and O-H bond energies of 1-propanol and 2-propanol match well with that of the primary and secondary C-H and O-H bond energies of glycerol molecule respectively. In addition to the electronics, the use of 1-propanol and 2-propanol as model systems also allow us to the mimic the steric features present around the primary and secondary carbon centers of the glycerol molecule respectively.

Table 4.1: Comparison of bond strengths of glycerol with the model propanol molecule

Bond	DFT calculated bond strength for glycerol (kJ/mol)	Bond strength for propanol[46] (kJ/mol)
Primary C-H bond	390	392
Secondary C-H bond	386	384
Primary O-H bond	408	433
Secondary O-H bond	422	442

Herein we examine the mechanism and kinetics of oxidation of propanol molecule in acidic and alkaline media respectively (sections 3.1 and 3.2) and use the results to draw analogies back to the GEOR (section 3.3). We subsequently use the insights gained from the mechanistic studies to propose various strategies that can be employed for selective electro-oxidation of glycerol to form DHA (section 3.4).

4.3. Computational methods

All of the calculations reported herein were carried out using plane wave based density functional theory codes implemented in Vienna Ab-Initio Simulation Program (VASP).[163–166] The GGA corrected PBE exchange correlation functional[167] was used along with PAW pseudopotentials[168,169] which describe the core electron potentials to calculate the exchange and correlation energies. Van-der-Waals interactions were modeled using the DFT-D3 approach.[283] A 400 eV energy cutoff was used for the construction of plane waves. A k-point grid of 3 x 3 x 1 was used to perform numerical integrations. In order to model the Pt (111) surface, the bulk crystal structure of Pt with a lattice constant of 3.92 Å was cleaved along the 111 plane. The resultant slab used consisted of three layers of Pt with a 15 Å of vacuum space above the surface, with the

bottom layer frozen at the bulk Pt distances. The electronic energies were converged with an SCF convergence criteria of 10^{-6} eV. The geometric structures were optimized using force tolerance criterion of 0.05 eV/Å. Transition states were isolated by using the Nudge Elastic Band (NEB) approach which follows the reaction path from the optimized reactant to the product states,[172,173] to provide a reliable initial transition state structure. This structure was subsequently used as an input to carry out dimer calculations[174] to isolate the saddle point of the reaction. Frequency calculations were subsequently carried out to determine the entropies as well as the corrections to the electronic energies to establish the enthalpies and free energies of the elementary adsorption, surface reaction and desorption steps. For reactions involving adsorption or dissociative adsorption, the entropic corrections to the electronic energies was determined according to the formulae established by Campbell.[175]

In order to model electrochemical systems, wherein the reactions occur at constant potentials rather than at constant charge, the energies for different intermediate and transition states along the reaction pathway need to be compared at constant potentials. This allows us to obtain changes in the free energy for the different reaction steps as a function of potential. In order to perform the potential dependent calculations, the double reference method developed by Filhol and Neurock was used.[284,285] These calculations require modeling of explicit solvent molecules for which initially the vacuum space above the model Pt surface was completely filled with explicit water molecules to match its density. *Ab-initio* MD simulations were carried out to establish reliable low energy configurations of the water solvent. The *ab-initio* MD simulations were run in an NVT ensemble for 3 picoseconds with a time step of 1 femtosecond and a temperature of 300 K. The solvent configuration obtained from the output of the MD simulation was then used as the starting point for our subsequent calculations. The propanol molecule was firstly added into the simulation box by substituting in for three water molecules. The system with the propanol and water molecules was then charged by subtracting electron density from the metal (+q), which is balanced by a homogeneously distributed counter charge of the same magnitude (-q) to maintain neutrality within the periodic cell. The optimization and transition state calculations were then run at these differently charged systems, with the potentials corresponding to each of the intermediate and transition state structures determined by comparing to two reference potentials. The first reference relates the potential at the metal/solution

interface for the uncharged system to that of vacuum phase potential. This is done by inserting a 10 Å vacuum slab separating the solvent layers. The second reference relates the potential in the middle of the solvent layer for charged metal/solution interfaces to that of the uncharged system, which is then indirectly referred to the vacuum referenced metal surface potential at zero charge. This overall allows for calculation of the potentials at different charged states which is referred to the NHE by adding -4.28 V to the calculated absolute potential. The total energy of each state at different potentials were then determined by correcting for the excess charge and interactions with the background charge to the VASP calculated energies.

4.4. Results and Discussion

4.4.1. Acidic media

4.4.1.1. Mechanism of 1-propanol oxidation

Oxidation of small molecule alcohols such as methanol and ethanol usually typically proceed via adsorption and subsequent activation of the C-H or O-H bonds on the metal surface.[4,40,286–288] 1-propanol examined here adsorbs on the Pt (111) surface via its oxygen atom in an on-top configuration with an adsorption free energy of –30 kJ/mol. 1-propanol can be oxidized to 1-propanal via the three paths shown in Figure 4.2 which include: 1) the initial activation of the C-H bond to form the hydroxypropyl intermediate which then reacts via O-H activation to form 1-propanal, 2) the initial activation of the O-H bond to form the alkoxide intermediate followed by C-H bond activation to form 1-propanal, or 3) the initial activation of the C-H bond to form the hydroxypropyl intermediate followed by a second C-H activation to form 1-propenol which subsequently can undergo tautomerization in solution phase upon desorption to form the thermodynamically more favored product 1-propanal.

The DFT-calculated reaction energies and activation barriers for the steps of all three paths were carried out in the gas phase on the clean Pt (111) surface (see Supplementary Information for the optimized reactant state, transition state and product state structures). The results, presented in Figure 4.3, show that the free energy barrier for the initial C-H activation step (20 kJ/mol) is lower than that for the initial O-H activation step (58 kJ/mol), suggesting that the initial C-H activation is favored. The hydroxypropyl intermediate that forms is found to be thermodynamically more favored

over formation of the alkoxide intermediate by 95 kJ/mol. The strong preference to form the hydroxypropyl is the result of the much stronger Pt-C bond versus the Pt-O bond. Pt is not very oxophilic and as such results in a Pt-O bond energy that is -370 kJ/mol, 280 kJ/mol weaker than the Pt-C bond energy (-650 kJ/mol). Similar results have also been reported for DFT studies done to examine methanol and ethanol oxidation reactions over late-transition metals like Pt and Pd.[4,40,286,288,289]

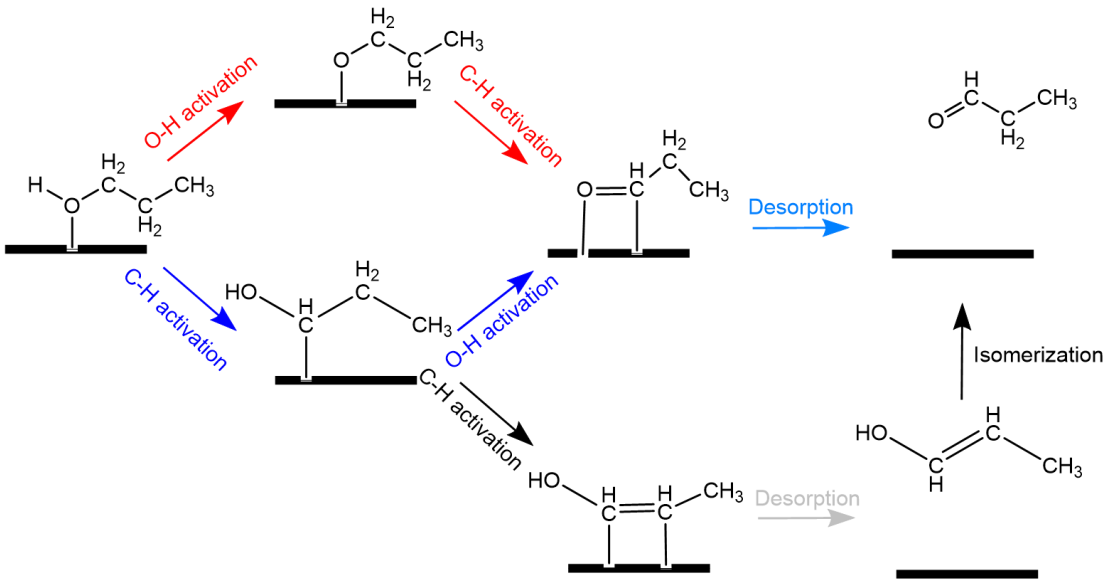

Figure 4.2: Schematic representation of the specific intermediates involved in the pathways for electro-catalytic oxidation of 1-propanol to 1-propanal

The hydroxypropyl intermediate that forms can undergo either a C-H or O-H activation. Both C-H and O-H activation proceed with similar barriers of 56 kJ/mol. The resulting 1-propenol intermediate that forms from C-H activation, however, is more strongly bound to the surface (ΔG_{rxn} = -40 kJ/mol) as compared to the 1-propanal intermediate (ΔG_{rxn} = 34 kJ/mol) that forms via O-H activation. This would suggest that the mechanism likely proceeds via formation of the enol intermediate on the surface and subsequent isomerization to 1-propanal in the solution phase. A similar mechanism was proposed by Koper et al. to account for the DHA and GALD formation during GEOR over Pt (111) surface.[278] However, subsequent calculations that were carried out to compare the free energies of desorption with that of further C-H activation shown in Figure 4.3 indicate that the desorption of the enol intermediate to be 98 kJ/mol less favorable. Thus, while the formation of 1-propenol intermediate is thermodynamically more favored, the strong binding of the 1-propenol intermediate limits its subsequent

desorption. The 1-propenol intermediate formed instead likely undergoes subsequent successive dehydrogenation steps and C-C cleavage steps to form CO on the surface. Such a mechanism for CO formation has been proposed previously for the dehydrogenation of ethanol and glycerol over Pt and Pd surfaces.[277,288] In addition, in-situ FTIR studies carried out during glycerol electro-oxidation have shown that CO forms on Pt at potentials as low as 0.1 V and can result in coverages as high as 0.63 ML depending on the operating potentials.[251] Similar results have also been reported for the electro-oxidation of other alcohols including ethanol and ethylene glycol.[245,290] Hence, while mechanism 3 which involves two sequential C-H activation steps is thermodynamically favored, it likely leads to the formation of CO rather than the formation of 1-propanal.

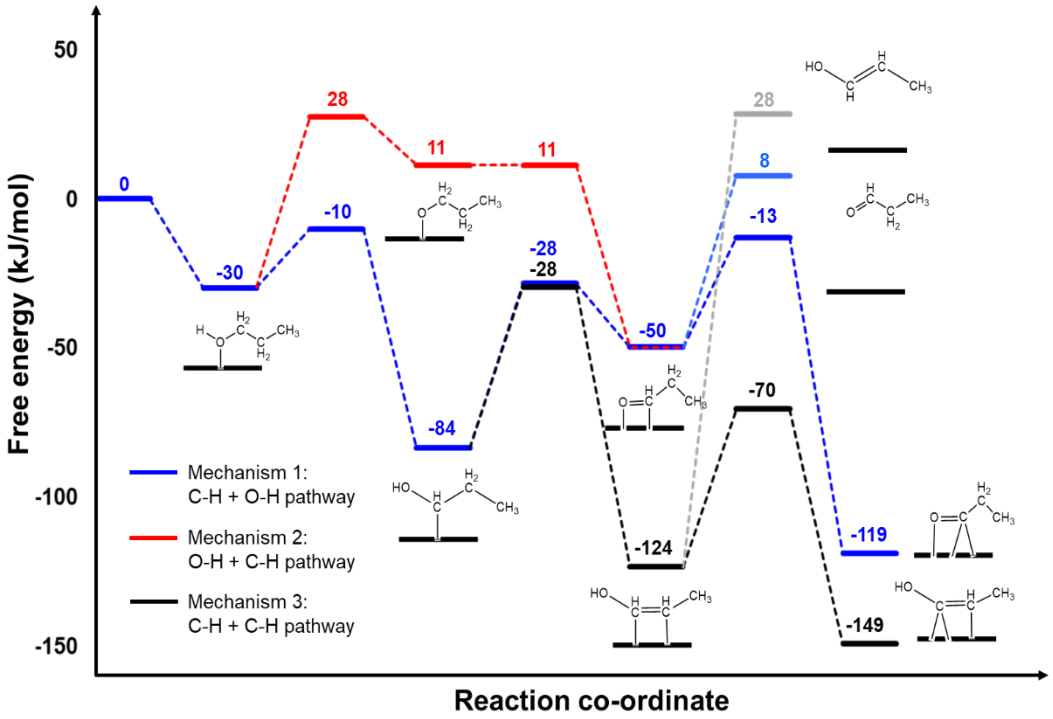

Figure 4.3: Free energy profile of the different considered mechanistic pathways for the primary oxidation of 1-propanol to 1-propanal over clean Pt (111) surface. The desorption of 1-propanal and 1-propenol are denoted by light blue and grey lines respectively.

Comparing the desorption free energies with the free energy barrier for further dehydrogenation of 1-propanal, we see that while the dehydrogenation barrier (37 kJ/mol) is still lower than the desorption energies (58 kJ/mol), the difference is

significantly less (21 kJ/mol). As such, the 1-propanal intermediate is more likely to desorb than the 1-propenol intermediate. While the energetics still indicate that C-H activation is more prevalent than desorption, one should note that under reaction conditions, the surfaces are likely covered by other reactive intermediates that weaken the binding energies of the adsorbed intermediates due to lateral repulsive interactions.[20,291,292] Thus, the binding energy of the 1-propanal intermediate to the Pt (111) surface at the more representative higher coverage conditions would be lower, which is demonstrated herein via calculations done over a 2/9 ML CO covered Pt (111) surface. The desorption free energy for the n-propanal intermediate was found to be 37 kJ/mol, 23 kJ/mol lower than the free energy barrier for its dehydrogenation (60 kJ/mol), thus favoring the desorption of the n-propanal intermediate over its further dehydrogenation.

The results reported here suggest that 1-propanal likely proceeds via mechanism 1 which involves initial activation of the C-H bond to form the hydroxyalkyl intermediate followed by the subsequent activation of the O-H bond. On further examination of this pathway in Figure 4.3, it can be seen that the overall free energy barrier for the initial C-H activation step is highest (with the adsorbed alcohol as the reference state) and hence is likely the rate determining step for 1-propanol oxidation to 1-propanal in acidic media. These results can be further corroborated with the Tafel analysis done for electro-oxidation of methanol occurring in acidic media, which similarly suggest the initial C-H activation to be the rate determining step.[293]

4.4.1.2. Comparison of 1-propanol and 2-propanol oxidation kinetics

As discussed, 1-propanol oxidation to 1-propanal in acidic media proceeds via an initial C-H activation step followed by O-H activation. The presence of a more facile path involving subsequent C-H activation steps likely results in the formation of CO which can cover the surface and block sites. In an effort to examine the influence of CO coverages that form under the reaction conditions on the kinetics, we carried out calculations with 0.55 ML of CO on the Pt (111) surface as shown in Figure S4.27.

While the mechanistic evaluations in section 3.1.1 were carried out using 1-propanol, it can be envisioned that 2-propanol will follow a similar mechanism, albeit with different kinetics. Since the initial C-H activation step was found to be the rate determining step for oxidation of 1-propanol to 1-propanal, the free energy barrier of

this initial C-H activation step was used as a descriptor to differentiate between the reactivity of 1-propanol and 2-propanol to form the corresponding alkanal species. The difference between the reactivity of 1-propanol and 2-propanol can then be translated back to the selectivity differences seen between glyceraldehyde (GALD) and dihydroxyacetone (DHA) in GEOR which is discussed in section 3.3. The 0.55 ML CO covered surface was used to examine gas phase free energies for the C-H activation of both 1- and 2-propanol as shown in Figure 4.4. The DFT free energy barrier for the C-H activation of 2-propanol (136 kJ/mol) was calculated to be significantly higher than that of 1-propanol (91 kJ/mol). The CO coverages on flat Pt surface sterically hinder the approach of 2-propanol towards the surface to activate its secondary C-H bond as evident from the larger Pt-C distance of 3.40 Å, which result in the high activation barrier. The activation of 1-propanol at the primary C-H position has a much lower barrier as 1-propanol can approach the surface by orienting the adjacent C_2H_5 group away from the surface and thus minimizing or eliminating steric effects from the surface bound CO. This allows primary CH_2OH group to easily access the metal center, as can be seen from the lower Pt-C bond distance of 3.17 Å in Figure 4.4. This thus suggests that the steric hindrance posed by the CO groups limit the activation of the secondary C-H bond in 2-propanol.

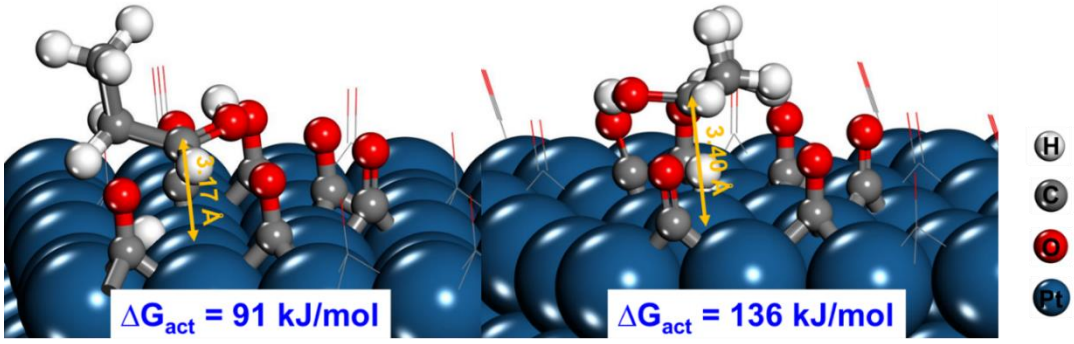

Figure 4.4: DFT optimized transition state structures for the initial C-H activation step of n-propanol (left) and sec-propanol (right) over 0.55 ML CO covered surface

The gas-phase calculations reported above provide initial insights into the differences between the kinetics of C-H activation of 1-propanol (terminal/primary C-H bond) and 2-propanol (secondary C-H bond). The extension of the gas phase kinetics discussed here to the reaction kinetics in the electrochemical system is challenging as the reactions in the electrochemical system occur in solution and proceed at a constant potential

rather than at constant charge. To model the electrochemical system, we fill the vacuum region with explicit water molecules to match the density of water, sequentially charge the system and follow the energies for the 1-propanol and 2-propanol reactant states, their transition states and their corresponding product states as a function of the applied electrochemical potential using the double reference method.[284,285] The calculated free energies for the adsorbed 1-propanol and 2-propanol are plotted against their C-H activated transition state energies as a function of potential in Figure 4.5a and Figure 4.5b, respectively.

Herein we focus our calculations only on potentials up to 0.66 V vs NHE as water dissociates at potentials greater than 0.66 V on Pt (111) to form hydroxyl groups that can oxidize the CO that forms, thus leading to changes in the surface coverage.[4,294,295] The mechanism that proceeds at potentials >0.66 V NHE in acidic media is likely very similar to the mechanism that proceeds in alkaline media (discussed in section 3.2) as both are driven by OH groups which likely cover the surface.[252,286,295] Thus, up to potentials of 0.66 V vs NHE, the trends seen in the activation barriers for 2-propanol versus 1-propanol in Figure 4.5 follow those shown in Figure 3 for the gas phase energies, suggesting 1-propanol C-H activation to be more facile compared to 2-propanol C-H activation despite the stronger bond strengths (390 kJ/mol vs 386 kJ/mol). As discussed previously, this can be attributed to the steric repulsion between the secondary –CHOH- group of 2-propanol that is activated and the adsorbed CO molecules on the surface. This can readily be seen by the much longer Pt-C bond distances for 2-propanol C-H activation (3.52 Å) versus that for 1-propanol C-H activation (2.64 Å) in solution as shown in Figure 4.5. The repulsive interactions between the CO and the full backbone of the 2-propanol molecule block access to the secondary carbon center and prevent its stabilization and bonding to the metal as noted by the long Pd-C bond distance in Figure 5b and activation barriers that are ~50 kJ/mol higher than those for the oxidation of 1-propanol. The results indicate that CO blocks C-H activation at the more sterically hindered secondary and tertiary carbon sites in acidic media below 0.66 V NHE. As discussed later in section 3.4, new catalyst formulations that can inhibit the formation of CO on the surface and maintain lower surface coverages may aid in selective activation of the weaker secondary C-H bond over the primary/terminal C-H bond which has applications in selective glycerol electro-oxidation to DHA.

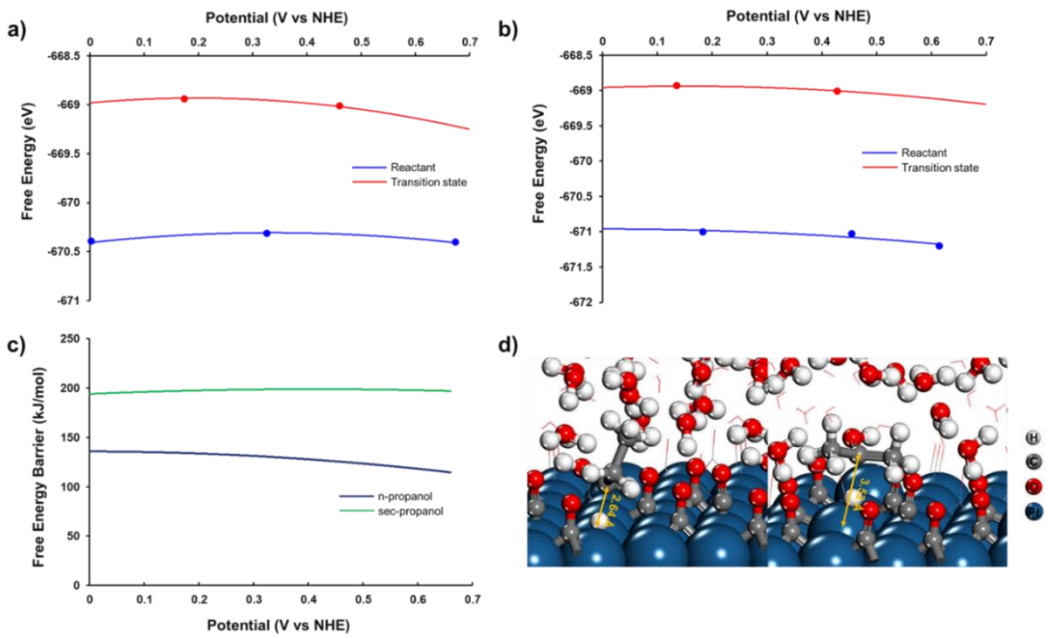

Figure 4.5: Potential dependent free energies of the reactant and transition state for the initial rate determining C-H activation step for a) n-propanol and b) sec-propanol; c) Potential dependent free energy barrier for the C-H activation of n-propanol and sec-propanol; d) DFT optimized transition state structures for the initial C-H activation step of n-propanol (left) and sec-propanol (right) over 0.55 ML CO covered surface in solvent media at zero charge

4.4.2. Alkaline media

4.4.2.1. Mechanism of 1-propanol oxidation

The use of alkaline media typically results in significantly higher activities and differences in selectivity compared to those found in acidic media. In acidic media, glycerol is selectively oxidized to glyceraldehyde with the formation of small amounts (~ 5%) of dihydroxyacetone also being formed. In alkaline media, on the other hand, glycerol oxidizes primarily to glyceric acid starting at potentials as low as 0.40 V.[53] Herein, we examine the mechanism of the glycerol electro-oxidation reaction in alkaline media and try to identify the factors that influence the product distribution.

Previous in-situ FTIR studies for GEOR in acidic media have shown that CO covers the Pt (111) surface with coverages reaching up to 0.63 ML.[251] In alkaline media, the OH^- ions in solution from the base can readily adsorb on to the Pt surface at the positive potentials at which the electrode is operated. Thus, to model the Pt surfaces found in

alkaline media, we used a Pt (111) surface with 8/9 ML coverage of hydroxyl (OH) groups (Figure S4.27). Similar models were used to examine alcohol oxidation reactions over Pt, Pd, and Au surfaces in alkaline media.[252,286]

The OH covered Pt surface model was used here to examine the oxidation of 1- and 2-propanol in alkaline media. The energetics for oxidation via the OH-covered Pt are summarized in Figure 4.6 (see Supplementary Information for relevant figures). In acidic media, the initial O-H activation step was found to be inherently more difficult and proceeded with a barrier of 58 kJ/mol. In alkaline media however, the O-H activation step is facile as the reaction preferentially proceeds via the bound OH rather than the Pt metal. The bound OH is rather basic and as such readily abstracts a proton from the vicinally bound alcohol, thus resulting in formation of water and a bound alkoxide intermediate as shown in Figure S4.8. This O-H deprotonation step was calculated to be almost barrierless compared to the 20 kJ/mol barrier computed for the C-H activation step examined in section 3.1.1. This thus suggests that in alkaline media, 1-propanol oxidation proceeds via an initial O-H activation step. This is consistent with previous DFT studies for alcohol oxidation over metal surfaces in the presence of base.[252,286]

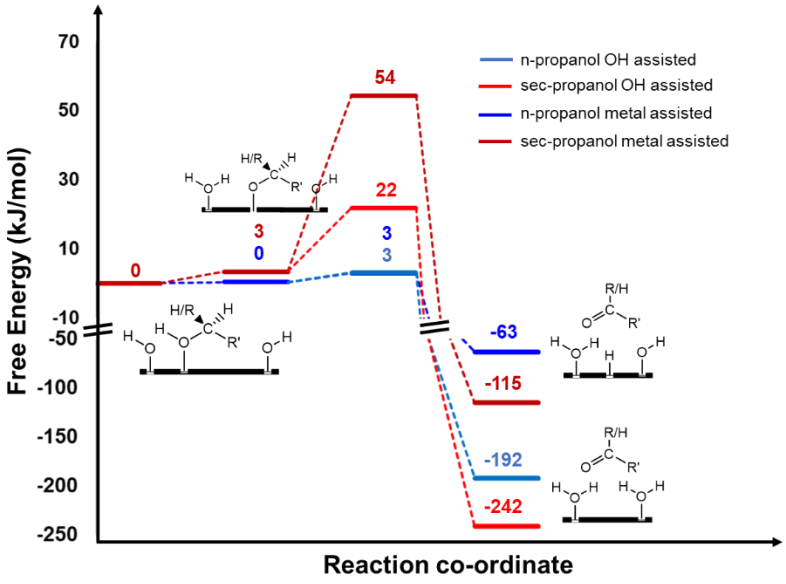

Figure 4.6: Free energy profile of the different considered mechanistic pathways for the primary oxidation of 1-propanol/2-propanol to 1-propanal/2-propanal over OH covered Pt (111) surface. R=R'=CH_3 for 2-propanol, R=H and R'=C_2H_5 for 1-propanol

The alkoxide that forms upon the initial O-H activation can subsequently undergo C-H activation to form the resulting aldehyde product. In alkaline media, this C-H activation step can be catalyzed either by the metal sites on the surface or via the bound OH group which is basic. The energetics for both the metal as well as the OH* catalyzed C-H activation steps for the bound 1-propoxide intermediate are shown in Figure 4.6 with the resultant structures shown in Figure 4.7. The metal and the OH* assisted C-H activation both proceed with similar barriers of 3 kJ/mol. This suggests that both pathways are likely to be equally prevalent in the C-H activation of the 1-propoxide intermediate. However, under the reaction conditions, the concentration of free metal sites is likely to be more limited compared to that of OH* sites on the surface. Thus, despite the similar barriers, the OH* assisted C-H activation is likely more dominant compared to the metal assisted C-H activation pathway due to the higher concentration of OH* sites. Further, we see from Figure 4.6 that since O-H activation was found to be nearly barrierless, the subsequent C-H activation step is likely the rate determining step of the reaction in alkaline media as well.

Charge analysis of the transition state involving C-H activation by the adsorbed OH groups shows an accumulation of 0.072 e^- over the intermediate and a depletion of 0.244 e^- over the adsorbed OH groups (The rest of the 0.173 e^- are accumulated over the Pt surface). This suggests that OH* acts as a base and abstracts the hydrogen as a proton resulting in the formation of carbanionic like transition state (TS) in case of OH* assisted C-H activation. For the metal-assisted C-H activation, charge analysis calculations show a depletion of 0.123 e^- over the intermediate and an accumulation of 0.449 e^- over the metal surface suggesting the C-H activation to occur via hydride-like abstraction thus resulting in the formation of carbocationic like transition state (TS).

4.4.2.2. Comparison of n-propanol and sec-propanol oxidation kinetics

Performing a similar analysis for 2-propanol (Figure 4.6), we see that the OH* catalyzed deprotonation of the secondary O-H bond is also very facile, proceeding with a low free energy of reaction and an activation free energy barrier of 3 kJ/mol to form the 2-propoxide intermediate. The subsequent activation of the C-H of the 2-propoxide via the metal is significantly more difficult with a barrier of 51 kJ/mol. This is significantly higher than the metal-catalyzed C-H activation barrier for 1-propoxide which had a barrier of only 3 kJ/mol. This is due to the steric hinderance that result

from the high coverage of the OH groups on the surface which block the activation of the C-H bond of the 2-propoxide intermediate in the same manner as the bound CO species blocked the C-H activation of 2-propanol.

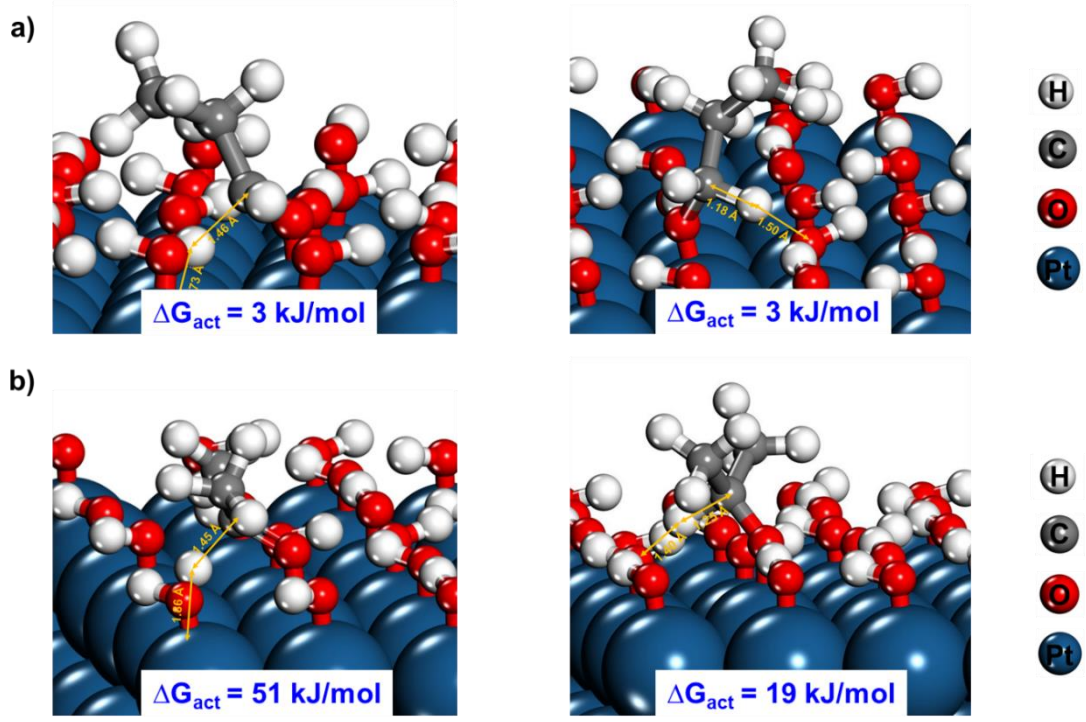

Figure 4.7: DFT optimized transition state structures for metal-assisted C-H activation (left) and OH* assisted C-H activation (right) of a) n-propoxide and b) sec-propoxide intermediates over OH covered Pt (111) surface

The C-H bond of the bound 2-propoxide, however, can be activated by the bound OH which has a lower barrier of 19 kJ/mol. The reduction in steric constraints act to favor the OH* assisted activation of the C-H bond at the secondary position. However, the free energy barrier is still significantly higher than that of the OH* assisted C-H activation of the 1-propoxide intermediate (3 kJ/mol). Charge analysis of the transition state shows results similar to that for the OH* assisted C-H activation of the 1-propoxide intermediate wherein there is a net accumulation of 0.151 e^- over the intermediate and a depletion of 0.263 e^- over the adsorbed OH groups, suggesting that the hydrogen that is activated is transferred as a proton to the adsorbed OH entity. While the homolytic dissociation of the C-H bond of 2-propanol is more favored than 1-propanol (Table 4.1), deprotonation energy (DPE) calculations indicate that it easier to deprotonate the C-H bond of 1-propanol (DPE = 920 kJ/mol) than that of 2-propanol (DPE = 925 kJ/mol). In addition, there is also less steric constraints for OH* to activate

the C-H bond of the 1-propoxide over that of the 2-propoxide. Thus, while the OH* catalyzed reaction removes most of the steric constraints associated with the metal catalyzed route, there is still a constraint of activating secondary C-H bond over the primary.

In alkaline media particularly, high selectivity towards glyceric acid formation (GLA) is observed. Glyceric acid (GLA) is thought to be formed by the oxidation of glyceraldehyde (GALD) and is thought to proceed via an OH addition to the carbonyl carbon atom followed by a successive C-H activation.[252] We therefore examined barriers for this subsequent oxidation path involving n-propanal as shown in Figure 4.8. The barrier for OH addition into the carbonyl carbon of n-propanal was calculated to be 8 kJ/mol, which suggests that the OH addition into the carbonyl carbon is quite facile.

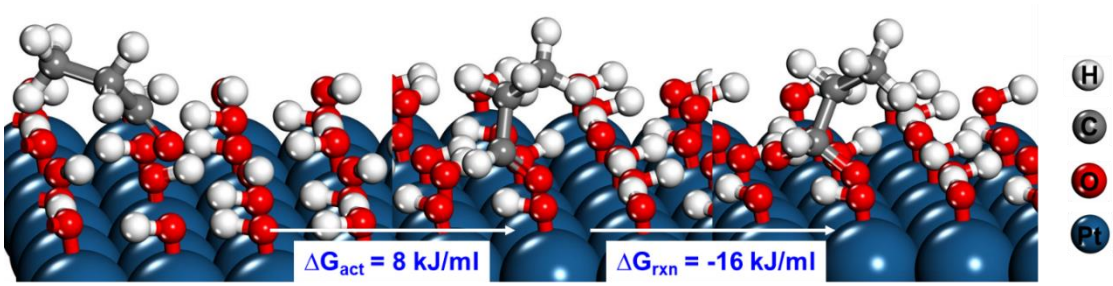

Figure 4.8: DFT optimized reactant, transition and product state for OH addition into 1-propanal over OH* covered Pt (111) surface

4.4.3. Analogies between propanol electro-oxidation and glycerol electro-oxidation

Glycerol electro-oxidation reaction (GEOR) in acidic media is assumed to proceed via a similar mechanism as propanol oxidation involving initial rate determining C-H activation step followed by O-H activation to form glyceraldehyde (GALD) or dihydroxyacetone (DHA), along with a parallel mechanism involving subsequent C-H activations and C-C cleavage steps forming CO. The relative product distribution (GALD vs DHA) would thus depend on the relative kinetics of C-H bond activation at the primary versus the secondary carbon center respectively. Based on the results from studies on model propanol system in acidic media, the activation of the weaker secondary C-H bond of glycerol would similarly be hindered compared to its stronger terminal primary C-H bond, due to the sterics effects of the adsorbed CO groups. The dominant pathway for GEOR in acidic media would thus likely proceed via C-H bond

activation at the terminal carbon center, en route to forming GALD, as observed experimentally.[53]

In alkaline media, as seen for propanol oxidation, GEOR can similarly be expected to proceed via formation of an alkoxide intermediate, with the resulting kinetics of the subsequent C-H activation step dictating the selectivity towards formation of GALD or DHA. Similar to model propanol system, the access to the metal center for the secondary C-H bond of the dehydrogenated glycerol intermediate (CH_2OH-CHO*-CH_2OH) would be hindered by the adsorbed OH groups, thus blocking access to the metal-assisted route. The OH mediated C-H activation route, while more accessible, would however, similarly favor the subsequent activation of the primary C-H bond over the secondary C-H bond to yield GALD, given the carbanionic nature of the transition state involved in this pathway. Overall, in alkaline media as well, the primary C-H bond of glycerol is more likely to be activated over its secondary C-H bond post initial facile O-H activation step, which in turn would lead to the dominant formation of GALD.

Further, GALD once formed can similarly as n-propanal undergo facile addition reaction with the OH either adsorbed on the surface or present in the solution phase to ultimately form glyceric acid (GLA). The low barriers for OH addition to the carbonyl along with the higher concentrations of base in alkaline solutions would drive the high glyceric acid selectivities that are observed experimentally.[53] Similar effects are also seen in acidic media at potentials higher than 0.66 V, wherein there is a sharp increase in the concentrations of glyceric acid.[53] This is likely the result of the dissociation of water to form hydroxyl groups adsorbed on the surface which occurs at potentials > 0.66 V NHE.[295] Thus, the highly facile OH addition promotes glyceric acid formation in alkaline media and at high potentials above 0.66 V in acidic media as has been shown experimentally for glycerol electro-oxidation over Pt, Au, and other metallic surfaces in alkaline media.[252]

4.4.4. Strategies to influence DHA selectivity

From our analysis of the mechanisms so far, we see that both the CO coverages in acidic media and OH coverages in alkaline media limit the activation of the secondary C-H bond on Pt surface. Thus, the surface coverages play an important role in the selectivity towards the primary versus the secondary oxidation product. In alkaline media, since the OH^- ions are inherently present in the solution phase, the OH coverages on the

surface are unavoidable. The CO coverages in acidic media are however formed by the decomposition of the substrate and hence can be eliminated or controlled. The elimination of the CO coverages could then potentially lead to increased selectivity for oxidation of the secondary alcohol.

In order to explore this, we examined the potential-dependent energetics for C-H activation of 1-propanol and 2-propanol over a clean Pt surface, results of which are shown in Figure 4.9. The results clearly show that over the range of potentials examined, the barrier for 1-propanol C-H activation is higher compared to that for 2-propanol C-H activation, which suggests 2-propanol C-H activation to be more facile over clean Pt surface compared to 1-propanol C-H activation. Thus, in case of GEOR, selective activation of the secondary C-H bond over the primary C-H bond over a clean Pt surface would lead to higher selectivity towards DHA compared to GALD.

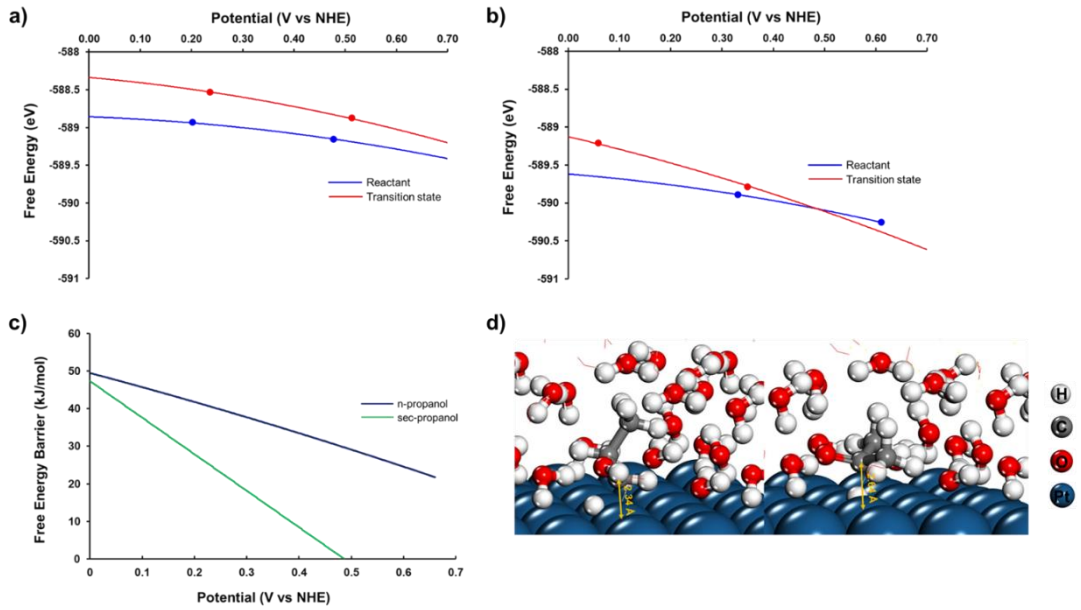

Figure 4.9: Potential dependent free energies of the reactant and transition state for the initial rate determining C-H activation step for a) n-propanol and b) sec-propanol; c) Potential dependent free energy barrier for the C-H activation of n-propanol and sec-propanol; d) DFT optimized transition state structures for the initial C-H activation step of n-propanol (left) and sec-propanol (right) over clean Pt (111) surface in solvent media at zero charge

To obtain a clean Pt surface and to reduce CO coverages, one can either change the structure or the composition of the catalyst which could be done by alloying the Pt

surface or by changing the surface structure. In order to test this hypothesis, we examined the C-C bond dissociation energies (BDEs) for different alloy overlayer configurations as well as for different Pt surface terminations. The results are reported in Table 4.2 (see Supplementary Information for the optimized structures). The C-C BDEs are used provide a simple measure of how easy or difficult it is to activate the C-C bond of glycerol to form C1 products and is used as a simple descriptor to characterize the extent of CO formation over the Pt surface. From the table, we see that Pt (100) and Pt (110) surfaces in particular have more exothermic C-C BDEs and therefore glycerol is more likely to dissociate in the early stages of the dehydrogenation leading to higher CO coverages. This is in line with the experimental results for GEOR done over single crystal Pt (100) and Pt (110) surfaces wherein CO coverages begin to appear at potentials as low as 0.05 V for the GEOR.[255,296]

Alloying Pt with other metals such as Bi or Cu can lead to significantly weaker adsorbate surface bond strengths which may inhibit C-C dissociation and CO formation. Herein we examine the activation of C-C activation of 1-propanol at the C1-C2 bond as a function of number of hydrogens removed in Table 4.2 (see Supplementary Information for the optimized structures) on the pseudomorphic overlayers of Pt on Bi and Cu. The results show and see that the C-C BDEs are significantly more endothermic on the pseudomorphic overalayers of Pt on Cu and Bi than on the Pt (111) surface which suggests that the C-C bond dissociation is more difficult and hence CO formation is less favored on the alloyed structures. This in turn would lead to lower CO coverages, which could lead to improvement in selectivity as well as activity as reported before. Such overlayer configurations can obtained by the galvanic displacement technique involving Pt deposition over a Bi or Cu surface and can be effective in increasing the DHA selectivity.[297] Another similar strategy that can be adopted is the addition of adatoms on the Pt surface which basically lowers the amount of contiguous Pt atoms present which are needed for CO formation.[298] Such strategies have been tested and shown to lead to lowering of CO coverages and subsequent increase in the selectivity towards the DHA.[269,272] However, as mentioned earlier, this strategy may not work in alkaline media since the nature of the adsorbed groups present are different and OH^- ions which are inherently present in the reaction media would still be adsorbed on the surface. These adsorbed OH groups have been shown in section 3.2 to preferably catalyze the activation of the primary C-H bond over

the secondary C-H bond. Hence, irrespective of the catalyst modifications, the selectivity would likely still be higher towards glyceric acid (GLA) in alkaline media which has also been shown experimentally.[275,276]

Table 4.2: Comparison of C-C bond dissociation energies at different stages of dehydrogenation over different Pt terminations and overlayer configurations

Surface	Stage of dehydrogenation	$\Delta E_{C\text{-}Cscission}$ (kJ/mol)
Pt(111)	First ($CH_3\mathbf{C}H_2\mathbf{C}HOH^*$)	10
	Second ($CH_3\mathbf{C}H\mathbf{C}HOH^*$)	69
	Third ($CH_3\mathbf{C}H\mathbf{C}OH^*$)	21
	Fourth ($CH_3\mathbf{C}\mathbf{C}OH^*$)	-5
Pt(100)	First ($CH_3\mathbf{C}H_2\mathbf{C}HOH^*$)	-28
	Second ($CH_3\mathbf{C}H\mathbf{C}HOH^*$)	-50
	Third ($CH_3\mathbf{C}H\mathbf{C}OH^*$)	75
	Fourth ($CH_3\mathbf{C}\mathbf{C}OH^*$)	47
Pt(110)	First ($CH_3\mathbf{C}H_2\mathbf{C}HOH^*$)	-49
	Second ($CH_3\mathbf{C}H\mathbf{C}HOH^*$)	-65
	Third ($CH_3\mathbf{C}H\mathbf{C}OH^*$)	-54
	Fourth ($CH_3\mathbf{C}\mathbf{C}OH^*$)	33
Pt(111)/Bi	First ($CH_3\mathbf{C}H_2\mathbf{C}HOH^*$)	52
	Second ($CH_3\mathbf{C}H\mathbf{C}HOH^*$)	81
	Third ($CH_3\mathbf{C}H\mathbf{C}OH^*$)	49
	Fourth ($CH_3\mathbf{C}\mathbf{C}OH^*$)	-10
Pt(111)/Cu	First ($CH_3\mathbf{C}H_2\mathbf{C}HOH^*$)	73
	Second ($CH_3\mathbf{C}H\mathbf{C}HOH^*$)	124
	Third ($CH_3\mathbf{C}H\mathbf{C}OH^*$)	73
	Fourth ($CH_3\mathbf{C}\mathbf{C}OH^*$)	42

Besides catalyst composition and surface modification, another strategy to increase the DHA selectivity would be to look at small number of atom clusters which would limit the CO formation as well as limit the sterics. Presence of dual metal sites would present

optimal effects for GEOR since the two metal sites present would aid in the activation of the C-H and O-H bond whilst limiting the formation of the CO due to the absence of contiguous atoms. Current efforts in our group are thus aimed at studying propanol and glycerol electro-oxidation reactions in acidic media over deposited Pt_2 clusters.

4.5. Conclusion

First-principle electrocatalytic studies were carried out in the presence of explicit solution as well as applied potential to gain insights into the factors and mechanisms that control the selective electro-oxidation of glycerol over Pt using a model propanol molecule. The simulation results show that in acidic media, alcohol oxidation proceeds via an initial C-H activation step followed by an O-H activation step. The C-H activation step is higher in energy and is likely the rate determining step. Pt electrode surfaces in acidic media are typically covered with CO that is likely formed via successive C-H activation and subsequent C-C bond breaking steps. The rate-determining C-H activation step at high coverages of CO was found to be more facile for 1-propanol than for 2-propanol despite the higher C-H bond strengths. This is attributed to the steric repulsions of the neighboring methyl groups present on 2-propanol with the adsorbed CO groups, which in turn limits the activation of the secondary C-H bond, and hence dihydroxyacetone (DHA) formation in glycerol electro-oxidation reaction (GEOR). In alkaline media, on the other hand, the Pt surfaces are typically covered by hydroxyl groups, and the mechanism proceeds via an initial O-H activation step which is subsequently followed by the rate-determining C-H activation step. While the presence of OH groups on the surface block access to the metal-assisted pathway for the activation of the secondary C-H bond, they promote the activation of the primary C-H bond over that of secondary C-H bond via the OH-assisted path, which in turn likely leads to higher glyceraldehyde (GALD) formation rates in case of GEOR. The presence of OH on the surface and solution under alkaline conditions also promotes the facile addition of OH addition to the carbon of the bound carbonyl of glyceraldehyde to drive the high selectivity seen towards glyceric acid (GLA) for GEOR. While it is seemingly unfavorable to form DHA in alkaline media due to the inherent presence of OH groups, the selectivity towards DHA can be tuned in acidic media by modifying the surface coverage and limiting CO formation. Pseudomorphic overlayers of Pt (111) on Bi or Cu can be an effective strategy to limit

the CO coverages which in turn can lead to higher selectivity towards DHA via selective activation of the secondary C-H bond.

4.6. Acknowledgements

The authors would like to thank the National Science Foundation CCI program (award 1740656) for the funding support and the Minnesota Supercomputing Institute (MSI) at the U. of Minnesota for use of computing resources.

4.7. Supplementary Information

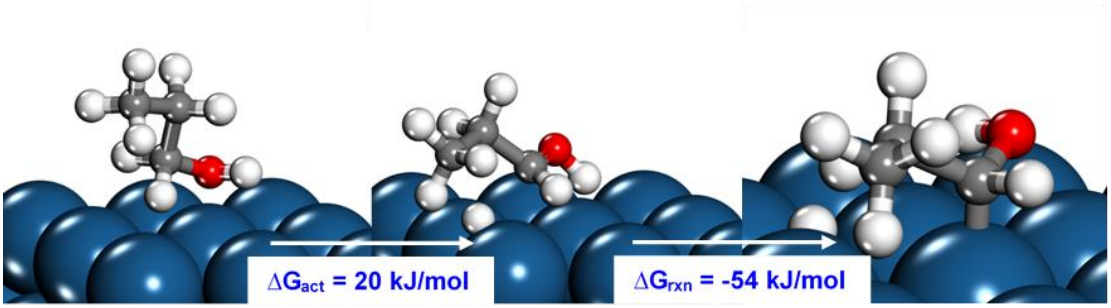

Figure S4.1: DFT-optimized reactant, transition, and product state structures for initial C-H activation of the adsorbed n-propanol over Pt (111) surface

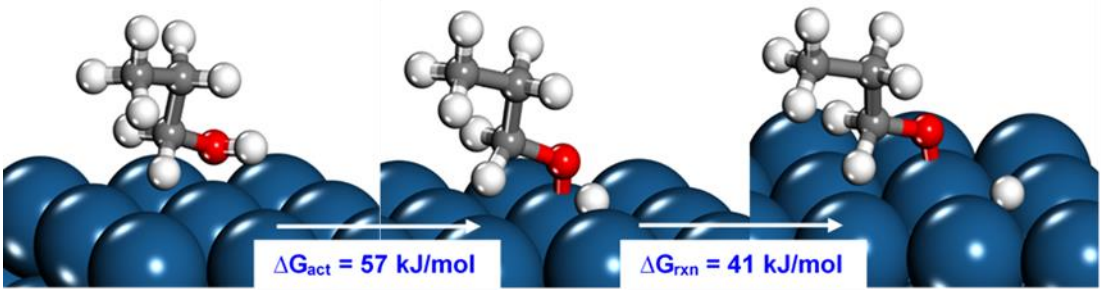

Figure S4.2: DFT-optimized reactant, transition, and product state structures for initial O-H activation of the adsorbed n-propanol over Pt (111) surface

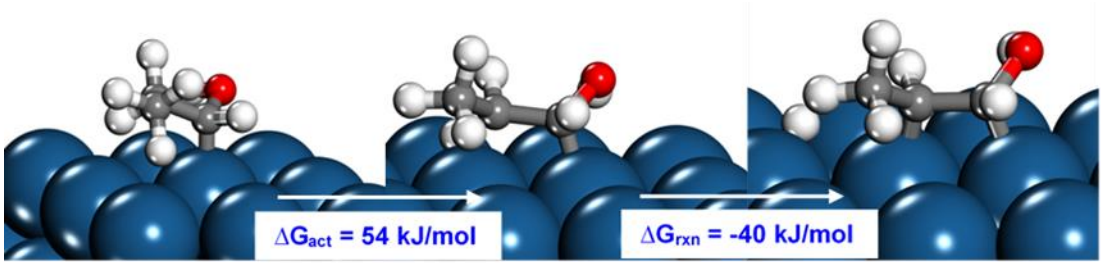

Figure S4.3: DFT-optimized reactant, transition, and product state structures for C-H activation of the adsorbed hydroxypropyl intermediate over Pt (111) surface

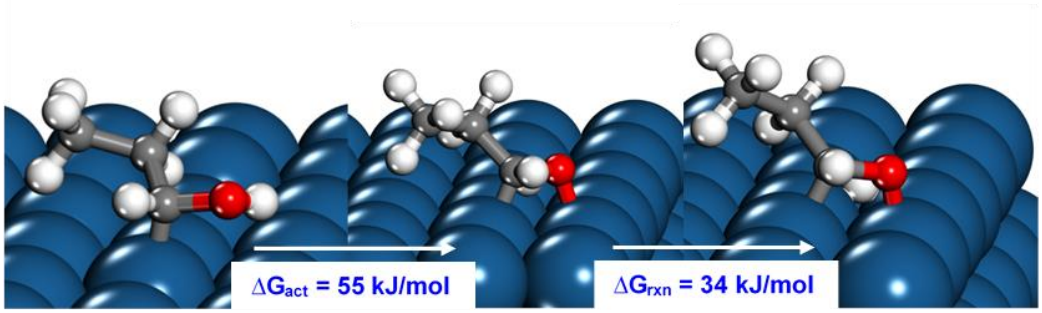

Figure S4.4: DFT-optimized reactant, transition, and product state structures for the O-H activation of the adsorbed hydroxypropyl intermediate over Pt (111) surface

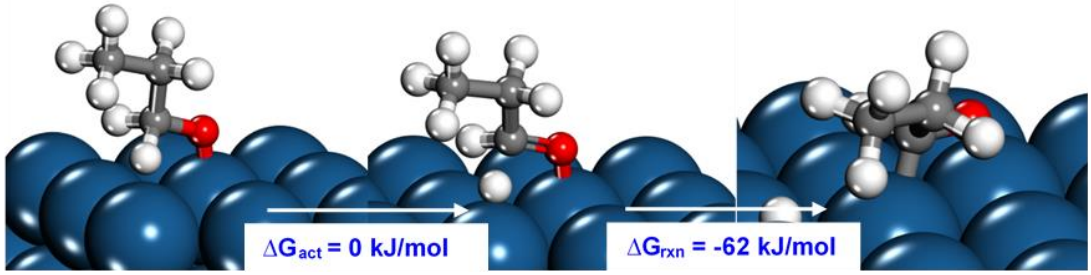

Figure S4.5: DFT-optimized reactant, transition, and product state structures for the C-H activation of the adsorbed 1-propoxy intermediate over Pt (111) surface

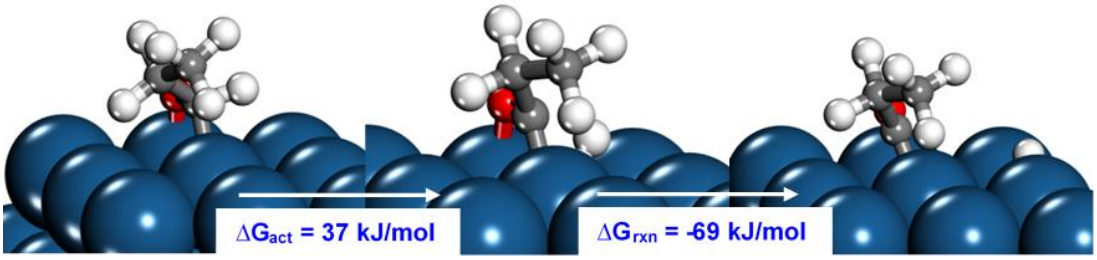

Figure S4.6: DFT-optimized reactant, transition, and product state structures for the C-H activation of the adsorbed n-propanal over Pt (111) surface

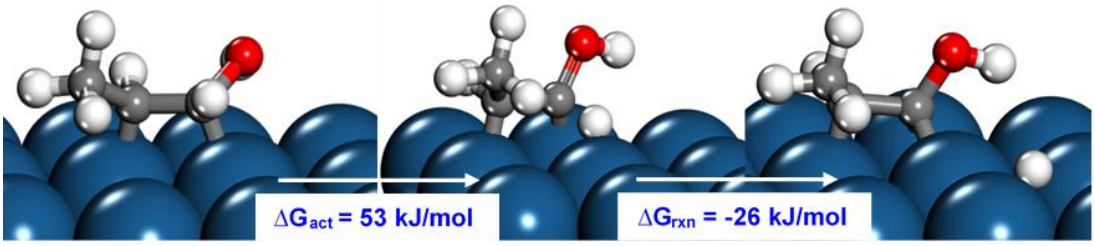

Figure S4.7: DFT-optimized reactant, transition, and product state structures for the C-H activation of the adsorbed n-propenol over Pt (111) surface

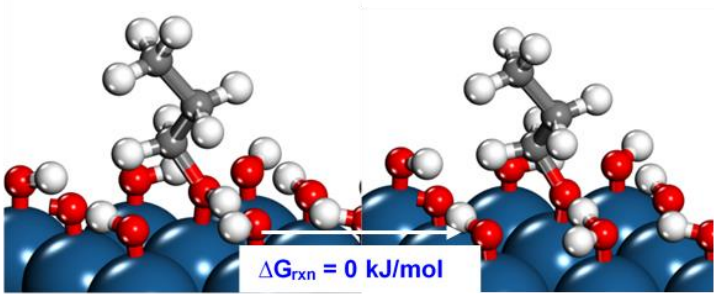

Figure S4.8: DFT-optimized reactant and product state structures for the OH* assisted O-H activation of the adsorbed n-propanol over 8/9 ML OH* covered Pt (111) surface

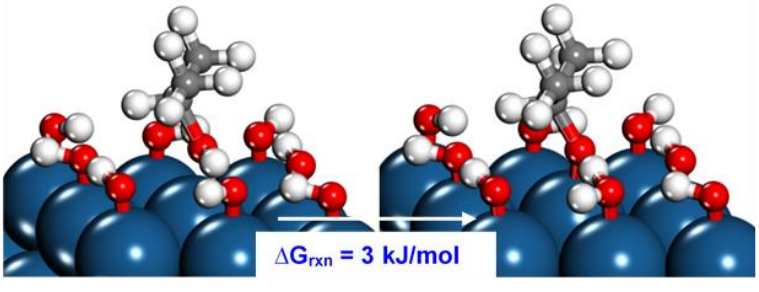

Figure S4.9: DFT-optimized reactant and product state structures for the OH* assisted O-H activation of the adsorbed sec-propanol over 8/9 ML OH* covered Pt (111) surface

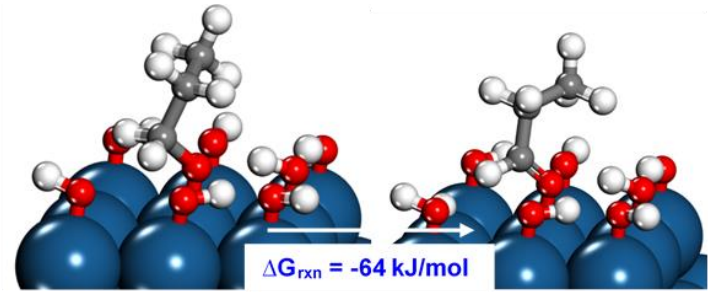

Figure S4.10: DFT-optimized reactant and product state structures for the metal assisted C-H activation of the adsorbed 1-propoxy intermediate over 7/9 ML OH* covered Pt (111) surface

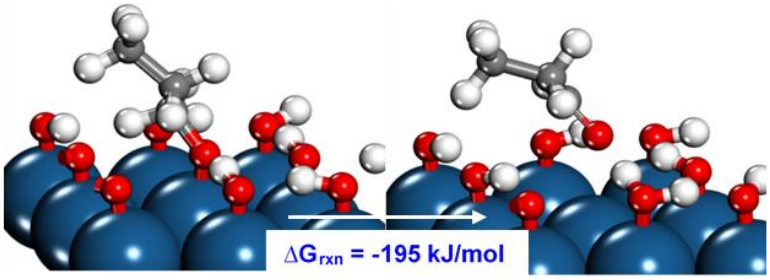

Figure S4.11: DFT-optimized reactant and product state structures for the OH* assisted C-H activation of the adsorbed 1-propoxy intermediate over 8/9 ML OH* covered Pt (111) surface

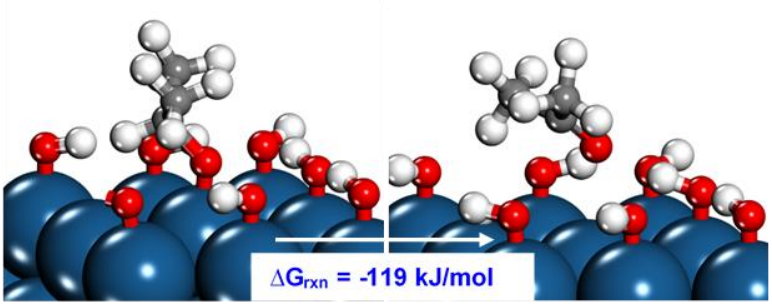

Figure S4.12: DFT-optimized reactant and product state structures for the metal assisted C-H activation of the adsorbed 2-propoxy intermediate over 7/9 ML OH* covered Pt (111) surface

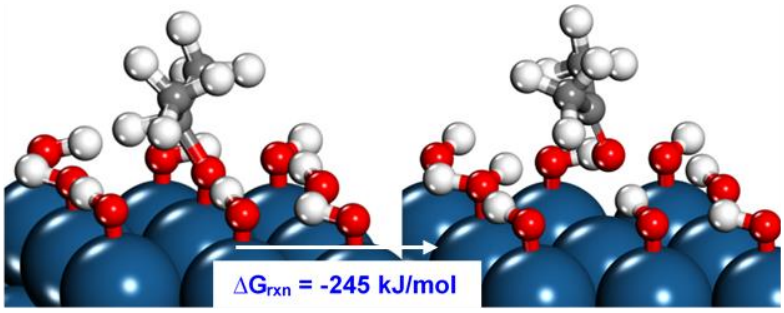

Figure S4.13: DFT-optimized reactant and product state structures for the OH* assisted C-H activation of the adsorbed 2-propoxy intermediate over 8/9 ML OH* covered Pt (111) surface

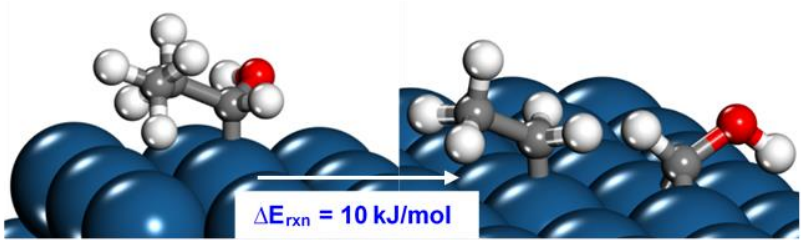

Figure S4.14: DFT-optimized reactant and product state structures for the C-C bond dissociation of the dehydrogenated CH_3CH_2CHOH* intermediate over Pt (111) surface

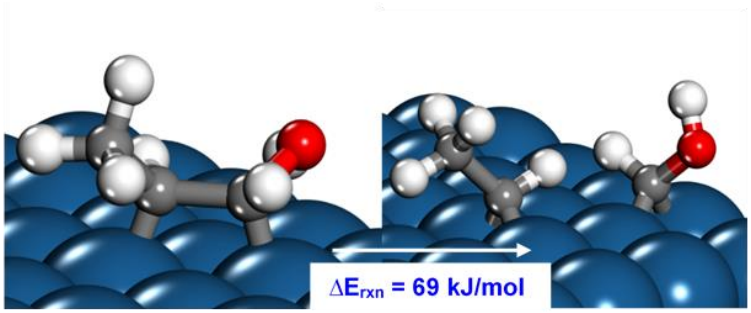

Figure S4.15: DFT-optimized reactant and product state structures for the C-C bond dissociation of the dehydrogenated $CH_3CHCHOH$* intermediate over Pt (111) surface

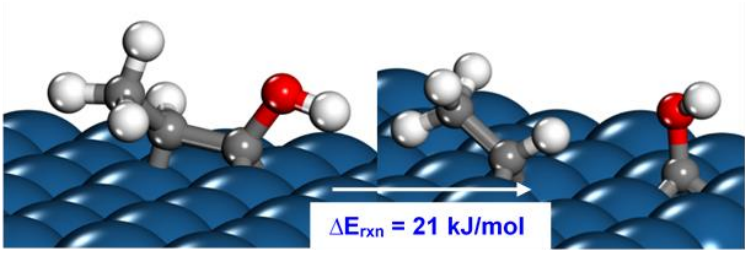

Figure S4.16: DFT-optimized reactant and product state structures for the C-C bond dissociation of the dehydrogenated CH_3CHCOH^* intermediate over Pt (111) surface

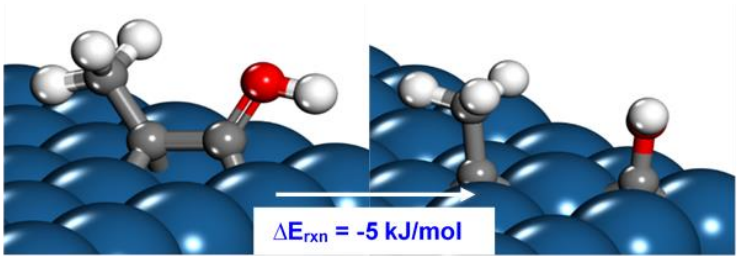

Figure S4.17: DFT-optimized reactant and product state structures for the C-C bond dissociation of the dehydrogenated CH_3CCOH^* intermediate over Pt (111) surface

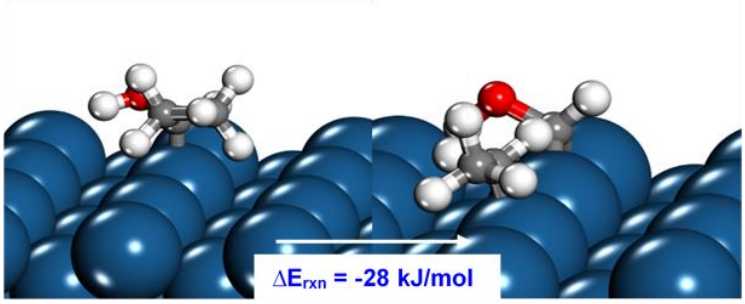

Figure S4.18: DFT-optimized reactant and product state structures for the C-C bond dissociation of the dehydrogenated $CH_3CH_2CHOH^*$ intermediate over Pt (110) surface

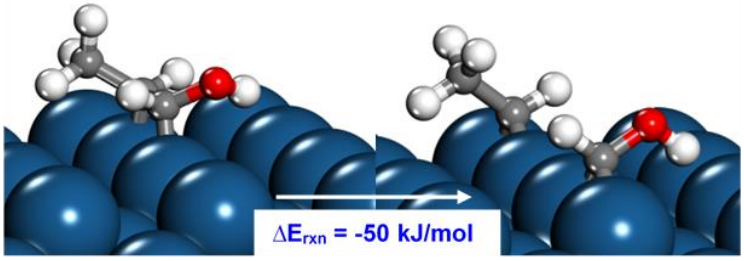

Figure S4.19: DFT-optimized reactant and product state structures for the C-C bond dissociation of the dehydrogenated $CH_3CHCHOH^*$ intermediate over Pt (110) surface

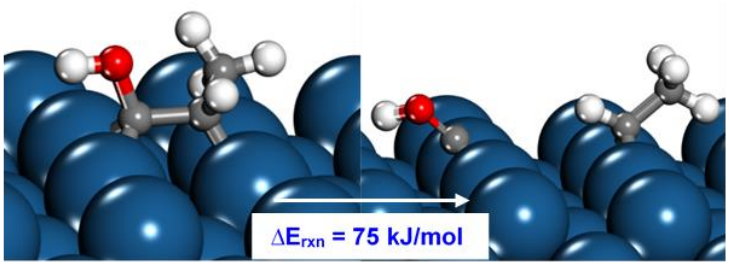

Figure S4.20: DFT-optimized reactant and product state structures for the C-C bond dissociation of the dehydrogenated CH_3CHCOH^* intermediate over Pt (110) surface

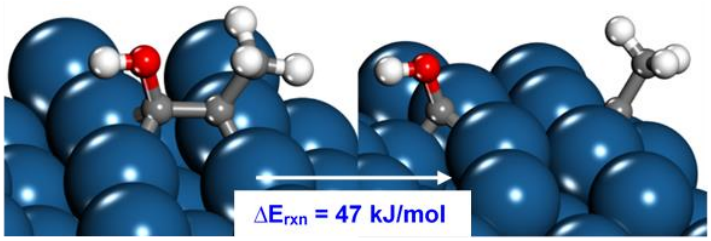

Figure S4.21: DFT-optimized reactant and product state structures for the C-C bond dissociation of the dehydrogenated CH_3CCOH^* intermediate over Pt (110) surface

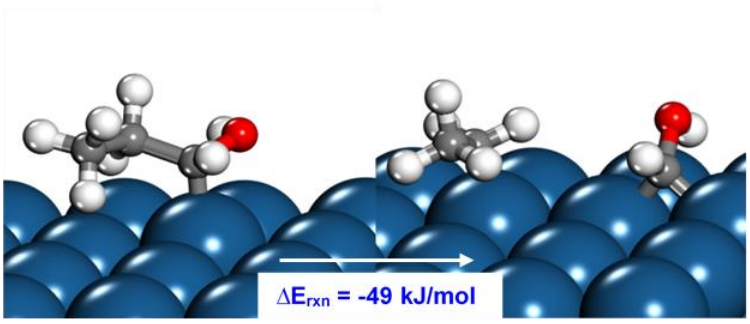

Figure S4.22: DFT-optimized reactant and product state structures for the C-C bond dissociation of the dehydrogenated $CH_3CH_2CHOH^*$ intermediate over Pt (100) surface

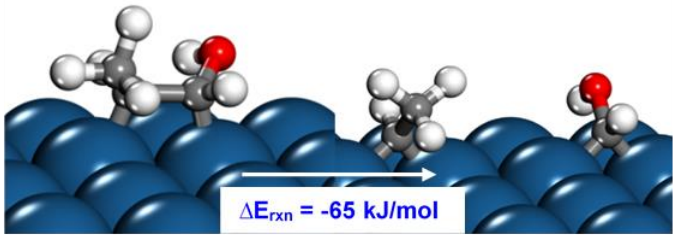

Figure S4.23: DFT-optimized reactant and product state structures for the C-C bond dissociation of the dehydrogenated $CH_3CHCHOH^*$ intermediate over Pt (100) surface

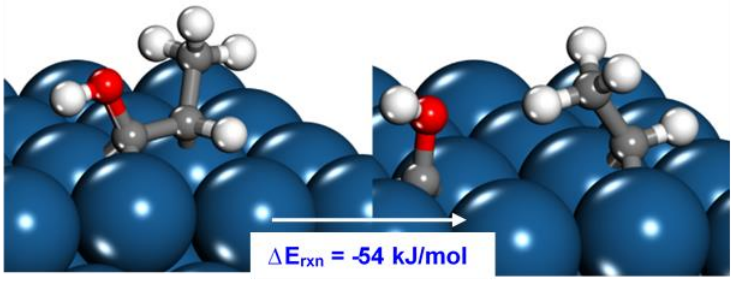

Figure S4.24: DFT-optimized reactant and product state structures for the C-C bond dissociation of the dehydrogenated CH_3CHCOH^* intermediate over Pt (100) surface

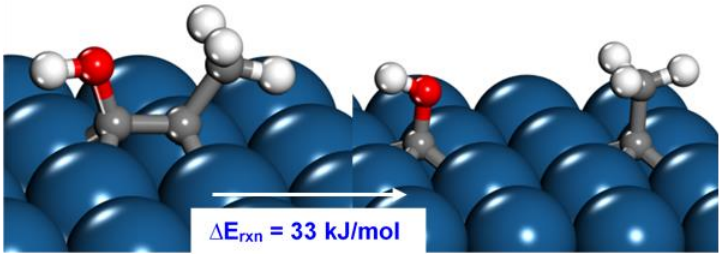

Figure S4.25: DFT-optimized reactant and product state structures for the C-C bond dissociation of the dehydrogenated CH_3CCOH^* intermediate over Pt (100) surface

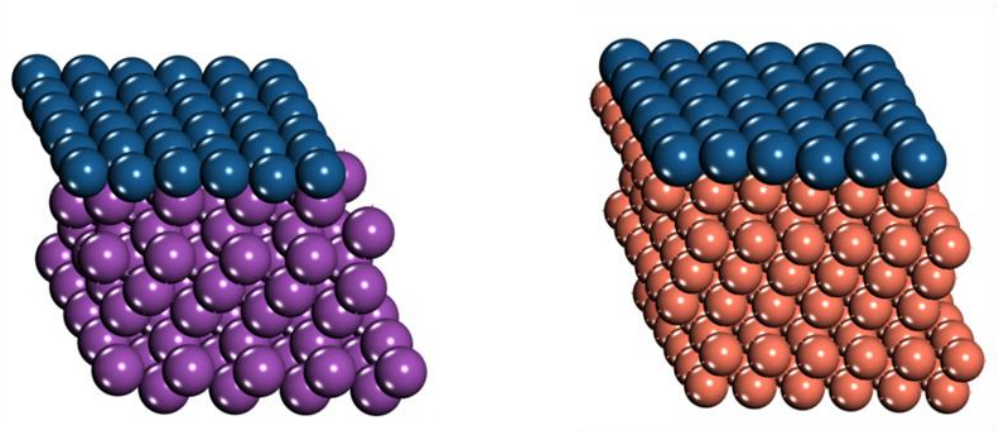

Figure S4.26: DFT-optimized structures for the Pt (111)/Bi (left) and Pt (111)/Cu (right) used for the calculations of the C-C bond dissociation energies of the different dehydrogenation intermediates of n-propanol. The resultant DFT-optimized dehydrogenated structures and dissociated structures are similar to Figures S4.14-S4.17

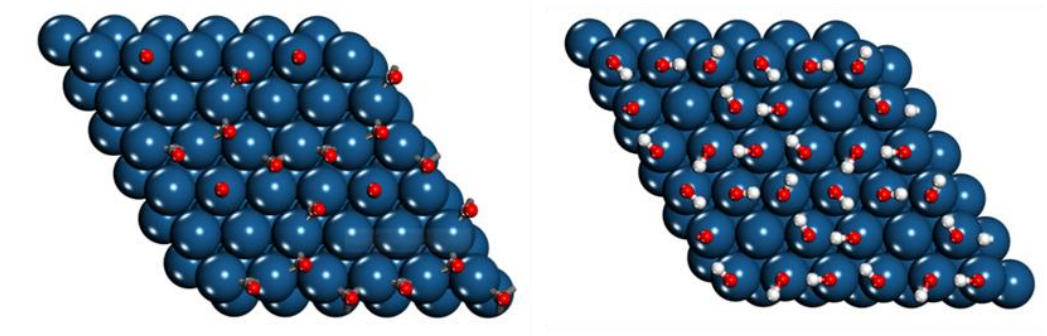

Figure S4.27: 5/9 ML CO* covered Pt (111) (left) and 8/9 ML OH* covered Pt (111) (right) surface models used for comparison of n-propanol and sec-propanol C-H activation kinetics in acidic media and alkaline media respectively

Chapter 5 - Field Effect Modulation of Electrocatalytic Hydrogen Evolution at Back-Gated Two-Dimensional MoS_2 Electrodes

5.1. Synopsis

Electrocatalytic activity for hydrogen evolution at monolayer MoS_2 electrodes can be enhanced by the application of an electric field normal to the electrode plane. The electric field is produced by a gate electrode lying underneath the MoS_2 and separated from it by a dielectric. Application of a voltage to the back-side gate electrode while sweeping the MoS_2 electrochemical potential in a conventional manner in 0.5 M H_2SO_4 results in up to a 140-mV reduction in overpotential for hydrogen evolution at current densities of 50 mA/cm^2. Tafel analysis indicates that the exchange current density is correspondingly improved by a factor of 4 to 0.1 mA/cm^2 as gate voltage is increased. Density functional theory calculations support a mechanism in which the higher hydrogen evolution activity is caused by gate-induced electronic charge on Mo metal centers adjacent the S vacancies (the active sites), leading to enhanced Mo-H bond strengths. Overall, our findings indicate that the back-gated working electrode architecture is a convenient and versatile platform for investigating the connection between tunable electronic charge at active sites and overpotential for electrocatalytic processes on ultrathin electrode materials.

5.2. Introduction

Previously, we have reported field effect modulation of outer-sphere electrochemistry at two-dimensional (2D) semiconductors,[299–301] such as monolayer MoS_2 and 5-nm-thick ZnO films grown by atomic layer deposition (ALD). In these experiments, the 2D material is supported on a dielectric such as SiO_2 with a backside gate electrode, forming a metal-oxide-semiconductor (MOS) heterostructure, as shown in Figure 5.1a. The backside gate may be a true metal electrode or, because of convenience, a heavily-doped Si substrate. Application of a back-gate voltage V_{BG} between the gate and an electrical contact to the 2D semiconductor simultaneously shifts the conduction and

valence band edges and accumulates or depletes charge carriers in the semiconductor; this is the conventional field effect employed in silicon field effect transistors (MOSFETs).[302] In some sense this field effect modification of the 2D working electrode is akin to chemical doping in that the offset between the Fermi level (E_F) and the band edges is controllably changed (as in n-doping or p-doping). However, the field effect is distinctly different from chemical doping in that (1) it is electronically controlled, continuously variable, and easily reversible; (2) it is the band edges that shift in response to the field, not E_F, which means that the positions of these edges with respect to redox couples in solution are changed, which in turn implies that the heterogeneous electron transfer rate constants can be tuned.

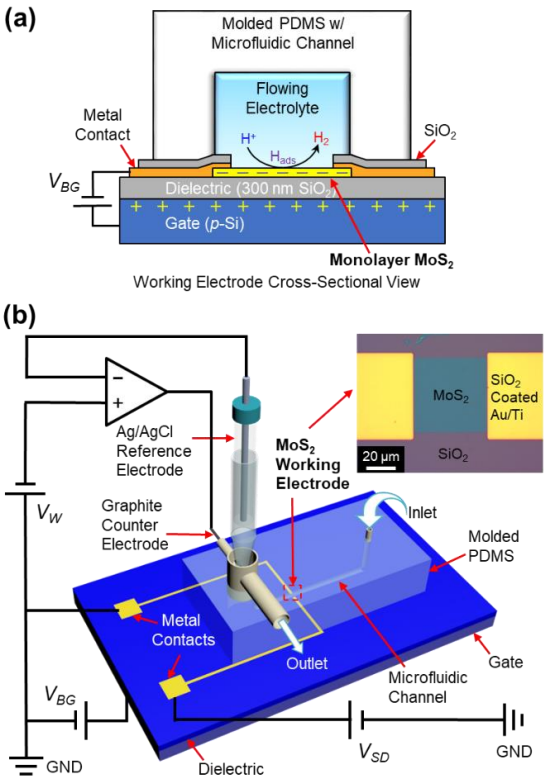

Figure 5.1: (a) Cross-sectional view of MoS_2 working electrode and (b) 3D structure of the back-gated electrochemical flow cell (not to scale) with the electrical/electrochemical configuration. The inset optical image in (b) shows a plan view of a MoS_2 electrode. The symbols used in the schematics are as follows: working electrode potential (V_W), source-to-drain bias (V_{SD}), and back-gate bias (V_{BG}).

We have shown that field effect modulation of the band edges and carrier concentration in monolayer MoS_2 and ultrathin ZnO can control heterogeneous charge transfer

kinetics between the 2D material and simple, outer-sphere redox couples in electrolyte on the "front" side of the semiconductor. These initial experiments demonstrated the concept of field effect modulation of outer-sphere electrochemistry.[299–301] Here, we take the next step and demonstrate that field effect modulation can modify the rate of an inner-sphere, electrocatalytic reaction, namely the hydrogen evolution reaction (HER) on MoS_2. Prior reports by others have demonstrated that both polymorphs of MoS_2 (metastable, metallic 1T and semiconducting 2H) are catalytically active for HER.[60,61,303–310] The activity of 2H MoS_2, our focus here, derives from coordinatively unsaturated Mo active sites, *i.e.*, Mo centers adjacent S vacancies or at exposed crystal edges. Consequently, S vacancy (active site) formation is a commonly adopted strategy to activate electrocatalysis on MoS_2,[60,311] though heteroatom doping is also employed.[312–314]

Prior to this work, the field effect has been reported to improve HER activity at back-gated *multilayer* MoS_2 electrodes.[315] However, in that work (see also a related paper on gated multilayer VSe_2[316]), the enhanced HER activity was attributed to increased conductivity of the multilayer MoS_2 (20-30 nm thick) upon gating and not to any changes in the intrinsic reactivity of the active sites. Herein, we demonstrate by a combination of experiment and density functional theory (DFT) calculations that field effect enhancement of HER activity on *monolayer* MoS_2 occurs by a different mechanism, namely the gate-induced charging of the localized Mo d-states at the active (S-vacancy) sites, and the resultant increase of the Mo-H binding energy. In this mechanism, the increase in HER activity is due to an increase in the intrinsic reactivity of the active sites in monolayer MoS_2 on applying a positive gate bias V_{BG}. Experimentally, we achieve a 140-mV decrease in η at 50 mA/cm^2 and a 4-fold increase in the exchange current density i_0 by varying V_{BG}. We systematically eliminate the possibility that the enhancement in i_0 and the decrease in η are due to changes in the MoS_2 conductivity or the resistance of the electrical contacts to MoS_2. Further, using DFT, we demonstrate that the charging of the Mo centers at the active sites leads to a 140% increase in the Mo-H bond energy, which provides a clear explanation for the enhanced HER activity. We believe these experiments and associated theoretical calculations open up new possibilities for investigating and understanding electrocatalysis at 2D materials, as we describe below.

5.3. Results and Discussion

Monolayer MoS_2 was synthesized by chemical vapor deposition (CVD) at 850 ℃ following a modification of previously reported methods.[317,318] Large monolayer flakes that are desirable for back-gated electrocatalysis experiments were characterized by atomic force microscopy (AFM), Raman spectroscopy, and photoluminescence and confirmed the 2H phase (Figure S5.2). After the transfer of a monolayer of MoS_2 onto SiO_2/p-Si back gates, fabrication of MoS_2 electrodes was accomplished in a series of steps including photolithography, plasma etching, e-beam evaporation of Ti/Au metal contacts, and SiO_2 passivation (see the Supporting Information for details of synthesis and device fabrication). The two Ti/Au contacts (source and drain) were made to the front-side of MoS_2 and the completed structure in Figure 5.1a can thus be viewed as a FET. From the MoS_2 sheet conductance-gate voltage (G_S-V_{BG}) characteristics, Figure S6, we confirmed the n-type behavior of MoS_2 with an on/off current ratio of $\sim 10^4$ and a FET electron mobility of ~ 22 $cm^2\ V^{-1}s^{-1}$, which further confirmed that the monolayer MoS_2 was the 2H phase.

To perform electrochemical measurements, a molded polydimethylsiloxane (PDMS) block with an embedded 200-μm wide microfluidic channel was assembled onto a MoS_2 electrode, Figure 5.1b. Integration of this flow cell structure facilitated forced convection of electrolyte, thereby minimizing mass transport effects on voltammetry and helping to sweep away gas bubbles generated on the MoS_2 working electrode. Figure 2a displays our principal results, namely the polarization curves in flowing 0.5 M H_2SO_4 upon sweeping the MoS_2 working electrode potential V_W while applying a constant V_{BG}. At $V_{BG} = 0\ V$, the HER overpotentials ($\eta = |V_w - U^0|$) at current densities of 10 and 50 mA/cm^2 were 294 ± 11 and 478 ± 5 mV, respectively. These η values at $V_{BG} = 0\ V$ are comparable to those previously reported for HER on monolayer MoS_2.[60,311,319,320] As V_{BG} increased from 0 V to +100 V at 20 V intervals, η progressively decreased to 176 ± 27 mV (at 10 mA/cm^2) and 334 ± 3 mV (at 50 mA/cm^2), respectively (Table 5.1), indicating an overall improved catalytic activity for HER. Negative V_{BG}, on the other hand, suppressed HER on back-gated MoS_2, resulting in an increased η. The effect of V_{BG} on HER activity was reversible, *i.e.*, switching of V_{BG} to higher and lower values produced corresponding voltammograms that retraced themselves. As a control, we tested back-gated working electrodes in which MoS_2 was

replaced with graphene, Figure 5.2a. We observed no significant HER activity for back-gated graphene at any value of V_{BG} (Figure S5.9), consistent with expectations. We also verified that the observed shift in η was not a result of the ohmic drop across the MoS_2 working electrode. To check that, we measured the sheet resistance of MoS_2 electrodes simultaneously during the electrochemical measurement (Figure S5.8a). The calculated in-plane polarization at varying V_{BG} and V_W was always smaller than 11 mV (Figure S5.8b) and accounted for less than 1% of the overall polarization (*i.e.* η) at current densities of 10 and 50 mA/cm^2 (Figure S5.8c). Therefore, it is clear that the reduced η did not result from changes in the in-plane ohmic losses.

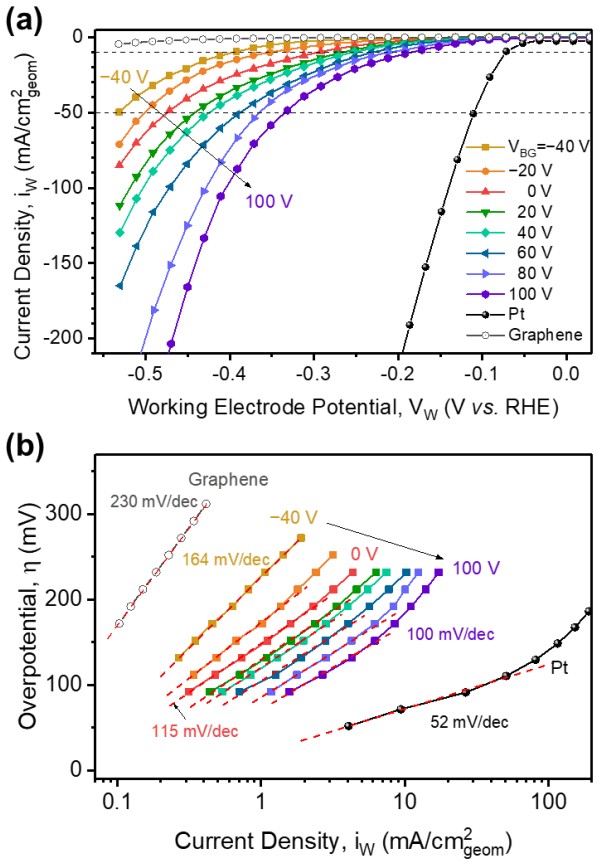

Figure 5.2: (a) Representative polarization curves and (b) corresponding Tafel plots for a back-gated MoS_2 electrode at different back-gate biases V_{BG} and in contact with 0.5 M H_2SO_4. Results on Pt and graphene electrodes are included for comparison. The polarization curves are iR-corrected for solution resistance. All the electrochemical measurements were performed at a working electrode potential scan rate of 50 mV/s and an electrolyte volumetric flow rate of 10 µL/min.

Table 5.1: Overpotential, Tafel Slope, and Exchange Current Density at Varying Back-Gate Biases

V_{BG} (V)	η at 10 mA/cm^2 (mV)	η at 50 mA/cm^2 (mV)	Tafel Slope* (mv/dec)	i_0 (mA/cm^2)
-40	388 ± 9	524 ± 8	164 ± 1	0.030 ± 0.001
-20	374 ± 20	500 ± 6	130 ± 4	0.032 ± 0.004
0	294 ± 11	478 ± 5	115 ± 2	0.034 ± 0.002
20	271 ± 8	451 ± 10	113 ± 3	0.047 ± 0.005
40	254 ± 9	421 ± 4	111 ± 3	0.054 ± 0.005
60	237 ± 7	390 ± 9	106 ± 6	0.068 ± 0.013
80	218 ± 11	371 ± 10	105 ± 4	0.098 ± 0.012
100	176 ± 27	334 ± 3	100 ± 6	0.122 ± 0.024

*The standard deviations for Tafel slope were calculated from fitting representative polarization curves to the Tafel equation.

The polarization curves in Figure 5.2a were converted into corresponding Tafel plots, Figure 5.2b, to assess the reaction mechanism. Tafel slopes (b) and exchange current densities (i_0) were obtained by fitting the plots to $\eta = b\,(\log(i_w) - \log(i_0))$. As expected, a Tafel slope of 115 ± 2 mV/decade is observed for HER on MoS_2 at V_{BG} = 0 V, consistent with ~120 mV/decade that others have reported for monolayer MoS_2 on Si/SiO_2.[305] The Tafel slope gradually decreases to 100 ± 6 mV/decade with increasing V_{BG}, while it increases to 164 mV/decade at negative V_{BG}. It is widely accepted that HER on MoS_2 follows the Volmer-Heyrovsky mechanism, where $H^+ + e^- \rightleftharpoons H_{ads}$ (Volmer) and $H^+ + e^- + H_{ads} \rightleftharpoons H_2$ (Heyrovsky) are the elementary steps.[321] Tafel slopes of ~120 mV/decade or larger suggest that the Volmer reaction, namely the coupled adsorption and charge transfer step, limits the overall reaction rate.[322] The slight decrease in the Tafel slope indicates that there is likely not a significant change in the reaction mechanism upon varying V_{BG}. However, the exchange density i_0 increases by a factor of 4 from 0.034 ± 0.002 to 0.122 ± 0.024 mA/cm^2 as V_{BG} increases

to +100 V, as shown in Table 5.1 and Figure 5.3. These i_0 values obtained on back-gated MoS_2 are among the highest reported to date,[60,61,305,307] and the considerable increase in i_0 and suggests substantially enhanced catalytic activity at equilibrium. Figure 5.3 also shows the estimated turn over frequency per S vacancy (right axis) calculated from i_0 and average S vacancy concentration.

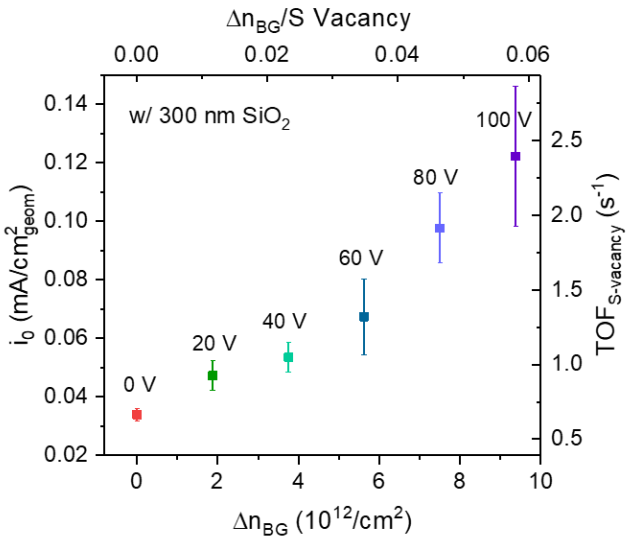

Figure 5.3: Exchange current density (i_0) and turn over frequency per S vacancy ($TOF_{S\text{-}vacancy}$) as a function of the back-gate induced charge carrier density, Δn_{BG}. The x-axis is quoted in electrons/cm^2 and electrons/S vacancy.

With more than a 100 mV shift in η at 10 mA/cm^2 and a 4-fold increase in i_0, it is reasonable to conclude that the overall HER activity of monolayer 2H MoS_2 is improved by the field effect. In order to clarify the mechanism for enhanced activity, DFT calculations were performed. The Mo centers adjacent to S vacancies on the MoS_2 basal plane are considered to be the active sites for HER.[7] X-ray photoelectron spectroscopy (XPS) analysis of the CVD monolayer MoS_2 used in this study indicated that there are ~7 ± 2% S vacancies (Figure S5.3) that function as active sites. We therefore constructed a monolayer MoS_2 surface comprised of 5.5% S vacancies to serve as a model for DFT calculations, as shown in Figure 5.4a. The creation of S vacancies within the MoS_2 surface resulted in the formation of mid-gap electronic states (see Figure 5.4b and S5.10) comprised predominantly of localized Mo d-states that favorably bind protons.[60] To model the electrostatic doping effect of the back-gate bias on these mid-gap states, we charged the model substrate with extra electrons

corresponding to the excess electron densities obtained experimentally (see Supporting Information for further details on the computational methods). Excess electron densities of nearly 1×10^{13} cm^{-2} as calculated by $\Delta n_{BG} = C_{SiO_2} \times V_{BG}$ ($C_{SiO_2}$is the specific capacitance of 300 nm SiO_2, measured to be ~15 nF/cm^2, Figure S5.10), are induced experimentally at V_{BG} = +100 V. Figure 5.4c displays the DFT-calculated electron density difference map corresponding to the difference in charge density at V_{BG} = +100 V (Δn_{BG}= 10^{13} cm^{-2}) versus that at 0 V (Δn_{BG} = 0). From this figure, it is evident that the excess electron density induced upon the application of V_{BG} is concentrated on the Mo atoms near the S vacancy site. This accumulation of excess electron density on the Mo centers in turn leads to a downward shift of the mid-gap states closer to E_F as V_{BG} is increased from 0 to +100 V as shown in Figure 5.4b. This downward shift of the energy levels is in agreement with expectations based on the known operating principles for field effect devices.

The hydrogen adsorption free energy ($\Delta G_H = \Delta E_H + \Delta ZPE - T\Delta S$, where ΔE_H is the hydrogen adsorption energy, ΔZPE is the zero point energy difference, and ΔS is the entropy change between the adsorbed and the gas phase hydrogen) to an electrode surface has been shown to be a good descriptor for trends in HER activity.[5] In the present study, the changes in ΔZPE and ΔS aren't expected to depend on charge. As such, we use ΔE_H to provide the important qualitative trends as described below. We calculated ΔE_H for the binding of hydrogen to the S vacancy site at charge densities corresponding to the applied back-gate voltages. As shown in Figure 5.5a, ΔE_H becomes significantly more exothermic at higher Δn_{BG}. Importantly, this stronger H binding provides a clear rationale for higher activity of adsorption-limited HER on MoS_2; increased ΔE_H lowers the activation energy for the Volmer step and leads to a higher fraction of hydrogenated active sites, *i.e.*, equilibrium is shifted in favor of H_{ads}.

In keeping with this analysis, we observed an exponential dependence of the experimental i_0 on the calculated ΔE_H values as shown in Figure 5.5b. This exponential increase is expected as i_0 is an exponential function of the activation barrier for the rate-limiting Volmer step.[323,324] The Figure 5.5b trend is also consistent with previous reports that show i_0 increases exponentially with ΔE_H for electrocatalysts that lie on the right side of the i_0 *vs.* ΔE_H "volcano plot", that is those that bind hydrogen weakly ($\Delta E_H > -0.2\ eV$).[303,324–326] Thus, the detailed DFT calculations reported here strongly

support a mechanism in which the gate-induced charge enhances the intrinsic activity of the MoS_2 active sites, in particular by stabilizing H_{ads}.

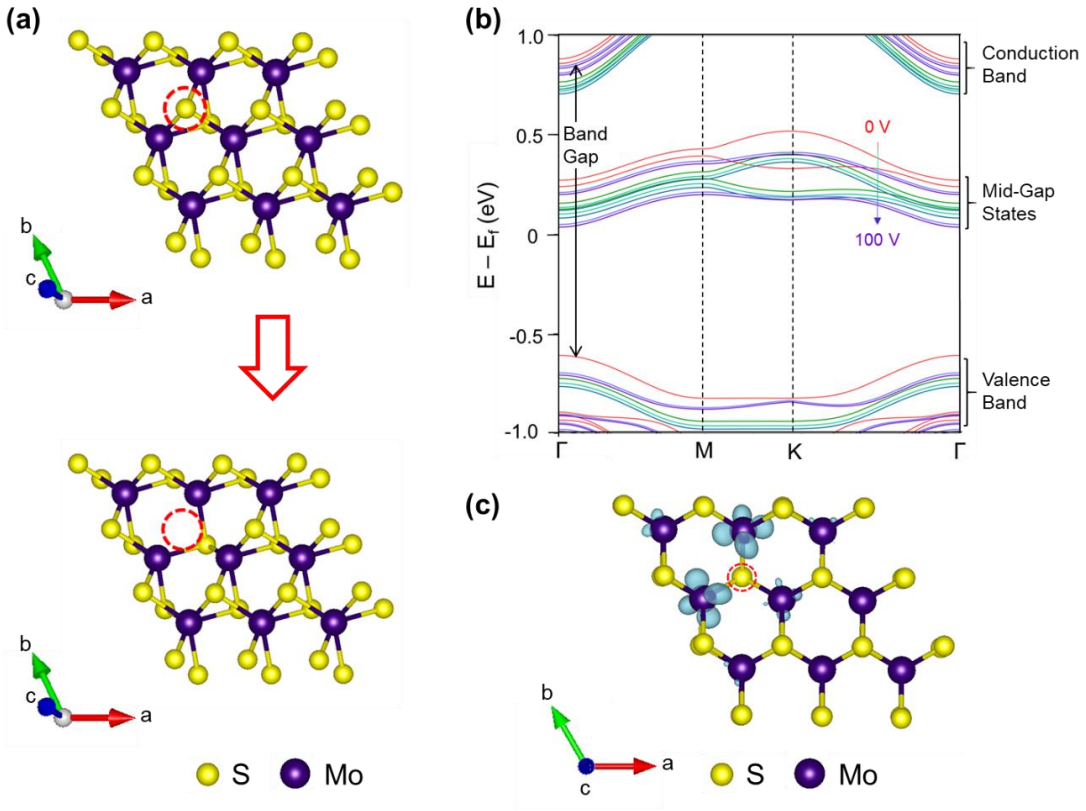

Figure 5.4: (a) Schematic of the S vacancy site (denoted by red dotted circle) created on model MoS_2 surface used for DFT calculations (b) Computed band structures of MoS_2 surface with 5.5 % S vacancy at different induced charges varying from $\Delta n_{BG} = 0$ ($V_{BG} = 0$ V) to $\Delta n_{BG} = 10^{13}$ cm^{-2} ($V_{BG} = 100$ V). The band structure at $V_{BG} = 0$ V is shown in red. (c) Charge density difference map (isosurface value = 0.0002 e-/Bohr^3) of monolayer MoS_2 with 5.5 % S vacancy showing the positive difference in electron density at an induced charge carrier density of 10^{13} cm^{-2} versus that at no excess charge density. The maps show localization of excess charge on the Mo atoms near the sulfur vacancy denoted by red circle.

The results reported here are distinctly different than previous work reported on field effect modulation of HER at multilayer (30-nm thick) MoS_2, which indicate that the decrease in η with applied gate voltage is the result of conductance changes across the MoS_2 flake, *i.e.*, to changes in the ohmic transport of charge from the contacts to the catalytic interface.[315] As mentioned above, using methods that we have previously

reported[299] we categorically rule out the possibility that the changes in η are due to in-plane transport effects or to contact resistance.[305,315] The changes in η that we observe are instead due to changes in inherent catalytic activity of monolayer MoS_2. This is a distinctly different mechanism from that proposed previously. Moreover, it does not seem likely that appreciable gate-induced enhancement of S-vacancy activity could be observed in 25-30 nm thick multilayer MoS_2 due to electrostatic confinement and screening of the gate-induced charge at the MoS_2/gate dielectric interface. For example, we estimate the Thomas-Fermi screening length in MoS_2 at $\Delta n_{BG} = 10^{13}$ cm^{-2} to be approximately 1-3 nm, smaller than the 25-30 nm thickness of multilayer MoS_2.

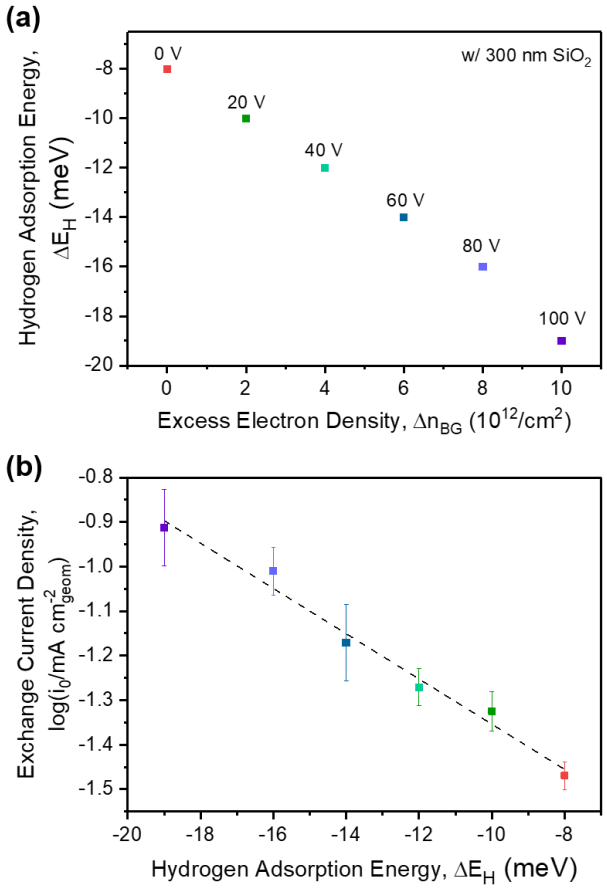

Figure 5.5: (a) Hydrogen adsorption energies (ΔE_H) as function of induced excess electron density (Δn_{BG}) for values ranging from 0 to 10^{13} cm^{-2} (b) Experimentally determined exchange current densities i_0 for hydrogen evolution on back-gated monolayer MoS_2 versus calculated ΔE_H.

To our knowledge this is the first report of field-effect modulation to change the intrinsic activity of electrocatalytic sites on ultrathin, back-gated electrodes. To be

clear, by "field-effect modulation" we mean the back-gating method we have employed here, not the normal double-layer charging that occurs in conventional electrochemical experiments. It is important to note that the back gate provides a degree of freedom that is not generally available in conventional electrocatalysis experiments. In a conventional electrocatalysis experiment, double-layer charging of active sites surely occurs but there is no ability to reversibly change the degree of charging independent of the electrochemical potential. With the back gate on sufficiently thin electrocatalyst layers, the amount of charge in the active sites is independently controlled and the impact on the overpotential can then be assessed directly and immediately, as demonstrated here.

There are other reports of electronic modification of gas-phase heterogeneous catalysts that have intriguing analogies to our experiments.[327,328] An example is the use of voltage-controlled Schottky junctions to manipulate electronic occupation in thin catalytic layers grown on doped semiconductors.[328] However, the use of an intervening dielectric in the platform we describe here can dramatically boost accumulated charge concentrations and provides flexibility in 2D electrode design as the alignment of the electrode band edges with the substrate is not a primary consideration.

5.4. Conclusion

The back-gated platform described here offers ample opportunities for further investigations of electrocatalysis at 2D electrodes for several reasons. First, the advent of ALD and 2D materials synthesis provides a rich palette of ultra-thin materials that can be coupled to gate/dielectric stacks and implemented as back-gated working electrodes. Second, the continuous, reversible electrostatic doping that is achieved in this platform can be a powerful complement to chemical (*e.g.*, heteroatom) doping strategies for optimizing 2D electrocatalysts. It will be interesting to understand in what ways electrostatic doping and chemical doping are similar or dissimilar. Third, as noted above, the independent control of electrode charging afforded by the back gate portends important opportunities to understand the differences in active site promotion by field-effect versus double-layer charging.

We note that the electrode architecture we have presented here is not fully optimized. For example, switching to high dielectric constant insulators, such as HfO_2, offers the possibility of simultaneously decreasing the required gate voltages and increasing the

gate-induced carrier densities up to 10^{14} cm^{-2}. Preliminary computational results suggest a nearly 10-fold stronger hydrogen binding ($\Delta E_H = -146\, meV$) at such induced carrier densities, which should further enhance the utility of this platform for understanding HER (and other reactions) at ultrathin electrodes.

5.5. Materials and Methods

Sulfuric acid (H_2SO_4, 95-98%, ACS grade), was purchased form BDH ARISTAR. Water used to prepare aqueous solutions was purchased from Fisher Chemical. P-type highly boron doped silicon wafers with thermally grown 300-nm-thick SiO_2 (SiO_2/*p*-Si), used in both chemical vapor deposition (CVD) and device fabrication, were purchased from Silicon Valley Microelectronics. Molybdenum oxide (MoO_3, 99.97%), sulfur powder (99.98%), molybdenum sulfide powder (particle size < 2μm, 99%), ammonium persulfate ($(NH_4)_2S_2O_8$, 98%, reagent grade), and poly(methyl methacrylate) (PMMA, molecular weight: 350 kDa) were purchased from Sigma-Aldrich. Polydimethylsiloxane (PDMS) precursor and its curing agent (Sylgard 184 silicone elastomer kit) were purchased from Dow Corning. Ag/AgCl reference electrodes (CHI111P) were purchased from Fisher Scientific. Graphite rods (99.95%) with a diameter of 1.0 mm used as counter electrodes were purchased from Sigma-Aldrich. CVD monolayer graphene grown on Cu foil was purchased from Graphene Square Inc. (Seoul, South Korea).

Synthesis of Monolayer MoS_2

Monolayer MoS_2 was synthesized by CVD using MoO_3 and sulfur as precursors in a horizontal hot-wall reactor system (PlanarTECH, Planar GROW-5S). In a typical CVD growth, an alumina boat (50 mm×12 mm×10 mm) containing 0.5 mg MoO_3 powder was placed at the center of the hot-wall furnace. Another alumina boat of same size, holding 200 mg sulfur powder, was placed upstream of the furnace, 25 cm away from the furnace center. A receiving substrate (SiO_2/*p*-Si, 30×30 mm^2) was mounted face-down on the MoO_3-containing boat. At room temperature, the quartz tube was first pumped down to vacuum and then purged by flowing Ar gas at a flow rate of 500 sccm for about 10 min until the pressure reached 760 torr again. After purging, the furnace temperature was ramped to 850 ˚C in 30 min and was kept at 850 ˚C for 15 min, while the flow rate of Ar gas was held at 67.5 sccm. At 850 ˚C furnace temperature, the temperature of sulfur precursor was measured to be approximately 300 ˚C. After

growth, the furnace was first naturally cooled to 650 ˚C and then was moved to the downstream side to cool the receiving substrate rapidly to room temperature.

Device Fabrication

The fabrication process was described in detail in our prior work.[300,301] Briefly, the as-grown MoS_2 was spin-coated with PMMA and the resulting PMMA film holding MoS_2 flakes was separated from the growth substrate by etching the interfacial SiO_2 layer with KOH solution (aqueous, 30 wt%) and then transferred onto a SiO_2/*p*-Si substrate that is used as the dielectric/back gate stack. After removing PMMA with acetone, the MoS_2 flake with a desirable size and minimal cracks was patterned into a rectangular stripe by selective O_2 plasma etching following photolithography. Another step of photolithography was carried out before e-beam evaporation of Ti/Au (3 nm/ 30 nm) metal contacts on MoS_2. To prevent electrochemical reactions from occurring on the surface of Au, a layer of 30 nm thick SiO_2 was e-beam evaporated on top of the peripheral metal area of MoS_2, with the help of a shadow mask. After lift-off, the fabricated MoS_2 working electrode was ready to assemble with a molded PDMS microfluidic flow cell. Similarly, graphene electrodes were prepared through these steps described above, except the etchant solution used to separate the PMMA film holding graphene from Cu foil in the transfer step was 100 g/L ammonium persulfate aqueous solution. Pt electrodes were prepared via photolithography and e-beam evaporation of Ti/Pt (3 nm/ 50 nm) on SiO_2/*p*-Si wafers.

The master mold for PDMS microfluidic channels (200-μm wide, 50-μm tall) was fabricated on a 4-inch Si wafer with a negative photoresist, SU8 2050 (MicroChem), via photolithography.[301] PDMS precursor mixed with its curing agent (10:1 by weight) was poured onto the master mold and cured at 70 ˚C in an oven for 3 to 4 h. The cured PDMS was cut into separate blocks where the inlet and outlet holes were made with 1- and 3-mm diameter punch tools, respectively. A molded PDMS flow cell was bonded onto a back-gated MoS_2 electrode substrate through a condensation reaction with SiO_2 at 120 ˚C, following O_2 plasma treatment of the bonding surfaces[301] (note that MoS_2 was covered by a shadow mask in this O_2 plasma treatment).

Characterization

Raman and photoluminescence spectra were obtained with a 532 nm laser using a confocal Raman spectrometer (Witec Aphas300R). Atomic force microscopy (AFM) images were collected in the contact mode on a scanning probe microscope (Bruker Nanoscope V Multimode 8). X-ray photoelectron spectroscopy (XPS) measurements were carried out in ultra-high vacuum (10^{-7} pascal) with an Al Kα X-ray monochromatic source (1486.6 eV) on a PHI VersaProbe III scanning XPS Microprobe.

Electrical and Electrochemical Measurements

The electrical and electrochemical configuration used in experiments is shown in Figure 5.1b. To obtain MoS_2 sheet conductance as a function of back-gate bias V_{BG} without electrolyte, Keithley 2400 and 2611 source meters were used to apply V_{BG} and source-to-drain bias V_{SD}, respectively, while measuring currents. To perform electrochemical experiments while testing sheet conductance of MoS_2, an Ag/AgCl reference electrode and a graphite rod counter electrode were introduced to the setup. The Ag/AgCl (filled with 1 M KCl) reference electrode was plugged into a Luggin capillary (filled with 0.5 M H_2SO_4) whose tip was placed at the outlet of the flow cell. The graphite counter electrode was inserted 3 to 5 mm away from the outlet. The MoS_2 working electrode was aligned in the microfluidic channel and placed ~100 μm away from the outlet, as shown in Figure 5.1b. During the sweep of working electrode potential, the source metal contact on the MoS_2 working electrode was grounded while a 5 mV bias was applied at the drain metal contact. The reaction current was obtained by adding up the currents measured at both source and drain contacts (detailed explanation can be found in our prior reports[299,301]). We used four source meters (Keithley 2400, 2611, 2612 and 236) to apply potentials and measure currents and data were collected with an in-house LabView program. The working electrode potential V_W was iR corrected to account for ohmic losses in the electrolyte using the same method as reported before,[301] where a value of 211 mS/cm found in the literature[329] was used as the bulk conductivity of 0.5 M H_2SO_4. All the electrical and electrochemical measurements were conducted in ambient environment at room temperature.

Computational

Spin polarized density functional theory (DFT) calculations reported herein were carried out using plane wave DFT code implemented in Vienna Ab-initio Simulation Package (VASP).[5-8] All of the calculations presented herein were carried using nonlocal gradient calculations using the RPBE functional within the Generalized Gradient Approximation (GGA) to determine the exchange and correlation gradient corrections. [9] PAW pseudopotentials were used to describe the core electrons and their interaction with the valence electrons.[10,11] An optimized lattice constant of a = 3.19 Å was computed for the 2H phase of bulk MoS_2 which is in agreement with the experimentally determined value of a = 3.16 Å.[12] A 3x3 supercell of monolayer MoS_2 was then constructed by cleaving along the (001) plane of the 2H-MoS_2 crystal. A vacuum space of 20 Å was employed for the calculations to minimize interaction between periodic layers. This monolayer MoS_2 surface with a surface area of 79.31 $Å^2$ was then used as the model for our calculations. An energy cutoff of 1000 eV was used to construct the plane waves for the DFT calculations. The structural optimizations were carried out until the maximum force on each of the ions was less than 0.05 eV/Å. A tolerance of 10^{-6} eV was specified for the convergence of the SCF cycle. A 3x3x1 gamma-centered k-point grid was used for structural optimizations, while a 6x6x1 k-point grid was used for energy calculations. The band structure was calculated along the high symmetry k-point path of Γ-M-K-Γ for MoS_2 with 25 intersections between each of the k-points. The S vacancy was created by removing a S atom from the pristine monolayer MoS_2 surface, thus generating a 5.55% S vacancy concentration which results in the formation of the mid-gap states shown in Figure S5.10 which is consistent with the states previously reported for vacancies in the monolayer surfaces of MoS_2.[13] These mid gap states consist mainly of Mo d-states (Figure S5.11).

Hydrogen adsorption studies examined the binding of atomic H to the S vacancy on the MoS_2 surface as shown in Figure S5.12. Previous reports suggest that these S vacancies serve as the active sites for HER on MoS_2.[13] To examine the effect of gate bias, the system was charged with excess electrons depending on the excess charge carrier density determined experimentally corresponding to the applied bias, summarized in Table S5.1. The hydrogen adsorption energy (ΔE_H) was calculated as a function of charge using the following equation:

$$\Delta E_H = E(MoS_2\text{-}H)\ (q) - E(MoS_2)\ (q) - 0.5E(H_2)\ (q=0) \quad (5.1)$$

where $E(MoS_2\text{-}H)\ (q)$ is the energy of the model MoS_2 surface used with the H adsorbed on the S vacancy site at charge q, $E(MoS_2)\ (q)$ is the energy of the model MoS_2 used without adsorbed H at charge q and $E(H_2)$ is the energy of the hydrogen molecule.

5.6. Acknowledgements

The authors would like to thank the National Science Foundation CCI program (award 1740656) for the funding support and the Minnesota Supercomputing Institute (MSI) at the U. of Minnesota for use of computing resources.

5.7. Supporting Information

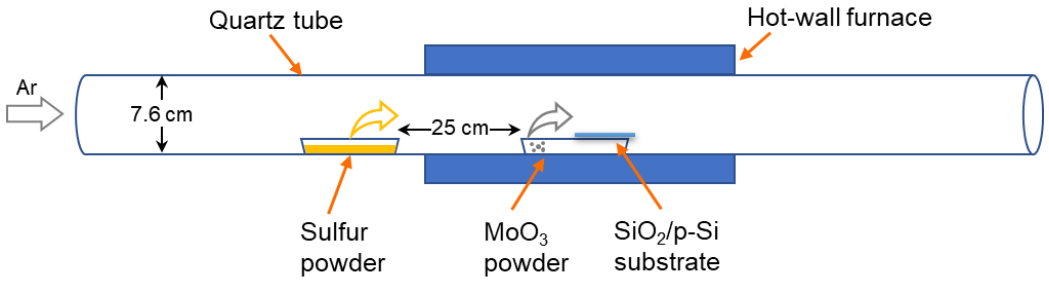

Figure S5.1: Schematic illustration of the CVD setup used in this study

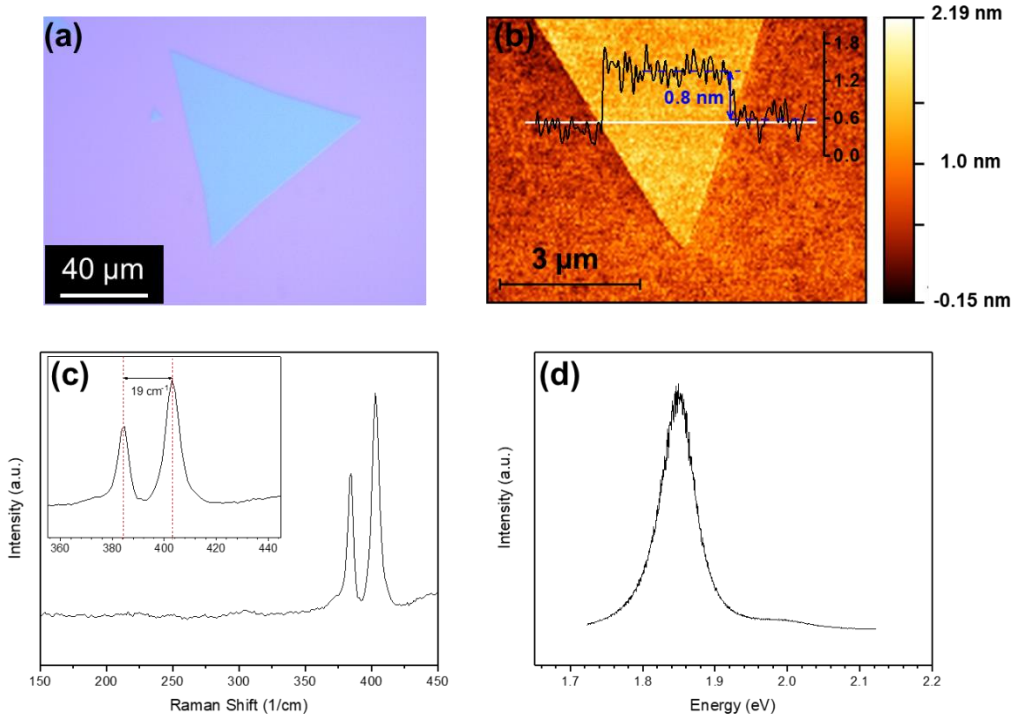

Figure S5.2: (a) Optical image of CVD grown MoS_2 supported on SiO_2/*p*-Si substrate; (b) AFM image obtained at the edge of a MoS_2 flake; The inset of (b) shows the height profile measured along the white line; (c) Raman and (d) photoluminescence spectra collected on the large MoS_2 flake in (a).

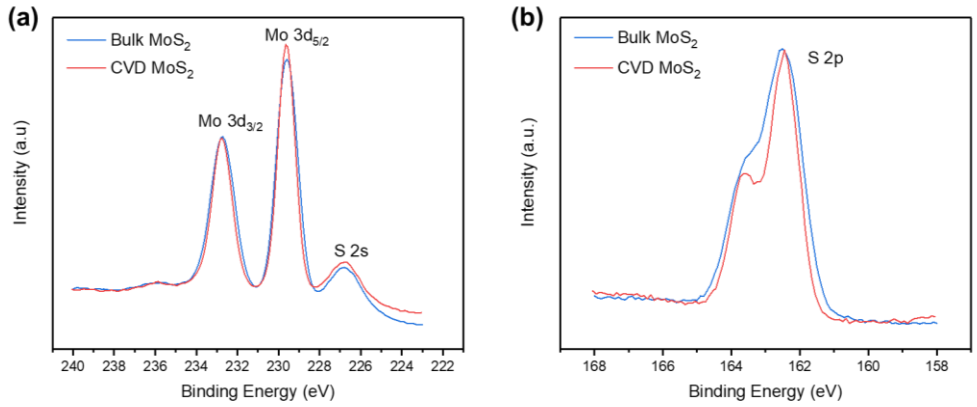

Figure S5.3: High-resolution X-ray photoelectron spectra of CVD monolayer MoS_2 flakes and bulk MoS_2 powder: (a) Mo 3d states and (b) S 2p states. The high-resolution Mo 3d and S 2p peaks shown in (a) and (b) were used to calculate the S/Mo ratios. The S vacancy concentration of CVD monolayer MoS_2 samples was estimated to be 7 ± 2% by comparing the S/Mo atomic ratio of CVD monolayer MoS_2 to that of bulk MoS_2 powder.

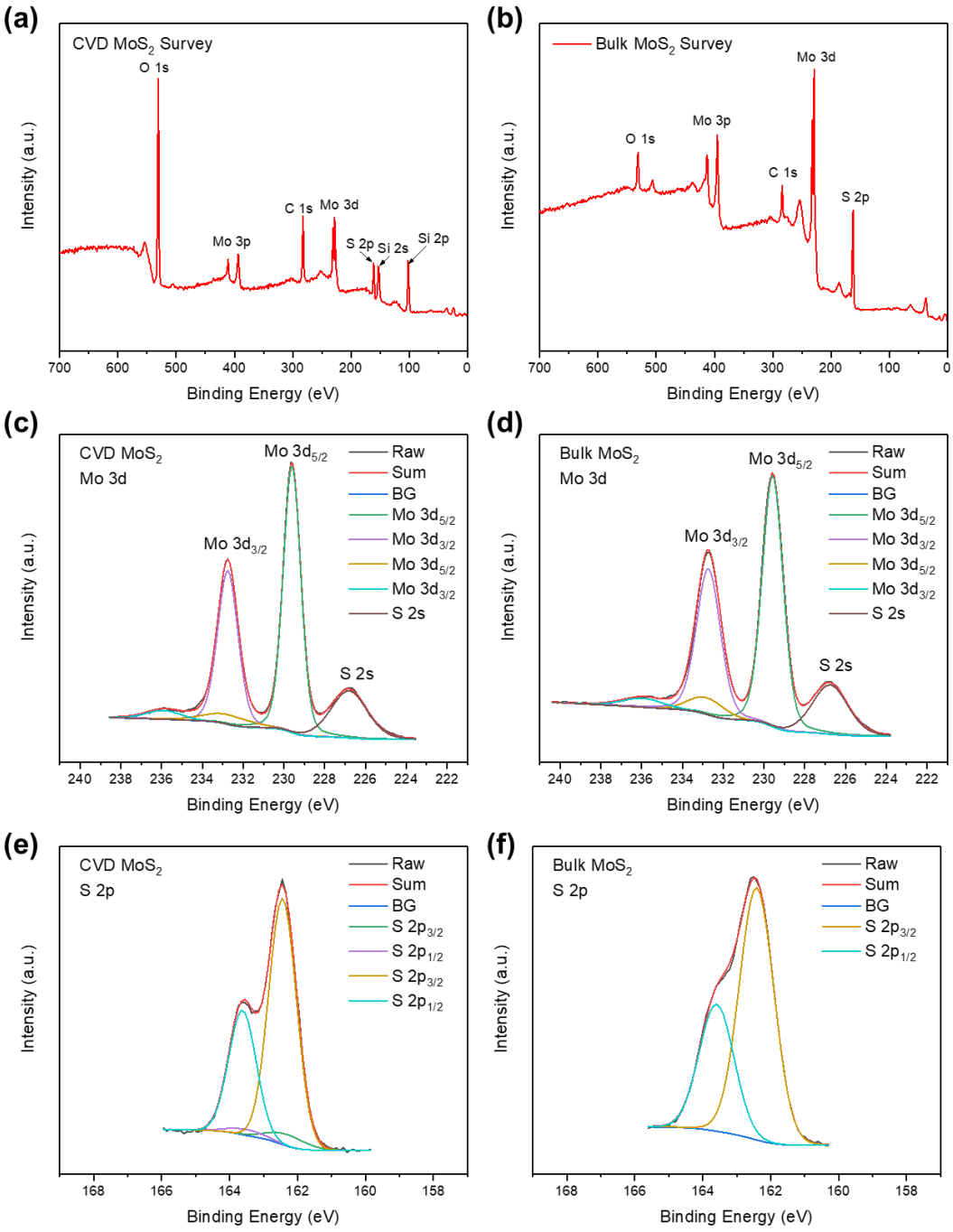

Figure S5.4: (a) and (b) X-ray photoelectron spectroscopy (XPS) survey spectra taken from 0 to 700 eV; (c) and (d) Mo 3d raw XPS spectra and fitted curves; (e) and (f) S 2p raw XPS spectra and fitted curves. (a), (c) and (e) are for CVD monolayer MoS_2 samples on SiO_2/Si. (b), (d) and (f) are for bulk MoS_2 powder on conductive aluminium foil tape.

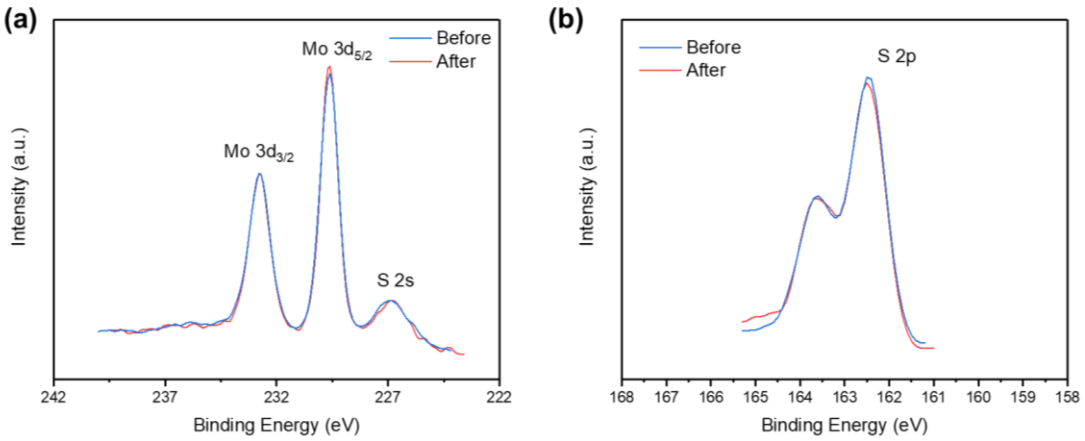

Figure S5.5: High-resolution x-ray photoelectron spectra of MoS_2 electrode before and after potential cycling in 0.5 M H_2SO_4: (a) Mo 3d states and (b)) S 2p states. The electrode was cycled 12 times between 0 and -0.6 V vs RHE at 50 mV/s, and there was a ~ 1 min time interval between two cycles. The S vacancy concentration was estimated to be 7% both before and after the electrolysis.

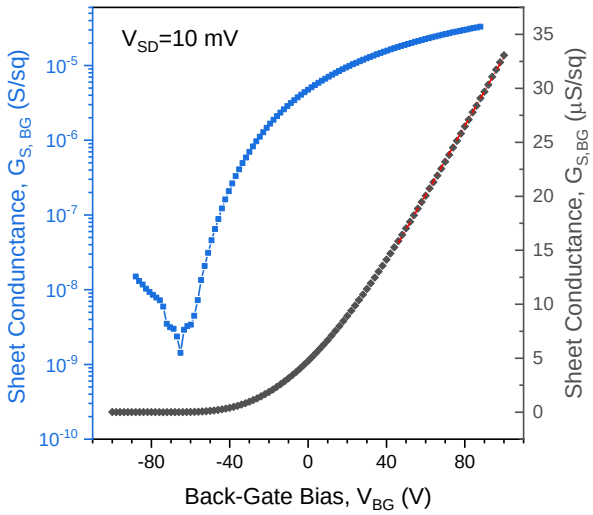

Figure S5.6: Sheet conductance, G_S, of a representative MoS_2 electrode (50×50 um^2) measured by applying a constant source-to-drain bias, $V_{SD} = 10\ mV$, while sweeping back-gate bias V_{BG} from -100 to +100 V at a sweep rate of 2V/s. The blue and gray plots are shown in semilog and linear scale, respectively. The sheet conductance was obtained without any electrolyte or encapsulation layer on top of MoS_2. The field effect electron mobility μ was calculated using the following equation: $\mu = \frac{dG_S}{dV_{BG}} \cdot \frac{1}{C_{BG}}$, where C_{BG} is the specific capacitance (capacitance per unit area) of 300-nm-thick SiO_2 dielectric layer, which was estimated to be 15 nF/cm^2 via displacement measurements (see Figure S5.9). The slope of the red dashed line shown here was used as $\frac{dG_S}{dV_{BG}}$ to calculate μ.

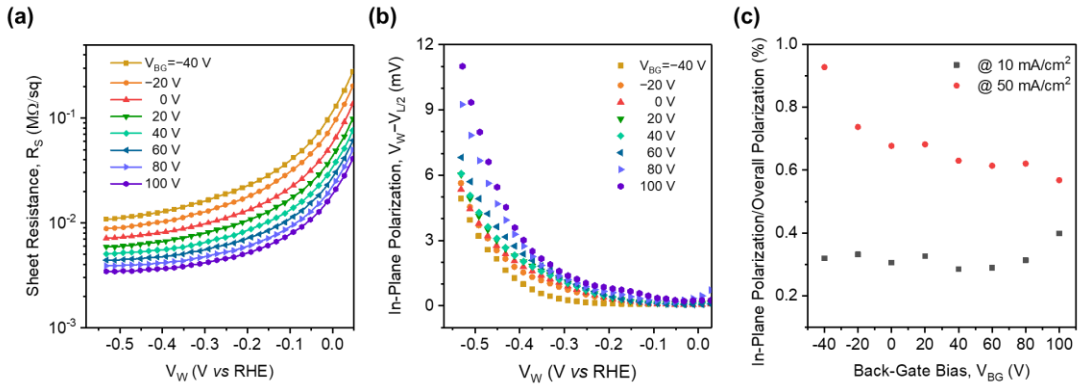

Figure S5.7: (a) Sheet resistance, R_S, of a back-gated MoS_2 electrode (50×50 μm^2) simultaneously obtained during sweep of working electrode potential V_W in 0.5 M H_2SO_4 at different back gate biases V_{BG} (Note that a source-to-drain bias $V_{SD} = 5\ mV$ was applied to measure R_S); (b) corresponding in-plane polarization calculated (The method used to calculate in-plane polarization was described in detail in our previous report.[299]); (c) percentage of in-plane polarization to overall polarization at current density $i_w = 10\ and\ 50\ mA/cm^2$ as a function of applied back-gate bias V_{BG}.

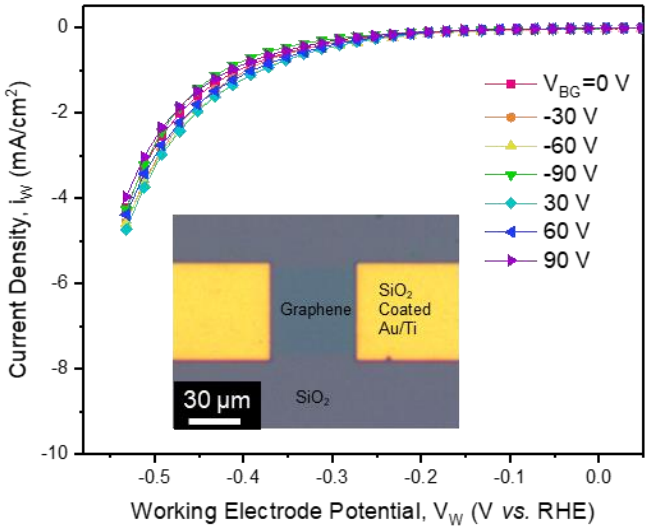

Figure S5.8: Polarization curves obtained in flowing 0.5 M H_2SO_4 on a back-gated graphene electrode (50×50 μm^2) at varying back-gate biases V_{BG}. The inset optical microscopy image shows a plan view of a back-gated graphene electrode. The scan rate of the working electrode potential is 50 mV/s and the volumetric flow of the electrolyte is 10 μL/min.

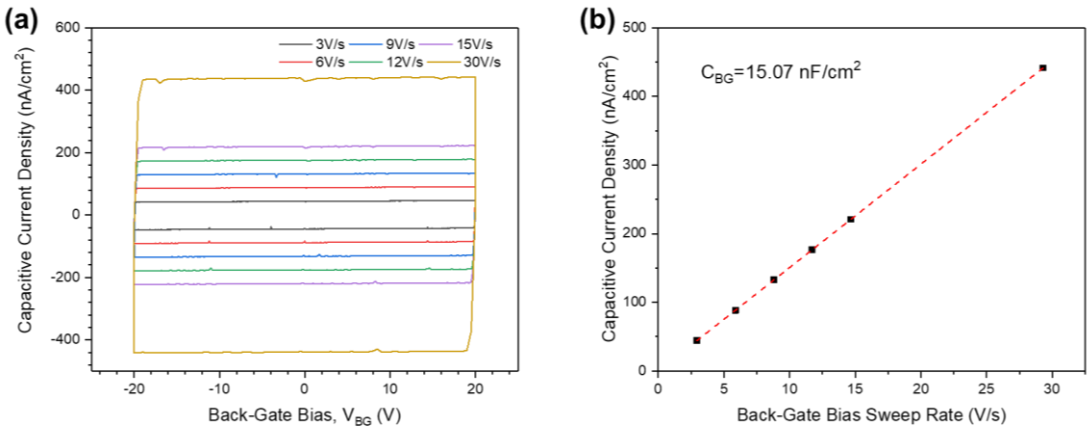

Figure S5.9: (a) Capacitive current density measured by sweeping back-gate bias V_{BG} applied on an Au/SiO_2/*p*-Si structure at different V_{BG} sweep rates; (b) Averaged capacitive current density as a function of V_{BG} scan rates in (a). A 9 mm^2 gold electrode was used in this measurement and it was prepared in a similar procedure as described in S3 via photolithography and e-beam evaporation of Ti/Au (3 nm/30 nm thick).

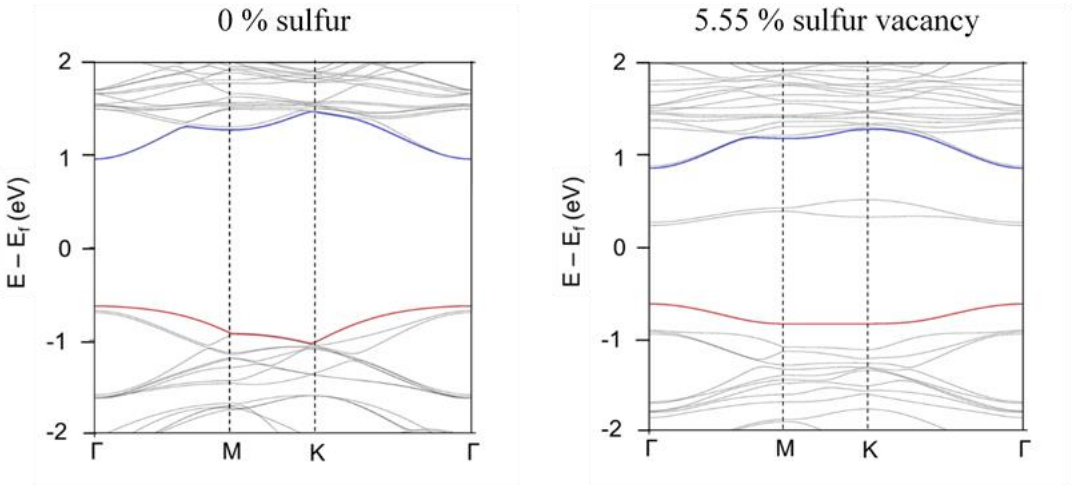

Figure S5.10: Band structures of pristine MoS_2 with 0% S vacancy and MoS_2 with 5.55 % S vacancy showing introduction of mid-gap states at zero system charge.

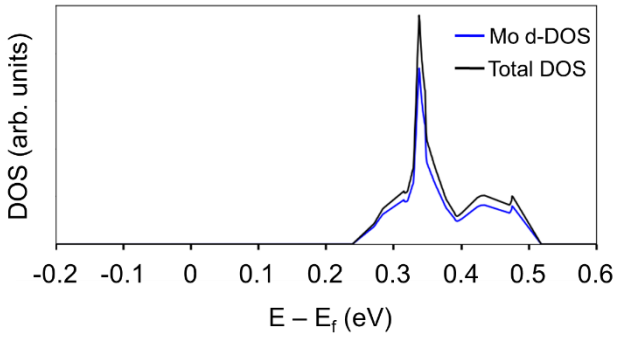

Figure S5.11. Projected Mo d-density of states and total density of states of MoS_2 surface with 5.55% S vacancy at zero charge.

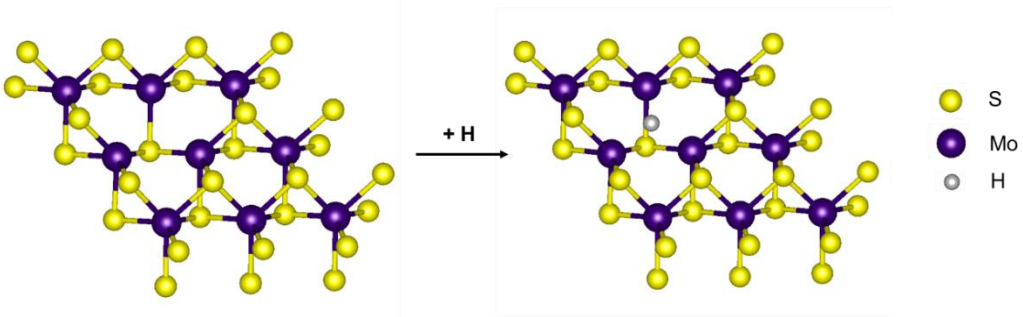

Figure S5.12. Hydrogen adsorption on S vacancy site.

Table S5.1. Number of excess electrons used to charge the system corresponding to the different voltage bias and excess charge carrier density

Back-gate voltage (V_{BG})	Excess charge carrier density (e^-/cm^2)	Excess electrons added to the model system (e^-)
0	0	0
20	$2x10^{12}$	0.016
40	$4x10^{12}$	0.032
60	$6x10^{12}$	0.048
80	$8x10^{12}$	0.064
100	10^{13}	0.08

Chapter 6 - Synthetic applications and mechanistic aspects of the Li-ion battery inspired organic electroreduction

Reproduced in part from Peters, B. K., Rodriguez, K. X., Reisberg, S. H., Beil, S. B., Hickey, D. P., Kawamata, Y., Collins, M., Starr, J., Chen, L., Udyavara, S., Klunder, K., Gorey, T. J., Anderson, S.L., Neurock, M., Minteer, S. D., and Baran, P. S. Scalable and safe synthetic organic electroreduction inspired by Li-ion battery chemistry, Science **2019**, 363, 838-845. Reprinted with permission from AAAS.

Theoretical calculations were done by SU under the guidance of MN

6.1. Synopsis

Reductive electrosynthesis has faced long-standing challenges in applications to complex organic substrates at scale. Here, we show how decades of research in lithium-ion battery materials, electrolytes, and additives can serve as an inspiration for achieving practically scalable reductive electrosynthetic conditions for the Birch reduction. Specifically, we demonstrate that using a sacrificial anode material (magnesium or aluminum), combined with a cheap, nontoxic, and water-soluble proton source (dimethylurea), and an overcharge protectant inspired by battery technology (tris(pyrrolidino)phosphoramide) can allow for multigram-scale synthesis of pharmaceutically relevant building blocks. We show how these conditions have a very high level of functional-group tolerance relative to classical electrochemical and chemical dissolving-metal reductions including McMurry couplings, reductive ketone deoxygenations, and epoxide openings. Detailed electroanalytical and computational analyses show the electrochemical Birch reduction to operate via a different mechanism compared to the traditional chemical Birch reduction reaction wherein the electron and proton transfer events occur near the electrode surface rather than in the solution phase via Li^0 to affect these reductive transformations. These mechanistic insights are then further used to examine the role of the metal (zinc cathode), electrolyte (lithium bromide), solvent (tetrahydrofuran), proton source (dimethyl urea), and additive (tris(pyrrolidino)phosphoramide) used in the reaction to probe the nature of their influence in directing changes that lead to the observed increased product yields for wide range of tested substrates.

6.2. Introduction

The use of alkali metals as reagents for strongly reductive chemistry has found limited use in the modern era due to safety considerations and immense difficulty in industrial scale-up. The Birch reduction, a flagship example, is one of the first reactions taught in undergraduate organic chemistry lectures for the rapid access it affords to sp^3 complexity from simple feedstock arenes.[330–333] Yet typical procedures call for the hazardous condensation of ammonia, or other volatile amines, as solvent, combined with pyrophoric metals at cryogenic temperatures. Milder alternatives have been reported that rely on finely-dispersed silica-impregnated Na (SiGNa-S1) and Na/K[334–336] or various mineral oil dispersions combined with superstoichiometric amounts of an expensive/toxic crown ether additive.[337] However, these reagents either fail to access the same reactivity space as, for example, Li/NH_3, or still require extreme caution in reaction setup on account of the alkali metal. Perhaps the most compelling modern Birch application stems from Pfizer's kilogram-scale synthesis of the anti-Parkinson's drug candidate sumanirole (**2**) (Figure 6.1a).[338] The tandem aziridine opening and debenzylation of the direct precursor **1** is a noteworthy achievement in process chemistry and engineering; it required the use of custom equipment to administer lithium metal, as well as enough ammonia to fill three Boeing 747 airliners in the gas phase. At the end of the reaction, which was conducted at cryogenic temperature (–35°C), 2300 liters of H_2 were liberated—an understandably intimidating occurrence.

In this context, electrochemical reduction is an appealing alternative. Indeed, several groups have explored the idea of electrochemical surrogates for alkali metal reductions (Figure 6.1b and Figure 6.1c)[63,339,340] with a key report by Kashimura demonstrating proof-of-concept for electrochemically-driven Birch reactivity.[341] Nonetheless, electrochemical reductions have been hindered by a myriad of unwanted side-reactions that typically overpower the desired reactivity, including competing proton reduction, electrode passivation from excessive electrolysis of solvent, and diminished yields caused by adventitious O_2. Perhaps most telling, to synthesize sumanirole (**2**) on process scale, Pfizer utilized chemical Birch over any then-known electrochemical alternatives. For Pfizer, a kilogram-scale chemical Birch reduction was more practical to scale than any electrochemical method, despite the enormous engineering challenges associated with the former. Corroborating these limitations, in our hands, attempts to

reduce **1** using a variety of the known electrochemical conditions were completely fruitless (See Supplementary Information).

Concurrent with these initial forays into electrochemical reduction, the quest to achieve a cyclable, safe, and high energy density Li-ion battery has faced similar challenges, culminating in a better understanding of the role that additives, solvent, and electrolyte play in the formation of a solid electrolyte interphase (SEI).[342,343] Importantly, the SEI prevents buildup of an excessive passivating layer at the electrode while enabling a more active and stable electrode interface under extreme potentials (Figure 6.1d).[344,345] Application of these concepts to Li-ion battery technology is largely responsible for their widespread use in virtually all modern electronics, including smart phones, laptops, and electric vehicles. Inspired by this transformative technology, we sought to optimize electroorganic synthesis using the approaches originally developed for Li-ion batteries.[346] We show herein that such strongly reducing conditions can thereby be accessed in a simple and safe way, at ambient temperature without rigorous exclusion of air or moisture and can be applied to the most popular reaction classes in this arena such as Birch, debenzylation, epoxide/aziridine opening, and McMurry couplings.

Electrochemistry represents a convenient way to precisely select redox potentials for use in organic synthesis. However, cathodic reductions[347–349] have received considerably less use in modern preparative synthesis. This lower utility is mainly due to the significant engineering challenges in high throughput screenings and scale-up contexts, and the low chemoselectivity under highly reductive conditions which is needed for Birch reductions. Most common electrolytes typically disintegrate on approach of strongly reductive conditions (including those required to access Li^0).[350,351] Thus, while accessing this extreme reactivity using cathodic reduction is not a new idea, accessing it in a way that is both practical and scalable is a goal that has not been achieved. Birch himself reported the first electrochemically-mediated arene reduction of toluene (with $NaOEt/NH_3$).[62] Additional reports following up on that pioneering study have appeared, including the key report by Kashimura (*vide supra* and Figure 6.1c). However, all of them exhibit narrow scopes — Kashimura's method is limited to hydrocarbons — and they require procedures (e.g., continuous sonication) that are no more scalable than a purely chemical Birch.[63,339,341,352–365]

6.3. Results and Discussion

6.3.1. Li-ion battery interphase design applied to electroreduction and applications

Accordingly, the current study began with an extensive evaluation of this prior art (partial results in Figure 6.1e; for a complete listing, see Supplementary Information), of which select efforts are summarized in entries 1–4.[63,339,341,353,354,361,366]

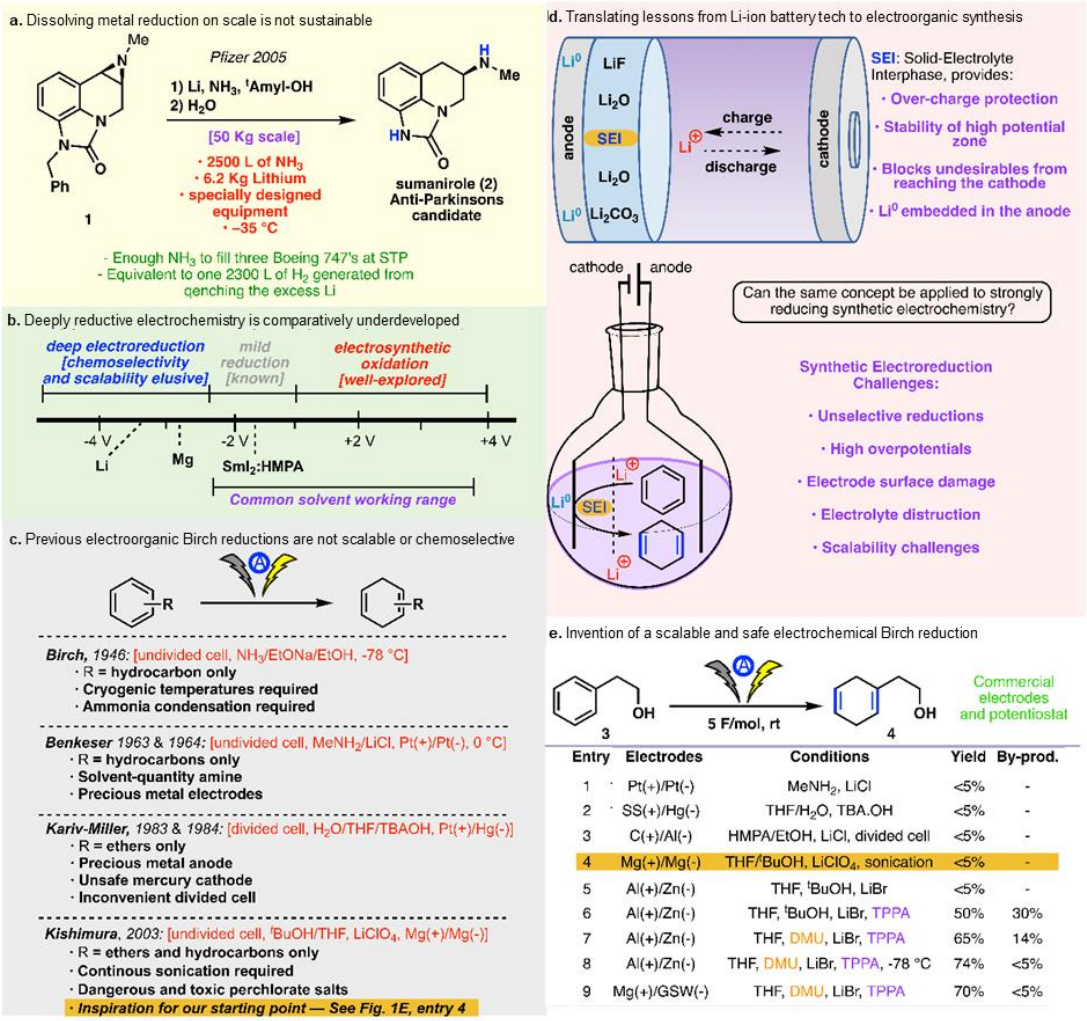

Figure 6.1: Background and reaction development. **a)** Dissolving metal reduction on scale is not sustainable, **b)** Voltage range challenges for reductive electrochemistry, **c)** Electrochemical Birch precedence, **d)** Applying Li-ion battery technology to synthetic electrochemistry, **e)** Optimization of a simple electrochemical alternative to Birch reduction; GSW = Galvanized Steel Wire.

To help probe the functional-group tolerance of these prior works, we opted for phenyl-ethanol (**3**) as a model substrate. The conditions reported by Kashimura[341] were chosen

as a baseline from which to launch more extensive optimization (entry 4); however, the limitations of that state-of-the-art method were clearly demonstrated in that **3**'s alcohol moiety completely shut down reactivity in Kashimura's conditions. Through optimization of the reaction system by changing the electrolyte to LiBr, proton source to 1,3-dimethyl urea (DMU), the anode to magnesium (Mg), cathode to galvanized steel wire (GSW) so as to increase the current density on the cathode and adding in the additive TPPA, we were able to achieve yields as high as 70 % (entry 9) for reduction of the arene **3** to its diene product **4**. (See Supplementary Information for further details on the step-by-step optimization of the system).

The above optimized reaction conditions exhibited a broad scope across a range of different arenes such as polyarenes, aryl ethers, silyl ether, alcohol and ketone-containing arenes, benzoic acids, heterocyclic arenes, and complex natural products. Further, wide range of other reductive transformations including the ring opening/closing, protecting group removal, transition metal mediated reactions could also be carried using the dissolving metal reduction conditions. Finally, the scalability of the protocol was also demonstrated in both batch and flow conditions on *tert*-butyldimethyl silyl *o*-methyl phenyl ether (Compound **12** in SI**)** without any losses in efficiency (see Supplementary Information for further details regarding the substrate scope and its scalability).

6.3.2. Mechanistic investigation

With an optimized set of conditions in hand, we then proceeded to examine the mechanism and kinetics of the reaction. Further, the role that each of the sub-components in the reaction mixture play towards optimization of the yields across a wide variety of tested substrates are also discussed. The understanding of the mechanistic nuances and the role of the sub-components used herein for electrochemical Birch reduction could help aid in the identification of electrolyte/solvent/additive systems to design other similar reductive chemistries for applications ranging from organic synthesis to batteries which also employ similar harsh reductive environments.

6.3.2.1. Isolation of the mechanism

The mechanism of electroreduction of arenes can proceed via two possible mechanisms as summarized in Figure 6.2. In the first mechanism, like the traditional Birch

reaction,[64,65,367] Li^0 which can be postulated to be formed via reduction of the electrolyte LiBr at the electrode surface acts as an electron transfer medium to reduce the arene to the corresponding diene in presence of a proton source. The reactions in this mechanism all occur in the solution phase away from the electrode surface. In the second mechanism, rather than Li^0 acting as an electron source, the electron and proton transfer processes both occur over the electrode surface wherein the substrate stays adsorbed over the electrode surface. In order to evaluate the mechanism of the reaction, we chose to start with using phenyl-ethanol (**3**) as our model substrate.

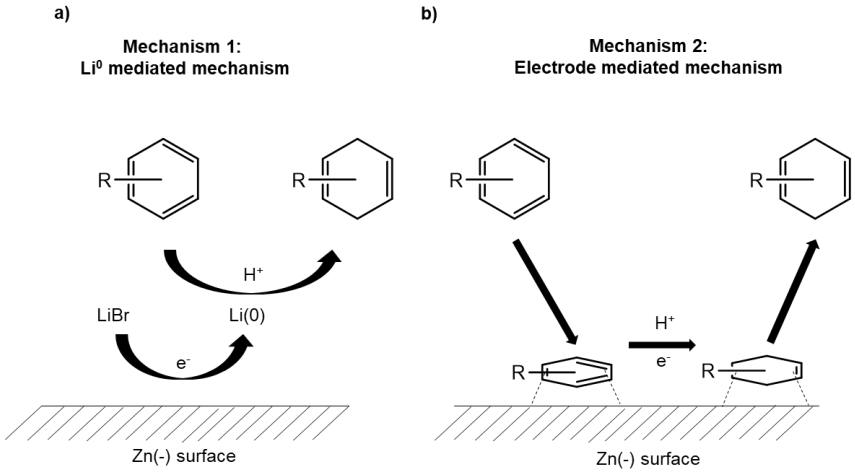

Figure 6.2: Schematic representation of the different possible mechanistic pathways for the electrochemical Birch reduction: a) Li^0 mediated mechanism b) Electrode mediated mechanism

To test first whether Li^0 catalyzes the reaction, a degassed reaction solution — with the substrate and DMU omitted — was electrolyzed as normal, under an inert atmosphere at -78 ^oC, to putatively accumulate electrochemically-generated Li^0 species. After electrolysis was completed (1.5 hours, 5 F/mol), the substrate was then added, and the reaction was stirred, with samples drawn at 30-minute intervals (Figure 6.3a). There was a small decrease in the substrate concentration over time, but no desired product or well-defined side products could be detected during this time. Similar trends held true for an analogous experiment run at room temperature (see Supplementary Information). Furthermore, on treating a pre-electrolyzed LiBr solution (at -78 ^oC) with a more reductively labile aldehyde, we did not observe any of the reduced alcohol or pinacol products (see Figure 6.3a and Supplementary Information). This data rules out the mechanistic possibility of solvated electrons as the active reductant. The apparent

disconnect between putative Li^0 generation, and lack of Birch reactivity, strongly suggested that a typical Li^0 species is not the active reductant in our reaction manifold. We hypothesized that instead, arene substrate was getting reduced directly on the electrode surface which are further confirmed by the computational studies detailed below.

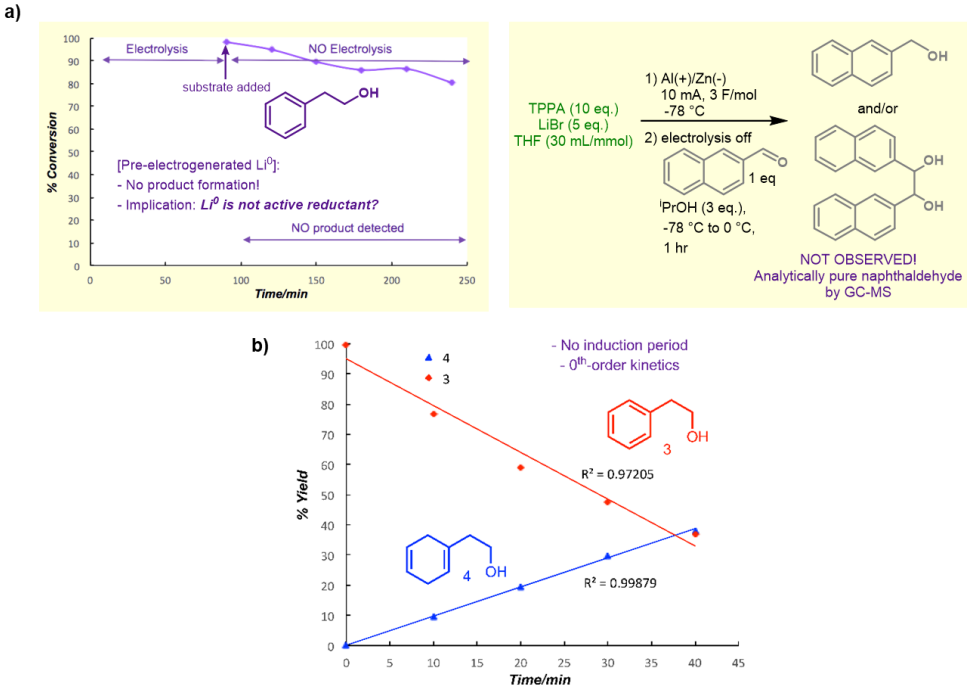

Figure 6.3: Mechanistic and kinetic analysis of the electroreduction of phenyl-ethanol (**3**). a) Kinetic profile for the relative concentration of arene (**3**) and diene (**4**) in a control experiment involving pre-electrolysis of LiBr solution and Li^0/solvated electrons detection experiment with naphthaldehyde. b) Plot of concentration of **4** generated per time under the standard reaction conditions, indicating zero order kinetics with respect to both the formation of **4** and consumption of **3**.

To further investigate the reaction kinetics, the reaction was monitored (*via* GC/MS analysis of quenched aliquots) under standard electrochemical conditions at five-minute intervals (Figure 6.3b). Essentially no induction period was observed, and no competitive processes were detected based on the absence of side-products. Furthermore, analysis suggests zero-order kinetics in substrate: Consumption of phenyl ethanol and formation of product were both well-fitted by linear regression (r^2 = 0.97 and 1.00, respectively). The slight deviation from linearity observed is likely due to the small dataset collected. Further, estimations of the KIE for the reaction using

deuterated urea as the proton source show a KIE value of 4.92, which suggest that the protonation step is likely the rate determining step of the reaction (see Supplementary Information for details regarding determination of the KIE).

In order to validate the mechanistic and kinetic study described above, we then performed a computational study of the different possible mechanisms proposed in Figure 6.2. First, ab initio calculations (see Supplementary Information for detailed methods) were undertaken to determine the kinetics of the solution-phase reduction of phenyl ethanol via Li^0 species (Figure 6.4). As shown in Figure 4, the single electron transfer step proceeds via a barrier of 27 kJ/mol and a reaction energy of 21 kJ/mol to form the phenyl-ethanol radical anion species (**3a**). Upon electron transfer, the subsequent protonation step in presence of DMU then proceeds with an intrinsic barrier of 39 kJ/mol to form the protonated phenyl-ethanol radical (**3b**), thus giving an overall apparent barrier of 60 kJ/mol. The next subsequent electron transfer and proton transfer steps to form the diene product (**4**) are exothermic in nature and proceed with lower barriers compared to the first electron and proton transfer steps. A parallel occurrence of a two electron reduction pathway via Li^0 was ruled out since the transfer of another electron to **3a** had a high intrinsic reaction energy of 104 kJ/mol (Figure 6.4). Hence, for the Li^0 mediated mechanism, the mechanism for the reduction of phenyl-ethanol likely proceeds via electron-proton-electron-proton (ECEC) transfer steps with the first protonation step as the rate determining step of the reaction with an overall apparent barrier of 60 kJ/mol.

To eliminate the possibility of hydrogen atom transfer (HAT) pathways contributed by the other components present in the reaction mixture such as the solvent THF, additive TPPA, and the methyl groups on the DMU, we also computed the barriers for the HAT reactions involving these components. The intrinsic free energy barriers for HAT transfer reactions via THF, TPPA, and DMU to the phenyl-ethanol radical anion (**3a**) were found out to be 112, 165, and 142 kJ/mol respectively (see Supplementary Information for the transition state structures), significantly higher than that determined for the protonation of **3a** via DMU (39 kJ/mol). These studies thus suggest that DMU most likely functions as the dominant source of hydrogen and the role of other HAT agents is minimal, thus ruling out the possibility of another parallel electron transfer-HAT (EC') mechanism.

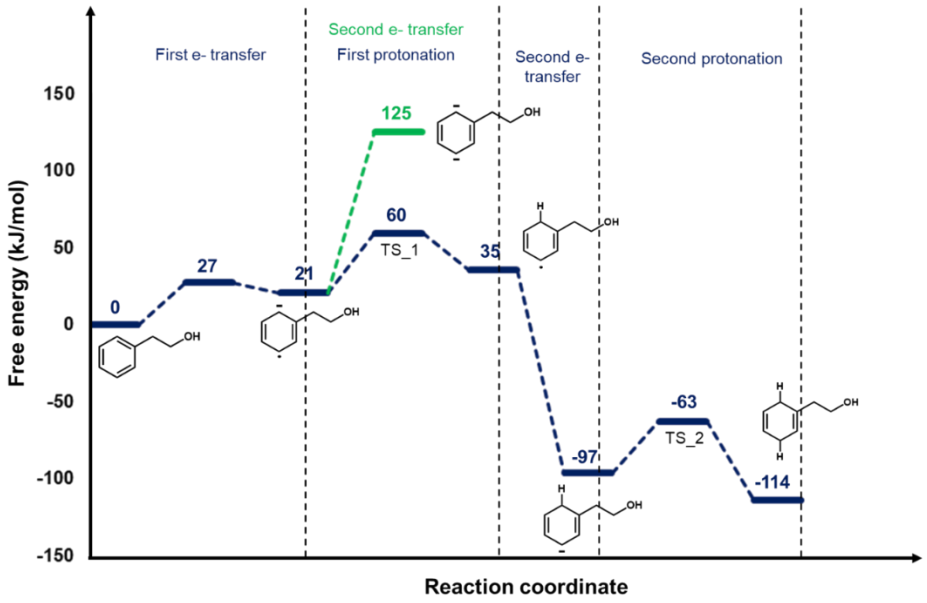

Figure 6.4: Free energy profile for the Li^0 mediated electrochemical Birch reduction of phenyl-ethanol (**3**). TS_1, Transition state for the first protonation step; TS_2, Transition state for the second protonation step.

The computational studies are further validated by experimental analysis which show only 5% deuterium incorporation in the diene product (**4**) for reduction of phenyl-ethanol (**3**) when deuterated d8-THF is used as the solvent. Since, the computed barriers suggest THF to be better at HAT chemistry than either pyrrolidine or DMU, it can be assumed that HAT by pyrrolidine and DMU is similarly negligible. Further, we tested the deuterium incorporation in the product (**4**) under standard conditions with 0.033 M TBS-PE and 2 eq. d4-urea and found the amount of deuterium incorporation to be only 37%. However, if the concentration of d4-urea and the substrate is doubled (0.066 M) the incorporation climbs to 65%, which suggests that the proton source used (DMU or urea) is the main source of hydrogen. The remaining unaccounted incorporation of hydrogen (~30%) can likely be attributed to the exogenous water that might be inadvertently present in the reaction mixture since both TPPA and LiBr are highly hygroscopic in nature. Computations of the free energy barriers for the proton transfer process with water show it to be barrierless which do suggest that water, if present, can act as a hydrogen donor, thus accounting for the unaccounted deuterium incorporation. However, since utmost precautions are taken to maintain dry conditions during the reaction (Wet conditions thwart the reaction), the incorporation of the water hydrogen can be assumed to be a minor side reaction and thus for the purposes of this study, DMU

herein is considered as the major source of hydrogen and all the relevant kinetics are thus determined with DMU as the hydrogen donor.

The electrode-mediated kinetics were next computed at different potentials to compare with the kinetics of the Li^0 mediated mechanism, results for which have been summarized in Figure 6.5 (See Supplementary Information for relevant structures and potential dependent energy curves). The electrode mediated pathway begins with the adsorption of phenyl-ethanol (**3**) to the cathode accompanied by an electron transfer event from the cathode, to generate adsorbed phenyl-ethanol intermediate (**PEA_{ads}**). This electron transfer event is validated via Bader charge analysis[138] which shows an accumulation of 0.58 e^- on the adsorbed intermediate in absence of any applied potential. Depending on the operating potential, the adsorbed intermediate (**PEA_{ads}**) can either undergo a single electron transfer to form **$3a_{ads}$** or a double electron transfer to form **$3a'_{ads}$**. The adsorption cum heterogeneous electron transfer were calculated to be barrierless across all the examined potentials. The protonation of **PEA_{ads}** then results in the formation of the adsorbed protonated intermediate **$PEAH_{ads}$**. The protonated intermediate likely stays in the form of the adsorbed anion, **$3c_{ads}$**. In case of a single electron transfer occurring during the initial adsorption-cum-electron transfer step to form **$3a_{ads}$**, **$3c_{ads}$** is likely formed via a second electron transfer step occurring post the protonation step. For reaction occurring via the **$3a'_{ads}$** intermediate, **$3c_{ads}$** is directly formed via the protonation of **$3a'_{ads}$**. Finally, the second protonation steps then gives the adsorbed diene product **$PEAH_{2ads}$** (**4^{ads}**) which is then followed by a facile desorption step to give the solution-phase product **4**. Since the electron transfer step which accompanies the adsorption step is found to be facile, the protonation step thus likely controls the rate of the reaction which are also confirmed by the KIE studies discussed before.

The identity of the protonation step controlling the rate of the reaction was however found to depend on the operating potentials. Comparison of the potential dependent free energies shown in Figure S6.12 suggest that the first protonation step controls the initial rate of the reaction and is unlikely to proceed until a potential of -2.1 V is reached. Thus, looking at the overall energetics of the reaction, starting at -2.1 V, from Figure 6.5, it can be seen that at higher potentials, the first protonation step has a higher barrier compared to the second protonation step. As the potential drops down further, the barrier for both the protonation steps drop down. At computed potentials < -2.3 V, the

barrier for the second protonation step becomes higher than the first protonation. Hence, at these lower potentials, the second protonation becomes the rate determining step of the reaction.

The plausible cause for this change in the rate determining step on moving from high to low potentials point towards the nature of the intermediate formed upon adsorption. For a single electron transfer step upon adsorption, an adsorbed anion radical intermediate (**3a$_{ads}$**) would be present on the surface, whereas for a sequential two electron transfer step upon adsorption, a dianionic intermediate would be present on the surface (**3a'$_{ads}$**). Computations of the solution phase barriers for the different reduced intermediates of phenyl-ethanol suggest that the first protonation step for protonation of the radical anionic intermediate (**3a**) (39 kJ/mol) has a higher barrier compared to the second protonation step (34 kJ/mol). On the other hand, the solution phase kinetics dictates first protonation step for protonation of the dianionic intermediate (**3a'**) to be barrierless. Thus, it seems plausible that as the potentials are lowered, the nature of the adsorbed intermediate changes from an anionic radical like character (**3a$_{ads}$**) to a dianionic like character (**3a$_{ads}$'**) due to which we see a shift in the rate determining step from the first protonation to the second protonation. Thus, while at higher potentials, the first protonation is rate determining, as you lower the potentials, the second proton transfer step starts becoming rate determining. At the typical highly reductive operating potentials, it can be reasoned that the reaction operates in the lower potential regime, wherein a two electron transfer step occurs upon adsorption to the surface with the second protonation as the rate determining step.

From Figure 6.4 and Figure 6.5, comparing the overall barriers for the Li^0 mediated mechanism (60 kJ/mol) with the electrode mediated pathway (16-43 kJ/mol depending on the potential), it can be seen that the barriers for the electrode mediated pathway are lower than that for the Li^0 mediated mechanism. Hence, it can be hypothesized that the mechanism likely proceeds via electrode mediated pathway, which is in agreement with the experimental studies reporting the ineffectiveness of the electro-generated Li^0 for product formation. Further, the derivation of the rate orders for the different proposed mechanisms suggest a first order dependence in substrate for the Li^0 mediated pathway ($r = k_{PT1}K_{ET1}[\mathbf{3}][Li_{sol}][DMU]$, k_{PT1} = rate constant for first protonation step, K_{ET1} = equilibrium constant for the first electron transfer step), and a zero order dependence on the substrate for the on-electrode mediated pathway operating in the low potential

regime ($r' = k_{PT2}[DMU]S_p$, k_{PT1} = rate constant for second protonation step, S_p = specific surface area of the electrode) (see Supplementary Information for details on rate order derivation). The rate order data coupled with the comparison of the reaction kinetics thus overall point to the prevalence of the on-electrode mechanism over the Li^0 mediated mechanism operating under the electrochemical reaction conditions.

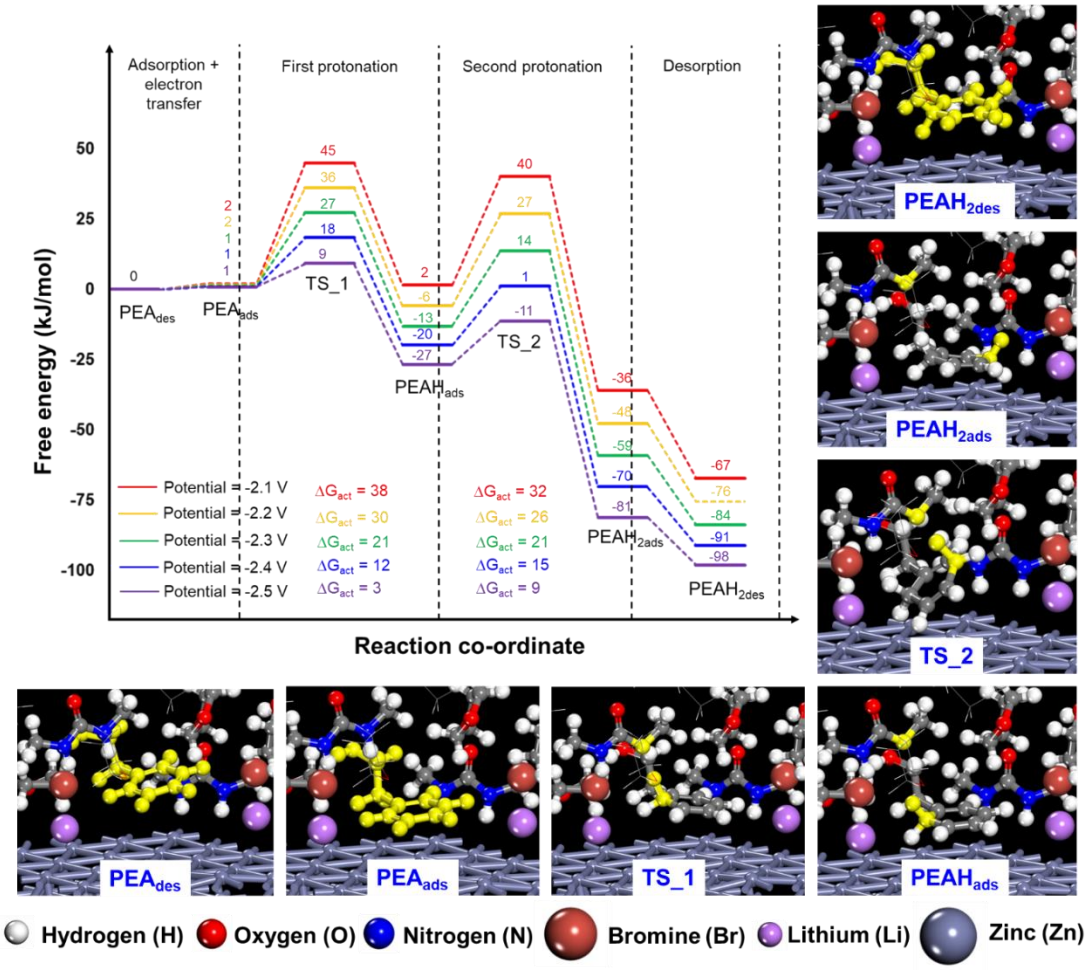

Figure 6.5: Potential dependent free energy profile for the electrode mediated Birch reduction of phenyl-ethanol (**3**). PEA_{des}: Desorbed phenyl-ethanol (**3**), PEA_{ads}: Adsorbed phenyl-ethanol (**3a$_{ads}$/3a'$_{ads}$**), TS_1: Transition state for the first protonation step, $PEAH_{ads}$: Adsorbed protonated phenyl-ethanol intermediate (**3c**), TS_2: Transition state for the second protonation step, $PEAH_{2ads}$: Adsorbed diene product (**4$_{ads}$**), $PEAH_{2des}$: Desorbed diene product (**4**). For the adsorption-cum-electron transfer step, transition state was found to be barrierless and hence only the reactant and product states have been shown in the figure.

6.3.2.2. Role of LiBr

With the likely mechanism isolated, CV experiments were done in order to isolate the role of individual components present in the reaction mixture. We initially hoped to use phenyl-ethanol (**3)** as a model. Unfortunately, under very similar conditions to our preparative reduction, lithium alkoxides are electrochemically generated at potentials higher (less negative) than that of redox potential of **3**, thereby obfuscating critical details of the electron transfer steps. Under the general assumption that a given mechanism (or set of mechanisms) is common to all substrates, our focus shifted to naphthalene (**5**) as a model substrate for voltammetric analysis under our optimized reaction conditions. The CV experiments shown in Figure 6.6 demonstrate that without LiBr, the scans showed good reversibility, highlighting the crucial role of Li^+ in guiding the reaction towards the product. Previous studies on CO_2 reduction have shown that the presence of cations and ionic liquids tend to promote the adsorption of the CO_2 on the electrode surface by stabilizing the CO_2^{*-} intermediate.[368,369] Similarly, we hypothesize herein that the Li cations in the LiBr electrolyte used here can adsorb over the Zn surface at the reductive operating potentials which can then similarly stabilize the anionic intermediate formed upon surface adsorption.

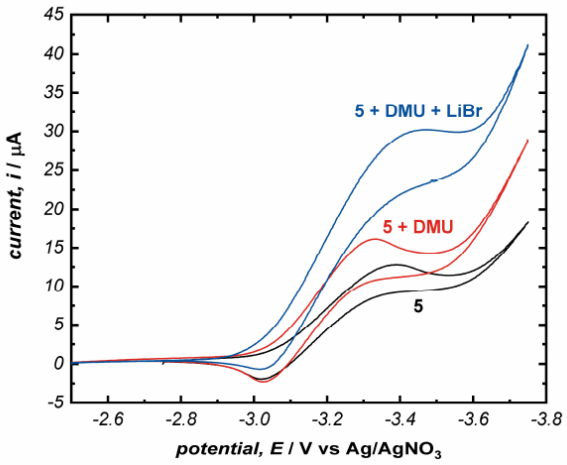

Figure 6.6: CVs of 1 mM naphthalene (**5**) alone (—), in the presence of 3.5 mM DMU (—), or in the presence of 3 mM DMU and 3 mM LiBr (—). CVs were performed using 100 mM TBABr in DMF at 25 mV s^{-1} and 25 °C.

In order to test this hypothesis, we looked at the potential dependent energetics of the adsorption cum electron transfer step with and without the presence of adsorbed LiBr

on the surface (Figure 6.7). We see that across the range of different potentials tested, adsorption and electron transfer in presence of LiBr is more exothermic and hence more favored compared to that in its absence due to the stabilization of the adsorbed anionic intermediate by the lithium cations. Hence, the presence of adsorbed LiBr on the surface translates to better electron transfer kinetics which thus guides the reaction towards the formation of product. While the initial models used tested the role of the LiBr adsorbed on a clean Zn surface to stabilize the adsorbed intermediate, XPS studies (discussed further in section 2.2.4) done for post-reaction Zn cathode show the growth of a thin layer known as the solid electrolyte interphase (SEI) layer composed predominantly of Li, C, and O over the Zn surface with some amount of zinc still being exposed. Preliminary adsorption studies of the substrate over more realistic models comprising of exposed Zn surface in presence of an SEI layer growth (see Supplementary Information for further details on modeling of the SEI covered Zn surface) similarly show adsorption to be more favored in presence of the surrounding SEI layer (see Supplementary Information for further details). Thus, similar to the role of LiBr, the Li cations in the Li-alkoxides/Li-oxides formed from decomposition of LiBr and THF also can stabilize the adsorbed anionic intermediate.

Besides its role as a stabilizing reagent for guiding the electron transfer step, LiBr can also promote proton transfer through complexation with DMU. This is evidenced by attenuated total reflectance (ATR, Figure 6.8) studies which show a complete, quantitative shift in the C=O stretching frequency of DMU from 1620 cm^{-1} to 1660 cm^{-1} in the absence and presence of LiBr, respectively. This unique ability of Li^+ to form a relatively strong coordinative complex to DMU may be critical to co-localize DMU. To support this hypothesis for Li^+'s role in the reaction manifold, we attempted control experiments with NaBr and KBr in place of LiBr. While no reaction was observed, these salts' inherent insolubility dramatically altered the resistivity of the solution, and thus thwarted direct comparisons to the LiBr system. More soluble surrogates of these non-lithium cations, such as NaI, nonetheless did not afford any product.

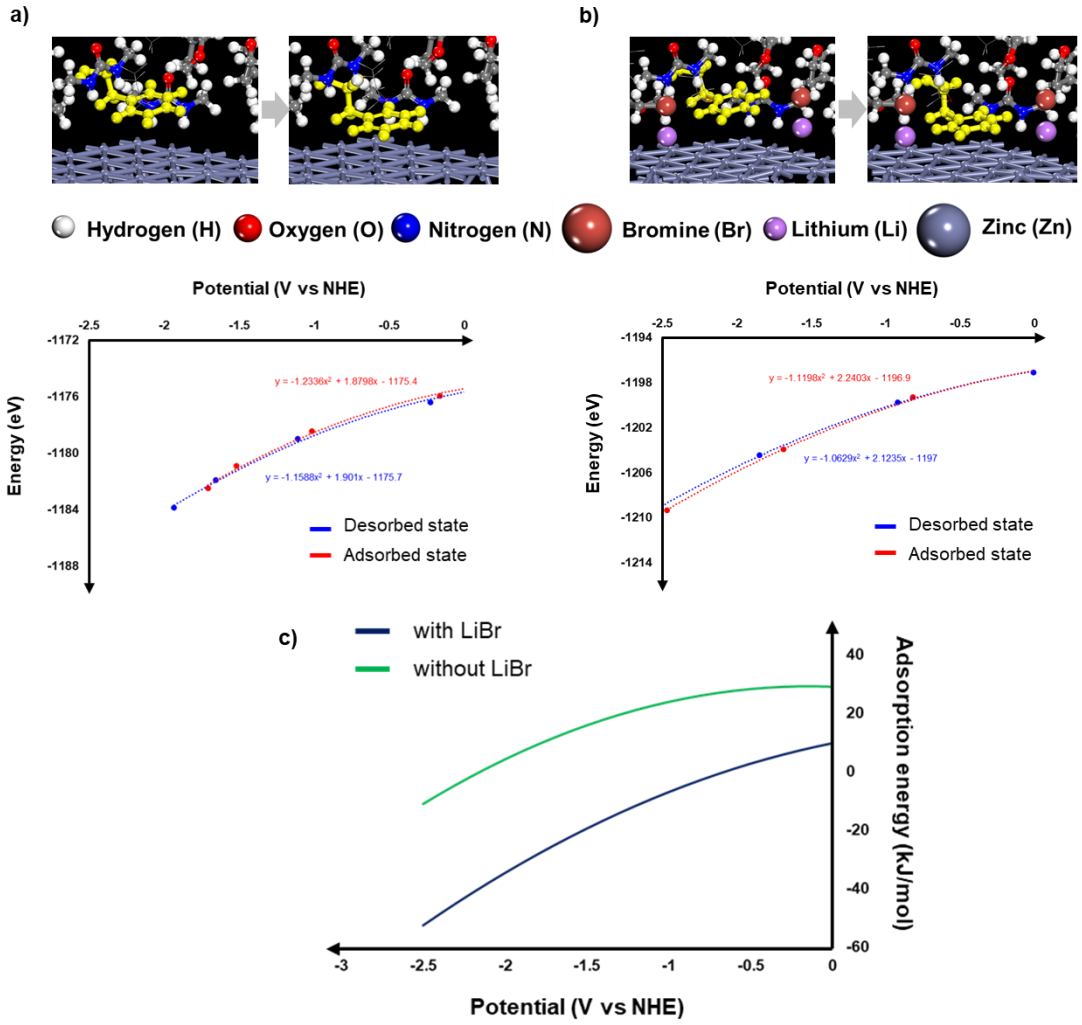

Figure 6.7: Potential dependent energetics for the reactant (PEA + *) (blue) and product state (PEA_{ads}) (red) involved in the adsorption of phenyl-ethanol (**3**) (PEA + * → PEA_{ads}) over Zn surface in a) absence of adsorbed LiBr and in b) presence of adsorbed LiBr, fitted to a parabolic curve c) Potential dependent energies for the adsorption of phenyl-ethanol (**3**) (PEA + * → PEA_{ads}) without (green) and with LiBr (blue).

Computational studies examining the complexation effects of different metal cations to DMU and the reduced model naphthalene substrate ($naphthalene^{\cdot-}$) show that the binding energy of Li^+ is the strongest to DMU (-81 kJ/mol) and $naphthalene^{\cdot-}$ (-71 kJ/mol) among the other tested cations (Na^+ and K^+) (Table 6.1). Such strong binding eventually leads to the co-localization of the reagents via formation of an Li-DMU-substrate complex, following which the substrate is then protonated. Evaluation of the protonation barriers suggest minimal differences between the different cations when

compared with the differences seen in the binding energy with protonation barriers of 81, 71, and 75 kJ/mol for Li^+, Na^+, and K^+ respectively. Thus, the binding of the metal cation to the reduced substrate and the proton source is likely the key distinguishing factor between the different cations. Lithium, which binds strongly with the other reagents due to its smaller cationic radii thus tends to catalyze the proton transfer reaction more so over other cations. This overall suggests that Li^+ plays a crucial dual role in directing the reaction towards the product formation by stabilizing the adsorbed intermediate to increase the electron transfer rates as well as by co-localizing the proton source and the substrate to increase the proton transfer rates.

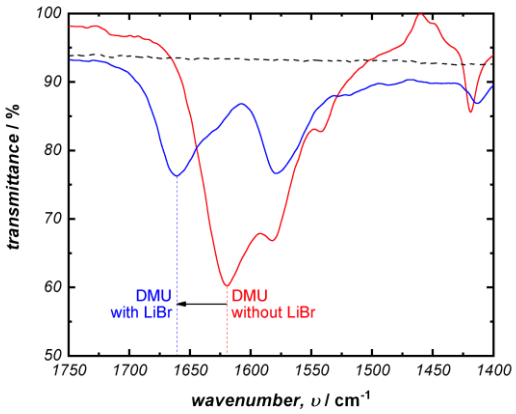

Figure 6.8: ATR IR of DMU without (red) and with (blue) LiBr

6.3.2.3. Role of TPPA

The addition of TPPA to the Naphthalene/DMU/LiBr solution does not result in the increased electron transfer rates that would be expected if it were to play a role in the reaction mechanism (Figure 6.6). This suggests that the role of TPPA may not be intrinsically tied to the mechanistic cycle, but rather may be involved in ancillary electrochemical processes. Structurally similar molecules (such as HMPA) have been employed in Li-ion batteries to aid in dissolving Li_2O layers formed at the electrode interface.[370] With this in mind, the unique speciation at the electrode surface was interrogated using X-ray photoelectron spectroscopy (XPS).

In general, a major problem with electro-organic synthesis under extreme reductive potentials is the formation of thick passivation layers on the electrode surface that inhibit product formation. Evidence of this passivation in our system was demonstrated in the absence of TPPA, as shown in the Supplementary Information. Although

optimized conditions still evidenced a thin film on the electrode surface (see Supplementary Information), this film ceased to grow within minutes and appeared to stabilize along the working electrode. XPS analysis revealed Mg, P, N and large amounts of lithium deposited on the electrode surface, as well as increased levels of oxygen and carbon; detailed analysis of the spectra is provided in the Supplementary Information. The observed Li, O, and C are likely a result of THF decomposition to form Li alkoxide.[371] Surprisingly, zinc was still observed in the post-reaction film, providing evidence that the underlying electrode material is still accessible to the bulk solution. The film may also be involved in both forming a stable SEI and providing an active electrode surface for the reaction. Although the exact mechanism of film growth and suppression are not yet known, it is clear that all system components are incorporated into the film and may cooperatively maintain electrode activity.

Table 6.1: DFT-computed binding energies for binding of DMU and naphthalene anion radical ($Nap^{\cdot-}$) to different screened metal cations and protonation barriers for subsequent protonation of $Nap^{\cdot-}$ to $NapH^{\cdot}$ with DMU as the proton source

Cation	Binding energy to DMU (kJ/mol)	Binding energy to $Naphthalene^{\cdot-}$ (kJ/mol)	Protonation barrier (kJ/mol)
Li	-81	-71	81
Na	-58	-53	71
K	-44	-48	75

Among the additives tested, TPPA in particular was the only one affording the reaction products. Thus, to examine this unique protective effect of TPPA, we did some preliminary calculations to compute the adsorption energies of the different additives tested over the Zn surface (Table 6.2). TPPA is shown to have one of the highest adsorption energies of -214 kJ/mol on the Zn surface. This strong binding nature of TPPA suggest that the surface would be predominantly be covered by TPPA preventing the solvent from interacting with the surface, thus blocking the delivery of excess electrons to the solvent and preventing its decomposition. Similar effects have been seen with HMPA, an analogue of TPPA for electrochemical reduction of benzene

conducted in HMPA-EtOH solutions. Use of HMPA has been shown to block the side reaction of hydrogen production from ethanol occurring at the cathode via blocking ethanol's access to the cathode surface.[355] From Table 6.2, it can also be seen that a few other similar additives which have similar high binding energies as TPPA were found to be ineffective. The reason for ineffectiveness of these other strongly binding additives is currently unknown and studies are currently ongoing to identify the other additive properties that make TPPA unique in its function as an overcharge protection agent.

Table 6.2: DFT-computed adsorption energies of the different screened additives over the Zn (001) surface

Additive	Adsorption energy (kJ/mol)	Reaction yields (%)	Additive	Adsorption energy (kJ/mol)	Reaction yields (%)
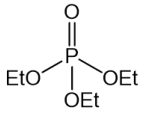	-127	NR	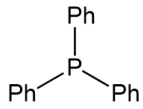	-228	NR
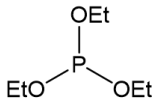	-122	NR	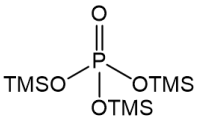	-227	NR
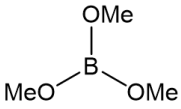	-131	NR	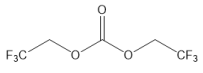	-55	NR
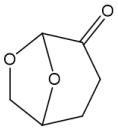	-57	NR	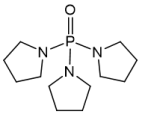	-214	74

6.4. Conclusion

Reductive electrochemical synthesis has been an approach discussed in the literature for nearly a century. Despite its obvious conceptual appeal, adoption of preparative methods in this subfield has been extremely limited because of issues related to pragmatism and chemoselectivity. Inspired by Li-ion battery technology, we have developed a general set of electrochemical reductive conditions involving Zn as the cathode, LiBr as the electrolyte, DMU as the proton source and TPPA as an additive, and demonstrated its practicality, safety, scalability, and chemoselectivity. Further, mechanistic investigations examining the selective reduction of phenyl-ethanol (**3**) used

herein as a probe reaction system suggest that the Birch reduction proceeds via electron and proton transfer events occurring over the Zn electrode with the sequence of the events depending on the operating potentials of the reaction. At low negative potentials, the reaction progresses likely via electron-proton-electron-proton transfer steps (ECEC mechanism), wherein the first protonation is the rate determining step of the reaction. As the potential is tuned to more negative potentials, the mechanism progressively shifts to a sequence of electron-electron-proton-proton transfer events (EECC mechanism) with the second protonation step as rate determining. DMU used here was shown to function as the major source of hydrogen with HAT transfer events to be minimal. Li^+ while not involved directly in the mechanism has been shown to aid in the electron transfer and proton transfer steps of the reaction by stabilization of the adsorbed anionic intermediate and by co-localization of the proton source DMU and the substrate either in the form of LiBr or Li-alkoxides. TPPA used herein was identified to function as an overcharge protection agent, thus preventing the electrode surface from passivation, leading to increased electrode stability. Preliminary computational studies suggest the strong nature of binding of TPPA to the Zn surface as one of the properties that lead to its effective functioning as an overcharge protection agent. We believe that inspiration from the fast-evolving research areas of battery technologies and electroactive materials coupled with the fundamental mechanistic insights gained here will have an important impact in synthetic organic electrochemistry, in ways such as the discovery of new oxidative and reductive mediators, milder access to harsh reducing agents, and generation of low-valent catalytic systems based on transition metals.

6.5. Methods

Computational

Ab initio density functional theory calculations were used herein to simulate the mechanism of the electrochemical Birch reduction using phenyl-ethanol as a model substrate. Li^0 mediated mechanism was modeled using density functional theory (DFT) calculations in Gaussian 09 program with a continuum model to simulate the solvent. The potential-dependent DFT surface simulations (electrode mediated Birch mechanism) was modeled in Vienna Ab-initio Simulation Package (VASP) using a Zn electrode surface and explicit solvent THF molecules.

Gaussian calculations

Solution phase quantum chemical calculations reported in the paper were carried out using the Gaussian 09 program.[213] The PBE functional[167] was used along with a 6-311++G(d,p) basis set[216–218] to carry out the geometry optimizations and transition state searches for intermediates and transition states involved in the Li^0 mediated mechanism. For other calculations described in this study involving screening of different metal cations, M062X functional[214] was used along with a 6-311++G(d,p) basis set[216–218] Frequency calculations were carried out on the optimized structures to ensure that the geometry optimizations converged to stable structures with no imaginary frequencies and transition state structures which have a single imaginary frequency along the reaction coordinate of interest. Entropic and zero-point energy corrections were employed to convert the electronic energies to free energies at 1 atm and 298.15 K. The gas phase optimized structures were then used to run single point energy calculations using the SMD solvation model[219] with tetrahydrofuran (THF) as the solvent to examine solvation effects. The free energy in solvent phase was then computed as,

$$G_{sol} = G_{gas} + (E_{sol} - E_{gas}) \quad (6.1)$$

where, G_{sol} is the solvent phase Gibbs free energy, G_{gas} is the gas phase Gibbs free energy, E_{sol} is the solvent phase electronic energies, E_{gas} is the gas phase electronic energies.

Calculation of the free energy barrier for electron transfer reactions

The free energy barrier for electron transfer reaction carried out by Li^0 in solution was determined using Marcus theory[372] as,

$$\Delta G_{act} = \frac{(\Delta G_{rxn} + \lambda)^2}{4\lambda} \quad (6.2)$$

wherein ΔG_{rxn} is the free energy of reaction of the electron transfer step and λ is the reoroganization energy which is defined as the sum of the inner sphere reorganization energy (λ_i) and the outer sphere reorganization energy (λ_o) as follows:

$$\lambda = \lambda_o + \lambda_i \quad (6.3)$$

The inner sphere reorganization energy (λ_i) for homogeneous reactions was estimated as,

$$\lambda_i = [E(D^*) - E(D^+)] + [E(A^*) - E(A^-)] \quad (6.4)$$

wherein, E(D*) is the electronic energy of the donor species (solvated lithium in this case) in its cationic state with neutral geometry, $E(D^+)$ is the energy of the cationic state of the donor species in its optimized cationic geometry, E(A*) is the energy of the acceptor species (the aromatic substrate) in its anionic state with neutral geometry and, $E(A^-)$ is the energy of the anionic state of the acceptor species in its optimized anionic geometry.

The outer sphere reorganization energy (λ_o) for homogeneous electron transfer reactions is given as,[372]

$$\lambda_o = \frac{e^2}{4\pi\varepsilon_0}\left(\frac{1}{2a_1} + \frac{1}{2a_2} - \frac{1}{(a_1+a_2)}\right)\left(\frac{1}{\varepsilon_{op}} - \frac{1}{\varepsilon_s}\right) \quad (6.5)$$

wherein the dielectric constants (static dielectric constant (ε_s) and optical dielectric constant (ε_{op})) for the solution is assumed to be that of THF and the radii of the donor and acceptor species (a_1 and a_2) involved in the electron transfer is approximated to be the distance between the two farthest atoms within the molecule.

VASP calculations

Periodic density functional theory calculations were carried out to simulate reactions at the electrode surface using the Vienna Ab initio Simulation Program (VASP).[163,165,171] The Perdew-Burke-Ernzerhof (PBE) functional[167] was used within the generalized gradient approximation (GGA) to calculate the exchange and correlation energies. The interactions between the core and the valence electrons were considered by using PAW pseudopotentials to describe the core electrons in the system.[168,169] D3-type dispersion corrections[283] were used to calculate dispersion interactions between phenyl-ethanol (PEA) molecules and the metal surface and, in addition, the interactions of THF and DMU molecules for the solution phase simulations. The transition states for different reactions were calculated using the nudged-elastic band (NEB) method[172,173] to establish reliable initial transition state structures which were subsequently used as input to the dimer method to isolate the transition states.[138] Plane waves were constructed using an energy cutoff of 450 eV. Numerical integrations were performed

using a k-point mesh of 2x2x1. A tolerance limit of 10^{-6} eV for the electronic energy and 0.05 eV/Å for the force were considered as the convergence criteria for geometry optimizations. Frequency calculations were done in order to determine the vibrational entropy contributions to the energies for determination of the free energies. The free energies for adsorption and desorption steps were computed by considering one-third loss in the gas phase entropy of the molecule upon adsorption. These changes in free energy were calculated as a function of potential using the double reference method developed by Filhol and Neurock.[284,285] The geometries and electronic structures in the double reference method were converged using a force convergence criterion of 0.3 eV/Å and energy convergence criteria of 10^{-4} eV.

Surface modeling

XPS studies done on the electrode surface post the reaction under optimized conditions show deposition of Mg, P, N, and large amounts of lithium, oxygen, and carbon as detailed out in the main text and in the SI. However, in addition to these elements, XPS analysis also revealed peaks for Zn which suggest that under the reaction conditions, some amount of zinc may still be exposed on the surface, which can catalyze the electron transfer reactions. Thus, in order to simulate the adsorption, electron transfer and protonation reactions that occur at the zinc electrode surface, we initially carried out periodic DFT calculations using a simple model of the most stable Zn surface i.e. the 001-terminated surface of hexagonally close packed (HCP) bulk Zn structure to construct a 5x5 supercell. A slab model with three layers of metal and a vacuum space of 15 Å was used for the calculations, keeping the bottom layer frozen to the bulk parameters. To model the effect of LiBr on the phenyl-ethanol (PEA) adsorption/electron transfer rates, two molecules of LiBr were adsorbed onto the Zn surface. This allows for the direct calculation of the PEA adsorption strength as well as the degree of electron transfer as a function of potential. Subsequent calculations reported below include the explicit THF solvent as well as DMU proton sources to extend the results to more faithful interfacial models.

6.6. Acknowledgements

The authors would like to thank the National Science Foundation CCI program (award 1740656) for the funding support and the Minnesota Supercomputing Institute (MSI) at the U. of Minnesota for use of computing resources.

6.7. Supporting Information

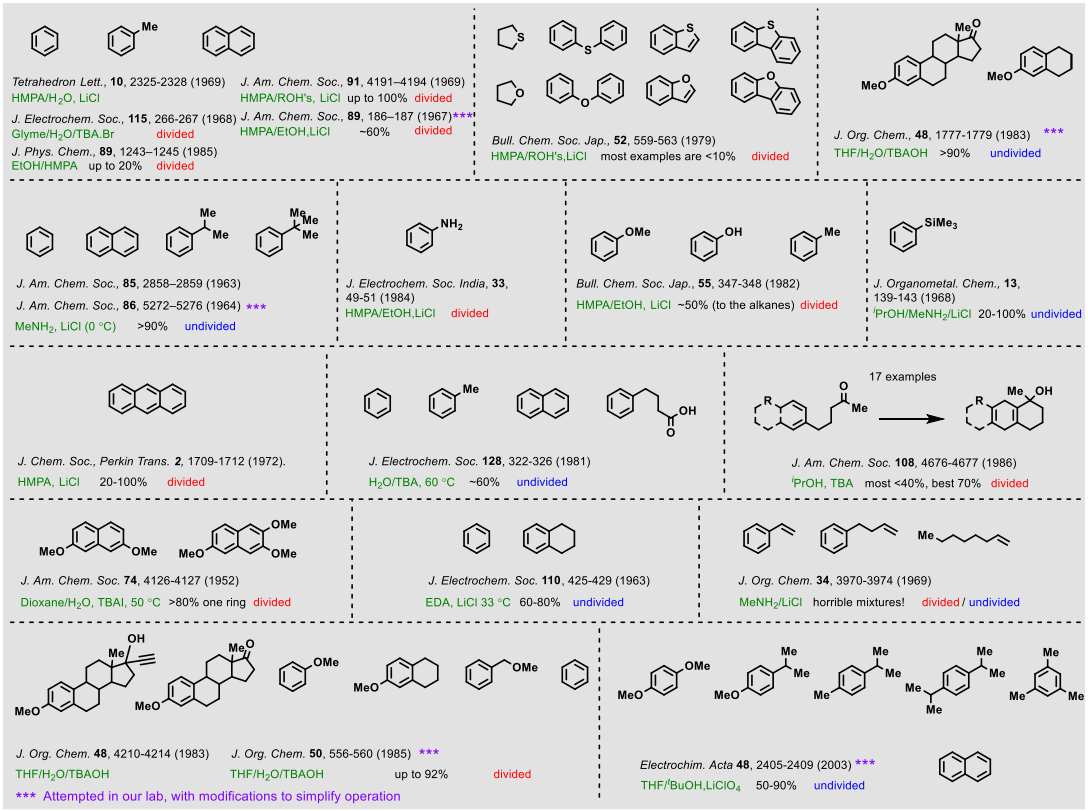

Figure S6.1: A Survey of Other (Selected) Electrochemical Birch reductions

6.7.1. Optimization of the reaction conditions

To optimize, $LiClO_4$ was first replaced with LiBr due to the bromide salt's higher stability, affordability, and similar range of solubility; however, only trace product was detected (entry 5). An accumulation of an apparently metallic substance at the cathode reacted violently with MeOH and water during cleaning, and so provided an initial clue for further study. We reasoned that this material was Li metal that had reductively plated out due to the poor solubility of Li^0 in THF. Indeed, similar events were observed in the early days of Li-ion battery exploration as a result of battery overcharging.[373] To combat this problem, several additives similar to those known for dampening the effects of overcharging in Li-ion batteries (including glyme, dioxane, and phosphoramides; see Table 6.2 for complete list) were evaluated, with tris(pyrrolidino)phosphoramide (TPPA), a non-carcinogenic surrogate for HMPA,[374] emerging as optimal (entry 6). Although the desired product was observed in 50% yield, it was accompanied by undesired isomers and over-reduced species in *ca*. 30% yield. Unsurprisingly, varying the proton source had a profound effect on the distribution of these compounds. After an extensive screen (See Table S6.4), we determined that 1,3-dimethylurea (DMU) was the most selective for the desired product (entry 7). As expected, reduced temperature afforded greater selectivity (entry 8). Consistent with Kashimura's findings,[341] it was found that switching from an Al to a Mg anode and increasing the current density on the cathode (by decreasing its surface area) rendered the reaction more selective and efficient at room temperature (entry 9). It is postulated that the anode is sacrificially oxidized, and it is possible that the identity of the resultant oxidized metal salts is relevant to the observed reactivity (*vide infra)*.

Table S6.1: Optimization summary

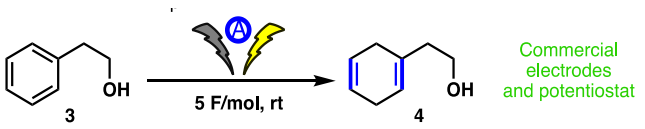

Entry	Ref	Electrodes	Conditions	Yield	By-prod.
1	42, 44	Pt(+)/Pt(-)	$MeNH_2$, LiCl	<5%	-
2	54	SS(+)/Hg(-)	THF/H_2O, TBA.OH	<5%	-
3	55, 56	C(+)/Al(-)	HMPA/EtOH, LiCl, divided cell	<5%	-
4	62	Mg(+)/Mg(-)	THF/^{t}BuOH, $LiClO_4$, sonication	<5%	-
5	-	Al(+)/Zn(-)	THF, ^{t}BuOH, LiBr	<5%	-
6	-	Al(+)/Zn(-)	THF, ^{t}BuOH, LiBr, TPPA	50%	30%
7	-	Al(+)/Zn(-)	THF, DMU, LiBr, TPPA	65%	14%
8	-	Al(+)/Zn(-)	THF, DMU, LiBr, TPPA, -78 °C	74%	<5%
9	-	Mg(+)/GSW(-)	THF, DMU, LiBr, TPPA	70%	<5%

Table S6.2: Survey of electrolyte, temperature, voltage and additives

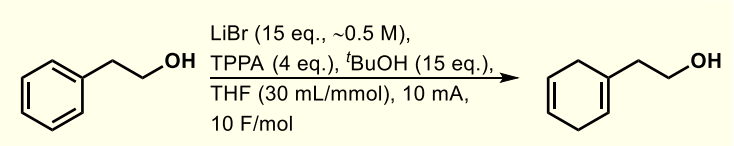

	entry	anode	cathode	other change	% prod.	% aliphatics	% isomers	% SM
conditions	1	Al	Zn	LiBr (45 eq.)	15	43	15	28
	2	Al	Zn	EtOH (15 eq.)	19	46	18	18
	3	Al	Zn	TPPA (45 eq.)	12	46	21	21
	4	Al	Zn	30 F/mol	29	31	21	19
	5	Al	Zn	-78 to -20 °C	37	33	21	10
	6	Al	Zn	LiBr (3.5 eq.) - 0.2 M	60	16	15	9
	7	Al	Zn	5 mA	32	22	17	29
	8	Al	Zn	20 mA	4	10	7	78
	9	Al	Zn	$TBA.BF_4$ + LiBr	Messy			

	entry	anode	cathode	other change	% prod.	% aliphatics	% isomers	% SM
conditions	1	Al	Zn	LiBr (45 eq.)	15	43	15	28
	2	Al	Zn	EtOH (15 eq.)	19	46	18	18
	3	Al	Zn	TPPA (45 eq.)	12	46	21	21
	4	Al	Zn	30 F/mol	29	31	21	19
	5	Al	Zn	-78 to -20 °C	37	33	21	10
	6	Al	Zn	LiBr (3.5 eq.) - 0.2 M	38	29	23	9
	7	Al	Zn	5 mA	32	22	17	29
	8	Al	Zn	20 mA	4	10	7	78
	9	Al	Zn	$TBA.BF_4$ + LiBr	Messy			

	entry	anode	cathode	other change	% prod.	% aliphatics	% isomers	% SM
additives	1	Al	Zn	NaO^tBu (15 eq.), $TBA.BF_4$	conductivity poor, no rxn			
	2	Al	Zn	LiOMe (15 eq.), $TBA.BF_4$				
	3	Al	Zn	LiO^tBu	43	21	0	37
	4	Al	Zn	LiHMDS	-	-	-	100
	5	Al	Zn	$LiN(Tf)_2$	39	18	13	31
	6	Al	Zn	$LiPF_6$	-	-	-	100
	7	Al	Zn	$LiBF_4$	-	-	-	100
	8	Al	Zn	$LiClO_4$	9	7	4	80
	9	Al	Zn	LiTFA	-	-	-	100
	10	Al	Zn	LiOTf	-	-	-	100
	11	Al	Zn	NaI	-	-	-	100
	12	Al	Zn	NaBr	Solubility issues			
	13	Al	Zn	KBr				
	14	Al	Zn	LiI	5	20	49	25
	15	Al	Zn	LiOAc	-	-	-	100
	16	Al	Zn	TMEDA (3.5 eq.)	33	20	19	28
	17	Al	Zn	LiO^tBu at 2 mA, 10 F/mol	9	7	4	80
	18	Al	Zn	PVP	38	20	3	39
	19	Al	Zn	K_2CO_3	30	8	10	52

In optimization tables, values represent % contribution by ^{1}H NMR

Table S6.3: Survey of electrodes

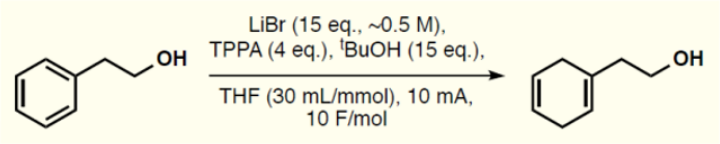

	entry	anode	cathode	other change	% prod.	% aliphatics	% isomers	% SM
anodes	1	Al	Zn		28	44	0	29
	2	Mg	Zn		18	33	21	28
	3	Cu	Zn		0	0	0	100
	4	Zn	Zn		10	30	4	56
cathodes	5	Al	Cu		27	29	18	27
	6	Al	Fe		28	27	18	27
	7	Al	GC		30	22	17	31
	8	Mg	Mg	AP = 10 min	10	30	4	56
	9	Al	RVC		26	54	14	6
	10	Al	Al	AP = 10 min				

- Highly sensitive to anode
- Insensitivity to cathode of similar surface area
- Higher surface area, more aliphatics cf. entry 9

Table S6.4: Screening of proton sources

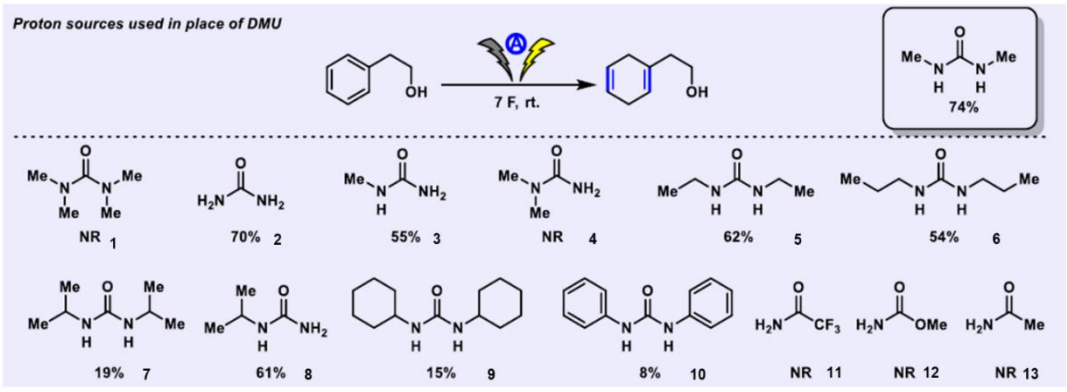

6.7.2. Applications of the Li-ion electroreduction to complex substrates

As shown in Figure S6.2, the electroreduction exhibited a broad scope across a range of different arenes. Under optimized conditions, every aryl group within a given polyarene was efficiently reduced (**6** and **7**), an achievement not accomplished by ammonia-free variants (e.g., SiGNa,[336] other dispersions,[337] and more weakly reductive conditions.[375] Simple arenes proved facile (**8** and **9**), as did aryl ethers, including those with both *meta* and *para* substituents (**10** and **11**). Silyl ethers performed well (**12** and **13**), despite their conspicuous absence from other ammonia-free alternatives. The

utility of these modular intermediates is evident from the large body of literature in which they appear.[376] Consistent with reactivity of the classical Birch, alcohol and ketone-containing arenes (**4**, **14** and **15**) were reduced in good yields (accompanied by the anticipated ketone reduction). Carbamate (**16**), amide (**17**), carboxylic acid (**18**, **19**, **21**, and **22**), and silane (**23**) functionalities were also preserved in the reduction of the aryl group. Even a sterically-guarded substrate, 1,3,5-tri-^{t}butylbenzene, could be reduced efficiently (**20**). Notably, benzoic acids were furnished in moderate yields (**18** and **19**); to our knowledge, this substrate class has historically been restricted to standard Birch conditions. The operational simplicity of this chemistry is displayed in the Birch reduction of substrate **3**; when no precautions were taken to exclude air or moisture, the reaction resulted in a similar conversion (68%).

Heterocyclic arenes, which are rarely subjected to Birch reductions, proved viable substrates. Indazole (**24**), indole (**25**, **26** and **27**), carbazole (**28**), acridine (**29**/**30**), and quinoline (**31**) moieties could be reduced on the carbocyclic ring in preference to the heterocycle, a reactivity only possible under a few classic Birch conditions. In our hands, SiGNa-S1 failed in all the examples tested (Figure S6.2), and Na-dispersion/15-crown-5 mixture gave only partial conversion with prolonged reaction times on some substrates.

The mildness of the reaction conditions was demonstrated *via* application to more complex natural products. Thus, chemo- and regioselective reduction gave access to the 1,4-dienyl derivatives of dextromethorphan (**32**), dehydroabietic acid (**33**), and estrone methyl ether (**34**). Overall, this methodology was competitive to the chemical Birch using lithium metal.

More broadly, the chemistry of dissolving metals has been applied to a wide range of reductive transformations, including ring opening/closing,[377] protecting group removal, transition metal-mediated reactions, among others. However, due to the poor solubility of alkali metals in reductively inert solvents (e.g., THF), these reactions have required either the use of ammonia as a co-solvent or the aid of a polyaromatic hydrocarbons (PAH) to act as electron shuttles.[378] In contrast, generation of separated Li^0 atoms can be precisely controlled in electrochemical systems; as a result, the limitations associated with bulk Li metal are simply eliminated. Encouraged by this realization, we began to explore the utility of our electroreduction protocol for non-Birch reductive

transformations (Figure S6.3A). Ether debenzylation proceeded smoothly (**35** → **36**) without competitive reduction of the more electron rich arene (in accord with Birch guidelines). Similarly, reductive deoxygenation was accomplished on fluorenone (**37** → **38**). Reductive cyclization, similar to an approach demonstrated by Rychnovsky,[379] (**39** → **40**) was successfully achieved. Ring opening of an epoxide (**41** → **42**) was facile, as was furan ring opening (**43** → **44**). Remarkably, McMurry couplings (**45** → **46**) could also be accomplished at room temperature. Returning to the sumanirole example outlined in Figure 6.1 in the main text, the same transformation was readily achieved at room temperature in 2 hours (**1** → **2**, 67% yield). It is worth noting that the most practical Birch-alternatives available (SiGNa-S1 and Na-disp./15-c-5) failed to deliver any product, as did all attempts to use previously-reported electrochemical methods (See Figure S6.4).

Finally, the scalability of the protocol was demonstrated in both batch (up to 100 g) and flow on **12** (the direct precursor to a key Pfizer intermediate), without any loss in efficiency. The modular flow setup (Figure S6.3B) is simple and allows an increase in scale by several orders of magnitude in a safe and sustainable fashion. Indeed, the very same transformation could be achieved in flow on 100 g scale, without significant changes to the protocol, special anhydrous precautions, or loss in yield.

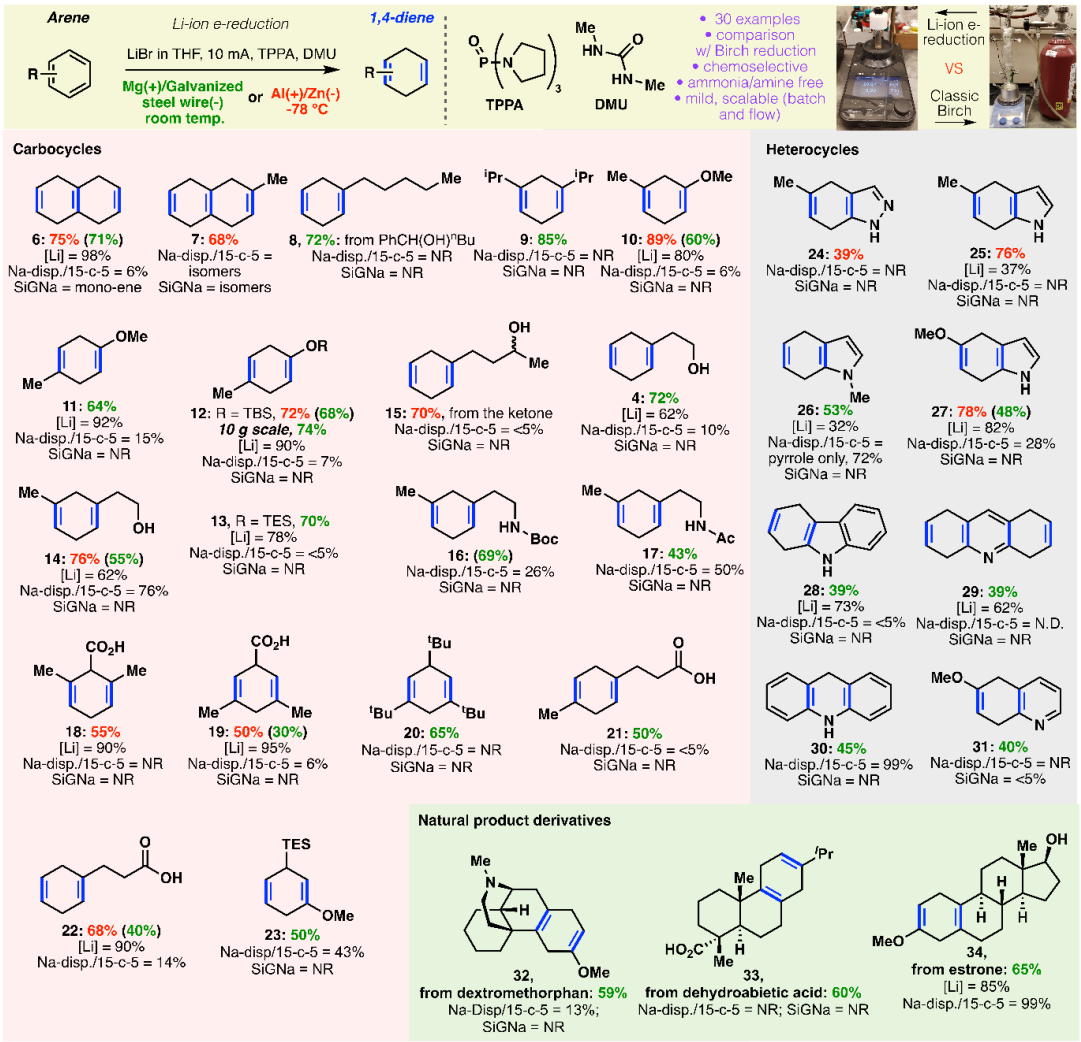

Figure S6.2: Scope of the reaction encompassing arenes and heterocycles, and comparison to other modern Birch alternatives. NR = no reaction.

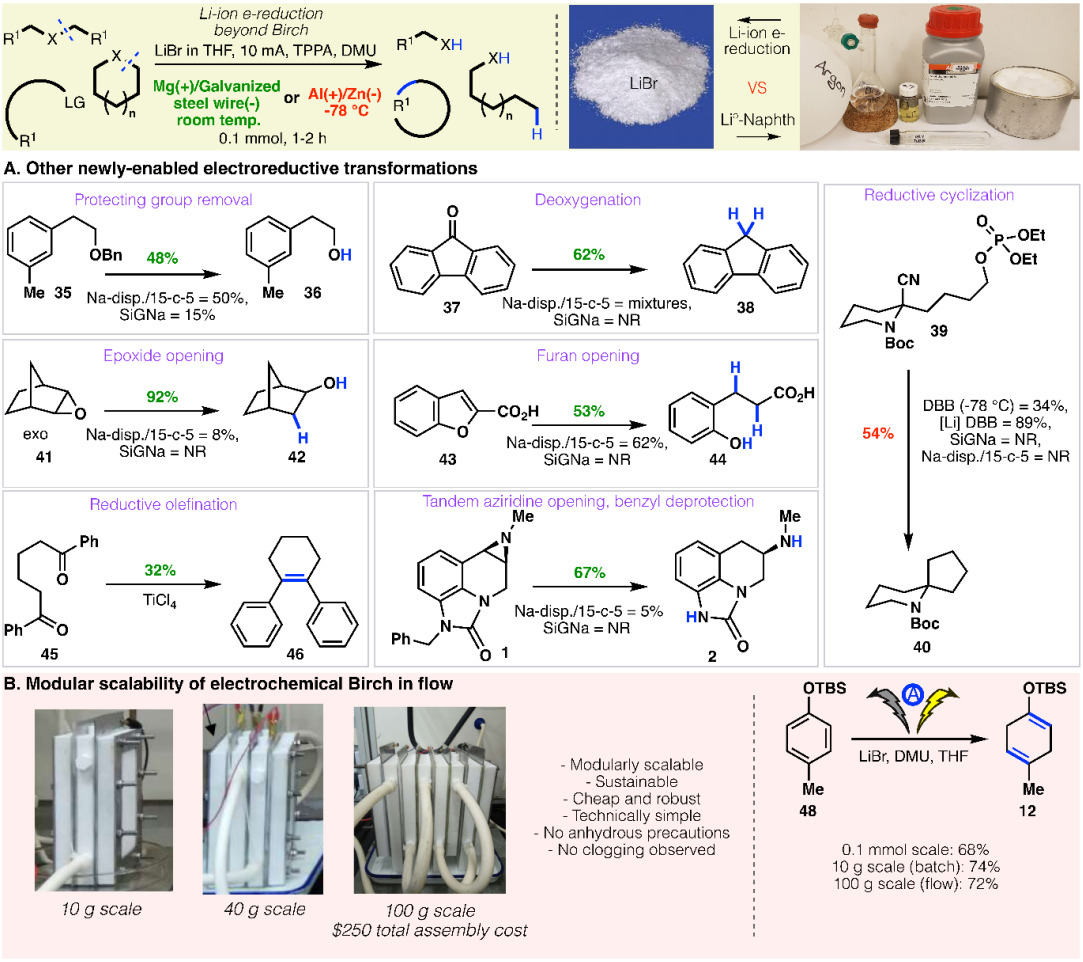

Figure S6.3: Scope of other reductive electroorganic transformations A) Scope of the electrochemical reduction in a variety of other reactions, **B)** Modular scaleup of Birch reduction in flow

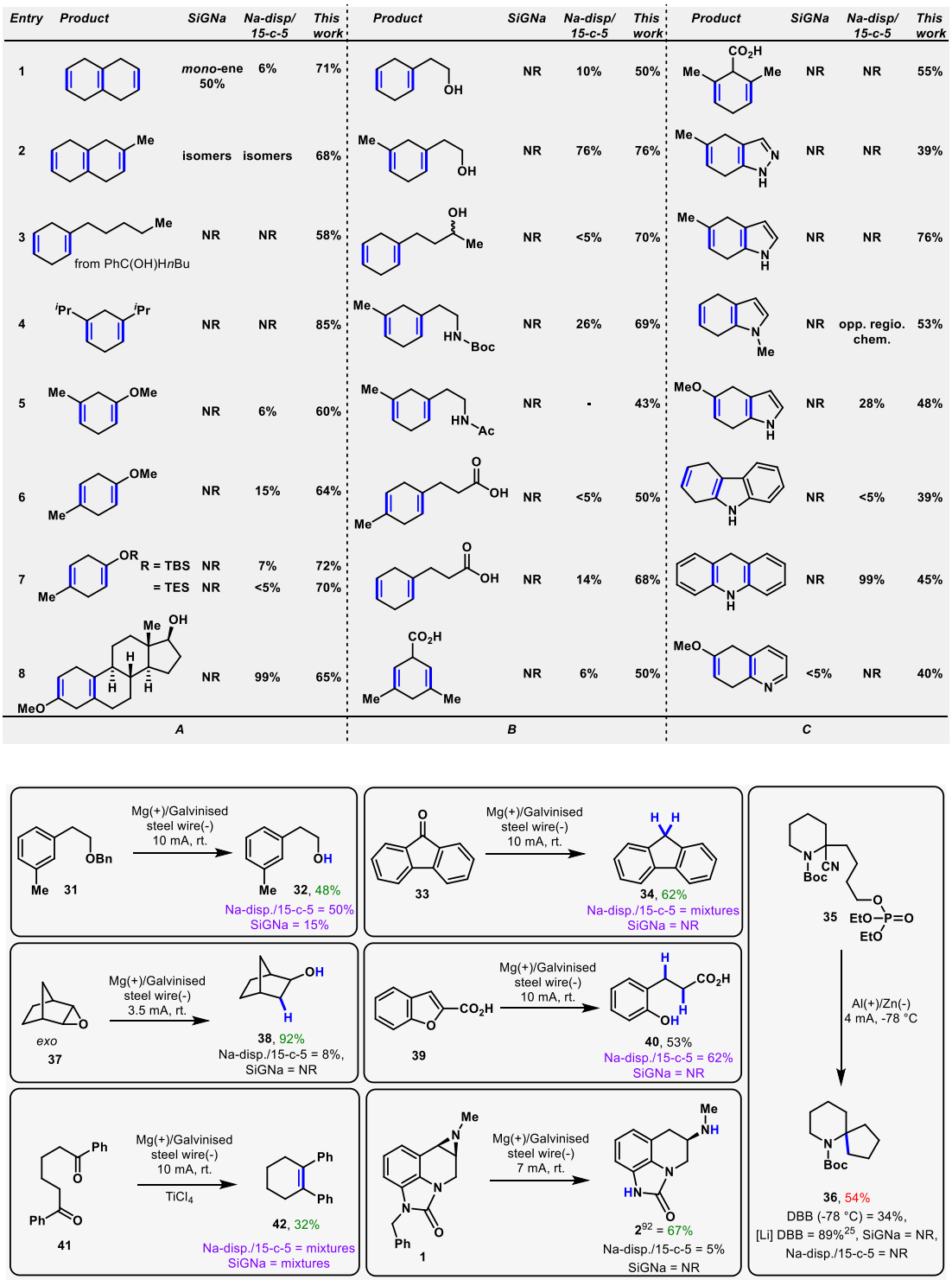

Figure S6.4: Comparison with other ammonia-free variants - SiGNa and Na dispersion/15-crown-5 in other reductive transformations

6.7.3. Scale-up optimization for EC-Birch reaction of Compound 12

Table S6.5: Optimization table

Entry/Scale (g)	Con. of SM (mmol/mL)	Anode(+)/ Cathode(-)	Electrolyte (in THF)	TPPA (eq./M)	DMU (eq.)	Temperature (°C)	F/mol	Current (mA) /Voltage (V)	CD (mA/cm²)	HPLC	
										SM	TP
2455/1.0 (4.5mmol)	0.14	Al plate(+)/S.S. plate(-)	3.0M LiBr	3.5eq/0.5M	3.0	30	6F/8h	100/25-32	11.90	2.67%	95.30%
2456/1.0 (4.5mmol)	0.14	Zn plate(+)/S.S. plate(-)	3.0M LiBr	3.5eq/0.5M	3.0	30	6F/8h	100/25-32	11.90	93.10%	5.88%
2451/2.0 (9.0mmol)	0.14	Mg plate(+)/S.S plate(-)	3.0M LiBr	3.5eq/0.5M	3.0	30	6F/15h	100/25-32	18.18	0.00%	100.00%
2452/3.0 (13.5mmol)	0.42	Mg plate(+)/S.S plate(-)	3.0M LiBr	1.2eq/0.5M	3.0	30	2F/7h	100/26-32	11.90	53.50%	46.45%
						30	3F/10.5h	100/26-32	11.90	42.12%	57.82%
						30	4F/14h	100/28-32	11.90	13.20%	85.45%
						30	5F/17.5h	100/32	11.90	0.00%	100.00%
2454/4.0 (18.0mmol)	0.14	Mg plate(+)/S.S plate(-)	3.0M LiBr	3.5eq/0.5M	3.0	45	4F/9.5h	200/23-32	3.63	50.92%	48.77%
						55	6F/14.5h	200/25-32	3.63	4.43%	95.16%
						55	8F/19h	200/25-32	3.63	2.09%	97.10%
2445/2.0 (9.0mmol)	0.28	Mg plate(+)/S.S plate(-)	3.0M LiBr	1.4eq/0.4M	3.0	30	6F/14h	100/25-32	11.90	0.00%	100.00%
2446/2.0 (9.0mmol)	0.28	Mg plate(+)/S.S plate(-)	3.0M LiBr	1.0eq/0.3M	3.0	30	6F/14h	100/25-32	11.90	0.00%	100.00%
2449/0.5 (2.25mmol)	0.07	Mg plate(+)/S.S plate(-)	3.0M LiBr	0/0	3.0	30	6F/3.5h	100/27-32	11.90	54.75%	45.23%
2450/0.5 (2.25mmol)	0.07	Mg plate(+)/S.S plate(-)	3.0M LiBr	0/0	8.0	30	6F/3.5h	100/23-28	11.90	7.19%	83.39%

On scale-up we observed that the reaction can successfully proceed in the absence of TPPA by replacement with excess DMU. It was ultimately determined that excess DMU gave reduced overall voltage and delivered higher current to give the desired product as high as 80% conversion.

6.7.4. Comparison of EC-Birch with known other electrochemical methods

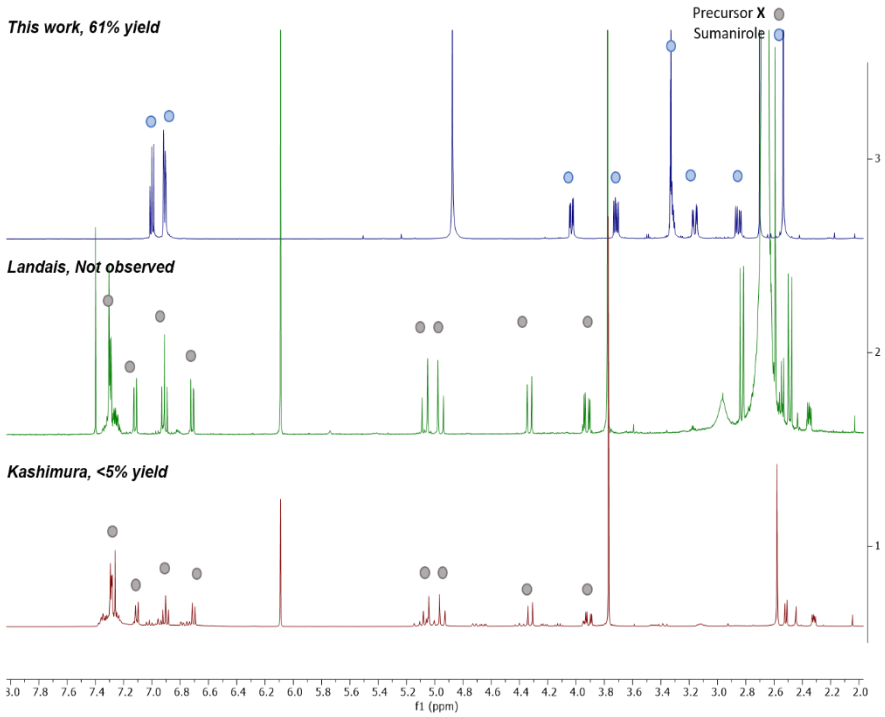

Figure S6.5: Comparisons of the NMR's against that of other electrochemical methods for production of sumanirole (**2**)

6.7.5. Li^0 detection experiment

The pre-electrolysis experiment in the case below was run at room temperature (blue line), and we suspect that the initial decrease in substrate concentration (in which this experiment did not reveal any product formation) was due to the formation of a variety of reactive species, which formed as a result of the absence of the substrate to act as an electron sink. These species likely act to polymerize the substrate, as no other like species could be detected by GC-FID-MS. This initial drop in substrate is less perverse when the reaction was run at -78 ºC (purple line), where only a minor drop in substrate concentration was observed, which we attribute to adsorption onto the electrode surface (not possible to circumvent by sampling for kinetic analysis), for which we found that reaction yields improved upon washing the electrodes. In order to better probe for the presence (or participation) of solvated electrons or Li^0, we sought to utilize a more susceptible electrophile. Therefore, a more reductively labile molecule, naphthaldehyde was chosen. The scheme below outlines the operation, whereby, in a similar fashion, pre-electrolysis was conducted at -78 ºC, delivering 3 F/mol. After electrolysis, the

aldehyde (and proton source, *i*PrOH) was then added and the stirred at -78 ºC for several minutes, followed by removal of the cooling bath, allowing the reaction to warm up to 0 ºC, which was maintained for the remainder of an hour, before being sampled for GC-MS/FID analysis. As before with the investigation on phenyl-ethanol, none of the potential products that would undoubtedly form from reaction with Li^0 or solvated electrons were detected; in fact, the chromatograms demonstrated that the added naphthaldehyde was chemically pure.

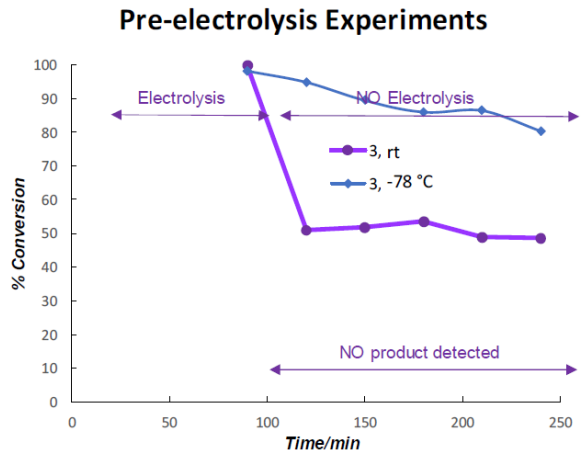

Figure S6.6: Li^0 test experiments, whereby, pre-electrolysis was run and then substrate added. Experiments were carried out at -78 ºC and rt

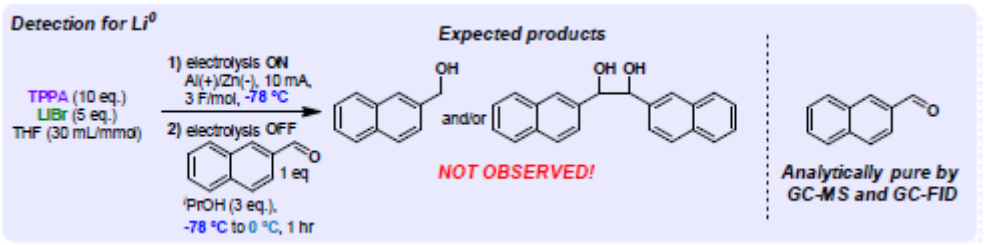

Figure S6.7: Test for Li^0, whereby pre-electrolysis was run followed by the addition of reductively labile naphthaldehyde

6.7.6. Determination of the kinetic isotope effect (KIE)

KIE studies were done using commercial 98% d4-urea as the proton source since commercial d2-DMU is not available and attempts to deuterated DMU in lab were able to afford deuteration of a maximum of only 72%. To determine the KIE, intermolecular competition experiments was run at 0.033M of TBS-protected phenyl-ethanol, with 3 eq. of urea and 3 eq. d4-urea. The amount of deuterium incorporation in the product

was found to be 7%, which would suggest the KIE value to be 13.29. However, studies investigating deuterium incorporation in the product under standard conditions (0.033 M TBS-PE, 2 eq. d4-urea), showed deuterium incorporation of only 37%, which suggests there are other sources of hydrogen present in the reaction mixture which may have skewed the KIE value upwards. Thus, by accounting for the hydrogenation of the substrate by other sources of hydrogen (primarily exogenous water that contaminates the reaction mixture given the highly hygroscopic nature of lithium bromide and TPPA that are used as reagents for the reaction), a KIE value of 4.24 was determined.

6.7.7. Solvated lithium modeling

Li metal in solution is typically solvated by the solvent molecules as seen in the case of ammonia.[380,381] The first solvation shell of lithium consists of four solvent molecules usually bound in a tetrahedral configuration. Hence, it is likely that Li in THF as well exists in a tetrahedral configuration which is also confirmed by crystallographic identification of various Li salts in THF solvent.[382–385] In addition, when TPPA is added as a polar additive, it is likely that TPPA replaces THF in the first solvation shell of lithium which is similar to the observations reported by Reich et al.[386] upon the addition of HMPA (another similar polar additive) to LiBr in THF. Therefore, in order to consider the additional solvation effects by TPPA, 2 THF molecules were replaced by 2 TPPA molecules in the first solvation shell (Figure S6.8) since 2-3 equivalents of TPPA are used per mole of LiBr.

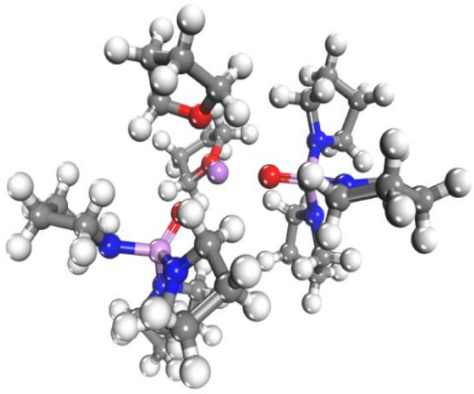

Figure S6.8: Solvated lithium atom model (Li^0) used to consider solvation by THF and TPPA. The carbon, hydrogen, oxygen, nitrogen and Li atoms are shown as grey, white, red, blue and purple spheres

6.7.8. Computational study of the electrode mediated kinetics of Birch reduction of phenyl-ethanol (PEA)

As discussed in the main text, the adsorption of PEA onto the Zn electrode and the electron transfer from the Zn to the PEA are likely coupled in a facile step. The rate thus appears to be subsequently controlled by proton transfer to the bound PEA substrate as also confirmed by the KIE investigations. In order to effectively probe proton transfer, we carried out rigorous calculations that explicitly include the THF solvent, DMU proton source as well as the potential in order to calculate the potential dependent reaction energies for all of the elementary steps including adsorption, electron transfer, protonation and desorption steps.

In order to simulate the liquid/solid interface, the vacuum space for the model system discussed above was filled with the explicit THF solvent molecules to match the density of THF. Two dimethyl urea (DMU) were added as proton source molecules. One of the DMU molecules is used to replace the bound THF molecule on the surface whereas the second replaces a THF molecule in the solution. In addition to the solvent and proton source, two molecules of the LiBr were added to the Zn surface via the Li cations and sit vicinal to adsorbed phenylethyl alcohol (PEA) as shown in Figure S6.9.

Ab-initio potential-dependent MD simulations were carried out to establish a reliable low energy configuration of the solvent, DMU, PEA and LiBr at the Zn surface at different electrode potentials that were subsequently used to carry out reaction energy calculations. The ab initio molecular dynamics simulations were run in an NVT ensemble for 3 picoseconds with a time step of 1 femtosecond. Simulated annealing simulations were subsequently carried out to establish the low energy system configurations. In the first 1500 steps, the system was annealed from 500 K to 300 K and the same was done for the next 1500 steps. The lowest energy configurations obtained from the MD simulations were then sampled and each of the lowest energy structures was optimized. The minimum energy structures obtained from the MD samples were then used in subsequent calculations.

The potential dependence of the various intermediates formed via electron transfer and proton transfer to the substrate (PEA^{des}, PEA^{ads}, $PEAH^{ads}$, $PEAH_2^{ads}$, $PEAH_2^{des}$) was calculated using the double reference method by Neurock and Filhol.[284,285] In this method, the system is charged by either adding or subtracting excess electron density

(-q) into the metal. This is counterbalanced by a homogeneous charge of the same magnitude (+q) distributed over the background in order to keep the overall system neutral. In the presence of solution, the charges create a double layer with a potential and an electric field that reliably represent those established by explicit electrolyte.

The optimizations and the transition state calculations were run at these differently charged systems. The potentials at different charges for a given intermediate structure were subsequently determined by comparing with two reference potentials. The first reference relates the potential at the metal/solution interface for the uncharged system to the vacuum reference. This is done by inserting a 20 Å vacuum slab in the middle of solvent layer. The second reference is the potential at the middle of the solvent layer which is referred to the vacuum referenced metal surface potential at zero charge. Thus, the potential at the middle solvent layer for different charged systems was calculated by referencing it to the middle solvent layer of the uncharged system which is in turn calculated via reference to the vacuum reference metal surface potential. This allows one to determine the potential of the charge system which is subsequently referenced to NHE by adding -4.8 V to the calculated potential. The total energy of the system at each potential was then determined by correcting the VASP calculated energies for the excess charge and the interaction with the background charge. The energies for the various intermediates are then plotted as a function of potential to determine the energy of each state as a function of potential which is shown below and used to determine the reaction energy differences as well as the activation energies at specific potentials.

The simulations reported herein explore the potential dependence for the following intermediates: free PEA in THF/DMU solution (PEA^{des}) (Figure S6.10 with relevant structures shown in Figure S6.9), adsorbed PEA (PEA^{ads}) which occurs with electron transfer to form either the bound radical anion PEA^{*-} or dianion PEA^{*-2} depending on the operating potential (Figure S6.10 with relevant structures shown in Figure S6.9), the protonated PEA intermediate ($PEAH^{ads}$) (Figure S6.12 with relevant structures shown in Figure S6.11), the subsequent proton transfer to form the bound reduced $PEAH_2^{ads}$ (Figure S6.14 with relevant structures shown in Figure S6.13) intermediate, and the desorbed $PEAH_2^{des}$ (Figure S6.16 with relevant structures shown in Figure S6.15) as well for the transition states involving the first protonation step (TS_1) (Figure S6.12 with relevant structures shown in Figure S6.11 and the second protonation step (TS_2) (Figure S6.14 with relevant structures shown in Figure S6.13).

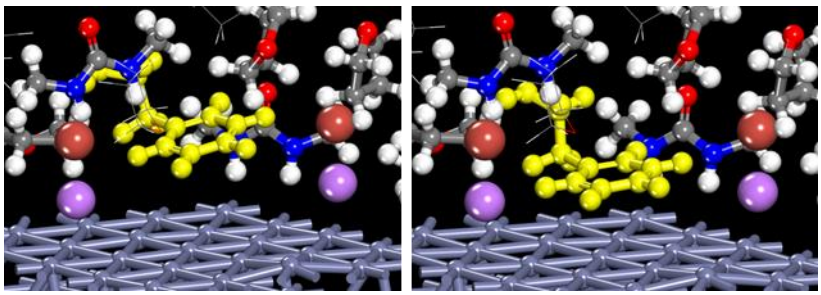

Figure S6.9: The lowest energy reactant (left) and product (right) states for the adsorption of phenylethyl alcohol (PEA) on the Zn (001) surface in the presence of the solution phase THF solvent and DMU protonation source and surface LiBr promoters. The adsorbing PEA molecule is highlighted in yellow. The violet, purple, maroon, red, blue, grey, and white spheres refer to the zinc surface atoms, the lithium cation, bromine anion, oxygen, nitrogen, carbon and hydrogen atoms.

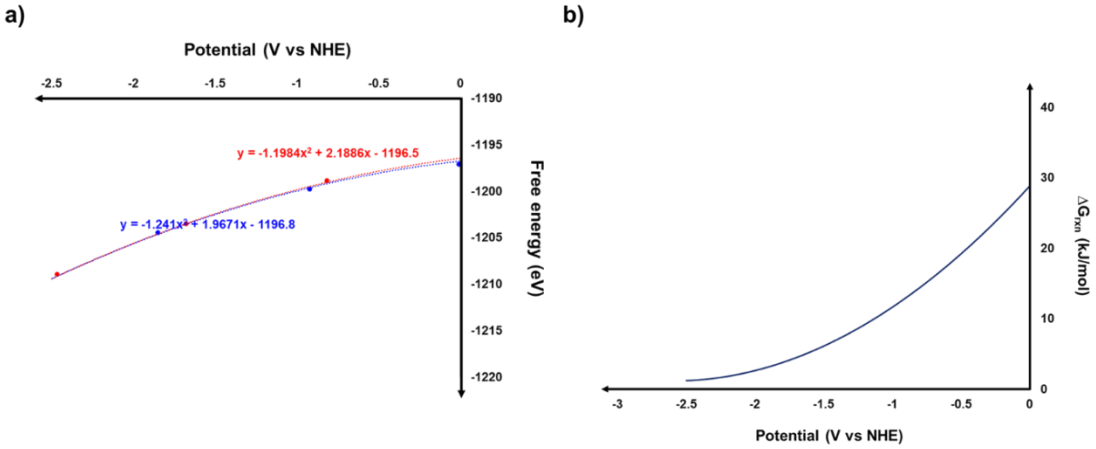

Figure S6.10: a) Potential dependent free energies for the reactant (PEA + *) (red) and product (PEA^{ads}) (blue) involved in the adsorption of phenyl-ethanol (PEA) (PEA + * → PEA^{ads}), fitted to a parabolic curve b) Potential dependent reaction free energies for the adsorption of phenyl-ethanol (PEA) (PEA + * → PEA^{ads})

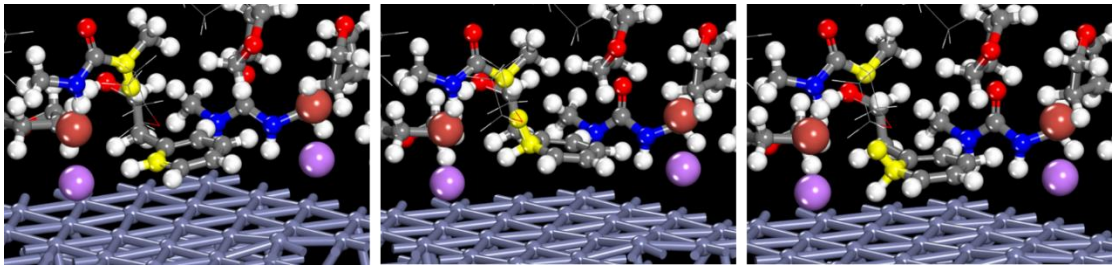

Figure S6.11: The lowest energy reactant (left), transition (center) and product (right) states in the first protonation step of bound phenylethyl alcohol (PEA) on the Zn (001) surface in the presence of the solution phase THF solvent and DMU protonation source and surface LiBr promoters. The reactive proton is highlighted in yellow. The violet, purple, maroon, red, blue, grey, and white spheres refer to the zinc surface atoms, the lithium cation, bromine anion, oxygen, nitrogen, carbon and hydrogen atoms.

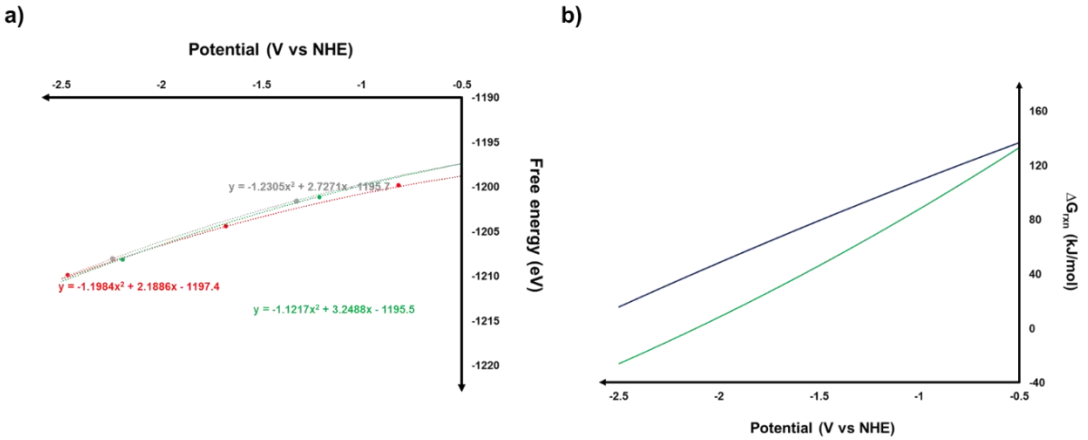

Figure S6.12: a) Potential dependent free energies for the reactant (PEA^{ads} + DMU-H) (red), transition (PEA^{ads}-H--DMU(-)) (grey) and product state ($PEAH^{ads}$--DMU(-)) (green) involved in the first protonation step ($PEA^{ads} + H^{+} \rightarrow PEAH^{ads}$) of phenylethyl alcohol (PEA) which is fitted to a parabolic curve b) Potential dependent free energy barriers (blue) and reaction energies (green) for the first protonation step of the adsorbed phenyl-ethanol (PEA^{ads}) ($PEA^{ads} + H^{+} \rightarrow PEAH^{ads}$)

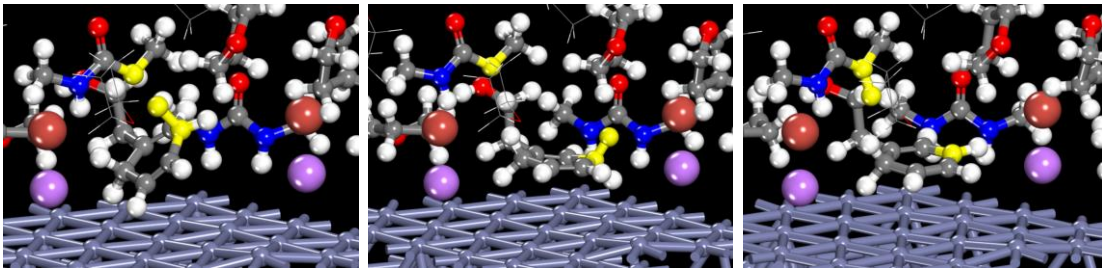

Figure S6.13: The lowest energy reactant (left), transition (center) and product (right) states in the second protonation step of bound phenylethyl alcohol (PEA) on the Zn (001) surface in the presence of the solution phase THF solvent and DMU protonation source and surface LiBr promoters. The violet, purple, maroon, red, blue, grey, and white spheres refer to the zinc surface atoms, the lithium cation, bromine anion, oxygen, nitrogen, carbon and hydrogen atoms.

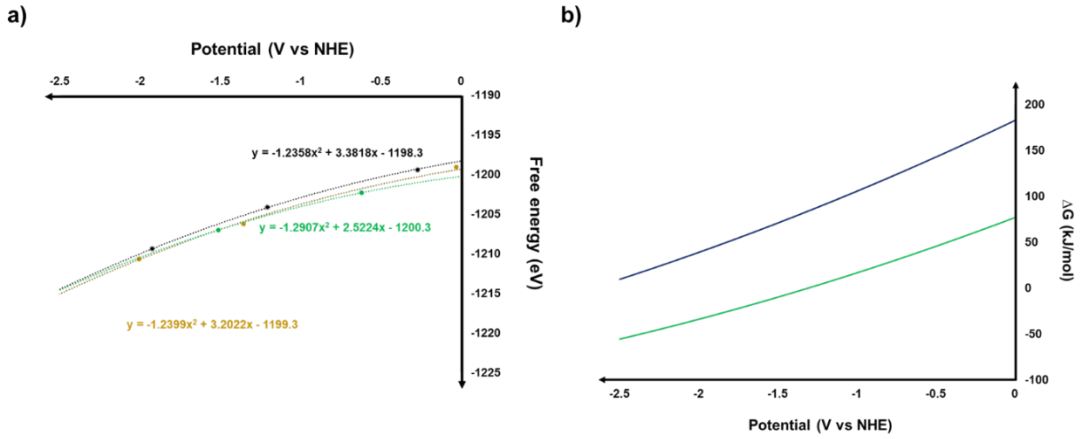

Figure S6.14: a) Potential dependent free energies for the reactant ($PEAH^{ads}$ + DMU-H) (green), transition ($PEAH^{ads}$-H--DMU(-)) (black) and product state ($PEAH_2^{ads}$--DMU(-)) (yellow) involved in the first protonation step ($PEAH^{ads} + H^+ \rightarrow PEAH_2^{ads}$) of phenylethyl alcohol (PEA) which is fitted to a parabolic curve b) Potential dependent free energy barriers (blue) and reaction energies (green) for the second protonation step of the protonated adsorbed phenyl-ethanol ($PEAH^{ads}$) ($PEAH^{ads} + H^+ \rightarrow PEAH_2^{ads}$)

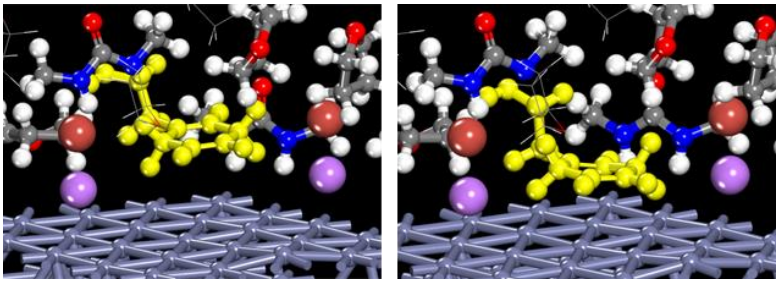

Figure S6.15: The lowest energy reactant (left) and product (right) states for the desorption of phenylethyl alcohol (PEA) on the Zn (001) surface in the presence of the solution phase THF solvent and DMU protonation source and surface LiBr promoters. The desorbing $PEAH_2^{ads}$ molecule is highlighted in yellow. The violet, purple, maroon, red, blue, grey, and white spheres refer to the zinc surface atoms, the lithium cation, bromine anion, oxygen, nitrogen, carbon and hydrogen atoms.

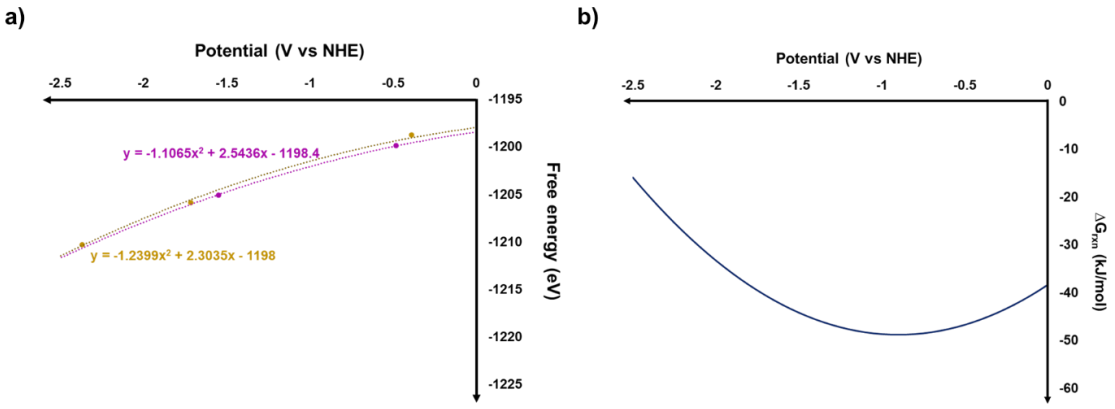

Figure S6.16: a) Potential dependent free energies for the reactant ($PEAH_2^{ads}$) (yellow) and product ($PEAH_2^{des}$ + *) (pink) involved in the desorption of the reduced phenyl-ethanol ($PEAH_2$) ($PEAH_2^{ads}$ → $PEAH_2^{des}$ + *), fitted to a parabolic curve b) Potential dependent reaction free energies for the desorption of the reduced phenyl-ethanol ($PEAH_2$) ($PEAH_2^{ads}$ → $PEAH_2^{des}$ + *)

6.7.9. Phenyl-ethanol adsorption on SEI covered Zn surface with exposed Zn

XPS studies suggest a build-up of an SEI layer on the surface as the reaction progresses consisting mainly of lithium alkoxides which are formed via decomposition of the solvent tetrahydrofuran (THF) which is used in the reaction. Thus, in order to determine whether the deposited SEI layer has a similar influence on the adsorption of phenyl-ethanol over the Zn surface, wherein similar to Li cations in LiBr, the Li atoms in the SEI layer stabilize the adsorbed intermediate, we looked at the gas phase zero charge adsorption energies of phenylethanol over the Zn surface with and without the SEI layer. The SEI layer was modeled as a layer of lithium oxide (Li_2O) adsorbed on both the sides of a three-layer 001-terminated Zn surface. The lithium oxide layer was built by cleaving along the most-stable Li-terminated (111) plane[387] of a cubic Li_2O crystal with bulk optimized lattice constants of 4.69 Å. A single unit thick layer of Li_2O of thickness 1.36 Å consists of a layer of oxygen atoms sandwiched between two layers of lithium atoms. The exposed zinc surface was constructed by removing 13 Li atoms and 9 O atoms from the top surface so as to accommodate the phenyl-ethanol (PEA) substrate. The resultant structure was then optimized, structures for which are shown in Figure S6.17. Phenyl-ethanol adsorption was then studied over this SEI covered surface with exposed and energies compared with that for pure Zn surface (Figure S6.17). Preliminary gas phase calculations suggest that in presence of SEI layer, phenyl-ethanol adsorption was more favored compared to that over pure Zn surface. This thus suggests that similar to simple models employed previously in our calculations with adsorbed LiBr, it is likely that the SEI layer which also contains Li atoms might similarly stabilize the adsorbed phenyl-ethanol substrate, leading to improved electron transfer rates.

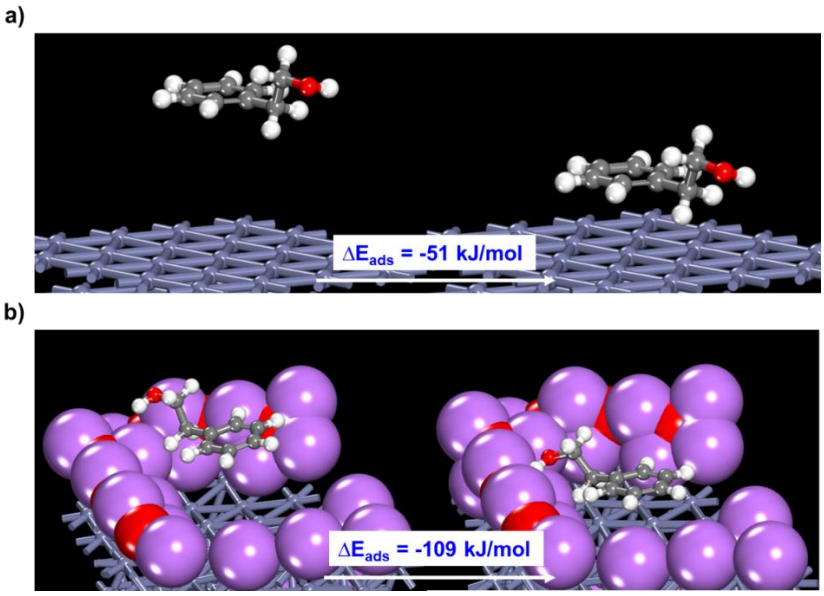

Figure S6.17: Adsorption of phenyl-ethanol (PEA) over a) pure 001-terminated Zn surface b) SEI (Li_2O) covered surface with exposed Zn atoms. The violet, purple, red, grey, and white spheres refer to the zinc, lithium, oxygen, carbon and hydrogen atoms.

6.7.10. Rate order derivation

Li^0 mediated mechanism

As discussed in the main text, the first step in the Li^0 mediated Birch reduction of phenyl-ethanol (**3**) involves an electron transfer step (eq. 6.6) in which the electron from the solvated lithium metal (Li_{sol}) is transferred to the reacting substrate (phenyl-ethanol) to form the anion radical intermediate. The solvated lithium cation (Li^+_{sol}) generated post the electron transfer likely interacts with the reduced substrate to form a metal-substrate complex.

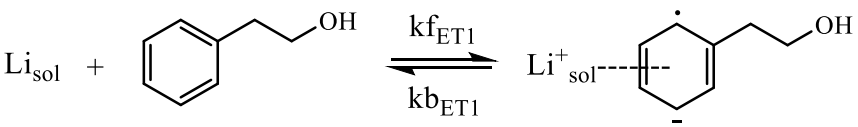

3 **3a_comp** (6.6)

After the electron transfer step, the reduced substrate then is protonated in presence of a proton source (DMU) to form the protonated radical intermediate as shown in eq. 6.7. The deprotonated proton source ($DMU\text{-}H^-$) in this step then complexates with the solvated Li cation to form $Li^+\text{-}DMU\text{-}H^-$.

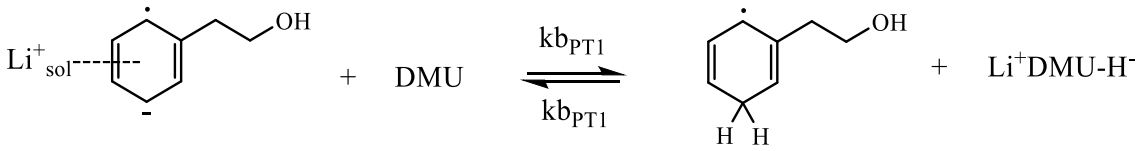

3a **3b** (6.7)

Following the first proton transfer step, the reduced radical intermediate then undergoes another cycle of electron transfer (eq. 6.8) and proton transfer (eq. 6.9) steps to finally form the desired diene product **4**.

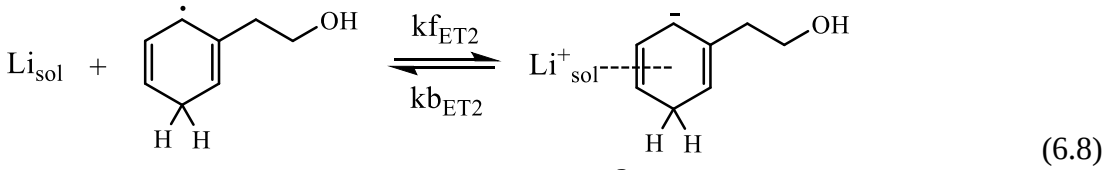

3b **3c_comp** (6.8)

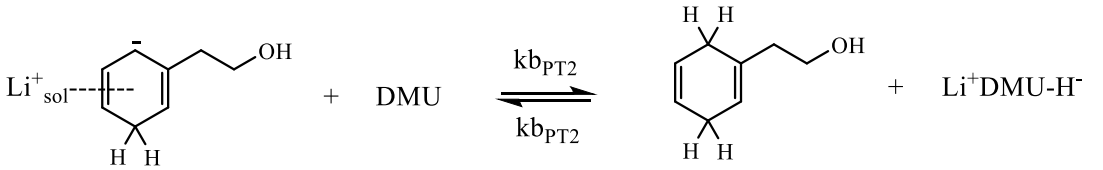

3c **4** (6.9)

From Figure 6.4 in the main text, the first protonation was found to be the rate determining step of the overall reaction. Hence, the rate law for the Li^0 mediated mechanism can be written as,

$$r = k_{PT1}[DMU][\mathbf{3a\_comp}] \quad (6.10)$$

where k_{PT1} is the rate constant for the first protonation step

Since the proton transfer step is the rate limiting step, the preceding electron transfer step can be assumed to be equilibrated and hence can be written as,

$$[\mathbf{3a\_comp}] = K_{ET1}[\mathbf{3}][Li_{sol}] \quad (6.11)$$

where, K_{ET1} is the equilibrium constant for the first electron transfer step

Using equations (6.10) and (6.11), the rate law for the Li^0 mediated mechanism can be further modified as,

$$r = k_{PT1}K_{ET1}[\mathbf{3}][Li_{sol}][DMU] \quad (6.12)$$

Hence, a first order rate with respect to the model substrate i.e. phenyl-ethanol (**3**) is observed for the Li^0 mediated mechanism, which is inconsistent with the experimentally derived kinetics

Electrode mediated mechanism

At high potentials (or low negative potentials), the adsorption of the substrate phenyl-ethanol (**3**) occurs in concurrence with a single facile electron transfer step to form the anion radical adsorbed intermediate (**3$_{ads}$**) as shown in eq. 6.13

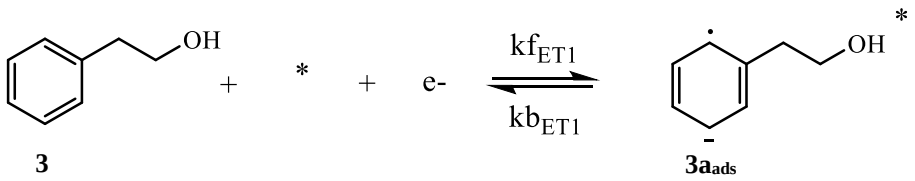

3 **3a$_{ads}$** (6.13)

Post adsorption, then the adsorbed intermediate (**3a$_{ads}$**) then likely undergoes a proton transfer in concert with another electron transfer step (eq. 6.14) to form the adsorbed protonated anion intermediate (**3c$_{ads}$**)

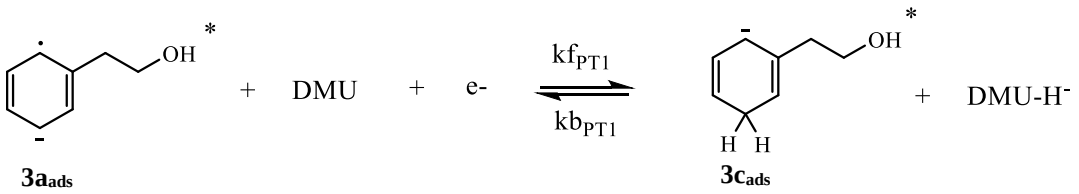

3a$_{ads}$ **3c$_{ads}$** (6.14)

The first proton-cum-electron transfer step is then followed by another proton transfer step (eq. 6.15) to give the adsorbed diene product (**4$_{ads}$**), which can then desorb (eq. 6.16) to form the final diene product (**4**) in solution.

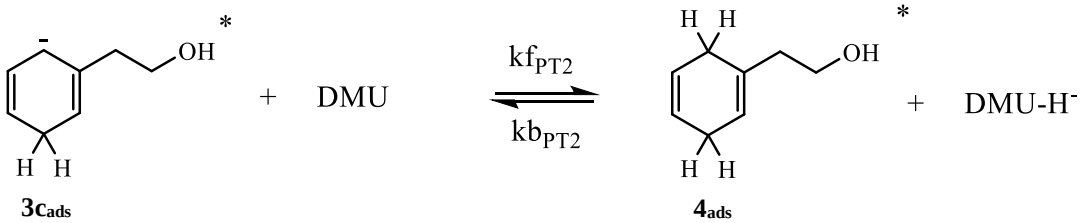

3c$_{ads}$ **4$_{ads}$** (6.15)

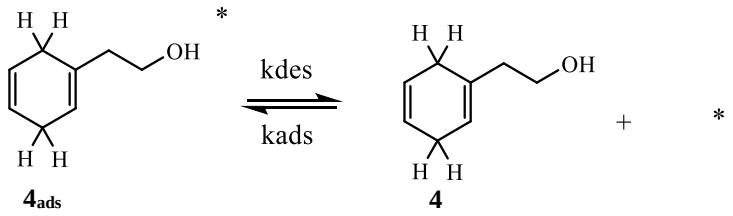

$\mathbf{4_{ads}}$ $\mathbf{4}$ (6.16)

The first protonation was found to be the rate determining step at high potentials (Potentials > -2.3 V). Hence, the rate law at high potentials can be written as,

$$r = k_{PT1}[DMU][\mathbf{3a_{ads}}] \quad (6.17)$$

where k_{PT1} is the rate constant for the first protonation step

Assuming the adsorbed phenyl-ethanol intermediate, $\mathbf{3a_{ads}}$ to be in equilibrium with its desorbed state, we get,

$$[\mathbf{3a_{ads}}] = K_{ET1}[\mathbf{3}][*][e^-] \quad (6.18)$$

where K_{ET1} is the equilibrium constant for adsorption-cum-electron transfer step

Using equations (6.17) and (6.18), the rate law for electrode mediated mechanism at high potentials can thus be written as,

$$r = k_{PT1}K_{ET1}[\mathbf{3}][*][DMU][e^-] \quad (6.19)$$

The total number of available sites (L) can be written as,

$$L = [*] + [\mathbf{3a_{ads}}] + [\mathbf{3c_{ads}}] + [\mathbf{4_{ads}}] \quad (6.20)$$

The intermediates $\mathbf{3c_{ads}}$ and $\mathbf{4_{ads}}$ are formed after the rate determining step and hence the concentrations of these surface intermediates can be assumed to be negligible. Further, from the free energy diagram shown in Figure 6.5, it can be seen that the free energy of adsorption to form $\mathbf{3a_{ads}}$ is endothermic by 2 kJ/mol. Hence, the free metal sites are likely the dominant surface sites present at higher potentials.

$$\text{Thus, } L \approx [*] \quad (6.21)$$

Using equations (6.19) and (6.21), we then get,

$$r' = \frac{r}{L} * S_p = k_{PT1}K_{ET1}[\mathbf{3}][DMU]S_p$$

where, S_p is the specific surface area of the electrode surface defined as,

$$S_p = \frac{\text{Electrode surface area (A)}}{\text{Volume (V)}} \tag{6.22}$$

Hence, for on-electrode kinetics at high potentials, we see a first order dependence with respect to the starting material (phenyl-ethanol), inconsistent with the experimentally determined kinetics.

At low potentials (or high negative potentials), the sequence of elementary steps can be written as follows wherein in the first adsorption-cum-electron step (eq. 6.23), instead of a single-electron process, there is a double electron transfer step that occurs, succeeded by two consecutive proton transfer steps (eqs. 6.24 and 6.15), followed by a desorption step (eq. 6.16) to give the desorbed diene product **4**,

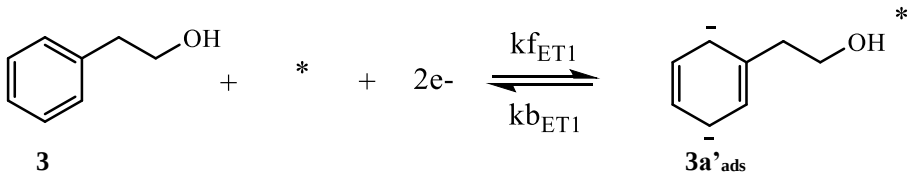

3 **3a'$_{ads}$** (6.23)

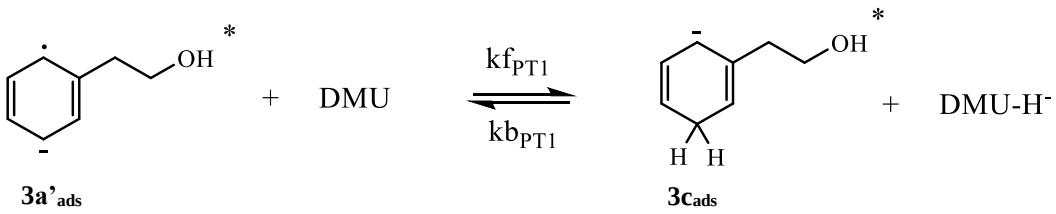

3a'$_{ads}$ **3c$_{ads}$** (6.24)

At lower potentials (Potentials < -2.3 V), the second protonation step becomes the rate determining step of the reaction. Hence, the rate law for on-electrode Birch reaction at low potentials can be written as,

$$r = k_{PT2}[DMU][\mathbf{3c_{ads}}] \tag{6.25}$$

where k_{PT2} is the rate constant for the second protonation step

From eq. 6.20, we have,

$$L = [*] + [\mathbf{3a_{ads}}] + [\mathbf{3c_{ads}}] + [\mathbf{4_{ads}}] \tag{6.20}$$

For reactions occurring at lower potentials, the lowest energy state preceding the rate determining step now corresponds to the adsorbed anionic intermediate (**3c$_{ads}$**) as can be seen from the free energy diagram in Figure 6.5. Hence, it can be assumed herein that

Thus, $L \approx [\mathbf{3c_{ads}}]$ (6.26)

Using equations (6.25) and (6.26), we then get,

$$r' = \frac{r}{L} * S_p = k_{PT2}[DMU]S_p \quad (6.27)$$

Hence, for on-electrode Birch reaction occurring at lower electrode potentials, we see a zeroth order dependence with respect to the starting material, which is consistent with the experimentally determined kinetics and hence is likely the operating mechanistic pathway for the Birch reaction.

6.7.11. XPS spectra of the electrode surface post reaction with and without TPPA

Experimental: X-ray Photoelectron spectroscopy (XPS)

Samples for XPS were generated using an IKA ElectraSyn 2.0 the optimized reaction conditions of a galvanized wire and magnesium anode were used. The substrate was naphalene (0.1 mmol) with the inclusion of TPPA (10 eq), DMU (3 eq) and LiBr (3.5 eq). The reaction was run for 3 hours at a constant current of 10 mA which realized nearly full conversion of the substrate determined via TLC. The post reaction electrodes were rinsed with THF and then placed under high vacuum in the XPS within a few hours after the electrochemical synthesis.

XPS was performed using a Physical Electronics Mg and Al kα X-ray source and energy spectrometer. The electrode was attached to a tantalum backing plate and analyzed in 1 x 10^{-10} torr ultra high vacuum. Survey and region scans were collected using Al Kα and Mg Kα radiation respectively. Al Kα was used for the surveys to allow observation of the full energy range, and Mg Kα was used for the region scans to increase the photoemission cross section for Li 1s. The energy scale was corrected for sample charging by reference to the reported binding energy for Zn $2p_{3/2}$ in ZnO, as reported in the NIST XPS database.[388] The shifts were 1.95 eV for a new, unreacted electrode, and 2.65 eV for the electrode analyzed after reaction.

High resolution region scans were integrated to estimate approximate atomic percentages. Intensities were corrected for their corresponding sensitivity factors, and concentrations were calculated as follows, where “I” is each emitting element present; “N” is corrected XPS intensity; “S” is the PHI atomic sensitivity factor; and “C” is concentration.

$$N_x = \frac{I_x}{S_x} \rightarrow C_x = \frac{N_x}{\sum_i N_i} \quad (6.28)$$

Note that this estimation method assumes that the sample is uniform over the sampling depth of XPS, i.e., roughly 2.5 – 5 nm depending on element.

Interpretation of XPS

The spectra from the unreacted electrode is quite different from that of the post-reaction electrode. A major change is the shift of the carbon peak to higher binding energies. The main carbon peak around 285 eV is shifted slightly to higher binding energies, indicating a greater number of C-O bonds. There is also a new carbon peak at a higher binding energy of ~ 290 eV (labeled oxC), that accounts for 9.6 % of the atomic percent in the sample. After electrolysis the oxC intensity doubles, relative to the intensity from adventitious carbon on the unreacted electrode. The source of the new carbon species is potentially from decomposition of the solvent, TPPA, or DMU which all contain C=O bond, thus supporting the idea that DMU and TPPA are involved at the electrode surface. The substantial increase in peaks for P (2.4%) and N (6.1%) in the post-reaction spectra also give evidence for the additives being present during electrolysis.

As expected, Lithium is present in relatively large quantities for the post-electrolysis electrodes. The lithium is most likely originating from solvent decomposition which can form lithium alkoxide, as well as lithium oxide species commonly found within the SEI layer of lithium ion batteries. The presence of magnesium in the post electrolysis electrode is logical as it could be acting as an electrolyte, especially at longer electrolysis times. The survey scan of a film generated with non-anhydrous conditions was drastically different than that with anhydrous conditions. The surface of the hydrous condition was composed almost entirely of Li, O, and C, indicating that surface chemistry is radically different if there is a readily available, labile proton source. The hydrous electrode also appeared to form a thicker film than the anhydrous electrode, as shown by the complete attenuation of Zn signal from the supporting electrode. In addition, the hydrous electrode also failed to achieve full electrolysis of the substrate. The hydrous electrode surface is completely devoid of N, P, and Mg, indicating that water is dominating the surface chemistry and the formation of the SEI layer.

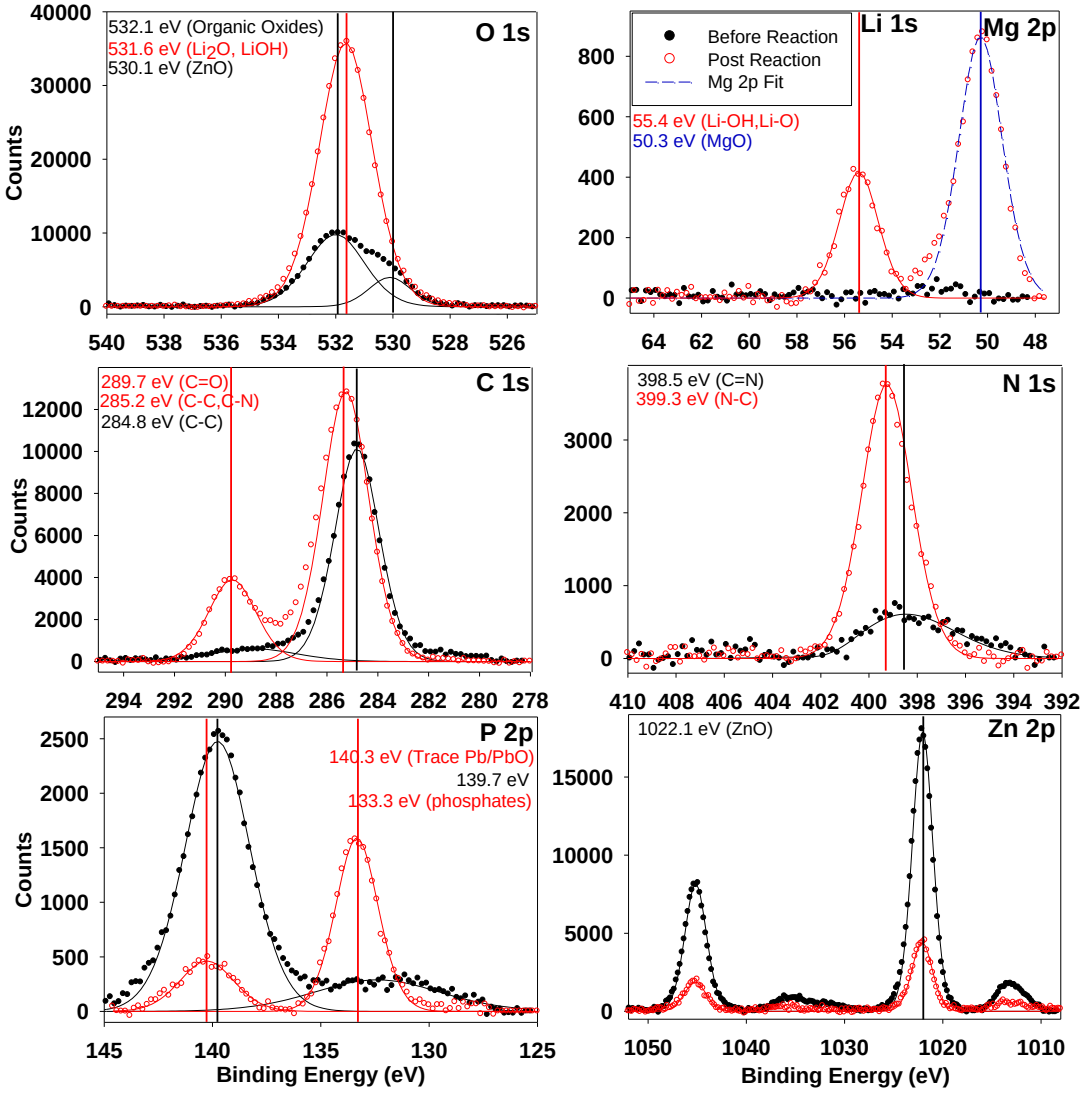

Figure S6.18: High resolution XPS spectra of zinc oxide (galvanized) steel wire before and post reaction. Inset values designate binding energies for specific chemical environments.

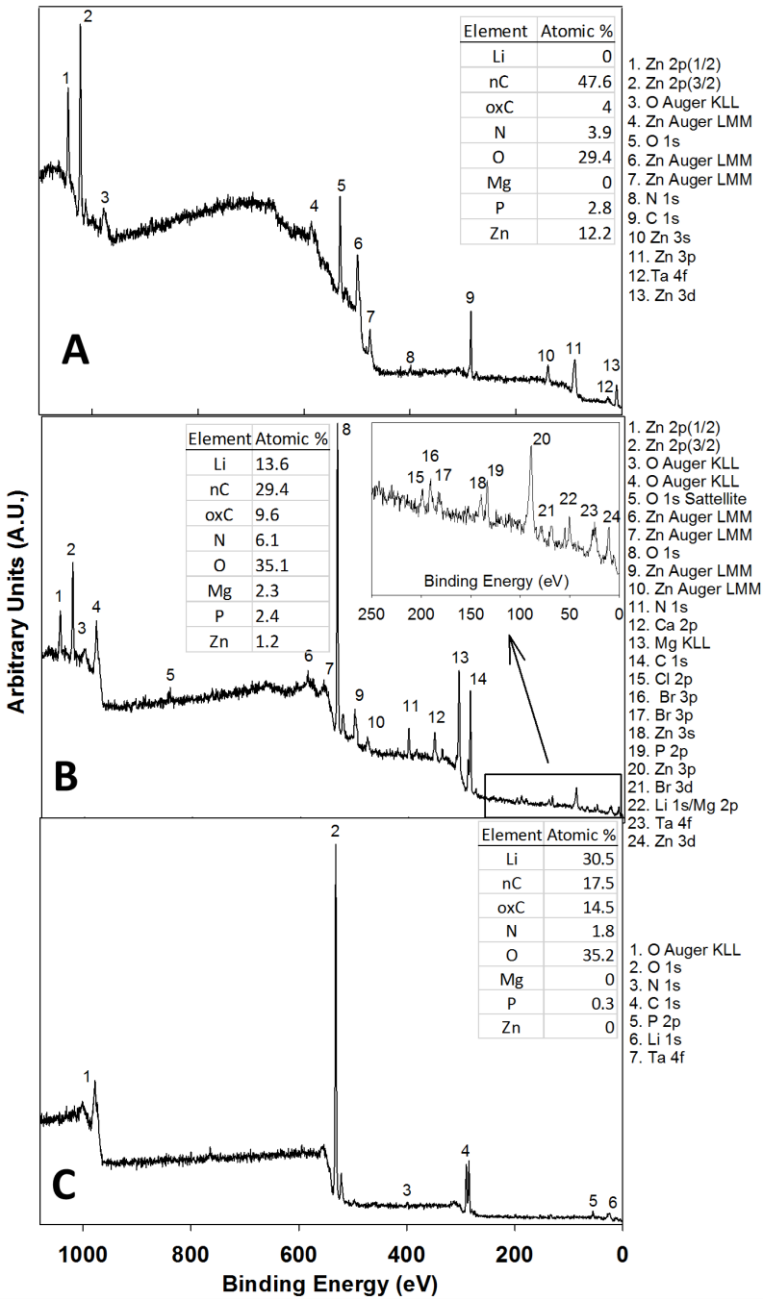

Figure S6.19: (A) Survey scan XPS spectra of zinc oxide (galvanized) steel wire before the electrochemical reaction and (B) post reaction. (C) Survey scan XPS of a zinc electrode post reaction that was run with wet THF stored in ambient conditions. The peaks are numbered and their corresponding identity is located to the right of the spectra. The inset shows atomic percent at the surface of the electrode. The percentages labeled nC and oxC refer to non-highly electron withdrawing groups attached to carbon (alkanes and alkenes) and highly oxidized carbons respectively.

6.7.12. Supplementary Figures

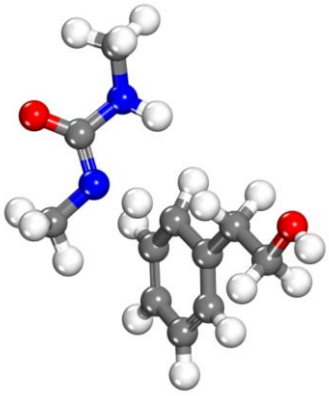

Figure S6.20: DFT-optimized transition state for protonation of $PEA^{-\cdot}$ (**3a**) using DMU. The red, blue, grey, and white spheres refer to the oxygen, nitrogen, carbon and hydrogen atoms respectively.

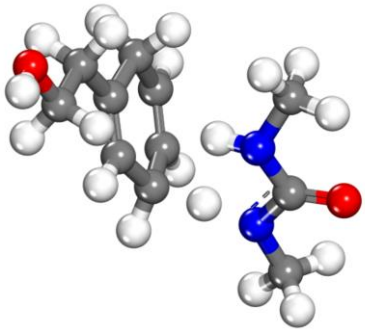

Figure S6.21: DFT-optimized transition state for protonation of $PEAH^{-}$ (**3c**) using DMU. The red, blue, grey, and white spheres refer to the oxygen, nitrogen, carbon and hydrogen atoms respectively.

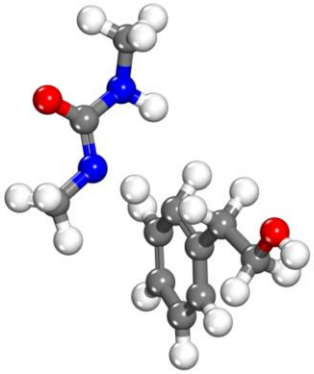

Figure S6.22: DFT-optimized transition state for protonation of PEA^{-2} (**3a'**) using DMU. The red, blue, grey, and white spheres refer to the oxygen, nitrogen, carbon and hydrogen atoms respectively.

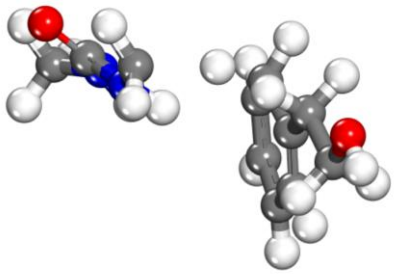

Figure S6.23: DFT-optimized transition state for HAT reaction of $PEA^{-\cdot}$ (**3a**) using DMU. The red, blue, grey, and white spheres refer to the oxygen, nitrogen, carbon and hydrogen atoms respectively.

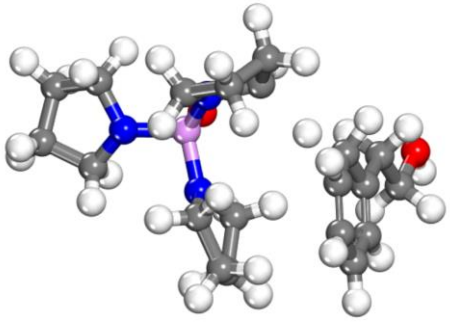

Figure S6.24: DFT-optimized transition state for HAT reaction of $PEA^{-\cdot}$ (**3a**) using TPPA. The pink, red, blue, grey, and white spheres refer to the phosphorous, oxygen, nitrogen, carbon and hydrogen atoms respectively.

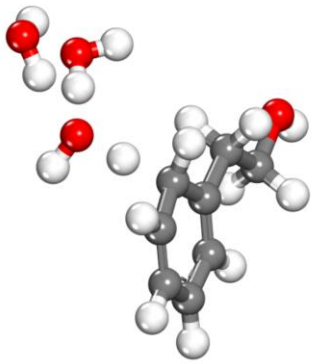

Figure S6.25: DFT-optimized transition state for protonation of $PEA^{-\cdot}$ (**3a**) using water. The red, grey, and white spheres refer to the oxygen, carbon and hydrogen atoms respectively.

Transition state for HAT via THF: Efforts to isolate the transition state for the HAT reaction using THF were unsuccessful. The transition state barrier for HAT reaction using THF was thus approximated as energies of the product state of the HAT reaction.

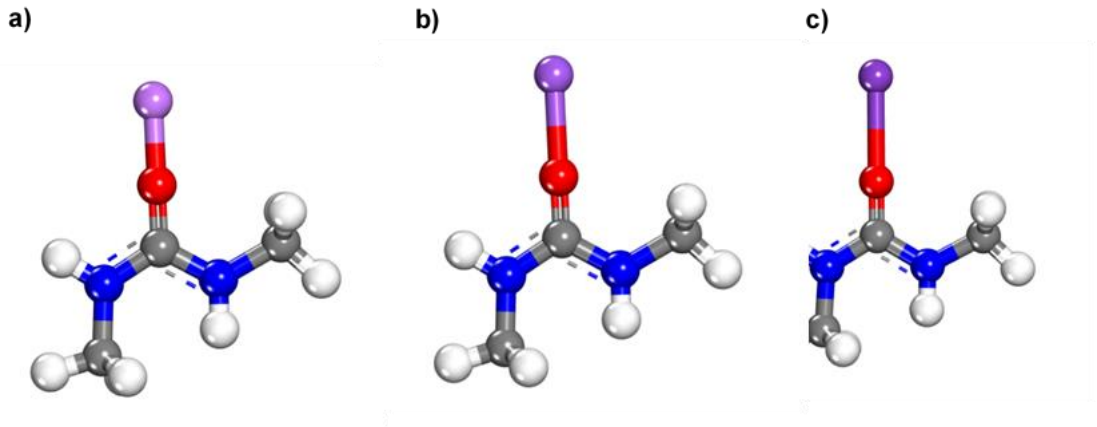

Figure S6.26: DFT-optimized structures for binding of DMU to a) Li^+ b) Na^+ and c) K^+. The purple, red, blue, grey, and white spheres refer to the oxygen, nitrogen, carbon and hydrogen atoms respectively.

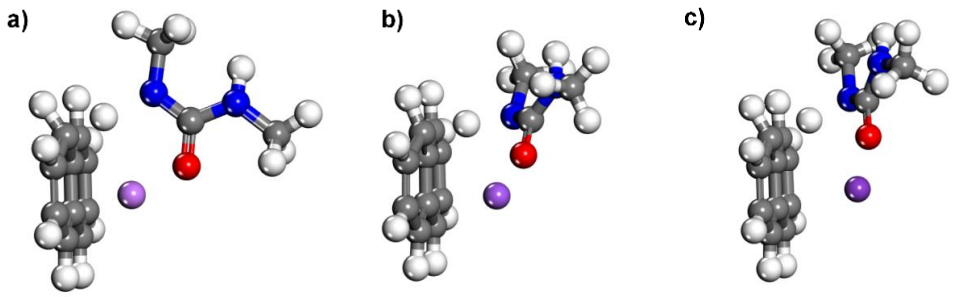

Figure S6.27: DFT-optimized structures for binding of naphthalene$^{\cdot-}$ to a) Li^{+}DMU b) Na^{+}DMU and c) K^{+}DMU. The purple, red, blue, grey, and white spheres refer to the oxygen, nitrogen, carbon and hydrogen atoms respectively.

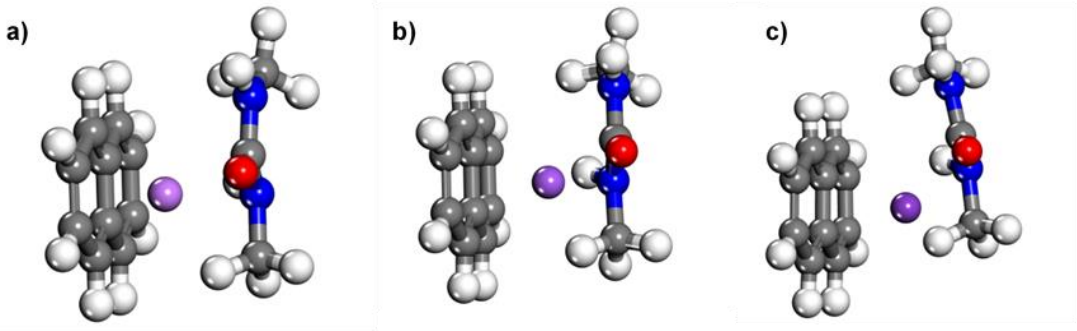

Figure S6.28: DFT-optimized transition structure for the dissociative protonation of naphthalene$^{\cdot-}$ involving a) Li^{+}-DMU-Naphthalene$^{\cdot-}$ b) Na^{+}-DMU-Naphthalene$^{\cdot-}$ and c) K^{+}-DMU-Naphthalene$^{\cdot-}$ complex. The purple, red, blue, grey, and white spheres refer to the oxygen, nitrogen, carbon and hydrogen atoms respectively.

Chapter 7 - Visualizing the Metal-MoS_2 Contacts in 2D Field Effect Transistors with Atomic Resolution

Reprinted with permission from Wu, R.J., Udyavara, S., Ma, R., Wang, Y., Chhowalla, M., Birol, T., Koester, S.J., Neurock, M., and Mkhoyan¸ K.A. Visualizing the Metal-MoS_2 Contacts in 2D Field Effect Transistors with Atomic Resolution, Phys. Rev. Mat. **2019**, 3, 111001.

Theoretical calculations were done by SU under the supervision of MN

7.1. Synopsis

Two-dimensional MoS_2 is an excellent channel material for ultra-thin field effect transistors, but high contact resistance across the deposited metal-MoS_2 interface continues to limit its full realization. Using atomic-resolution scanning transmission electron microscopy and first principle calculations, we showed that deposited metals with high affinity for sulfur could have a fundamental limitation. Ti-MoS_2 contact shows a destruction of the MoS_2 layers, a formation of clusters and void pockets, and penetration of Ti into MoS_2, resulting in many localized pinning states in the band gap. InAu-MoS_2 contact shows that it is possible to achieve van der Waals-type interface and dramatically reduced pinning states.

7.2. Introduction

Ultra-thin field effect transistors (FETs) using MoS_2 as the channel material have shown excellent performance, making them viable for sub-10 nm node devices.[66,67,389–391] However, the contact between the 2D MoS_2 and evaporated 3D metal electrode remains a challenge due to the high contact resistance[68,69,71] attributed to Fermi level pinning at the interface.[70,392–394] Although alternative approaches[69,395–400] to depositing the metal onto MoS_2 have been reported,[401–403] including direct metal film transfer which results in van der Waals (vdW) bonding,[404,405] the origin of high contact resistance using evaporated metals remained unclear. Previous reports have attributed the Fermi level pinning to the formation of surface states created by adsorbed contaminants[406] or damage by kinetic energy transfer from metal deposition.[404] While these factors could play a role, they should be resolvable by improving metal deposition. On the other hand, the actual bonding between metal and MoS_2 layer is a

more fundamental issue. The recent report by Wang et al[407] shows that when In or In_xAu_y is used as contact metal, low-resistant vdW contact can be achieved even with evaporated metal deposition. Therefore, understanding of the metal-MoS_2 interface from direct atomic-scale observations can be instrumental in mitigating Fermi level pinning.

To elucidate the structure of the metal-MoS_2 interface, we first studied deposited Ti contacts. In addition to Ti,[70,393,408,409] other metals, such as Au, Pt, Ag, Sc, Pd, Ni, and Cu, were also used as contact,[390,404,408,410] but Ti provides a good case for a metal-MoS_2 interface with strong bonds, as Ti possesses a very high affinity for sulfur (Ti-S bond dissociation energy is 4.35 eV compared to Mo-S at 3.69 eV).[282] We also studied the In_xAu_y-MoS_2 interface, where vdW-type bonding was reported.[407] Interfaces are studied using combination of atomic-resolution scanning transmission electron microscopy (STEM) imaging with electron energy-loss spectroscopy (EELS). Density functional theory (DFT) calculations are carried out to further clarify the structural and electronic changes occurring at the deposited metal-MoS_2 interface.

7.3. Results and Discussion

The STEM specimens were prepared by FIB thinning of working FETs (see SM, Methods and Materials, Figure S7.1) with characteristics similar to those reported in literature.[411,412] Figure 7.1(a,b) show the schematic layout of the FETs and a low-magnification cross-sectional ADF-STEM image where the Au/Ti contact and Si/SiO_2 substrate bookend the MoS_2 layers (see SM, Figure S7.2). High-magnification ADF-STEM image (Figure 7.1c) shows that along the Ti-MoS_2 interface, there are areas where the Ti contacts the MoS_2 and alters the structure of the topmost layer. Next to these areas, small void pockets are visible which leaves the topmost MoS_2 layer pristine. While there are reports suggesting that Ti form strong bonding with MoS_2,[406,409] to the best of our knowledge, this is the first direct observation of (i) degradation of the topmost MoS_2 layer and (ii) presence of the nm-size void pockets along the interface. The Ti atoms tend to not only bond, but also cluster on MoS_2 surface during deposition. Such Ti clustering behavior was predicted[406] but never observed experimentally (see SM, Figure S7.3, for additional images). It should be noted that under the conditions of Ti deposition used here, no damage to MoS_2 layers should be occurring.

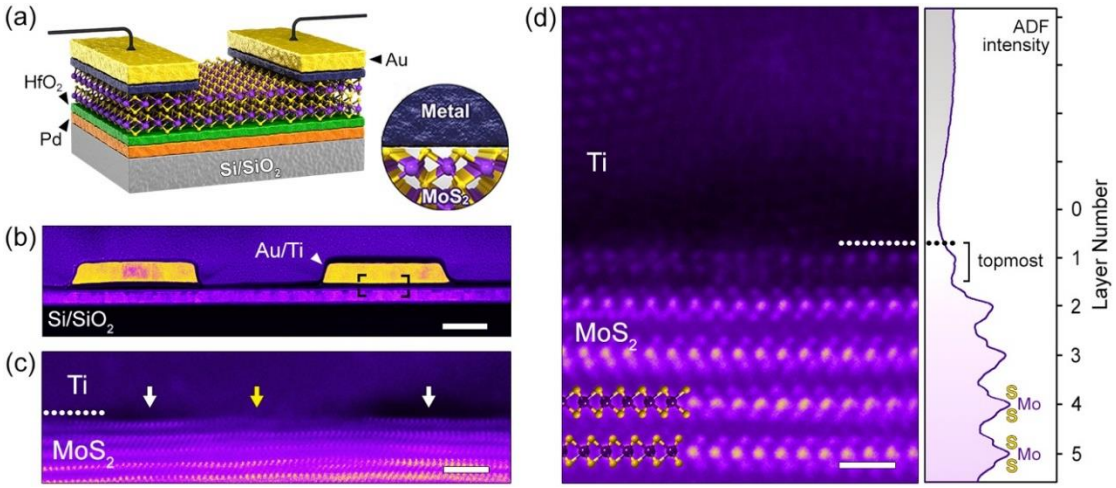

Figure 7.1 (a) Schematic layout of the FET with MoS_2 channel and metal contacts. (b) Low-magnification cross-sectional ADF-STEM image of the FET. The protective amorphous C/Pt layers are also visible here. Scale bar is 0.2 µm. (c) High-magnification image of the Ti-MoS_2 interface from the boxed area in (b). An area where Ti is clustered is indicated by a yellow arrow and areas with void pockets by white arrows. Scale bar is 2 nm. (d) Atomic-resolution ADF-STEM image of the Ti-MoS_2 interface. The horizontally-averaged ADF intensity is shown on the right. A ball-and-stick model of MoS_2 is overlaid on the image. Scale bar is 6 Å.

An atomic-resolution ADF-STEM image (Figure 7.1d) obtained from one of these Ti-clustered areas shows that the topmost MoS_2 layer is degraded and barely identifiable. The compromised integrity of the topmost MoS_2 layer indicates that the bonding between Ti and S is strong enough to restructure the contacting MoS_2 layer. This Ti-driven restructuring of the topmost MoS_2 layer is far beyond the effects of carbon or oxide contaminants on the surface of the MoS_2 as: (i) no degradation is observed in the sections of the MoS_2 layers under the void pockets which have same level of contaminants and (ii), in areas of the device not directly below the Ti contacts, the MoS_2 remains pristine (see SM, Figure S7.3). A slightly lower intensity of the ADF signal in the Ti region directly above the 1st MoS_2 layer is likely due to void pockets in projection, or nm-thick Ti sublayer with lower atomic density, or both.

To measure the changes in the electronic structure of MoS_2 caused by the Ti contact, layer-by-layer EELS analysis was performed. Core-level EELS edges measure localized changes in the element-specific electronic density of states (DOS) of the

conduction band.[413] Figure 7.2a shows two S $L_{2,3}$ edges measured from the MoS_2 channel: one from layer 1, the topmost MoS_2 layer directly in contact with Ti, and from layer 5. The dominating features of the S $L_{2,3}$ fine structure, peaks I and II, composed of S 3*s* and 3*d* partial-DOS[414] are different in these spectra. The peaks are more subdued in layer 1, which is consistent with observed loss of crystallinity of the top MoS_2 layer.[413] Additional S $L_{2,3}$ edge EELS measurements from the MoS_2 not in contact with Ti showed no differences between the first and fifth MoS_2 layers (see SM, Figure S7.4).

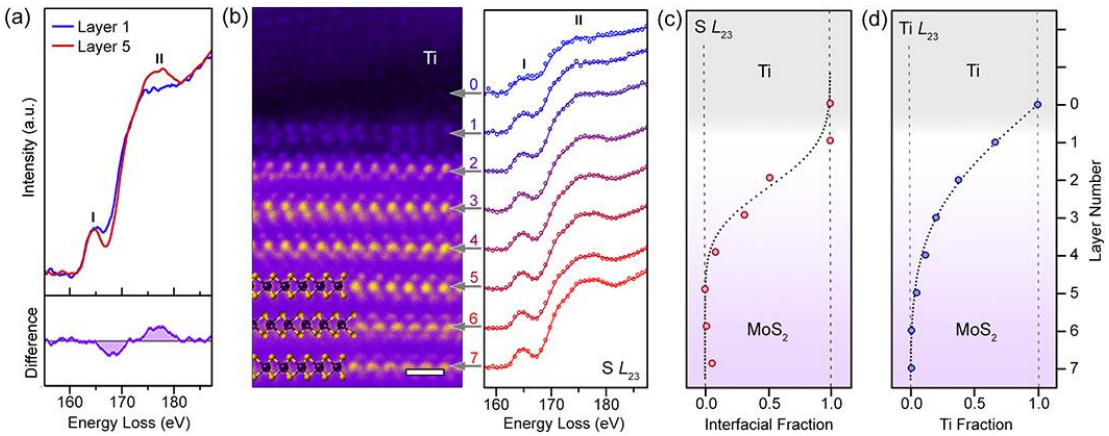

Figure 7.2: (a) EELS S $L_{2,3}$-edges measured from the first (contacting to Ti) and the fifth MoS_2 layers. The differences between the two spectra are shown below. (b) (left) Atomic-resolution ADF-STEM image of the MoS_2 layers and (right) EELS S $L_{2,3}$ edge measured from the layers. Scale bar is 5 Å. Measured spectra are shown as scatter points and fitted spectra are shown as lines. (c) The fractions of the interfacial (layer 1) character in each S L_{23} edge. (d) The fraction of Ti in MoS_2 layers. A $y = erf(x)$ fit through the data points in (c) and (d).

Figure 7.2b shows a set of core-level EELS measurements from each of the first seven MoS_2 layers and from the Ti contact layer directly above the MoS_2. Changes in peaks I and II of the S $L_{2,3}$ edge were quantified by fitting each spectrum to a linear superposition of the two reference spectra shown in Figure 7.2a,[415] and the fractions of the spectrum with interfacial and bulk characters were evaluated (Figure 7.2c). Layer 2 and even layer 3 of the MoS_2 have considerable interfacial character indicating that the effects of the Ti contact go beyond the surface layer (for minor effects of probe broadening, see Methods and Materials).

The presence of Ti atoms in deeper MoS_2 layers was also considered. The Ti $L_{2,3}$ edge was measured across the first seven MoS_2 layers (Figure 7.2d). Layers 2 and 3 also showed an appreciable amount of Ti present. The amounts of Ti present in layers 2 and 3 could be a factor in observed changes in the fine structure of the S $L_{2,3}$ edge at these depths. However, they are not high enough to affect the pristine-like view of the atomic structure imaged in projection (Figure 7.1d).

DFT calculations were carried out to understand the interactions of Ti atoms with MoS_2 layers. In these simulations, individual Ti atoms were systematically added onto the surface of a monolayer MoS_2 to mimic experimental deposition. This "single-atom-addition" approach provides new insight into atomic processes occurring at the metal-MoS_2 interface during deposition, and complements the "metal-MoS_2-slab" approach,[416–418] which models metal contacts directly transferred onto MoS_2.[404] Simulations were performed without the effects of temperature and Ti atoms were added without kinetic energy (for details, see SM, Methods and Materials).

Figure 7.3(a,b) shows the calculated lowest energy structures of the Ti-MoS_2 interfaces after the addition of one to five Ti atoms. As will be clear later, five-atom-cluster of Ti was sufficient to explain the main STEM observations discussed earlier. The interactions between the Ti and S is indeed strong enough to disrupt the MoS_2 by pulling S atoms out of the MoS_2 surface. Calculations also show the formation of a cluster, which degrades the pristine crystal structure of MoS_2. Furthermore, even with only five Ti atoms, relatively large opening in the MoS_2 layer is formed (Figure 7.3b). This "nanopore" in the MoS_2 is large enough to allow the sixth Ti atom to penetrate and cause more structural modifications (Figure 7.3c). These results match with the experimentally observed structural degradation of topmost MoS_2 layer and provide a pathway to how appreciable amounts of Ti could penetrate into the 2nd and 3rd layers of MoS_2. They also imply that the disruption of the MoS_2 crystal is inherent to Ti-MoS_2 bonding and cannot be avoided. Additional *ab-initio* molecular dynamic (AIMD) calculations for 5-Ti-atom cluster confirm its thermal stability at room temperature (T = 300K) (see SM).

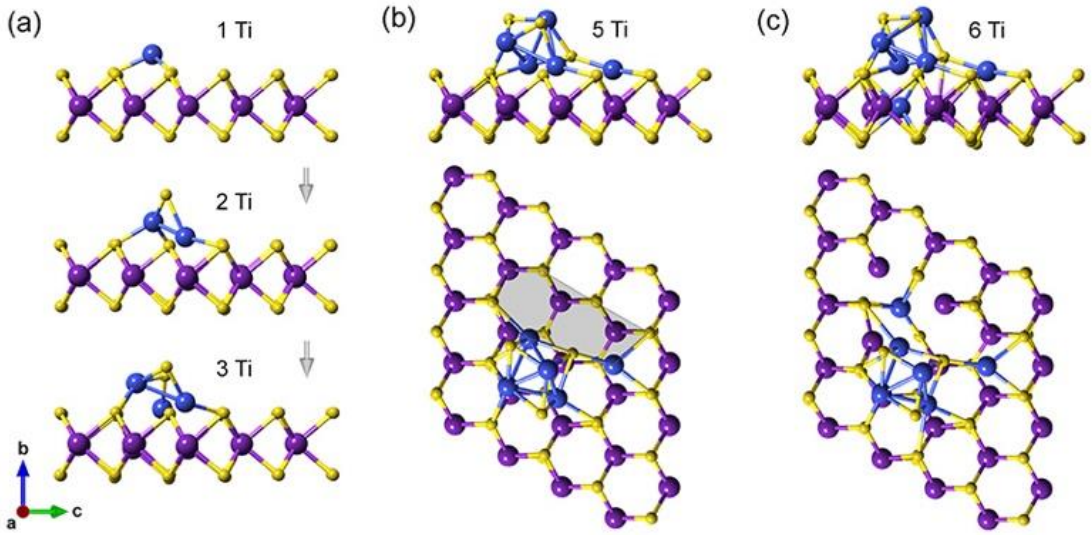

Figure 7.3: (a) Models showing the lowest energy optimized structures of the Ti-MoS_2 system following additions of one, two, and three Ti atoms (Mo – purple, S – yellow, Ti – blue). (b) Side view (above) and top view (below) of the Ti-MoS_2 system with five added Ti atoms. An opening in the MoS_2 layer is highlighted as the grey shaded region. (c) Side view (above) and top view (below) of the Ti-MoS_2 system showing the penetration of the sixth Ti atom into the opening highlighted in (b).

The electronic band structures and DOS for pristine monolayer MoS_2 and for the MoS_2 with five bonded Ti atoms, shown in Figure 7.3c, were calculated (Figure 7.4). As can been seen, a cluster of five Ti atoms will force the system to have many localized states in the band gap, some of which will act as pinning states for charge carriers. These band gap states appear to be located on all three atomic species (Mo, S, and Ti) and likely pin the Fermi level at the interface.[392,419]G The degradation of the crystallinity of the MoS_2 also results in removal of degeneracies in the band structure and the flattening of the bands leading to dispersed DOS, which was observed in S $L_{2,3}$ EELS measurements (Figure 7.2a).

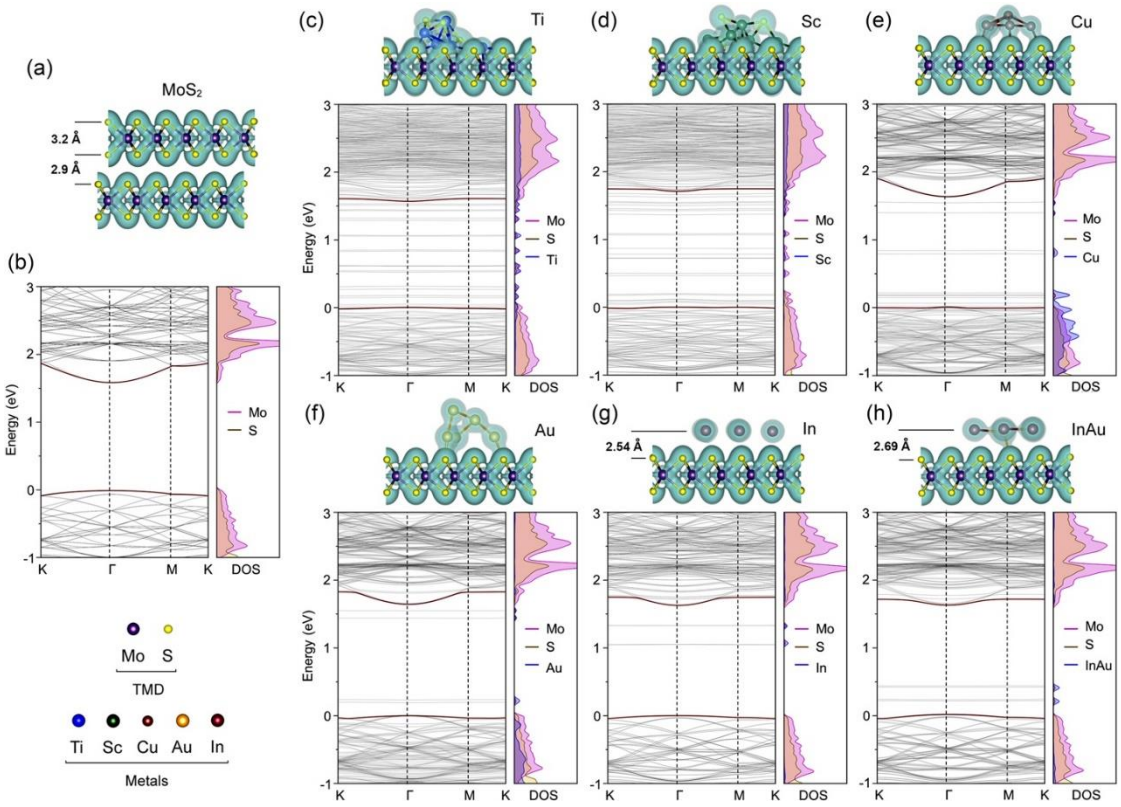

Figure 7.4: (a) The atomic structure of bilayer MoS_2 with distances between sulfur layers indicated. (b) Electronic band structure and element-specific DOS for pristine monolayer MoS_2. The atomic and electronic band structure of monolayer MoS_2 with five atoms of Ti, Sc, Cu, Au, In and In_xAu_y (with three In and two Au) (c-h). The charge densities for all structures are shown in transparent green on the top of the corresponding band structure. An iso-surface value of 0.042 was chosen conservatively to ensure that the charge densities of the Cu atoms overlap. The minimum of conduction band and maximum of valence band are highlighted by maroon colors.

The DFT calculations using the "single-atom-addition" approach, were extended to other metals: Sc, Cu, Au, In, In_xAu_y (Figure 7.4). The results show that Sc, a transition metal like Ti, clusters and disrupts the MoS_2 layer. Both, Sc and Ti disperse the valence and conduction bands and create a high number of pinning states in the band gap. In contrast, Cu and Au bind weakly to the surface sulfur and do not disrupt the structure of the MoS_2 layer. Their effects on the electronic band structure of MoS_2, including number of new band gap states, are also weaker. Of the metals studied, In and In_xAu_y are the least disruptive. The charge density plots in Figure 7.4 show that In and In_xAu_y bind to MoS_2 through vdW-type bonds, and leaves the MoS_2 structure intact (for thermal stability of 5-In-atom cluster at T = 300 K, see SM]). This is also reflected on

the electronic states, where the number of band gap states introduced by In or In_xAu_y is very low. The calculations suggest that In or In_xAu_y should show minimum pinning and very low contact resistance, which is consistent with measured low contact resistance in the FETs reported by Wang et al.[407] In case of In_xAu_y alloy, In provides vdW-type bonding to MoS_2 with very low number of gap states, while Au provides bonds with light ionic character without considerably modifying the surface of MoS_2 and, therefore, low-barrier electron transition paths across the vdW gap. Due to similarities between Au and Cu contacts to MoS_2 layer (Figure 7.4(e,f)), In_xCu_y alloy could also be good candidate for low-cost, higher melting point metal with vdW-type low contact resistance. Calculations show that even in the presence of S vacancy at the MoS_2 surface In atoms bind with vdW-type bond, while Ti atoms, as before, disrupt the MoS_2 with strong Ti-S bonds (see SM, Figure S7.5).

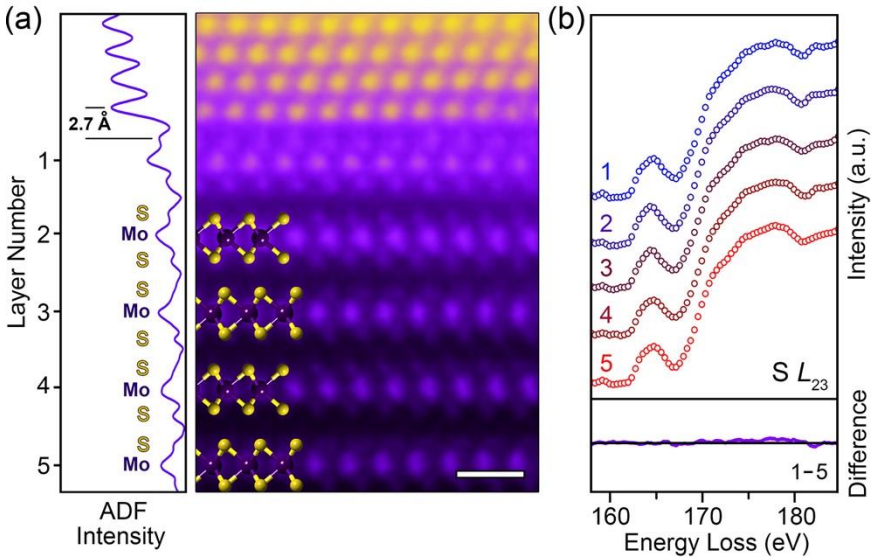

Figure 7.5: (a) Atomic-resolution ADF-STEM image of the In_xAu_y-MoS_2 interface. The horizontally-averaged ADF intensity is shown on the left. Scale bar is 5 Å. (b) EELS S $L_{2,3}$ edge measured from MoS_2 layers 1 to 5. The difference spectrum between the first (contacting to the In_xAu_y) and the fifth MoS_2 layers is shown below.

STEM-EELS experiments were performed for the In_xAu_y-MoS_2 interface[407] to compare with the results of DFT calculations based on "single-atom-addition" approach. Atomic-resolution ADF-STEM image and corresponding EELS characterization of the MoS_2 layers are presented in Figure 7.5. As can be seen the In_xAu_y-MoS_2 contact is non-disruptive and the topmost MoS_2 layer appears completely intact. The distance between top sulfur layer and first atomic layer In_xAu_y is 2.7 ± 0.1 Å, which matches

well with the DFT predicted distance of 2.69 Å. EELS measurements of S $L_{2,3}$ edge show no detectable differences between spectra from layer 1, the topmost MoS_2 layer directly in contact with In_xAu_y, and the bulk-like MoS_2 layer 5 (Figure 7.5b), which is also consistent with the results of DFT calculations showing very minor changes in conduction band DOS.

7.4. Conclusion

In conclusion, the atomic-resolution STEM-EELS study of a metal deposited metal-MoS_2 interface shows that for Ti the strength of the metal-sulfur interaction is sufficient to result in degradation of the surface MoS_2 layer, penetration of Ti into deeper layers, clustering of Ti atoms and formation of void pockets making the interface inhomogeneous. DFT calculations suggest such structural modifications of the metal-MoS_2 interface are inherent for systems where the metal has a very high affinity for sulfur (Ti, Sc, etc). Band structure calculations suggest that the Fermi level pinning in such systems is likely unavoidable. In contrast, for a metal with low affinity for sulfur, such as In, the resulting interface can become vdW-type. While the Fermi level pinning might still be present for a wide-variety of metals, including Au or Cu, they can be dramatically mitigated with the proper selection of a metal or alloy, such as In, In_xAu_y or In_xCu_y. Introduced here "single-atom-addition" approach in DFT calculations can be effective method to evaluate the effects of deposited metals on MoS_2 and other layered materials.

7.5. Methods and Materials

Ti-MoS_2 Deposition and FET Fabrication

The MoS_2 FETs were fabricated on a Si substrate with a 100 nm SiO_2 layer grown by dry thermal oxidation. Local back gate contacts were patterned on the substrate by first spin-coating polymethyl methacrylate (950 ka.u. PMMA) followed by e-beam lithography on a Vistec EBPG 5000+. After development in methyl isobutyl ketone (MIBK): IPA (1:3 ratio), a 5 s oxygen plasma (Vision 320) was used to remove the PMMA residues on the exposed SiO_2 regions. The exposed SiO_2 were then recessed by using reactive ion etching with CHF_3 /CF_4 /Ar (Vision 320) to create a 40 nm deep recess followed by a wet etch in 1:10 buffer oxide etch (BOE) for 12 s to create a 50

nm recess in total. The recess depth was confirmed with a KLA-Tencor P-7 surface profilometer.

The Ti/Pd gate electrodes (10nm/40nm) were evaporated using e-beam deposition (CHA SEC-600) in $8.7x10^{-7}$ Torr pressure (the base pressure) chamber. The measured pressure at the middle of the deposition was about $4.7x10^{-7}$ Torr. After lift-off in acetone, 7 nm HfO_2 gate dielectric was deposited by atomic layer deposition (Veeco Savannah) using tetrakis(dimethylamido) hafnium(IV) and water vapor as the precursors. MoS_2 flakes were then mechanically exfoliated and transferred onto polydimethylsiloxane (PDMS) stamps activated on glass slides. Few-layer MoS_2 flakes were identified, aligned, and transferred from the PDMS stamp onto the gate electrodes using an optical alignment station. The MoS_2 crystal (geological) was purchased from SPI (CAS #1317-33-5).

Finally, the Ti/Au (10nm/80 nm) source and drain contacts were patterned, developed, and evaporated using the same method as the gate electrodes and lifted off in acetone overnight to complete the device fabrication. A Ti slug was used as the source. Prior to deposition, two soak steps were used: (1) soak step with a 6 % beam power (36 mA beam current) for one minute, which is the outgassing step, and (2) soak step with an 8 % beam power (48 mA beam current) also takes one minute, which prepares the source to near its evaporation. The deposition rate for Ti and Au was 0.1 nm/s and 0.2 nm/s, respectively. According to previous work by Freedy et al,[420] this deposition rate leads to very-low Ti oxidation. Our additional layer-by-layer STEM-EELS measurements showed no detectable oxygen at the interface, but some trace amount of oxygen and other contaminates (below EELS detection limits) could still be present at the interface. Under these e-beam evaporation conditions, Ti atoms will land on the MoS_2 surface with thermal energy of about 0.2-0.3 eV,[421,422] which is an order of magnitude less than the energy needed to break a single Mo-S bond in MoS_2 (2.3 eV).[423]KomK No surface passivation was utilized. A Lakeshore CPX-VF vacuum probe station was used for device characterizations. The results of these measurements are shown in Figure S7.1. The measured on-off ratios and total resistivities of these devices are comparable to those reported previously in Liu et al.[412] and Kshirsagar et al.[411]

STEM Specimen Preparation

Cross-sectional lamellas of the FET samples were prepared using FEI Helios NanoLab G4 focused ion beam (FIB). To protect the samples, 50 nm a:C and 2 µm Pt layers were deposited prior to ion milling. The bulk of the ion milling was performed using 30 kV Ga ions. Subsequently, lower energy (5 keV, 2 keV, and 1 keV) Ga ions were used to remove damaged surface layers. The prepared TEM specimen was then plasma cleaned for 15s using a Fischione 1070 NanoClean plasma cleaner with a 30 sccm mixture of 75% Ar and 25% O_2 before insertion into the STEM.

STEM Operating Parameters

All STEM characterizations were performed using FEI Titan G2 60-300 aberration-corrected and monochromated STEM equipped with a CEOS DCOR probe corrector operating at 200 keV. The microscope is also equipped with a Gatan Enfinium ER EEL spectrometer and a SuperX EDX spectrometer for EELS and EDX acquisition, respectively. The probe convergence angle was measured to be 24 mrad. ADF-STEM images were acquired with 2048 x 2048 pixilation using a dwell time of 6 µs and a beam current of ~ 30 pA. The HAADF detector inner angle was ~ 50 mrad. At these operating conditions, the STEM spatial resolution is measured to be ~ 0.8 Å, determined by standard fast Fourier transform analysis of atomic resolution ADF-STEM images of a reference Au cross-grid sample. EDX spectrum images were collected using the Bruker (Esprit 1.9) software with frame-by-frame spatial drift correction. Frames were collected with a dwell time of 1 µs for a 1024x1024 pixel grid and summed together during continuous acquisition for 20-30 min. EDX signal was measured with an energy window from 0 to 20 keV with a dispersion of 1 eV/channel. All EELS measurements were collected in dual-mode to enable simultaneous collection of a zero-loss and a core-loss spectrum to compensate for energy drift during specimen acquisition. The energy drift was measured by continuously collecting zero-loss spectra for 5 mins and was determined to be about 0.06 eV/min. Each EELS acquisition was performed at 5-10 pA beam current with no detectable specimen damage at a camera length of 38 mm for total collection time of 100 s. The beam was allowed to scan continuously for the entire collection duration in the area of interest with a dwell time of 0.4 µs. The energy resolution was measured to be ~ 0.45 eV at 0.1 eV/channel dispersion for all core-level measurements.

Analysis of EELS S and Ti L_{23} Edges

The S L_{23} EELS spectrum from each MoS_2 layer in the measured datasets was linearly fitted as $I_n^S = \alpha_1 I_1^S + \alpha_2 I_5^S$, where I_1^S and I_5^S are the S L_{23} EELS spectra from layer 1 and layer 5, respectively, and I_n^S is the resulting best-fitted spectrum for layer n as determined by a standard least-squares fit.[424] α_1 and α_2 are normalized fitting parameters ($\alpha_1 + \alpha_2 = 1$) representing fractions of the interfacial and bulk-like contributions to layer n. Figure 2(c) of the main text shows the coefficient α_1 of each layer averaged over 5 different S $L_{2,3}$ EELS datasets (see Supplementary Figure 7.6). The EELS spectrum from MoS_2 layer 1 was selected as the interfacial reference because it is the nearest layer to the Ti. The spectrum from layer 5 was selected as the bulk-like reference because no detectable changes were observed between spectra from layer 5 and 6. Using layer 6 as the bulk-like reference results in insignificantly different fitting coefficients. Similarly, Ti $L_{2,3}$ EELS datasets from each MoS_2 layer, and the location directly above layer 1 (layer 0), were used to evaluate the fraction of total Ti in each layer relative to layer 0 as $I_n^{Ti} = \alpha I_0^{Ti}$, where I_0^{Ti} and I_n^{Ti} are the EELS spectra for layer 0 (the reference) and layer n, respectively, and α is the single fitting parameter. Figure 7.2d of the main text shows the coefficient α for each the layer averaged over 6 different EELS datasets.

Evaluation of Electron Beam Broadening

Electron beam propagation through MoS_2 was simulated using the TEMSIM Multislice package[425] in order to estimate the electron beam broadening in these experiments. The simulation carried out for a 200 keV aberration-free ($C_{s(3)}$, $C_{s(5)}$, $\Delta f = 0$) electron probe with probe convergence angle of 24 mrad. These simplified probe parameters approximate very well the aberration-corrected experimental conditions.[426] Transmission and probe functions were both calculated with 1024 x 1024 pixilation. Effects of thermal displacement were approximated using 20 frozen phonon configurations. Root mean square displacement values used were 0.071 Å and 0.045 Å, for sulfur and molybdenum, respectively.[427,428] The simulated STEM probe was positioned in 64 unique 2D locations of the MoS_2 unit cell along the [110] direction in order to capture possible beam channeling effects. At each probe location, the beam intensity was recorded at 1.5 Å increments during propagation through a 50-nm-thick slab of MoS_2. The resulting 2D beam intensity maps were convoluted with a 1 Å

FWHM Gaussian function to account for the finite source size.[425] The intensity maps from all the unique probe locations and thicknesses were first aligned by the initial beam position and then averaged into a single intensity map. Finally, the averaged 2D intensity map was averaged radially to generate a 1D radial intensity plot. The beam broadening reported in the main text is the distance at which the integrated beam intensity is half of the total intensity. The procedure yielded 5.5 Å which is less than the thickness of a single layer of MoS_2, d = 6.15 Å.[429]

Density Functional Theory Parameters

All of the reported DFT calculations were carried out using Vienna ab initio simulation program (VASP).[163–166] The generalized gradient approximation (GGA) along with the Perdew-Burke-Ernzerhof (PBE)[167] functional were used to determine the exchange and correlation gradient corrections. PAW pseudopotentials were used in order to define the interaction between the core and valence electrons.[168,169] We examine the adsorption of different metal atoms on the MoS_2 surface. Similar adsorption studies of gold and silver clusters on oxide surfaces show that dispersion interactions are important in establishing reliable structures and binding energies.[430,431] Therefore, DFT-D2 corrections provided by Grimme were employed to account for similar dispersion interactions between the metal atoms (especially weakly bound group 11 and post transition metals) and the MoS_2 monolayer.[170] Spin polarized calculations were carried out to treat unpaired electrons and magnetic systems. The optimized lattice constant for bulk MoS_2 was calculated to be 3.19 Å which is very close to the reported experimental value of 3.16 Å.[432] The monolayer of MoS_2 used in the calculations involving atom by atom deposition was formed by cleaving the optimized bulk MoS_2 along the (001) plane and then constructing a 6x6 supercell. A vacuum of 30 Å was then added above the metal surface to avoid any interactions between periodic layers. An energy cutoff of 400 eV was used to construct the plane wave basis set. A Gamma centered k-point grid of 3x3x1 was used to sample the Brillouin zone (BZ) for optimization calculations and a 6x6x1 grid for electronic property calculations. The spin up and spin down components of the DOS from the spin polarized calculations were added up for each of the elements present in the respective system to get the element specific DOS shown in the main text and SI. The band structures were computed along the high symmetry *K*-*Γ*-*M*-*K* path for MoS_2. The electronic energies were converged to within a tolerance of

10^{-6} eV. The structural relaxations were carried out until the maximum force acting on each ion was less than 0.05 eV/Å.

In order to evaluate the influence of temperature on the stability of the clusters, *ab-initio* molecular dynamics (AIMD) calculations were performed in NVT ensemble at room temperature (T = 300K) with a time step of 1 fs. The simulations were run for a total of 4500 steps. The AIMD calculations were performed at energy cut-off of 400 eV and electronic energy tolerance of 10^{-4} eV/Å.

Atom-by-Atom Deposition Method

The evaporative deposition of metal atoms onto the MoS_2 surface was modeled herein using an atom by atom addition approach. In the first step, a single metal atom was positioned at different possible adsorption sites on the MoS_2 surface and optimized to establish the lowest energy adsorption states. There are four symmetric sites on the MoS_2 surface that a metal atom can bind to: the 3-fold "hollow fcc" site bound to 3 S atoms, the 3-fold "hollow hcp" site bound to 3 S atoms, the "bridge" S-S site and the "on top S" site. The adsorption of a single metal on the MoS_2 surface was examined by placing the atom at each of these four different sites. The metal atom binding energies (E_b) at each of these sites were calculated as: $E_b = E_{MoS_2+M} - E_{MoS_2} - E_M$, where E_{MoS_2+M} is the total energy of the metal atom adsorbed on a monolayer (ML) MoS_2 surface, E_{MoS_2} is the energy of the ML MoS_2 surface, and E_M is the energy of a single isolated metal atom. The binding energies for one Ti on the MoS_2 surface (see Table S7.1) indicate that Ti preferentially adsorbs at the 3-fold "hollow fcc" site with a binding energy of -3.00 eV. This stable configuration was then used as the initial configuration for the next Ti atom addition (see Table S7.2). This process was repeated until 5 atoms were added to the initial MoS_2 structure. The same steps are performed for deposition of Au and In. Some metal atom configurations had energies close or comparable to that of the minimum energy structure. For such systems, we used all of these low energy configurations as initial states for the all subsequent metal atom additions.

7.6. Acknowledgements

The authors would like to thank the Minnesota Supercomputing Institute (MSI) at the University of Minnesota for use of its computing resources.

7.7. Supplementary Information

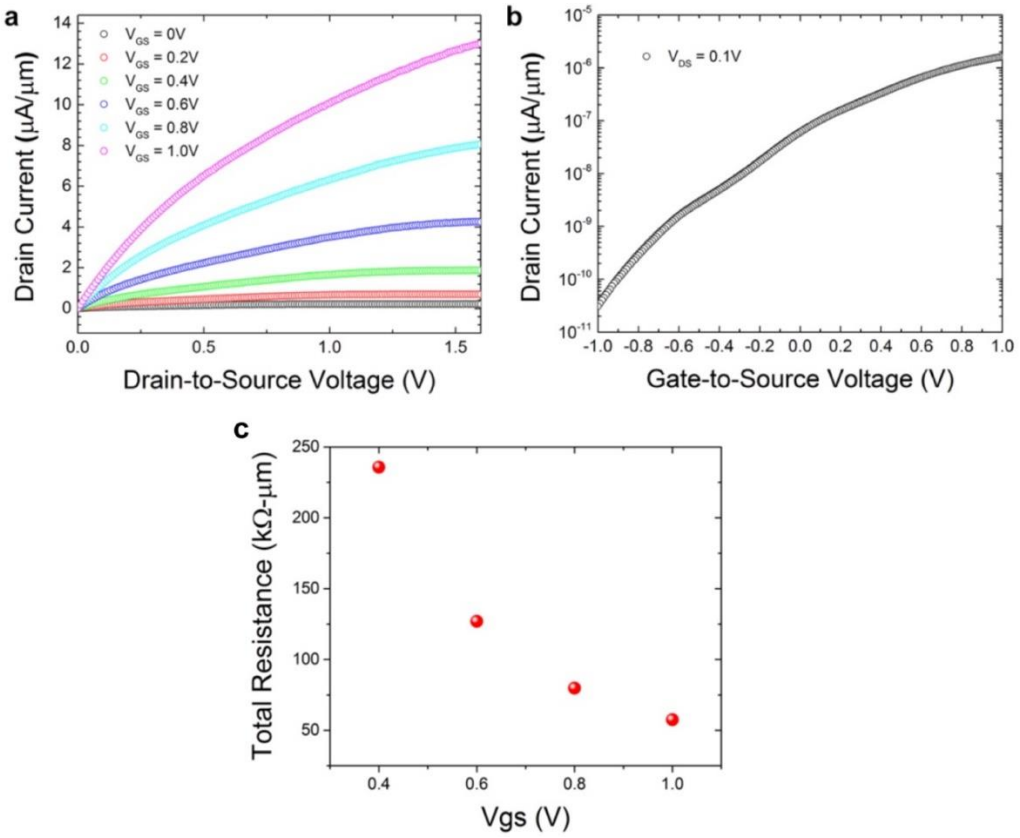

Figure S7.1: a, drain current *vs* drain-to-source voltage for a MoS_2 FET with channel length of 0.5 μm. The gate-to-source voltage was varied from V_{GS} = 0 V (bottom curve) to 1.0 V (top curve) with steps of 0.2 V. **b**, drain current *vs* gate-to-source voltage from the same device. The measurements were taken in the forward sweep direction. Here, the drain-to-source bias voltage was V_{DS} = 0.1 V. **c,** The extracted total resistance (2x the contact resistance plus the channel resistance).

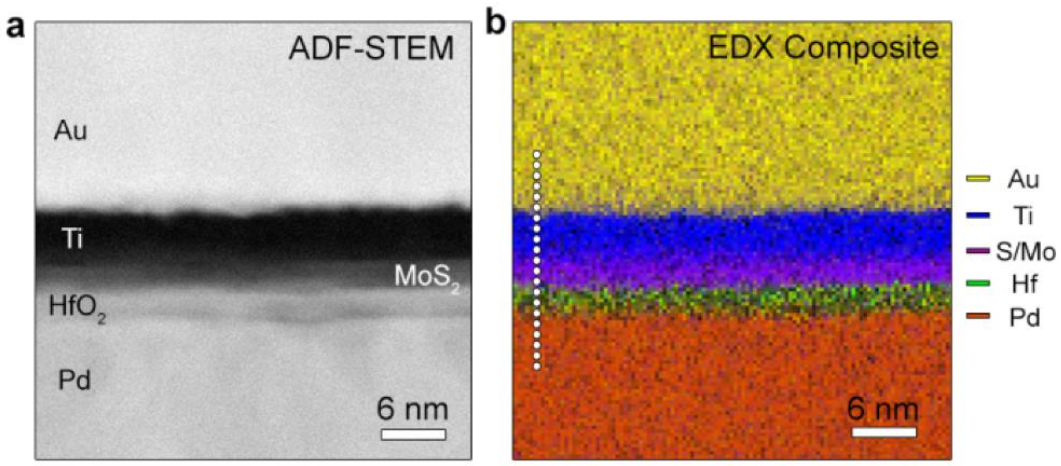

Figure S7.2: a, ADF-STEM image of the FET and **b,** corresponding EDX composite elemental map. The peaks of Mo L edge at 2.292 keV and S K edge at 2.307 keV overlap at the energy dispersions used to acquire the spectrum, and therefore, both the S and Mo signal are represented by the same map.

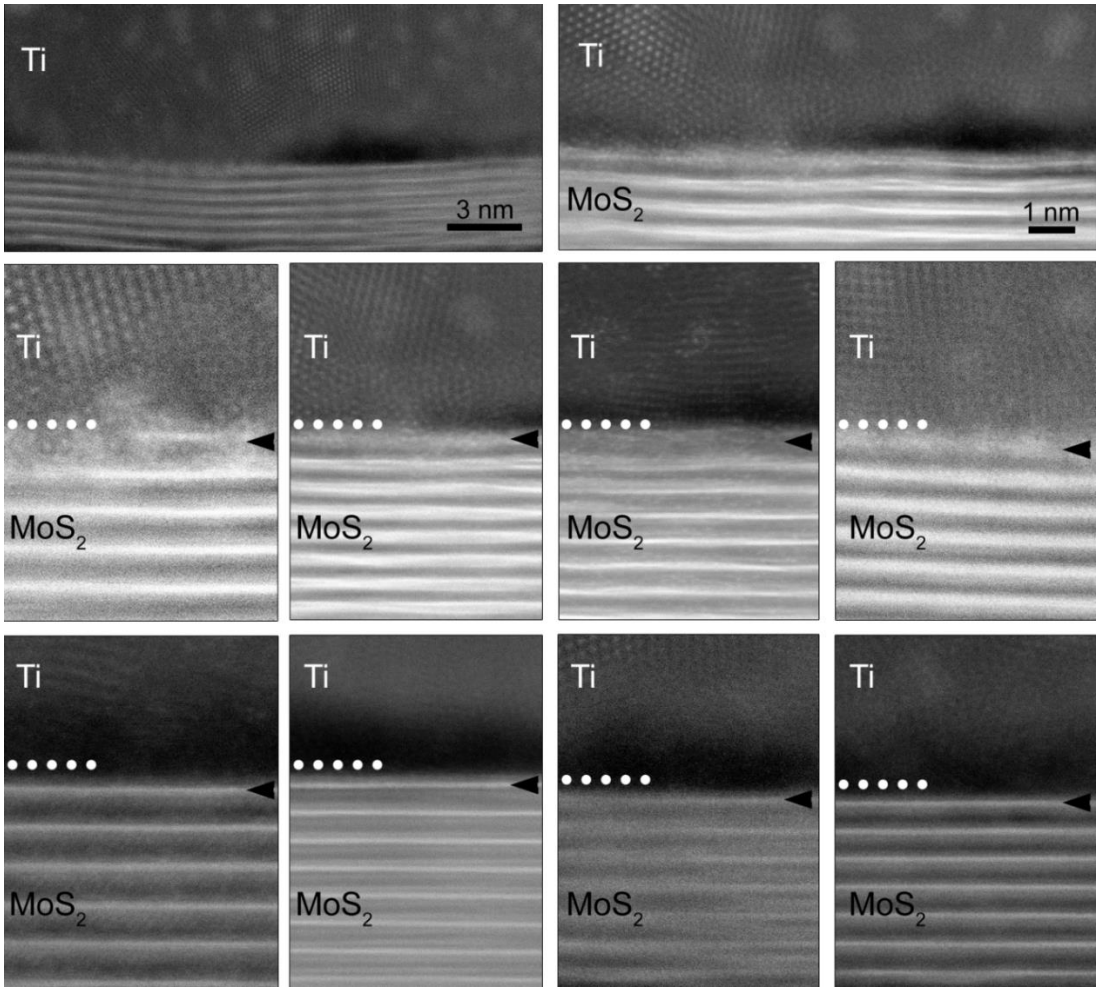

Figure S7.3: ADF-STEM images of Ti-MoS_2 interfaces from different samples and different locations. (Top panels) intermediate magnification images showing areas of Ti clustering and void pockets above the MoS_2 along the samples. (Middle panels) higher magnification images acquired from areas with Ti clusters. (Bottom panels) images acquired from areas with void pockets. The black arrows indicate the location of the 1st layer of MoS_2, which appears altered compared to underlying MoS_2 layers in the images from areas with Ti cluster, and pristine in the images from areas with void pockets. The dotted white lines provide an approximate position of the Ti-MoS_2 interface.

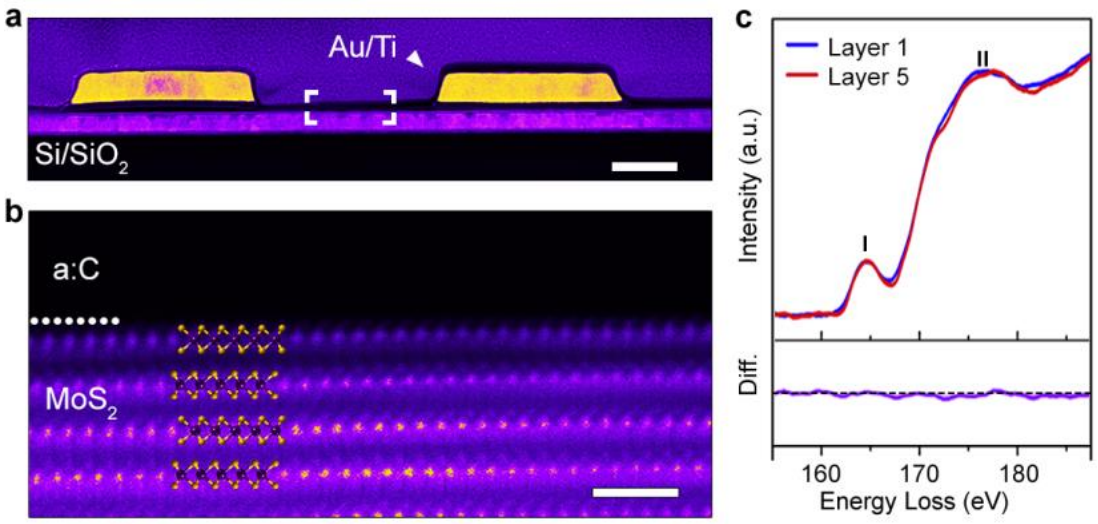

Figure S7.4: a, low magnification image of FET contact from Figure 7.1b of main text. Scale bar is 0.2 µm **b**, high-resolution image from region of MoS_2 not directly in contact with Ti, indicated by white box in **a**. a:C above the MoS_2 was deposited during TEM preparation is not part of the FET. Scale bar is 1 nm. **c**, S L_{23} edge EELS acquired from layer 1 and 5 of MoS_2 and difference spectrum showing to no detectable differences.

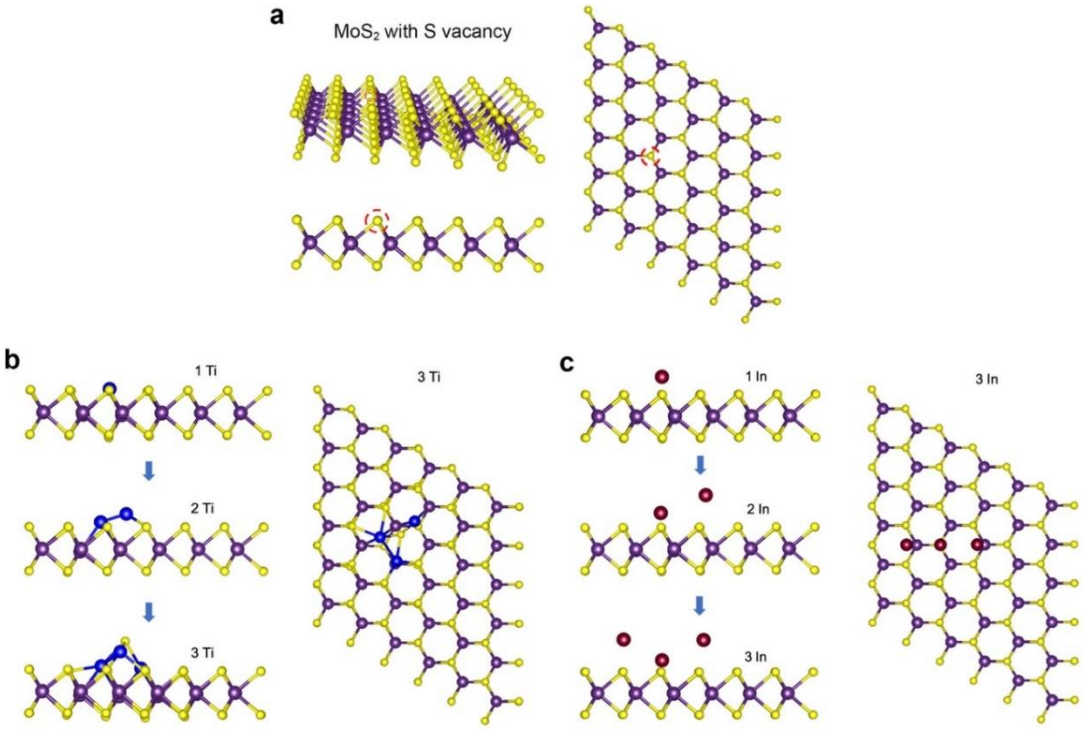

Figure S7.5. a, ball-and-stick models showing S vacancy in MoS_2 layer. **b**, ball-and-stick models showing the lowest energy optimized structures of the Ti-(MoS_2 with S vacancy) system following additions of one, two, and three Ti atoms (Mo – purple, S – yellow, Ti – blue). **c**, ball-and-stick models showing the lowest energy optimized structures of the In-(MoS_2 with S vacancy) system following additions of one, two, and three Ti atoms (In – maroon). The calculations were performed using the same "atom-by-atom" deposition method.

Table S7.1: Relative energies and the atomic structures for the different configurations for the one Ti atom on the MoS_2 surface

No.	Configuration		Relative energy (eV)
	Side view	**Top view**	
1	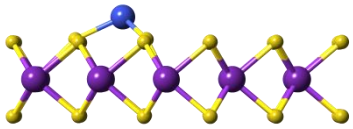	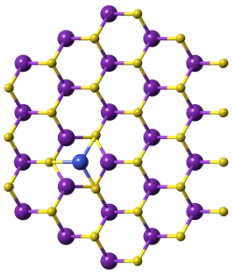	0 (-3.00)
2	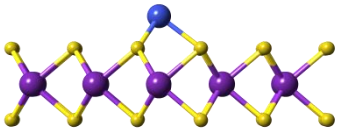	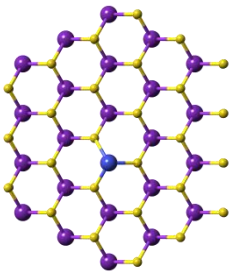	0.81
3	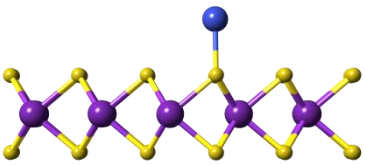	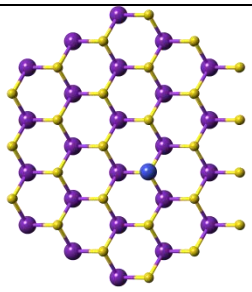	1.31

Table S7.2: Relative energies and the atomic structures for the different configurations for two Ti atoms on the MoS_2 surface, when one more Ti atom is added to low energy configuration in Table S7.1.

No.	Configuration		Relative Energy (eV)
	Side view	**Top view**	
1	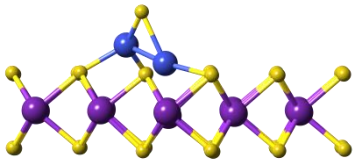	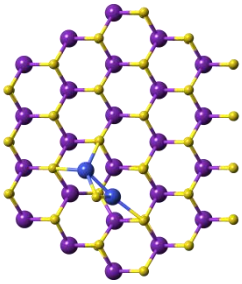	0
2	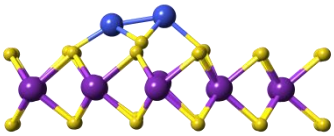	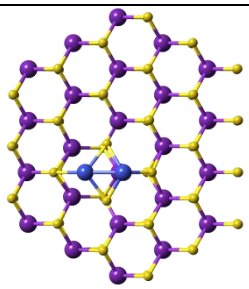	3.02
3	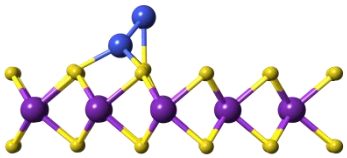	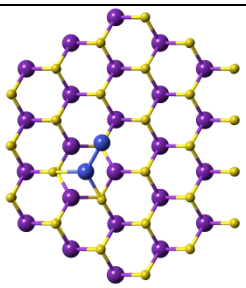	4.17

Chapter 8 - Summary and Recommendations

In **Chapters 2-4**, we looked at three distinct oxidation chemistries, elaborating on the factors that control the reaction selectivity in each of the chapters. In **Chapter 2**, detailed mechanistic and kinetic evaluations were done in conjunction with density functional theory calculations (DFT) to gain insights into the Sulfur Oxidative Coupling of Methane (SOCM) reaction. Experimental studies showed that the over-oxidation of methane to carbon-di-sulfide (CS_2) predominantly occurs via the primary route involving direct oxidation of the methane to CS_2. Further computational studies done which elaborated more on the role of distinct identified active sites in the mechanism, showed that the adsorbed sulfur sites (S_{dim}) predominantly catalyze the CS_2 formation process, whereas the Fe-S_{brid} site pairs, on the other hand, have been shown to exclusively lead to C_2 products formation. The studies done here point to the selective nature of the metal-sulfur site pairs and thus open up opportunities towards catalyst design for selective SOCM reactions in future experimental and computational studies. The studies done so far here have not yet looked into the role of gas phase reactions in the SOCM mechanism. Modeling of OCM kinetics have shown gas phase reactions to play an important role in the OCM mechanism leading to parallel formation routes for C_2H_4 and CO_x via radical propagation reactons.[433–436] Thus, future studies should focus on expanding the current SOCM model further to examine the prevalent gas phase reactions involved in the SOCM reaction network. This would aid to identify the influence of the surface and gas phase reactions and the interaction between the two on the reaction yields as well as lead to development of more robust kinetic models for catalyst and reactor design.

Chapter 3 went into evaluating the intrinsic characteristics of a homogeneous catalytic system that make it selective towards oxidation of cyclohexanone to cyclohexenone. Through detailed computational investigations of different possible reaction mechanisms, we showed that the cyclohexanone dehydrogenation reaction proceeds via a rate-determining intermolecular deprotonation transition state, with the cyclohexanone bound to the metal center via its carbonyl oxygen. We reported that the nature of the binding for both cyclohexanone and cyclohexenone to the metal center were similar – binding via the carbonyl oxygen. The distinguishing factors controlling the selectivity thus was more specific to the molecule which were identified through

distortion-interaction analysis. However, the homogeneity of the catalyst ensured that more favorable routes for cyclohexenone dehydrogenation involving adsorption via the alkene adduct remained inaccessible. Formation of Pd nanoparticles via disintegration of the homogeneous catalyst have been shown to drive the subsequent dehydrogenation reaction of cyclohexenone to phenol.[52] Thus, future studies should be aimed at examining cyclohexenone dehydrogenation reactions over metal nanoparticles/surfaces to study the influence of heterogeneity of the catalyst on reaction rates. This study will also be useful to identify the key differences in the mechanism and kinetics for dehydrogenation reactions occurring over a homogeneous system versus that over a heterogeneous system. Such a study can then possibly aid in employing similar selectivity control strategies for other similar systems of interest through tuning of the catalyst morphology.

Along similar lines of exploring the effect of catalyst size and morphology on the reaction selectivity, in **Chapter 4**, we particularly looked at coverage and steric effects on the selectivity of alcohol oxidation reactions, specifically glycerol oxidation. In our studies done using model propanol system (1-propanol and 2-propanol), we showed that the CO coverages that are built up on the single crystal Pt (111) surface during the glycerol electro-oxidation reaction (GEOR) sterically hinder the activation of the secondary C-H bond over primary C-H bond, translating to higher selectivity towards glyceraldehyde versus that over dihydroxyacetone, that is experimentally observed for GEOR over such single crystal Pt surfaces. Such steric effects as proposed can be overcome by either reducing the CO coverages on the surface through use of bimetallic alloy catalysts or via use of precisely engineered metal clusters. Thus, future directions looking at examination of the alcohol oxidation reactions over such atomically tuned clusters of different sizes would be of great significance. Such cluster size effect studies would help to evaluate the role and influence of cluster size on the reaction selectivity as well as activity, which can be extended further to look at targeted C-H activation reactions of other substrate molecules of synthetic utility.[437,438]

In **Chapters 5 and 6**, we talked about two different reduction chemistries. **Chapter 5** showed that through application of an electric field normal to the electrode surface via back-gating of the electrode, the overpotentials for the hydrogen evolution reaction (HER) reaction over MoS_2 catalysts can be lowered by ~140 mV. Our computations showed that effective gate-induced "charging" of the electrode surface leads to a

relative shift of the S-vacancy induced gap states towards the Fermi level, that lead to improvements in the binding energies of hydrogen over the active S-vacancy site of the electrode surface. In the chapter, we already mentioned that the use of a high dielectric medium such as HfO_2 instead of SiO_2 could further lower the overpotential for the HER reactions over MoS_2, based on calculations which suggest a 10-fold increase in the hydrogen binding energies to the electrode surfaces at the predicted induced carrier densities with HfO_2 as the dielectric medium. Of further interest, would be to model the behaviour of other subset of reactions over such "charged" 2D materials including CO_2 reduction over TMDs such as MoS_2[439] and WSe_2,[440] and HER over MXenes,[441] to evaluate the effect and possible future applications of back-gating on the other classes of reaction as well as for different materials.

Chapter 6 went through the optimization and synthetic utility of the electrochemical Birch reduction process. We further conducted mechanistic studies to evaluate the reduction pathway which we showed occurs via an electrode mediated mechanism through electron and proton transfer events. The different components present in the reaction mixture were shown to each have their unique role and functionality – dimethyl urea (DMU) used functioned as a proton source, lithium bromide (LiBr) used was shown to act as a promotor that promotes the electron transfer and proton transfer events occurring, while the tris(pyrrolidino)phosphoramide (TPPA) additive was hypothesized to function as an overcharge protection agent, preventing passivation of the electrode surface. The models used for the computations in this study consisted of an idealized Zn surface model. Under the highly reductive reaction conditions, however, as discussed in the chapter, a thin layer starts growing over the electrode surface, which eventually remains stable in presence of TPPA. Future studies thus looking at more complex models to evaluate the role of the interfacial layer growth on the resultant reaction kinetics would be of potential interest. In battery literature, formation of such interfacial layers, known as solid electrolyte interphase (SEI), have been shown to prevent solvent decomposition by blocking the flow of electrons to the surface but allowing for shuttling of the lithium cations through the pores of the layer, to allow the flow of charge across the cell.[442] Similar studies exploring the role of these interfacial layer growth on catalyzing the reductive chemistry while also preventing the electrode passivation is something that would be of interest to the electro-synthetic community for design of reductive transformation reactions operating under similar

highly reductive conditions. Further, some other directions that would be interesting to explore and of potential interest to the electro-synthetic community include simulating the growth mechanism of the interfacial layer formation in presence and absence of TPPA since this would lead to fundamental insights into the factors and key additive features required to prevent passivation of the electrode surface. Approaches used so far on examination of the growth mechanisms for SEI layer formation over the surfaces of electrodes used in Li-ion batteries can similarly be extended herein to model the growth behaviour.[442]

In **Chapter 7**, we showed that the principles of redox chemistry in chemical reactions can similarly be translated to other focal areas as well. In this chapter, in particular, we focused on the redox chemistry occurring at the interface of MoS_2 and metal contacts, which form an integral part of MoS_2-based transistor devices. Through our new computational methodology proposed in this chapter, we were able to accurately predict the interfacial structure of various MoS_2-metal contacts, which could not be predicted via previously employed "metal-slab" approach. We particularly saw that Ti disrupts the MoS_2 surface due to its strongly reducing nature whereas p-block and late transition metals such as In, Cu, and Au, on the other hand, form pristine interfaces, as is desired. Of further interest would be to expand on the current 5-atom model that we have currently to have a more realistic representation of the contact interface. This can be done by simulating the deposition of more metal atoms over the MoS_2 surface leading to eventual build-up of a monolayer. Having captured the interfacial structure with this model, the further deposition of the metal atoms can be simulated via simple deposition of a metal slab to this monolayer of deposited metal atoms. Such models then, in addition to accurately predicting the chemistry at the interface, can be further used to compute the electronic properties that are characteristic and predictive of the transistor performance such as Schottky and tunnel barriers,[443] thus guiding the future design of metal/metal-alloy contacts for transistor applications.

References

1. Yan, M., Kawamata, Y. & Baran, P. S. Synthetic Organic Electrochemical Methods since 2000: On the Verge of a Renaissance. *Chem. Rev.* **117**, 13230–13319 (2017).

2. Huber, G. W., Iborra, S. & Corma, A. Synthesis of transportation fuels from biomass: Chemistry, catalysts, and engineering. *Chem. Rev.* **106**, 4044–4098 (2006).

3. Alonso, D. M., Bond, J. Q. & Dumesic, J. A. Catalytic conversion of biomass to biofuels. *Green Chem.* **12**, 1493–1513 (2010).

4. Neurock, M. First-principles modeling for the electro-oxidation of small molecules. in *Handbook of Fuel Cells* 1–22 (2010).

5. Wang, D., Weinstein, A. B., White, P. B. & Stahl, S. S. Ligand-Promoted Palladium-Catalyzed Aerobic Oxidation Reactions. *Chem. Rev.* **118**, 2636–2679 (2018).

6. Schwach, P., Pan, X. & Bao, X. Direct Conversion of Methane to Value-Added Chemicals over Heterogeneous Catalysts: Challenges and Prospects. *Chem. Rev.* **117**, 8497–8520 (2017).

7. Gao, D., Arán-Ais, R. M., Jeon, H. S. & Roldan Cuenya, B. Rational catalyst and electrolyte design for CO_2 electroreduction towards multicarbon products. *Nat. Catal.* **2**, 198–210 (2019).

8. Crabtree, R. H. Alkane C – H activation and functionalization with homogeneous transition metal catalysts : a century of progress — a new millennium in prospect. *J. Chem. Soc., Dalt. Trans.* 2437–2450 (2001).

9. Foster, S. L. *et al.* Catalysts for nitrogen reduction to ammonia. *Nat. Catal.* **1**, 490–500 (2018).

10. De Luna, P. *et al.* What would it take for renewably powered electrosynthesis to displace petrochemical processes? *Science* **364**, (2019).

11. Chin, Y. H., Buda, C., Neurock, M. & Iglesia, E. Consequences of metal-oxide interconversion for C-H bond activation during CH_4 reactions on Pd catalysts. *J. Am. Chem. Soc.* **135**, 15425–15442 (2013).

12. Chin, Y. H., Buda, C., Neurock, M. & Iglesia, E. Selectivity of chemisorbed oxygen in C-H bond activation and CO oxidation and kinetic consequences for CH_4-O_2 catalysis on Pt and Rh clusters. *J. Catal.* **283**, 10–24 (2011).

13. Zhu, Q. *et al.* Sulfur as a selective 'soft' oxidant for catalytic methane conversion probed by experiment and theory. *Nat. Chem.* **5**, 104–9 (2013).

14. Peter, M. & Marks, T. J. Platinum Metal-Free Catalysts for Selective Soft Oxidative Methane --> Ethylene Coupling. Scope and Mechanistic Observations. *J. Am. Chem. Soc.* **137**, 15234–15240 (2015).

15. Anderson, J. R., Chang, Y. F., Pratt, K. C. & Foger, K. Reaction of methane and sulfur: Oxidative coupling and carbon disulfide formation. *React. Kinet. Catal.*

Lett. **49**, 261–269 (1993).

16. Cai, Y., Chou, L., Li, S., Zhang, B. & Zhao, J. Selective conversion of methane to C_2 hydrocarbons using carbon dioxide over Mn-$SrCO_3$ catalysts. *Catal. Letters* **86**, 191–195 (2003).

17. Wang, Y., Takahashi, Y. & Ohtsuka, Y. Carbon dioxide as oxidant for the conversion of methane to ethane and ethylene using modified CeO_2 catalysts. *J. Catal.* **186**, 160–168 (1999).

18. Roos, J. A., Korf, S. J., Veehof, R. H. J., van Ommen, J. G. & Ross, J. R. H. Kinetic and Mechanistic Aspects of the Oxidative Coupling of Methane over a Li/MgO Catalyst. *Appl. Catal.* **52**, 131–145 (1989).

19. Nowicka, E. *et al.* Elucidating the Role of CO_2 in the Soft Oxidative Dehydrogenation of Propane over Ceria-Based Catalysts. *ACS Catal.* **8**, 3454–3468 (2018).

20. Neurock, M. & Van Santen, R. A. First principles analysis of C-H bond formation in ethylene hydrogenation. *J. Phys. Chem. B* **104**, 11127–11145 (2000).

21. Ma, H.-Y. & Wang, G.-C. Selective Hydrogenation of Acetylene on Ptn/TiO_2 (n=1, 2, 4, 8) Surfaces: Structure Sensitivity Analysis. *ACS Catal.* **2**, 4922–4928 (2020).

22. Mei, D., Neurock, M. & Smith, C. M. Hydrogenation of acetylene-ethylene mixtures over Pd and Pd-Ag alloys: First-principles-based kinetic Monte Carlo simulations. *J. Catal.* **268**, 181–195 (2009).

23. Elsen, H., Färber, C., Ballmann, G. & Harder, S. $LiAlH_4$: From Stoichiometric Reduction to Imine Hydrogenation Catalysis. *Angew. Chemie* **130**, 7274–7278 (2018).

24. Van Brabandt, W., Dejaegher, Y., Van Landeghem, R. & De Kimpe, N. Reduction of 4-(haloalkyl)azetidin-2-ones with $LiAlH_4$ as a powerful method for the synthesis of stereodefined aziridines and azetidines. *Org. Lett.* **8**, 1101–1104 (2006).

25. Francke, R. & Little, R. D. Redox catalysis in organic electrosynthesis: Basic principles and recent developments. *Chem. Soc. Rev.* **43**, 2492–2521 (2014).

26. Wang, F. & Stahl, S. S. Electrochemical Oxidation of Organic Molecules at Lower Overpotential: Accessing Broader Functional Group Compatibility with Electron-Proton Transfer Mediators. *Acc. Chem. Res.* **53**, 561–574 (2020).

27. Nitopi, S. *et al.* Progress and Perspectives of Electrochemical CO_2 Reduction on Copper in Aqueous Electrolyte. *Chem. Rev.* **119**, 7610–7672 (2019).

28. Rosca, V., Duca, M., DeGroot, M. T. & Koper, M. T. M. Nitrogen Cycle Electrocatalysis. *Chem. Rev.* **109**, 2209–2244 (2009).

29. Kulkarni, A., Siahrostami, S., Patel, A. & Nørskov, J. K. Understanding Catalytic Activity Trends in the Oxygen Reduction Reaction. *Chem. Rev.* **118**, 2302–2312 (2018).

30. Siu, J. C., Fu, N. & Lin, S. Catalyzing Electrosynthesis: A Homogeneous Electrocatalytic Approach to Reaction Discovery. *Acc. Chem. Res.* **53**, 547–560 (2020).

31. Chin, Y. H., Buda, C., Neurock, M. & Iglesia, E. Reactivity of chemisorbed oxygen atoms and their catalytic consequences during CH_4-O_2 catalysis on supported Pt clusters. *J. Am. Chem. Soc.* **133**, 15958–15978 (2011).

32. Dinh, K. T. *et al.* Viewpoint on the Partial Oxidation of Methane to Methanol Using Cu- and Fe-Exchanged Zeolites. *ACS Catal.* **8**, 8306–8313 (2018).

33. Neugebohren, J. *et al.* Velocity-resolved kinetics of site-specific carbon monoxide oxidation on platinum surfaces. *Nature* **558**, 280–283 (2018).

34. Saavedra, J., Pursell, C. J. & Chandler, B. D. CO Oxidation Kinetics over Au/TiO_2 and Au/Al_2O_3 Catalysts: Evidence for a Common Water-Assisted Mechanism. *J. Am. Chem. Soc.* **140**, 3712–3723 (2018).

35. Rozanska, X., Fortrie, R. & Sauer, J. Oxidative dehydrogenation of propane by monomeric vanadium oxide sites on silica support. *J. Phys. Chem. C* **111**, 6041–6050 (2007).

36. Gorey, T. J. *et al.* Coking-Resistant Sub-Nano Dehydrogenation Catalysts: $Pt_n Sn_x/SiO_2$ (n=4, 7). *ACS Catal.* **2**, 4543–4558 (2020).

37. Bian, Y., Kim, M., Li, T., Asthagiri, A. & Weaver, J. F. Facile Dehydrogenation of Ethane on the IrO_2(110) Surface. *J. Am. Chem. Soc.* **140**, 2665–2672 (2018).

38. Zhao, Z. J. *et al.* Hydroxyl-Mediated Non-oxidative Propane Dehydrogenation over VO_x/γ-Al_2O_3 Catalysts with Improved Stability. *Angew. Chemie - Int. Ed.* **57**, 6791–6795 (2018).

39. Annamalai, L. *et al.* Influence of Tight Confinement on Selective Oxidative Dehydrogenation of Ethane on MoVTeNb Mixed Oxides. *ACS Catal.* **8**, 7051–7067 (2018).

40. Cao, D., Lu, G. Q., Wieckowski, A., Wasileski, S. A. & Neurock, M. Mechanisms of methanol decomposition on platinum: A combined experimental and ab initio approach. *J. Phys. Chem. B* **109**, 11622–11633 (2005).

41. Simões, M., Baranton, S. & Coutanceau, C. Electrochemical valorisation of glycerol. *ChemSusChem* **5**, 2106–2124 (2012).

42. Sigman, M. S. & Jensen, D. R. Ligand-modulated palladium-catalyzed aerobic alcohol oxidations. *Acc. Chem. Res.* **39**, 221–229 (2006).

43. Ravi, M., Ranocchiari, M. & van Bokhoven, J. A. The Direct Catalytic Oxidation of Methane to Methanol—A Critical Assessment. *Angew. Chemie - Int. Ed.* **56**, 16464–16483 (2017).

44. Horn, R. & Schlögl, R. Methane Activation by Heterogeneous Catalysis. *Catal. Letters* **145**, 23–39 (2015).

45. Lunsford, J. H. The catalytic oxidative coupling of methane. *Angew.\ Chem.* **35**, 970–980 (1995).

46. Lunsford, J. H. Catalytic conversion of methane to more useful chemicals and fuels:a challenge for the 21st century. *Catal. Today* **63**, 165–174 (2000).

47. Keller, G. E. & Bhasin, M. M. Synthesis of ethylene via oxidative coupling of methane I. Determination of active catalysts. *J. Catal.* **73**, 9–19 (1982).

48. Diao, T. & Stahl, S. S. Synthesis of cyclic enones via direct palladium-catalyzed aerobic dehydrogenation of ketones. *J. Am. Chem. Soc.* **133**, 14566–14569 (2011).

49. Iosub, A. V. & Stahl, S. S. Palladium-Catalyzed Aerobic Dehydrogenation of Cyclic Hydrocarbons for the Synthesis of Substituted Aromatics and Other Unsaturated Products. *ACS Catal.* **6**, 8201–8213 (2016).

50. Pun, D., Diao, T. & Stahl, S. S. Aerobic dehydrogenation of cyclohexanone to phenol catalyzed by $Pd(TFA)_2$/2-dimethylaminopyridine: Evidence for the role of Pd nanoparticles. *J. Am. Chem. Soc.* **135**, 8213–8221 (2013).

51. Izawa, Y., Pun, D. & Stahl, S. S. Palladium-Catalyzed Aerobic Dehydrogenation of Substituted Cyclohexanones to Phenols. *Science* **333**, 209–214 (2011).

52. Pun, D., Diao, T. & Stahl, S. S. Aerobic dehydrogenation of cyclohexanone to phenol catalyzed by $Pd(DMSO)_2(TFA)_2$: Evidence for ligand-controlled chemoselectivity. *J. Am. Chem. Soc.* **135**, 8213–8221 (2013).

53. Kwon, Y., Schouten, K. J. P. & Koper, M. T. M. Mechanism of the Catalytic Oxidation of Glycerol on Polycrystalline Gold and Platinum Electrodes. *ChemCatChem* **3**, 1176–1185 (2011).

54. Pan, Y. *et al.* Design of Single-Atom Co-N_5 Catalytic Site: A Robust Electrocatalyst for CO_2 Reduction with Nearly 100% CO Selectivity and Remarkable Stability. *J. Am. Chem. Soc.* **140**, 4218–4221 (2018).

55. Atifi, A., Boyce, D. W., Dimeglio, J. L. & Rosenthal, J. Directing the Outcome of CO_2 Reduction at Bismuth Cathodes Using Varied Ionic Liquid Promoters. *ACS Catal.* **8**, 2857–2863 (2018).

56. Jiang, B., Zhang, X. G., Jiang, K., Wu, D. Y. & Cai, W. Bin. Boosting Formate Production in Electrocatalytic CO_2 Reduction over Wide Potential Window on Pd Surfaces. *J. Am. Chem. Soc.* **140**, 2880–2889 (2018).

57. Morales-Guio, C. G. *et al.* Improved CO_2 reduction activity towards C_{2+} alcohols on a tandem gold on copper electrocatalyst. *Nat. Catal.* **1**, 764–771 (2018).

58. Hao, Y. C. *et al.* Promoting nitrogen electroreduction to ammonia with bismuth nanocrystals and potassium cations in water. *Nat. Catal.* **2**, 448–456 (2019).

59. Singh, A. R. *et al.* Computational Design of Active Site Structures with Improved Transition-State Scaling for Ammonia Synthesis. *ACS Catal.* **8**, 4017–4024 (2018).

60. Li, H. *et al.* Activating and optimizing MoS_2 basal planes for hydrogen evolution through the formation of strained sulphur vacancies. *Nat. Mater.* **15**, 48 (2015).

61. Li, G. *et al.* All The Catalytic Active Sites of MoS_2 for Hydrogen Evolution. *J. Am. Chem. Soc.* **138**, 16632–16638 (2016).

62. Birch, A. J. Electrolytic reduction in liquid ammonia. *Nature* **158**, 60 (1946).

63. Swenson, K. E., Zemach, D., Nanjundiah, C. & Kariv-Miller, E. Birch Reductions of Methoxyaromatics in Aqueous Solution. *J. Org. Chem.* **48**, 1777–1779 (1983).

64. Zimmerman, H. E. A Mechanistic Analysis of the Birch Reduction. *Acc. Chem. Res.* **45**, 164–170 (2012).

65. Greenfield, A. & Schindewolf, U. Kinetics of the Birch Reduction. *Ber. Bunsenges. Phy. Chem.* **102**, 1808–1814 (1998).

66. Radisavljevic, B., Radenovic, A., Brivio, J., Giacometti, V. & Kis, A. Single-layer MoS_2 transistors. *Nat. Nanotechnol.* **6**, 147–150 (2011).

67. Chhowalla, M., Jena, D. & Zhang, H. Two-dimensional semiconductors for transistors. *Nat. Rev. Mater.* **1**, 16052 (2016).

68. Allain, A., Kang, J., Banerjee, K. & Kis, A. Electrical contacts to two-dimensional semiconductors. *Nat. Mater.* **14**, 1195–1205 (2015).

69. Kappera, R. *et al.* Phase-engineered low-resistance contacts for ultrathin MoS_2 transistors. *Nat. Mater.* **13**, 1128–1134 (2014).

70. Du, Y., Yang, L., Liu, H. & Ye, P. D. Contact research strategy for emerging molybdenum disulfide and other two-dimensional field-effect transistors. *APL Mater.* **2**, (2014).

71. Liu, H., Neal, A. T. & Ye, P. D. Channel length scaling of MoS_2 MOSFETs. *ACS Nano* **6**, 8563–8569 (2012).

72. Liu, H. *et al.* Statistical study of deep submicron dual-gated field-effect transistors on monolayer chemical vapor deposition molybdenum disulfide films. *Nano Lett.* **13**, 2640–2646 (2013).

73. Guo, X. *et al.* Direct, nonoxidative conversion of methane to ethylene, aromatics, and hydrogen. *Science* **344**, 616–9 (2014).

74. Alshammari, A.; Kalevaru, D. V. N.; Bagabas, A.; Martin, A., Production of Ethylene and its Commercial Importance in the Global Market. 82-115 (2016).

75. Mallens, E., Hoebink, J. H. B. J. & Marin, G. An Investigation of the Oxygen Pathways in the Oxidative Coupling of Methane over MgO-Based Catalysts. *J. Catal.* **160**, 222–234 (1996).

76. Campbell, K. D., Morales, E. & Lunsford, J. H. Gas-Phase Coupling of Methyl Radicals during the Catalytic Partial Oxidation of Methane. *J. Am. Chem. Soc.* **109**, 7900–7901 (1987).

77. Zhou, S., Li, J., Schlangen, M. & Schwarz, H. Thermal Activation of Methane by $[HfO]^{\cdot+}$ and $[XHfO]^{+}$ (X=F, Cl, Br, I) and the Origin of a Remarkable Ligand Effect. *Angew. Chemie - Int. Ed.* **55**, 7685–7688 (2016).

78. Li, J., Zhou, S., Schlangen, M., Weiske, T. & Schwarz, H. Hidden Hydride Transfer as a Decisive Mechanistic Step in the Reactions of the Unligated Gold Carbide $[AuC]^{+}$ with Methane under Ambient Conditions. *Angew. Chemie* **128**,

13266–13269 (2016).

79. Li, J. *et al.* Mechanistic Variants in Gas-Phase Metal-Oxide Mediated Activation of Methane at Ambient Conditions. *J. Am. Chem. Soc.* **138**, 11368–11377 (2016).

80. Zhou, S., Li, J., Firouzbakht, M., Schlangen, M. & Schwarz, H. Sequential Gas-Phase Activation of Carbon Dioxide and Methane by $[Re(CO)_2]^+$: The Sequence of Events Matters! *J. Am. Chem. Soc.* **139**, 6169–6176 (2017).

81. Lee, J. S. & Oyamat, S. T. Oxidative Coupling of Methane to Higher Hydrocarbons. *Catal. Rev.* **30**, 249–280 (1988).

82. Weng, W., Chen, M., Wan, H. & Liao, Y. High-temperature in situ FTIR spectroscopy study of LaOF and BaF_2/LaOF catalysts for methane oxidative coupling. *Catal. Letters* **53**, 43–50 (1998).

83. Myrach, P. *et al.* Temperature-Dependent Morphology, Magnetic and Optical Properties of Li-Doped MgO. *ChemCatChem* **2**, 854–862 (2010).

84. Yildiz, M. *et al.* Support material variation for the MnxOy-Na_2WO_4/SiO_2catalyst. *Catal. Today* **228**, 5–14 (2014).

85. Peil, K. P., Goodwin, J. G. & Marcelin, G. Surface Concentrations and Residence Times of Intermediates on Sm_2O_3 during the Oxidative Coupling of Methane. *J. Am. Chem. Soc.* **112**, 6129–6130 (1990).

86. Beck, B. *et al.* Oxidative coupling of methane - A complex surface/gas phase mechanism with strong impact on the reaction engineering. *Catal. Today* **228**, 212–218 (2014).

87. Parishan, S., Littlewood, P., Arinchtein, A., Fleischer, V. & Schomäcker, R. Chemical looping as a reactor concept for the oxidative coupling of methane over the Mn_xO_y-Na_2WO_4/SiO_2 catalyst, benefits and limitation. *Catal. Today* **311**, 40–47 (2018).

88. Li, J. *et al.* Electronic Origins of the Variable Efficiency of Room-Temperature Methane Activation by Homo- and Heteronuclear Cluster Oxide Cations $[XYO_2]^+$ (X, Y = Al, Si, Mg): Competition between Proton-Coupled Electron Transfer and Hydrogen-Atom. *J. Am. Chem. Soc.* **138**, 7973–7981 (2016).

89. Langguth, J., Dittmeyer, R., Hofmann, H. & Tomandl, G. Studies on oxidative coupling of methane using high-temperature proton-conducting membranes. *Appl. Catal. A Gen.* **158**, 287–305 (1997).

90. Chen, L., Lin, L., Xu, Z., Zhang, T. & Li, X. Promotional effect of Pt on non-oxidative methane transformation over Mo-HZSM-5 catalyst. *Catal. Letters* **39**, 169–172 (1996).

91. Zhang, J., Yang, Y., Zhang, J., Liu, Q. & Tan, K. Non-Oxidative Coupling of Methane to C 2 Hydrocarbons under Above-Atmospheric Pressure Using Pulsed Microwave Plasma. *Energy & Fuels* **16**, 687–693 (2002).

92. Khan, M. S. & Crynes, B. L. Survey of Recent Methane Pyrolysis Literature. *Ind. Eng. Chem.* **62**, 54–59 (1970).

93. Jiang, H., Cao, Z., Schirrmeister, S., Schiestel, T. & Caro, J. A coupling strategy to produce hydrogen and ethylene in a membrane reactor. *Angew. Chemie - Int. Ed.* **49**, 5656–5660 (2010).

94. Sheng, H., Schreiner, E. P., Zheng, W. & Lobo, R. F. Non-oxidative Coupling of Methane to Ethylene Using Mo_2C/[B]ZSM-5. *ChemPhysChem* vol. 19 504–511 (2018).

95. Xiao, Y. & Varma, A. Highly Selective Nonoxidative Coupling of Methane over Pt-Bi Bimetallic Catalysts. *ACS Catal.* **8**, 2735–2740 (2018).

96. Meyer, B. Elemental Sulfur. *Chem. Rev.* **76**, 367–388 (1976).

97. Rau, H., Kutty, T. R. N. & Guedes de Carvalho, J. R. F. Thermodynamics of sulphur vapour. *J. Chem. Thermodyn.* **5**, 833–844 (1973).

98. Jackson, A. J., Davide, T. & Walsh, A. A universal chemical potential for sulfur vapours. *Chem. Sci.* **7**, 1082 (2016).

99. West, C., Lide, D. R. & Eds. Standard Thermodynamic Properties of Chemical Substances. in *CRC Handbook of Chemistry and Physics* vol. 13 5.4-5.41 (2012).

100. Stull, D. R. & Prophet, H. *JANAF thermochemical tables*. (1971).

101. Plier, M., Winkler, K., US1735409, 1929.

102. Bodenstein, P. H., US1981161, 1984.

103. Zavyalova, U., Holena, M., Schlögl, R. & Baerns, M. Statistical analysis of past catalytic data on oxidative methane coupling for new insights into the composition of high-performance catalysts. *ChemCatChem* **3**, 1935–1947 (2011).

104. Simon, U. *et al.* Contributions of phase composition and defect structure to the long term stability of Li/MgO catalysts. *Int. J. Mater. Res.* **103**, 1488–1498 (2012).

105. Arndt, S. *et al.* A Critical Assessment of Li/MgO-Based Catalysts for the Oxidative Coupling of Methane. *Catal. Rev.* **53**, 424–514 (2011).

106. Takanabe, K. & Iglesia, E. Mechanistic Aspects and Reaction Pathways for Oxidative Coupling of Methane on $Mn/Na_2WO_4/SiO_2$ Catalysts. *J. Phys. Chem. C* **113**, 10131–10145 (2009).

107. Li, L., Borry, R. W. & Iglesia, E. Design and optimization of catalysts andmembrane reactors for the non-oxidative conversion of methane. *Chem. Eng. Sci.* **57**, 4595–4604 (2002).

108. Jiang, J. Z. *et al.* Mechanochemical Synthesis of Fe-S Materials. *J. Solid State Chem.* **138**, 114–125 (1998).

109. Stojilovic, N. & Isaacs, D. E. Inquiry-Based Experiment with Powder XRD and FeS_2 Crystal: 'discovering' the (400) Peak. *J. Chem. Educ.* (2019).

110. Brion, D. Etude par spectroscopie de photoelectrons de la degradation superficielle de FeS_2, $CuFeS_2$, ZnS et PbS a l'air et dans l'eau. *Appl. Surf.* **5**, 133–152 (1980).

111. Carver, J. C., Schweitzer, G. K. & Carlson, T. A. Use of X-ray photoelectron spectroscopy to study bonding in Cr, Mn, Fe, and Co compounds. *J. Chem. Phys.* **57**, 982–990 (1972).

112. Baum, A. *et al.* Phonon anomalies in FeS. *Phys. Rev. B* **97**, 1–11 (2018).

113. Vogt, H., Chattopadhyay, T. & Stolz, H. J. Complete first-order Raman spectra of the pyrite structure compounds FeS_2, MnS_2 AND SiP_2. *J. Phys. Chem. Solids* **44**, 869–873 (1983).

114. Campbell, I. & Fauchet, P. M. The effects of microcrystal size and shape on the one phonon Raman spectra of crystalline semiconductors. *Solid State Commun.* **58**, 739–741 (1986).

115. Kitajima, M. *Defects in crystals studied by Raman scattering*. *Critical Reviews in Solid State and Materials Sciences* vol. 22 (1997).

116. Gao, Y., Zhao, X., Yin, P. & Gao, F. Size-Dependent Raman Shifts for nanocrystals. *Sci. Rep.* **6**, 1–5 (2016).

117. Kwapien, K. *et al.* Sites for methane activation on lithium-doped magnesium oxide surfaces. *Angew. Chemie - Int. Ed.* **53**, 8774–8778 (2014).

118. Hagen, J. *Industrial Catalysis: A Practical Approach*. (2006).

119. Burch, R., Tsang, S. C., Mirodatos, C. & Sanchez M., J. G. Kinetic isotope effects in methane coupling on a reducible oxide catalyst. *Catal. Letters* **7**, 423–430 (1990).

120. Nelson, P. F., Lukey, C. A. & Cant, N. W. Measurements of Kinetic Isotope Effects and Hydrogen/Deuterium Distributions over Methane Oxidative Coupling Catalysts. *J. Catal.* **120**, 216–230 (1989).

121. Cant, N. W., Lukey, C. A., Nelson, P. F. & Tyler, R. J. The rate controlling step in the oxidative coupling of methane over a lithium-promoted magnesium oxide catalyst. *J. Chem. Soc. Chem. Commun.* 766–768 (1988).

122. Bhore, N. A., Klein, M. T. & Bischoff, K. B. The Delplot Technique: A New Method for Reaction Pathway Analysis. *Ind. Eng. Chem. Res.* **29**, 313–316 (1990).

123. Ekstrom, A. & Lapszewicz, J. A. A study of the mechanism of the partial oxidation of methane over rare earth oxide catalysts using isotope transient techniques. *Phys.Chem* 5230–5237 (1989).

124. Hutchings, G. J. Studies of the Mechanism of the Oxidative Coupling of Methane Using Oxide Catalysts. in *Methane Conversion by Oxidative Processes* (ed. Wolf, E. E.) 200–258 (Springer Science+Business Media New York, 1992).

125. Gulcicek, E. E., Colson, S. D. & Pfefferle, L. D. Multiphoton ionization detection of methyl radicals from catalytic oxidation of methane. *J. Phys. Chem.* **94**, 7069–7074 (1990).

126. Cant, N. W., Kennedy, E. M. & Nelson, P. F. Magnitude and origin of the deuterium kinetic isotope effect during methane coupling and related reactions over lithium/magnesium oxide catalysts. *J. Phys. Chem.* **97**, 1445–1450 (1993).

127. Mims, C. A., Hall, R. B., Rose, K. D. & Myers, G. R. Oxidative Dimerization of CH_4/CD_4 Mixtures: Evidence for Methyl Intermediate. *Catal. Letters* **2**, 361–368 (1989).

128. Otsuka, K., Inaida, M., Wada, Y., Komatsu, T. & Morikawa, A. Isotopic Studies on Oxidative Methane Coupling over Samarium Oxide. *Chem. Lett.* 1531–1584 (1989).

129. Hutchings, G. J., Scurrell, M. S. & Woodhouse, J. R. Oxidative coupling of methane using oxide catalysts. *Chem. Soc. Rev.* **18**, 251–283 (1989).

130. Pak, S., Qiu, P. & Lunsford, J. H. Elementary reactions in the oxidative coupling of methane over $Mn/Na_2WO_4/SiO_2$ and $Mn/Na_2WO_4/MgO$ catalysts. *J. Catal.* **179**, 222–230 (1998).

131. Stansch, Z., Mleczko, L. & Baerns, M. Comprehensive Kinetics of Oxidative Coupling of Methane over the La_2O_3/CaO Catalyst. *Ind. Eng. Chem. Res.* **36**, 2568–2579 (1997).

132. Johnson, M. A., Stefanovich, E. V. & Truong, T. N. An ab Initio Study on the Oxidative Coupling of Methane over a Lithium-Doped MgO Catalyst: Surface Defects and Mechanism. *J. Phys. Chem. B* **101**, 3196–3201 (1997).

133. Lacombe, S., Zanthoff, H. & Mirodatos, C. Oxidative Coupling of Methane over Lanthana Catalysts II. A Mechanistic Study Using Isotope Transient Kinetics. *Journal of Catalysis* vol. 155 106–116 (1995).

134. Palmer, M. S., Neurock, M. & Olken, M. M. Periodic Density Functional Theory Study of Methane Activation over La_2O_3: Activity of O^{2-}, O^-, O_2^{2-}, Oxygen Point Defect, and Sr^{2+} Surface Sites. *J. Am. Chem. Soc.* **124**, 8452–8461 (2002).

135. Cummins, C. C., Baxter, S. M. & Wolczanski, P. T. Methane and Benzene Activation via Transient $(t\text{-}Bu_3SiNH)_2Zr{=}NSi\text{-}t\text{-}Bu_3$. *J. Am. Chem. Soc.* **110**, 8731–8733 (1988).

136. Cummins, C. C. *et al.* (Tri-tert-butylsilyl)imido complexes of titanium: Benzene C-H activation and structure of $[(^tBu_3SiNH)Ti]_2(mu\text{-}NSi^tBu_3)_2$. *J. Am. Chem. Soc.* **113**, 2985–2994 (1991).

137. Cundari, T. R., Grimes, T. V. & Gunnoe, T. B. Activation of carbon-hydrogen bonds via 1,2-addition across M-X (X = OH or NH_2) bonds of d^6 transition metals as a potential key step in hydrocarbon functionalization: A computational study. *J. Am. Chem. Soc.* **129**, 13172–13182 (2007).

138. Henkelman, G., Arnaldsson, A. & Jónsson, H. A fast and robust algorithm for Bader decomposition of charge density. *Comput. Mater. Sci.* **36**, 354–360 (2006).

139. Varghese, J. J., Trinh, Q. T. & Mushrif, S. H. Insights into the synergistic role of metal–lattice oxygen site pairs in four-centered C–H bond activation of methane: the case of CuO. *Catal. Sci. Technol.* **6**, 3984–3996 (2016).

140. Dai, G.-L., Liu, Z.-P., Wang, W.-N., Lu, J. & Fan, K.-N. Oxidative Dehydrogenation of Ethane over V_2O_5 (001): A Periodic Density Functional Theory Study. *J. Phys. Chem. C* **112**, 3719–25 (2008).

141. Ito, T. & Lunsford, J. H. Synthesis of ethylene and ethane by partial oxidation of methane over lithium-doped magnesium oxide. *Nature* **314**, 721–722 (1985).

142. Luo, L. *et al.* Gas-Phase Reaction Network of Li/MgO-Catalyzed Oxidative Coupling of Methane and Oxidative Dehydrogenation of Ethane. *ACS Catal.* **9**, 2514–2520 (2019).

143. Wolf, E. E. *Methane Conversion by Oxidative Processes*. (Springer: New York, 1992).

144. Pak, S., Qiu, P. & Lunsford, J. H. Thermal effects during the oxidative coupling of methane over $Mn/Na_2WO_4/SiO_2$ and $Mn/Na_2WO_4/MgO$ catalysts. *J. Catal.* **179**, 222–230 (1998).

145. Shi, C., Rosynek, M. P. & Lunsford, J. H. Origin of Carbon Oxides during the Oxidative Coupling of Methane. *J. Phys. Chem.* **98**, 8371–8376 (1994).

146. Lane, G. S. & Wolf, E. E. Methane utilization by oxidative coupling. I. A study of reactions in the gas phase during the cofeeding of methane and oxygen. *J. Catal.* **113**, 144–163 (1988).

147. Rezgui, S., Liang, A., Cheung, T. K. & Gates, B. C. Methane conversion to ethane in the presence of iron- and manganese-promoted sulfated zirconia. *Catal. Letters* **53**, 1–2 (1998).

148. Otsuka, K., Jinno, K. & Morikawa, A. The catalysts active and selective in oxidative coupling of methane. *Chem. Lett.* 499–500 (1985).

149. Dubois, J.-L., Rebours, B. & Cameron, C. J. Oxidative coupling of methane over thoria based catalysts. *Appl. Catal.* **67**, 73–79 (1990).

150. Blanksby, S. J. & Ellison, G. B. Bond dissociation energies of organic molecules. *Acc. Chem. Res.* **36**, 255–263 (2003).

151. Baulch, D. L. *et al.* Evaluated Kinetic Data for Combustion Modeling. Supplement I. *J. Phys. Chem. Ref. Data* **23**, 847–848 (1994).

152. Baulch, D. L. *et al.* Evaluated Kinetic Data for Combustion Modelling. *J. Phys. Chem. Ref. Data* **21**, 411–734 (1992).

153. Deshlahra, P. & Iglesia, E. Reactivity and selectivity descriptors for the activation of C-H bonds in hydrocarbons and oxygenates on metal oxides. *J. Phys. Chem. C* **120**, 16741–16760 (2016).

154. Labinger, J. A. & Ott, K. C. Mechanistic Studies on the Oxidative Coupling of Methane. *J. Phys. Chem.* **91**, 2682–2684 (1987).

155. Takanabe, K. & Iglesia, E. Rate and selectivity enhancements mediated by OH radicals in the oxidative coupling of methane catalyzed by $Mn/Na_2WO_4/SiO_2$. *Angew. Chemie - Int. Ed.* **47**, 7689–7693 (2008).

156. Beck, B. *et al.* Oxidative coupling of methane - A complex surface/gas phase mechanism with strong impact on the reaction engineering. *Catal. Today* **228**, 212–218 (2014).

157. Arndt, S. *et al.* A critical assessment of Li/MgO-Based catalysts for the oxidative

coupling of methane. *Catal. Rev. - Sci. Eng.* **53**, 424–514 (2011).

158. Rosso, K. M., Becker, U. & Hochella, M. F. Atomically resolved electronic structure of pyrite {100} surfaces: An experimental and theoretical investigation with implications for reactivity. *Am. Mineral.* **84**, 1535–1548 (1999).

159. Nesbitt, H. W. Sulfur and iron surface states on fractured pyrite surfaces. *Am. Mineral.* **83**, 1067–1076 (1998).

160. Siebert, D. & Stocker, W. Investigation of a (100) Surface of Pyrite by STM. *Phys. Status Solidi* **134**, K17–K20 (1992).

161. Alfonso, D. R. Computational investigation of FeS_2 surfaces and prediction of effects of sulfur environment on stabilities. *J. Phys. Chem. C* **114**, 8971–8980 (2010).

162. Hung, A., Muscat, J., Yarovsky, I. & Russo, S. P. Density-functional theory studies of pyrite FeS_2 (100) and (110) surfaces. *Surf. Sci.* **520**, 111–119 (2002).

163. Kresse, G. & Hafner, J. Ab initio molecular-dynamics simulation of the liquid-metal–amorphous-semiconductor transition in germanium. *Phys. Rev. B* **49**, 14251–14269 (1994).

164. Kresse, G. & Furthmüller, J. Efficiency of ab-initio total energy calculations for metals and semiconductors using a plane-wave basis set. *Comput. Mater. Sci.* **6**, 15–50 (1996).

165. Kresse, G. & Furthmüller, J. Efficient iterative schemes for ab initio total-energy calculations using a plane-wave basis set. *Phys. Rev. B* **54**, 11169–11186 (1996).

166. Kresse, G. & Hafner, J. Ab initio molecular dynamics for liquid metals. *Phys. Rev. B* **47**, 558–561 (1993).

167. Perdew, J. P., Ernzerhof, M. & Burke, K. Rationale for mixing exact exchange with density functional approximations. *J. Chem. Phys.* **105**, 9982 (1996).

168. Blöchl, P. E. Projector augmented-wave method. *Phys. Rev. B* **50**, 17953–17979 (1994).

169. Kresse, G. From ultrasoft pseudopotentials to the projector augmented-wave method. *Phys. Rev. B* **59**, 1758–1775 (1999).

170. Grimme, S. Semiempirical GGA-Type Density Functional Constructed with a Long-Range Dispersion Correction. *J. Comput. Chem.* **27**, 1787–1799 (2006).

171. Moroni, E., Kresse, G., Hafner, J. & Furthmüller, J. Ultrasoft pseudopotentials applied to magnetic Fe, Co, and Ni: From atoms to solids. *Phys. Rev. B* **56**, 15629–15646 (1997).

172. Henkelman, G. & Jónsson, H. Improved tangent estimate in the nudged elastic band method for finding minimum energy paths and saddle points. *J. Chem. Phys.* **113**, 9978–9985 (2000).

173. Henkelman, G., Uberuaga, B. P. & Jónsson, H. Climbing image nudged elastic band method for finding saddle points and minimum energy paths. *J. Chem. Phys.* **113**, 9901–9904 (2000).

174. Henkelman, G. & Jónsson, H. A dimer method for finding saddle points on high dimensional potential surfaces using only first derivatives. *J. Chem. Phys.* **111**, 7010–7022 (1999).

175. Campbell, C. T. & Sellers, J. R. V. The entropies of adsorbed molecules. *J. Am. Chem. Soc.* **134**, 18109–18115 (2012).

176. Folkins, H. O., Miller, E. & Hennig, H. Carbon Disulfide from Natural Gas and Sulfur. Reaction of Methane and Sulfur over a Silica Gel Catalyst. *Ind. Eng. Chem.* **42**, 2202–2207 (1950).

177. Karan, K. & Behie, L. A. CS_2 Formation in the Claus Reaction Furnace: A Kinetic Study of Methane−Sulfur and Methane−Hydrogen Sulfide Reactions. *Ind. Eng. Chem. Res.* **43**, 3304–3313 (2004).

178. Fisher, R. A. & Smith, J. M. Kinetics of Reaction between Methane and Sulfur Vapor. *Ind. Eng. Chem.* 704–709 (1950).

179. Nabor, G. W. & Smith, J. M. Kinetics of the Sulfur-Methane Reaction. *Ind. Eng. Chem.* **45**, 1272–1281 (1953).

180. Palmer, M. S., Neurock, M. & Olken, M. M. Periodic Density Functional Theory Study of the Dissociative Adsorption of Molecular Oxygen over La_2O_3. *J. Phys. Chem. B* **106**, 6543–6547 (2002).

181. Sit, P. H. L., Cohen, M. H. & Selloni, A. Interaction of oxygen and water with the (100) surface of pyrite: Mechanism of sulfur oxidation. *J. Phys. Chem. Lett.* **3**, 2409–2414 (2012).

182. Mardirossian, N. & Head-Gordon, M. Thirty years of density functional theory in computational chemistry: An overview and extensive assessment of 200 density functionals. *Mol. Phys.* **115**, 2315–2372 (2017).

183. Fasiska, E. J. Some defect structures of iron sulfide. *Phys. Status Solidi* **10**, 169–173 (1972).

184. Reuter, K. & Scheffler, M. First-Principles Atomistic Thermodynamics for Oxidation Catalysis: Surface Phase Diagrams and Catalytically Interesting Regions. *Phys. Rev. Lett.* **90**, 046103 (2003).

185. Labinger, J. A. Platinum-Catalyzed C − H Functionalization. *Chem. Rev.* **117**, 8483–8496 (2017).

186. Lyons, T. W., Sanford, M. S. & Formation, I. C. N. B. Palladium-Catalyzed Ligand-Directed C - H Functionalization Reactions. *Chem. Rev.* **110**, 1147–1169 (2010).

187. Davies, D. L., Macgregor, S. A. & Mcmullin, C. L. Computational Studies of Carboxylate-Assisted C − H Activation and Functionalization at Group 8 − 10 Transition Metal Centers. *Chem. Rev.* **117**, 8649–8709 (2017).

188. Chen, M. S. & White, M. C. A Predictably Selective Aliphatic C–H Oxidation Reaction for Complex Molecule Synthesis. *Science* **318**, 783–788 (2007).

189. He, J., Wasa, M., Chan, K. S. L., Shao, Q. & Yu, J. Palladium-Catalyzed Transformations of Alkyl C − H Bonds. *Chem. Rev.* **117**, 8754–8786 (2017).

190. Gunsalus, N. J. *et al.* Homogeneous Functionalization of Methane. *Chem. Rev.* **117**, 8521–8573 (2017).

191. Burk, M. J. & Crabtree, R. H. Selective Catalytic Dehydrogenation of Alkanes to Alkenes. *J. Am. Chem. Soc.* **109**, 8025–8032 (1987).

192. Kumar, A., Bhatti, T. M. & Goldman, A. S. Dehydrogenation of Alkanes and Aliphatic Groups by Pincer-Ligated Metal Complexes. *Chem. Rev.* **117**, 12357–12384 (2017).

193. Fang, H., Liu, G. & Huang, Z. Dehydrogenation of Alkanes Using Molecular Catalysts. *Alkane Funct.* **2**, 467–483 (2018).

194. Sattler, J. J. H. B., Ruiz-Martinez, J., Santillan-Jimenez, E. & Weckhuysen, B. M. Catalytic dehydrogenation of light alkanes on metals and metal oxides. *Chem. Rev.* **114**, 10613–10653 (2014).

195. Dobereiner, G. E., Crabtree, R. H. & Nucleophiles, E. Dehydrogenation as a Substrate-Activating Strategy in Homogeneous Transition-Metal Catalysis. *Chem. Rev.* **110**, 681–703 (2010).

196. Chae, S. Y. & Do, W. L. Efficient dehydrogenation of amines and carbonyl compounds catalyzed by a tetranuclear ruthenium-μ-oxo-μ-hydroxo-hydride complex. *Organometallics* **28**, 947–949 (2009).

197. Choi, J., MacArthur, A. H. R., Brookhart, M. & Goldman, A. S. Dehydrogenation and related reactions catalyzed by iridium pincer complexes. *Chem. Rev.* **111**, 1761–1779 (2011).

198. Zhang, X., Wang, D. Y., Emge, T. J. & Goldman, A. S. Dehydrogenation of ketones by pincer-ligated iridium: Formation and reactivity of novel enone complexes. *Inorganica Chim. Acta* **369**, 253–259 (2011).

199. Muzart, J. One-pot syntheses of α,β-Unsaturated carbonyl compounds through palladium-mediated dehydrogenation of ketones, aldehydes, esters, lactones and amides. *European J. Org. Chem.* 3779–3790 (2010).

200. Heumann, A., Jens, K.-J., Réglier, M. Palladium Complex Catalyzed Oxidation Reactions. *Prog. Inorg. Chem.* **42**, 483−576 (1994).

201. Hosokawa, T. & Murahashi, S. I. New Aspects of Oxypalladation of Alkenes. *Acc. Chem. Res.* **23**, 49–54 (1990).

202. Ito, Y., Hirao, T. & Saegusa, T. Synthesis of α, β-Unsaturated Carbonyl Compounds by Palladium(II)-Catalyzed Dehydrosilylation of Silyl Enol Ethers. *J. Org. Chem.* **43**, 1011–1013 (1978).

203. Muzart, J. Palladium-catalysed oxidation of primary and secondary alcohols. *Tetrahedron* **59**, 5789–5816 (2003).

204. Nishimura, T., Onoue, T., Ohe, K. & Uemura, S. Palladium(II)-catalyzed oxidation of alcohols to aldehydes and ketones by molecular oxygen. *J. Org. Chem.* **64**, 6750–6755 (1999).

205. Brink, G. J. Ten, Arends, I. W. C. E., Papadogianakis, G. & Sheldon, R. A. Catalytic conversions in water. Part 10. † Aerobic oxidation of terminal olefins

to methyl ketones catalysed by water soluble palladium complexes. *Chem. Commun.* 2359–2360 (1998).

206. Kopylovich, M. N. *et al.* Catalytic oxidation of alcohols: Recent Advances. *Adv. Organomet. Chem.* **63**, 91–173 (2015).

207. Steinhoff, B. A., Guzei, I. A. & Stahl, S. S. Mechanistic Characterization of Aerobic Alcohol Oxidation Catalyzed by $Pd(OAc)_2$/Pyridine Including Identification of the Catalyst Resting State and the Origin of Nonlinear [Catalyst] Dependence. *J. Am. Chem. Soc.* **126**, 11268–11278 (2004).

208. Izawa, Y., Zheng, C. & Stahl, S. S. Aerobic oxidative heck/dehydrogenation reactions of cyclohexenones: Efficient access to meta-substituted phenols. *Angew. Chemie - Int. Ed.* **52**, 3672–3675 (2013).

209. Gorelsky, S. I., Lapointe, D., Fagnou, K., Lilly, E. & Zeneca, A. Analysis of the Concerted Metalation-Deprotonation Mechanism in Palladium-Catalyzed Direct Arylation Across a Broad Range of Aromatic Substrates. *J. Am. Chem. Soc.* **130**, 10848–10849 (2008).

210. Davies, D. L., Donald, S. M. A. & Macgregor, S. A. Computational Study of the Mechanism of Cyclometalation by Palladium Acetate. *J. Am. Chem. Soc.* **127**, 13754–13755 (2005).

211. Yang, Y.-F. *et al.* Palladium-Catalyzed Meta -Selective C–H Bond Activation with a Nitrile-Containing Template: Computational Study on Mechanism and Origins of Selectivity. *J. Am. Chem. Soc.* **136**, 344–355 (2014).

212. Lapointe, D. & Fagnou, K. Overview of the mechanistic work on the concerted metallation-deprotonation pathway. *Chem. Lett.* **39**, 1118–1126 (2010).

213. Frisch, M. J. *et al.* Gaussian 09, Revision D.01. *Gaussian Inc.* (2013).

214. Zhao, Y. & Truhlar, D. G. A new local density functional for main-group thermochemistry, transition metal bonding, thermochemical kinetics, and noncovalent interactions. *J. Chem. Phys.* **125**, 194101 (2006).

215. Andrae, D., Häußermann, U., Dolg, M., Stoll, H. & Preuß, H. Energy-adjusted ab initio pseudopotentials for the second and third row transition elements. *Theor. Chim. Acta* **77**, 123–141 (1990).

216. Hariharan, P. C. & Pople, J. A. Accuracy of AH_n equilibrium geometries by single determinant molecular orbital theory. *Mol. Phys.* **27**, 209–214 (1974).

217. Krishnan, R. *et al.* functions Self-consistent molecular orbital methods . XX . A basis set for correlated wave functions. *J. Chem. Phys.* **72**, 650 (1980).

218. Ditchfield, R., Hehre, W. J. & Pople, J. A. Self-Consistent Molecular-Orbital Methods . IX . An Extended Gaussian-Type Basis for Molecular-Orbital Studies of Organic Molecules. *J. Chem. Phys.* **54**, 724 (1971).

219. Marenich, A. V., Cramer, C. J. & Truhlar, D. G. Universal solvation model based on solute electron density and on a continuum model of the solvent defined by the bulk dielectric constant and atomic surface tensions. *J. Phys. Chem. B* **113**, 6378–6396 (2009).

220. Nielsen, R. J., Keith, J. M., Stoltz, B. M. & Goddard, W. A. A Computational Model Relating Structure and Reactivity in Enantioselective Oxidations of Secondary Alcohols by (-)-Sparteine-Pd^{II} Complexes. *J. Am. Chem. Soc.* **126**, 7967–7974 (2004).

221. Goossen, L. J., Koley, D., Hermann, H. L. & Thiel, W. Mechanistic Pathways for Oxidative Addition of Aryl Halides to Palladium (0) Complexes: A DFT Study. *Organometallics* **24**, 2398–2410 (2005).

222. Goossen, L. J., Koley, D., Hermann, H. L. & Thiel, W. The Palladium-Catalyzed Cross-Coupling Reaction of Carboxylic Anhydrides with Arylboronic Acids : A DFT Study. *J. Am. Chem. Soc.* **127**, 11102–11114 (2005).

223. Gooßen, L. J., Koley, D., Hermann, H. & Thiel, W. The mechanism of the oxidative addition of aryl halides to Pd-catalysts : a DFT investigation. *Chem. Commun.* 2141–2143 (2004).

224. Yang, Y. F. *et al.* Palladium-catalyzed meta-selective C-H bond activation with a nitrile-containing template: Computational study on mechanism and origins of selectivity. *J. Am. Chem. Soc.* **136**, 344–355 (2014).

225. Biswas, B., Sugimoto, M. & Sakaki, S. C-H bond activation of benzene and methane by $M(\eta^2\text{-}O_2CH)_2$ (M = Pd or Pt). A theoretical study. *Organometallics* **19**, 3895–3908 (2000).

226. Initial attempts towards optimization of the product state for the intramolecular deprotonation pathway gave back the reactant state suggesting that the hydrogen by itself was not stabilized on the oxygen of the TFA group. The hydrogen however when stabil.

227. Fabre, I. *et al.* Autocatalytic intermolecular versus intramolecular deprotonation in C-H bond activation of functionalized arenes by ruthenium(II) or palladium(II) complexes. *Chem. - A Eur. J.* **19**, 7595–7604 (2013).

228. Pascual, S., de Mendoza, P., Braga, A. A. C., Maseras, F. & Echavarren, A. M. Bidentate phosphines as ligands in the palladium-catalyzed intramolecular arylation: the intermolecular base-assisted proton abstraction mechanism. *Tetrahedron* **64**, 6021–6029 (2008).

229. Schultz, M. J., Adler, R. S., Zierkiewicz, W., Privalov, T. & Sigman, M. S. Using mechanistic and computational studies to explain ligand effects in the palladium-catalyzed aerobic oxidation of alcohols. *J. Am. Chem. Soc.* **127**, 8499–8507 (2005).

230. Zierkiewicz, W. & Privalov, T. A Theoretical Study of the Essential Role of DMSO as a Solvent / Ligand in the $Pd(OAc)_2$/DMSO Catalyst System for Aerobic Oxidation. *Organometallics* **24**, 6019–6028 (2005).

231. Nielsen, R. J. & Goddard, W. A. Mechanism of the aerobic oxidation of alcohols by palladium complexes of N-heterocyclic carbenes. *J. Am. Chem. Soc.* **128**, 9651–9660 (2006).

232. Using the methodology described under Computational Methods section to calculate free energy in solvent, the activation barrier for the beta hydride elimination step was found to be 112 kJ/mol, lower than the reaction energy of

114 kJ/mol. Since the free .

233. Konnick, M. M. & Stahl, S. S. Reaction of molecular oxygen with a Pd^{II}-hydride to produce a Pd^{II}-hydroperoxide: Experimental evidence for an HX-reductive-elimination pathway. *J. Am. Chem. Soc.* **130**, 5753–5762 (2008).

234. Keith, J. M., Goddard, W. A. & Oxgaard, J. Pd-mediated activation of molecular oxygen: Pd(0) versus direct insertion. *J. Am. Chem. Soc.* **129**, 10361–10369 (2007).

235. Konnick, M. M., Knapp, S. M. M. & Stahl, S. S. Mechanism of the reaction of an NHC-coordinated palladium(II)-hydride with O_2 in acetonitrile. *Polyhedron* **182**, 114501 (2020).

236. Bickelhaupt, F. M. & Houk, K. N. Analyzing Reaction Rates with the Distortion/Interaction-Activation Strain Model. *Angew. Chemie - Int. Ed.* **56**, 10070–10086 (2017).

237. Legault, C. Y., Garcia, Y., Merlic, C. A. & Houk, K. N. Origin of regioselectivity in palladium-catalyzed cross-coupling reactions of polyhalogenated heterocycles. *J. Am. Chem. Soc.* **129**, 12664–12665 (2007).

238. Wang, D. & Stahl, S. S. Pd-Catalyzed Aerobic Oxidative Biaryl Coupling: Non-Redox Cocatalysis by $Cu(OTf)_2$ and Discovery of $Fe(OTf)_3$ as a Highly Effective Cocatalyst. *J. Am. Chem. Soc.* **139**, 5704–5707 (2017).

239. Diao, T., White, P., Guzei, I. & Stahl, S. S. Characterization of DMSO Coordination to Palladium (II) in Solution : Insights into the Aerobic Oxidation Catalyst. *Inorg. Chem.* **51**, 11898–11909 (2012).

240. Wang, B. *et al.* Electrocatalytic Oxidation of Small Molecule Alcohols over Pt, Pd, and Au Catalysts: The Effect of Alcohol's Hydrogen Bond Donation Ability and Molecular Structure Properties. *Catalysts* **9**, 387 (2019).

241. Liu, J., Ye, J., Xu, C., Jiang, S. P. & Tong, Y. Electro-oxidation of methanol, 1-propanol and 2-propanol on Pt and Pd in alkaline medium. *J. Power Sources* **177**, 67–70 (2008).

242. Coutanceau, C., Baranton, S. & Kouamé, R. S. B. Selective electrooxidation of glycerol into value-added chemicals: A short overview. *Front. Chem.* **7**, 1–15 (2019).

243. Houache, M. S. E., Hughes, K. & Baranova, E. A. Study on catalyst selection for electrochemical valorization of glycerol. *Sustain. Energy Fuels* **3**, 1892–1915 (2019).

244. Rafiee, M., Konz, Z. M., Graaf, M. D., Koolman, H. F. & Stahl, S. S. Electrochemical Oxidation of Alcohols and Aldehydes to Carboxylic Acids Catalyzed by 4-Acetamido-TEMPO: An Alternative to 'anelli' and 'pinnick' Oxidations. *ACS Catal.* **8**, 6738–6744 (2018).

245. Heinen, M., Jusys, Z. & Behm, R. J. Ethanol, acetaldehyde and acetic acid adsorption/electrooxidation on a pt thin film electrode under continuous electrolyte flow: An in situ atr-ftirs flow cell study. *J. Phys. Chem. C* **114**, 9850–9864 (2010).

246. Walgode, P. M., Faria, R. P. V, Rodrigues, A. E. & Faria, R. P. V. A review of aerobic glycerol oxidation processes using heterogeneous catalysts : a sustainable pathway for the production of dihydroxyacetone production of dihydroxyacetone. *Catal. Rev.* 1–90 (2020).

247. Katryniok, B. *et al.* Selective catalytic oxidation of glycerol: Perspectives for high value chemicals. *Green Chem.* **13**, 1960–1979 (2011).

248. Liu, B. & Gao, F. Navigating glycerol conversion roadmap and heterogeneous catalyst selection aided by density functional theory: A review. *Catalysts* **8**, (2018).

249. Dodekatos, G., Schünemann, S. & Tüysüz, H. Recent Advances in Thermo-, Photo-, and Electrocatalytic Glycerol Oxidation. *ACS Catal.* **8**, 6301–6333 (2018).

250. Talebian-Kiakalaieh, A., Amin, N. A. S., Rajaei, K. & Tarighi, S. Oxidation of bio-renewable glycerol to value-added chemicals through catalytic and electro-chemical processes. *Appl. Energy* **230**, 1347–1379 (2018).

251. Schnaidt, J., Heinen, M., Denot, D., Jusys, Z. & Jürgen Behm, R. Electrooxidation of glycerol studied by combined in situ IR spectroscopy and online mass spectrometry under continuous flow conditions. *J. Electroanal. Chem.* **661**, 250–264 (2011).

252. Zope, B. N., Hibbitts, D. D., Neurock, M. & Davis, R. J. Reactivity of the gold/water interface during selective oxidation catalysis. *Science (80-.).* **330**, 74–78 (2010).

253. Kimura, H. & Tsuto, K. Catalytic synthesis of dl-serine and glycine from glycerol. *J. Am. Oil Chem. Soc.* **70**, 1027–1030 (1993).

254. Hekmat, D., Bauer, R. & Fricke, J. Optimization of the microbial synthesis of dihydroxyacetone from glycerol with Gluconobacter oxydans. *Bioprocess Biosyst. Eng.* **26**, 109–116 (2003).

255. Gomes, J. F., De Paula, F. B. C., Gasparotto, L. H. S. & Tremiliosi-Filho, G. The influence of the Pt crystalline surface orientation on the glycerol electro-oxidation in acidic media. *Electrochim. Acta* **76**, 88–93 (2012).

256. Roquet, L., Belgsir, E. M., Léger, J. M. & Lamy, C. Kinetics and mechanisms of the electrocatalytic oxidation of glycerol as investigated by chromatographic analysis of the reaction products: Potential and pH effects. *Electrochim. Acta* **39**, 2387–2394 (1994).

257. Gomes, J. F. & Tremiliosi-Filho, G. Spectroscopic Studies of the Glycerol Electro-Oxidation on Polycrystalline Au and Pt Surfaces in Acidic and Alkaline Media. *Electrocatalysis* **2**, 96–105 (2011).

258. Fernández, P. S. *et al.* How do random superficial defects influence the electro-oxidation of glycerol on Pt(111) surfaces? *Phys. Chem. Chem. Phys.* **18**, 25582–25591 (2016).

259. Thia, L. *et al.* Copper-Modified Gold Nanoparticles as Highly Selective Catalysts for Glycerol Electro-Oxidation in Alkaline Solution. *ChemCatChem* **8**,

3272–3278 (2016).

260. Zhang, Z. *et al.* Selective electro-oxidation of glycerol to tartronate or mesoxalate on Au nanoparticle catalyst via electrode potential tuning in anion-exchange membrane electro-catalytic flow reactor. *Appl. Catal. B Environ.* **147**, 871–878 (2014).

261. Arjona, N. *et al.* Glycerol electro-oxidation in alkaline media using Pt and Pd catalysts electrodeposited on three-dimensional porous carbon electrodes. *New J. Chem.* **41**, 1854–1863 (2017).

262. Zalineeva, A., Baranton, S. & Coutanceau, C. Bi-modified palladium nanocubes for glycerol electrooxidation. *Electrochem. commun.* **34**, 335–338 (2013).

263. Almeida, T. S. D. *et al.* A Pd nanocatalyst supported on multifaceted mesoporous silica with enhanced activity and stability for glycerol electrooxidation. *RSC Adv.* **7**, 12006–12016 (2017).

264. Oliveira, V. L. *et al.* Studies of the reaction products resulted from glycerol electrooxidation on Ni-based materials in alkaline medium. *Electrochim. Acta* **117**, 255–262 (2014).

265. Oliveira, V. L. *et al.* Glycerol oxidation on nickel based nanocatalysts in alkaline medium - Identification of the reaction products. *J. Electroanal. Chem.* **703**, 56–62 (2013).

266. Kim, Y. *et al.* The Role of Ruthenium on Carbon-Supported PtRu Catalysts for Electrocatalytic Glycerol Oxidation under Acidic Conditions. *ChemCatChem* **9**, 1683–1690 (2017).

267. Lee, S. *et al.* Highly selective transformation of glycerol to dihydroxyacetone without using oxidants by a PtSb/C-catalyzed electrooxidation process. *Green Chem.* **18**, 2877–2887 (2016).

268. Sandrini, R. M. L. M. *et al.* Mechanistic aspects of glycerol electrooxidation on Pt(111) electrode in alkaline media. *Electrochem. commun.* **86**, 149–152 (2018).

269. Kwon, Y., Birdja, Y., Spanos, I., Rodriguez, P. & Koper, M. T. M. Highly selective electro-oxidation of glycerol to dihydroxyacetone on platinum in the presence of bismuth. *ACS Catal.* **2**, 759–764 (2012).

270. González-Cobos, J., Baranton, S. & Coutanceau, C. Development of Bismuth-Modified PtPd Nanocatalysts for the Electrochemical Reforming of Polyols into Hydrogen and Value-Added Chemicals. *ChemElectroChem* **3**, 1694–1704 (2016).

271. Ning, X. *et al.* Promoting role of bismuth and antimony on Pt catalysts for the selective oxidation of glycerol to dihydroxyacetone. *J. Catal.* **335**, 95–104 (2016).

272. Garcia, A. C., Birdja, Y. Y., Tremiliosi-Filho, G. & Koper, M. T. M. Glycerol electro-oxidation on bismuth-modified platinum single crystals. *J. Catal.* **346**, 117–124 (2017).

273. Kwon, Y., Hersbach, T. J. P. & Koper, M. T. M. Electro-Oxidation of Glycerol on Platinum Modified by Adatoms: Activity and Selectivity Effects. *Top. Catal.*

57, 1272–1276 (2014).

274. Ning, X. *et al.* Promoting role of bismuth and antimony on Pt catalysts for the selective oxidation of glycerol to dihydroxyacetone. *J. Catal.* **335**, 95–104 (2016).

275. De Souza, M. B. C. *et al.* Pb- And Bi-Modified Pt Electrodes toward Glycerol Electrooxidation in Alkaline Media. Activity, Selectivity, and the Importance of the Pt Atoms Arrangement. *ACS Catal.* **10**, 2131–2137 (2020).

276. De Souza, M. B. C. *et al.* Bi-modified Pt Electrodes toward Glycerol Electrooxidation in Alkaline Solution: Effects on Activity and Selectivity. *ACS Catal.* **9**, 5104–5110 (2019).

277. Liu, B. & Greeley, J. Decomposition pathways of glycerol via C-H, O-H, and C-C bond scission on Pt(111): A density functional theory study. *J. Phys. Chem. C* **115**, 19702–19709 (2011).

278. Garcia, A. C. *et al.* Strong Impact of Platinum Surface Structure on Primary and Secondary Alcohol Oxidation during Electro-Oxidation of Glycerol. *ACS Catal.* **6**, 4491–4500 (2016).

279. Xie, T., Sarupria, S. & Getman, R. B. A DFT and MD study of aqueous-phase dehydrogenation of glycerol on Pt(1 1 1): comparing chemical accuracy versus computational expense in different methods for calculating aqueous-phase system energies. *Mol. Simul.* **43**, 370–378 (2017).

280. Xiao, Y., Greeley, J., Varma, A., Zhao, Z.-J. & Xiao, G. An Experimental and Theoretical Study of Glycerol Oxidation to 1,3-Dihydroxyacetone over Bimetallic Pt-Bi Catalysts. *AIChE J.* **63**, 705–715 (2017).

281. Tereshchuk, P., Chaves, A. S. & Da Silva, J. L. F. Glycerol adsorption on platinum surfaces: A density functional theory investigation with van der Waals corrections. *J. Phys. Chem. C* **118**, 15251–15259 (2014).

282. Luo, Y. Bond dissociation energies. in *CRC Handbook of Chemistry and Physics* 65–98 (2009).

283. Grimme, S., Antony, J., Ehrlich, S. & Krieg, H. A consistent and accurate ab initio parametrization of density functional dispersion correction (DFT-D) for the 94 elements H-Pu. *J. Chem. Phys.* **132**, 154104 (2010).

284. Taylor, C. D., Wasileski, S. A., Filhol, J. S. & Neurock, M. First principles reaction modeling of the electrochemical interface: Consideration and calculation of a tunable surface potential from atomic and electronic structure. *Phys. Rev. B - Condens. Matter Mater. Phys.* **73**, 1–16 (2006).

285. Filhol, J. S. & Neurock, M. Elucidation of the electrochemical activation of water over Pd by first principles. *Angew. Chemie - Int. Ed.* **45**, 402–406 (2006).

286. Hibbitts, D. D. & Neurock, M. Influence of oxygen and pH on the selective oxidation of ethanol on Pd catalysts. *J. Catal.* **299**, 261–271 (2013).

287. Wang, H. F. & Liu, Z. P. Comprehensive mechanism and structure-sensitivity of ethanol oxidation on platinum: New transition-state searching method for resolving the complex reaction network. *J. Am. Chem. Soc.* **130**, 10996–11004

(2008).

288. Li, M., Guo, W., Jiangs, R., Zhao, L. & Shan, H. Decomposition of ethanol on Pd(111): A density functional theory stutdy. *Langmuir* **26**, 1879–1888 (2010).

289. Wang, H. F. & Liu, Z. P. Selectivity of direct ethanol fuel cell dictated by a unique partial oxidation channel. *J. Phys. Chem. C* **111**, 12157–12160 (2007).

290. Wang, H., Jusys, Z. & Behm, R. J. Electrochemical oxidation kinetics and mechanism of ethylene glycol on a carbon supported Pt catalyst: A quantitative DEMS study. *J. Electroanal. Chem.* **595**, 23–36 (2006).

291. Saeys, M., Reyniers, M. F., Marin, G. B. & Neurock, M. Density functional study of benzene adsorption on Pt(111). *J. Phys. Chem. B* **106**, 7489–7498 (2002).

292. Loveless, B. T., Buda, C., Neurock, M. & Iglesia, E. CO chemisorption and dissociation at high coverages during CO hydrogenation on Ru catalysts. *J. Am. Chem. Soc.* **135**, 6107–6121 (2013).

293. Herrero, E., Franaszczuk, K. & Wieckowski, A. Electrochemistry of methanol at low index crystal planes of platinum. An integrated voltammetric and chronoamperometric study. *J. Phys. Chem.* **98**, 5074–5083 (1994).

294. Janik, M. J., Taylor, C. D. & Neurock, M. First principles analysis of the electrocatalytic oxidation of methanol and carbon monoxide. *Top. Catal.* **46**, 306–319 (2007).

295. Rossmeisl, J., Nørskov, J. K., Taylor, C. D., Janik, M. J. & Neurock, M. Calculated phase diagrams for the electrochemical oxidation and reduction of water over Pt(111). *J. Phys. Chem. B* **110**, 21833–21839 (2006).

296. Sandrini, R. M. L. M. *et al.* Electrocatalytic Oxidation of Glycerol on Platinum Single Crystals in Alkaline Media. *ChemElectroChem* **6**, 4238–4245 (2019).

297. Papaderakis, A., Mintsouli, I., Georgieva, J. & Sotiropoulos, S. Electrocatalysts prepared by galvanic replacement. *Catalysts* **7**, (2017).

298. Cuesta, A. At least three contiguous atoms are necessary for CO formation during methanol electrooxidation on platinum. *J. Am. Chem. Soc.* **128**, 13332–13333 (2006).

299. Kim, C.-H. & Frisbie, C. D. Field Effect Modulation of Outer-Sphere Electrochemistry at Back-Gated, Ultrathin ZnO Electrodes. *J. Am. Chem. Soc.* **138**, 7220–7223 (2016).

300. Wang, Y., Kim, C.-H., Yoo, Y., Johns, J. E. & Frisbie, C. D. Field Effect Modulation of Heterogeneous Charge Transfer Kinetics at Back-Gated Two-Dimensional MoS_2 Electrodes. *Nano Lett.* **17**, 7586–7592 (2017).

301. Kim, C.-H., Wang, Y. & Frisbie, C. D. Continuous and Reversible Tuning of Electrochemical Reaction Kinetics on Back-Gated 2D Semiconductor Electrodes: Steady-State Analysis Using a Hydrodynamic Method. *Anal. Chem.* **91**, 1627–1635 (2019).

302. Sze, S. M. & Ng, K. K. Physics of Semiconductor Devices. in *Physics of Semiconductor Devices* 293–360 (John Wiley & Sons, Inc., 2006).

303. Jaramillo, T. F. *et al.* Identification of Active Edge Sites for Electrochemical H_2 Evolution from MoS_2 Nanocatalysts. *Science* **317**, 100–102 (2007).

304. Hinnemann, B. *et al.* Biomimetic Hydrogen Evolution: MoS_2 Nanoparticles as Catalyst for Hydrogen Evolution. *J. Am. Chem. Soc.* **127**, 5308–5309 (2005).

305. Voiry, D. *et al.* The role of electronic coupling between substrate and 2D MoS_2 nanosheets in electrocatalytic production of hydrogen. *Nat. Mater.* **15**, 1003–1009 (2016).

306. Li, Y. *et al.* MoS_2 Nanoparticles Grown on Graphene: An Advanced Catalyst for the Hydrogen Evolution Reaction. *J. Am. Chem. Soc.* **133**, 7296 (2011).

307. Wang, H. *et al.* Electrochemical tuning of vertically aligned MoS_2 nanofilms and its application in improving hydrogen evolution reaction. *Proc. Natl. Acad. Sci.* **110**, 19701–19706 (2013).

308. Voiry, D. *et al.* Conducting MoS_2 Nanosheets as Catalysts for Hydrogen Evolution Reaction. *Nano Lett.* **13**, 6222–6227 (2013).

309. Lukowski, M. A. *et al.* Enhanced Hydrogen Evolution Catalysis from Chemically Exfoliated Metallic MoS_2 Nanosheets. *J. Am. Chem. Soc.* **135**, 10274–10277 (2013).

310. Wang, H. *et al.* Electrochemical Tuning of MoS_2 Nanoparticles on Three-Dimensional Substrate for Efficient Hydrogen Evolution. *ACS Nano* **8**, 4940–4947 (2014).

311. Tsai, C. *et al.* Electrochemical generation of sulfur vacancies in the basal plane of MoS_2 for hydrogen evolution. *Nat. Commun.* **8**, 15113 (2017).

312. Deng, J. *et al.* Triggering the electrocatalytic hydrogen evolution activity of the inert two-dimensional MoS_2 surface via single-atom metal doping. *Energy Environ. Sci.* **8**, 1594–1601 (2015).

313. Shi, Y. *et al.* Energy Level Engineering of MoS_2 by Transition-Metal Doping for Accelerating Hydrogen Evolution Reaction. *J. Am. Chem. Soc.* **139**, 15479–15485 (2017).

314. Benson, E. E. *et al.* Balancing the Hydrogen Evolution Reaction, Surface Energetics, and Stability of Metallic MoS_2 Nanosheets via Covalent Functionalization. *J. Am. Chem. Soc.* **140**, 441–450 (2018).

315. Wang, J. *et al.* Field Effect Enhanced Hydrogen Evolution Reaction of MoS_2 Nanosheets. *Adv. Mater.* **29**, 1604464-n/a (2017).

316. Yan, M. *et al.* Field-Effect Tuned Adsorption Dynamics of VSe_2 Nanosheets for Enhanced Hydrogen Evolution Reaction. *Nano Lett.* **17**, 4109–4115 (2017).

317. Yoo, Y., Degregorio, Z. P. & Johns, J. E. Seed Crystal Homogeneity Controls Lateral and Vertical Heteroepitaxy of Monolayer MoS_2 and WS_2. *J. Am. Chem. Soc.* **137**, 14281–14287 (2015).

318. Yu, Y. *et al.* Controlled Scalable Synthesis of Uniform, High-Quality Monolayer and Few-layer MoS_2 Films. *Sci. Rep.* **3**, 1866 (2013).

319. Yu, Y. *et al.* Layer-Dependent Electrocatalysis of MoS_2 for Hydrogen Evolution. *Nano Lett.* **14**, 553–558 (2014).

320. Li, G. *et al.* Activating MoS_2 for pH-Universal Hydrogen Evolution Catalysis. *J. Am. Chem. Soc.* **139**, 16194–16200 (2017).

321. Seh, Z. W. *et al.* Combining theory and experiment in electrocatalysis: Insights into materials design. *Science* **355**, (2017).

322. Shinagawa, T., Garcia-Esparza, A. T. & Takanabe, K. Insight on Tafel slopes from a microkinetic analysis of aqueous electrocatalysis for energy conversion. *Sci. Rep.* **5**, 1–21 (2015).

323. Parsons, R. The Rate of Electrolytic Hydrogen Evolution and the Heat of Adsorption of Hydrogen. *Trans. Faraday Soc.* **54**, 1053 (1958).

324. Nørskov, J. K. *et al.* Trends in the Exchange Current for Hydrogen Evolution. *J. Electrochem. Soc.* **152**, J23 (2005).

325. Trasatti, S. Work function, electronegativity, and electrochemical behaviour of metals: III. Electrolytic hydrogen evolution in acid solutions. *J. Electroanal. Chem. Interfacial Electrochem.* **39**, 163–184 (1972).

326. Sheng, W., Myint, M., Chen, J. G. & Yan, Y. Correlating the hydrogen evolution reaction activity in alkaline electrolytes with the hydrogen binding energy on monometallic surfaces. *Energy Environ. Sci.* **6**, 1509–1512 (2013).

327. Zhang, Y., Kolmakov, A., Chretien, S., Metiu, H. & Moskovits, M. Control of Catalytic Reactions at the Surface of a Metal Oxide Nanowire by Manipulating Electron Density Inside It. *Nano Lett.* **4**, 403–407 (2004).

328. Baker, L. R., Hervier, A., Kennedy, G. & Somorjai, G. A. Solid-State Charge-Based Device for Control of Catalytic Carbon Monoxide Oxidation on Platinum Nanofilms Using External Bias and Light. *Nano Lett.* **12**, 2554–2558 (2012).

329. Weast, R. C. *CRC Handbook of Chemistry and Physics*. (CRC Press, 1989).

330. Peters, B. K. *et al.* Enantio- and Regioselective Ir-Catalyzed Hydrogenation of Di- and Trisubstituted Cycloalkenes. *J. Am. Chem. Soc.* **138**, 11930–11935 (2016).

331. Liu, J. *et al.* Regioselective Iridium-Catalyzed Asymmetric Monohydrogenation of 1,4-Dienes. *J. Am. Chem. Soc.* **139**, 14470–14475 (2017).

332. Paptchikhine, A., Itto, K. & Andersson, P. G. Sequential Birch reaction and asymmetric Ir-catalyzed hydrogenation as a route to chiral building blocks. *Chem. Commun.* **47**, 3989–3991 (2011).

333. Rabten, W., Margarita, C., Eriksson, L. & Andersson, P. G. Ir-Catalyzed Asymmetric and Regioselective Hydrogenation of Cyclic Allylsilanes and Generation of Quaternary Stereocenters via the Hosomi-Sakurai Allylation. *Chem. - A Eur. J.* **24**, 1681–1685 (2018).

334. Dye, J. L. *et al.* Alkali metals plus silica gel: Powerful reducing agents and convenient hydrogen sources. *J. Am. Chem. Soc.* **127**, 9338–9339 (2005).

335. Nandi, P. *et al.* Alkali metals in silica gel (M-SG): A new reagent for desulfonation of amines. *Org. Lett.* **10**, 5441–5444 (2008).

336. Costanzo, M. J., Patel, M. N., Petersen, K. A. & Vogt, P. F. Ammonia-free Birch reductions with sodium stabilized in silica gel, Na-SG(I). *Tetrahedron Lett.* **50**, 5463–5466 (2009).

337. Lei, P. *et al.* A Practical and Chemoselective Ammonia-Free Birch Reduction. *Org. Lett.* **20**, 3439–3442 (2018).

338. Joshi, D. K., Sutton, J. W., Carver, S. & Blanchard, J. P. Experiences with commercial production scale operation of dissolving metal reduction using lithium metal and liquid ammonia. *Org. Process Res. Dev.* **9**, 997–1002 (2005).

339. Benkeser, R. A. & Kaiser, E. M. An Electrochemical Method of Reducing Aromatic Compounds Selectively to Dihydro or Tetrahydro Products. *J. Am. Chem. Soc.* **85**, 2858–2859 (1963).

340. Bordeau, M., Biran, C., Pons, P., Léger-Lambert, M. P. & Dunogués, J. The Electrochemical Reductive Trimethylsilylation of Aryl Chlorides: A Good Route to Aryltrimethylsilanes and a Novel Route to Tris(trimethylsilyl)cyclohexadienes. *J. Org. Chem.* **57**, 4705–4711 (1992).

341. Ishifune, M. *et al.* Electroreduction of aromatics using magnesium electrodes in aprotic solvents containing alcoholic proton donors. *Electrochim. Acta* **48**, 2405–2409 (2003).

342. Goodenough, J. B. & Park, K. S. The Li-ion rechargeable battery: A perspective. *J. Am. Chem. Soc.* **135**, 1167–1176 (2013).

343. Goodenough, J. B. & Kim, Y. Challenges for rechargeable Li batteries. *Chem. Mater.* **22**, 587–603 (2010).

344. Peled, E. & Menkin, S. Review—SEI: Past, Present and Future. *J. Electrochem. Soc.* **164**, A1703–A1719 (2017).

345. Haregewoin, A. M., Wotango, A. S. & Hwang, B. J. Electrolyte additives for lithium ion battery electrodes: Progress and perspectives. *Energy Environ. Sci.* **9**, 1955–1988 (2016).

346. Mizushima, K., Jones, P. C., Wiseman, P. J. & Goodenough, J. B. Li_xCoO_2 ($0<x<1$): A new cathode material for batteries of high energy density. *Mater. Res. Bull.* **15**, 783–789 (1980).

347. Perkins, R. J., Pedro, D. J. & Hansen, E. C. Electrochemical Nickel Catalysis for sp^2-sp^3 Cross-Electrophile Coupling Reactions of Unactivated Alkyl Halides. *Org. Lett.* **19**, 3755–3758 (2017).

348. Sun, G., Ren, S., Zhu, X., Huang, M. & Wan, Y. Direct arylation of pyrroles via indirect electroreductive C-H functionalization using perylene bisimide as an electron-transfer mediator. *Org. Lett.* **18**, 544–547 (2016).

349. Edinger, C. & Waldvogel, S. R. Electrochemical deoxygenation of aromatic amides and sulfoxides. *European J. Org. Chem.* **2014**, 5144–5148 (2014).

350. Mousavi, M. P. S., Kashefolgheta, S., Stein, A. & Bühlmann, P. Electrochemical

Stability of Quaternary Ammonium Cations: An Experimental and Computational Study. *J. Electrochem. Soc.* **163**, H74–H80 (2016).

351. Mortensen, B. J. & Heinze, J. The Electrochemical Reduction of Benzene - First Determination of the Reduction Potential. *Angew. Chemie - Int. Ed.* **23**, 84–85 (1984).

352. Coleman, J. P. Reduction of Benzene and Related Compounds in Aqueous Solution and Undivided Cells. *J. Electrochem. Soc.* **128**, 322 (1981).

353. Misra, R. A. & Yadav, A. K. Reduction of Aromatic Compounds by Solvated Electrons Generated at Cathode. *Bull. Chem. Soc. Jpn.* **55**, 347–348 (1982).

354. Kariv-Miller, E., Swenson, K. E. & Zemach, D. Cathodic Birch Reduction of Methoxyaromatics and Steroids in Aqueous Solution. *J. Org. Chem.* **48**, 4210–4214 (1983).

355. Pasquariello, D. *et al.* Electrochemical reduction of benzene by solvated electrons in HMPA-alcohol solutions. *J. Phys. Chem.* **89**, 1243–1245 (1985).

356. Del, F. J. *et al.* Low-temperature sonoelectrochemical processes Part 2 : Generation of solvated electrons and Birch reduction processes under high mass transport conditions in liquid ammonia. *J. Electroanal. Chem.* **507**, 144–151 (2001).

357. Combellas, C., Marzouk, H. & Thiebault, A. Electrolytic equipment for reductions in liquid ammonia. *J. Appl. Electrochem.* **21**, 267–275 (1991).

358. van Andel-Scheffer, P. J. M., Wonders, A. H. & Barendrecht, E. Studies of solvated electrons in LiBr + HMPA solutions using the rotating ring-disk electrode technique. Part 2. The reaction of benzene with solvated electrons. *J. Electroanal. Chem.* **366**, 143–146 (1994).

359. Alpatova, N. M., Zabusova, S. E. & Tomilov, A. P. The Reduction of Organic Compounds by Solvated Electrons Generated Electrochemically. *Russ. Chem. Rev.* **55**, 99–112 (1986).

360. Sternberg, H. W., Markby, R. & Wender, I. Electrochemical Reduction of the Benzene Ring. *J. Electrochem. Soc.* **110**, 425 (1963).

361. Benkeser, R. A., Kaiser, E. M. & Lambert, R. F. The Selective Reduction of Aromatic Compounds to Dihydro or Tetrahydro Products by an Electrochemical Method. *J. Am. Chem. Soc.* **86**, 5272–5276 (1964).

362. Sternberg, H. W., Markby, R. E., Wender, I. & Mohilner, D. M. Electrolytic Generation of Solvated Electrons and Reduction of the Benzene Ring in Ethanol Containing Hexamethylphosphoramide. *J. Am. Chem. Soc.* **89**, 186–187 (1967).

363. Misono, A., Osa, T., Yamagishi, T. & Kodama, T. Selective Electroreduction of the Benzene Nucleus. *J. Electrochem. Soc.* **115**, 266 (1968).

364. Dubois, J. & Dodin, G. Reaction of the solvated electron and monomeric metal species with toluene and benzene in hexametapol. Hydrogen atom mobility. *Tetrahedron Lett.* **10**, 2325–2328 (1969).

365. Avaca, L. A. & Bewick, A. The Cathodic Reduction of Anthracene in Lithium

Chloride-Hexamethyl-phosphoramide. *J. C. S Perkin II* 1709–1712 (1972).

366. Landais, Y. & Zekri, E. Desymmetrization of cyclohexa-1,4-dienes - A straightforward route to cyclic and acyclic polyhydroxylated systems. *European J. Org. Chem.* 4037–4053 (2002).

367. Krapcho, A. P. & Bothner, A. A. Kinetics of the Metal-Ammonia-Alcohol Reductions of Benzene and Substituted Benzenes. *J. Am. Chem. Soc.* **81**, 3658–3666 (1959).

368. Chen, L. D., Urushihara, M. & Chan, K. Electric Field Effects in Electrochemical CO_2 Reduction. *ACS Catal.* **6**, 7133–7139 (2016).

369. Winikoff, S. G., Dimeglio, J. L., Ramos, J. M., Rosenthal, J. & Neurock, M. Cooperativity Between Bi Electrodes and Ionic Liquid Electrolytes Promotes Efficient Electrocatalytic Reduction of CO_2 to CO, *to be submitted*.

370. Zhou, B. *et al.* A High-Performance Li–O_2 Battery with a Strongly Solvating Hexamethylphosphoramide Electrolyte and a LiPON-Protected Lithium Anode. *Adv. Mater.* **29**, 2–7 (2017).

371. (Youngman) Chusid, O., Ein Ely, E., Aurbach, D., Babai, M. & Carmeli, Y. Electrochemical and spectroscopic studies of carbon electrodes in lithium battery electrolyte systems. *J. Power Sources* **43**, 47–64 (1993).

372. Bard, A. J. & Faulkner, L. R. Kinetics of Electrode Reactions. in *Electrochemical Methods: Fundamentals and Applications* (Wiley, 2001).

373. Liu, K., Liu, Y., Lin, D., Pei, A. & Cui, Y. Materials for lithium-ion battery safety. *Sci. Adv.* **4**, (2018).

374. Coste, J., Le-Nguyen, D. & Castro, B. PyBOP®: A new peptide coupling reagent devoid of toxic by-product. *Tetrahedron Lett.* **31**, 205–208 (1990).

375. Donohoe, T. J. & House, D. Ammonia free partial reduction of aromatic compounds using lithium di-tert-butylbiphenyl (LiDBB). *J. Org. Chem.* **67**, 5015–5018 (2002).

376. Heravi, M. M., Fard, M. V. & Faghihi, Z. Recent Applications of Birch Reduction in Total Synthesis of Natural Products. *Curr. Org. Chem.* **19**, 1491–1425 (2020).

377. Yus, M. & Foubelo, F. Reductive Opening of Heterocycles with Lithium Metal as a Source of Functionalized Organolithium Compounds: Synthetic Applications. *Targets Heterocycl. Syst.* **6**, 136–171 (2002).

378. Luisi, R. & Capriati, V. *Lithium Compounds in Organic Synthesis: From Fundamentals to Applications*. (Wiley-VCH, 2014).

379. Wolckenhauer, S. A. & Rychnovsky, S. D. Generation and utility of tertiary α-aminoorganolithium reagents. *Org. Lett.* **6**, 2745–2748 (2004).

380. Chaban, V. V & Prezhdo, O. V. Electron Solvation in Liquid Ammonia: Lithium, Sodium, Magnesium, and Calcium as Electron Sources. *J. Phys. Chem. B* **120**, 2500–2506 (2016).

381. Janesko, B. G., Scalmani, G. & Frisch, M. J. Quantifying solvated electrons' delocalization. *Phys. Chem. Chem. Phys.* **17**, 18305–18317 (2015).

382. Hunter, E., Rogers, D., Holton, J., Heath, T. & Wa, C. Neutral and Anionic Silylmethyl Complexes of the Group 3a and Lanthanoid Metals ; the X-Ray Crystal and Molecular Structure of $[Li(thf)_4][Yb\{CH(SiMe_3)_2)_3Cl]$ (thf = Tetrahydrofuran). *J. Chem. Soc, Chem. Commun.* 140–142 (1978).

383. Eaborn, C., Hitchcock, P. B., Smith, J. D. & Sullivan, A. C. Crystal Structure of the Tetrahydrofuran Adduct of Tris(trmethylsilyl)-methyl-lithium $[Li(thf)_4][Li(C(SiMe_3)_3)_2]$, an Ate Derivative of Lithium. *J. Chem. Soc, Chem. Commun.* 827–828 (1983).

384. Sime, A. C., Eaborn, C., Hitchcock, P., Smith, J. D. & Sullivan, A. C. Preparation and Crystal Structure of the Argentate Complex $[Li(tetrahydrofuran)_4][Ag(C(SiMe3)3)2]$. *J. Chem. Soc, Chem. Commun.* 870–871 (1984).

385. Edwards, P. G., Gellert, R. W., Marks, M. W., Bau, R. & Levy, R. M. Preparation and Structure of the $[Cu_5(C_6H_5)_6]^-$ Anion. *J. Am. Chem. Soc.* **104**, 2072–2073 (1982).

386. Solution, T. H. F. H., Reich, H. J., Borst, J. P., Dykstra, R. R. & Green, D. P. A Nuclear Magnetic Resonance Spectroscopic Technique for the Characterization of Lithium Ion Pair Structures in THF. *J. Am. Chem. Soc.* **115**, 8728–8741 (1993).

387. Radin, M. D., Rodriguez, J. F., Tian, F. & Siegel, D. J. Lithium peroxide surfaces are metallic, while lithium oxide surfaces are not. *J. Am. Chem. Soc.* **134**, 1093–1103 (2012).

388. Wagner, C. D. *et al.* X-ray Photoelectron Spectroscopy Database. in *NIST Standard Reference Database 20* (Web Version, 2002).

389. Shim, J. *et al.* Electronic and Optoelectronic Devices based on Two-Dimensional Materials: From Fabrication to Application. *Adv. Electron. Mater.* **3**, (2017).

390. Das, S., Chen, H. Y., Penumatcha, A. V. & Appenzeller, J. High performance multilayer MoS_2 transistors with scandium contacts. *Nano Lett.* **13**, 100–105 (2013).

391. Jena, D., Banerjee, K. & Xing, G. H. 2D crystal semiconductors: Intimate contacts. *Nat. Mater.* **13**, 1076–1078 (2014).

392. Gong, C., Colombo, L., Wallace, R. M. & Cho, K. The unusual mechanism of partial fermi level pinning at metal-MoS_2 interfaces. *Nano Lett.* **14**, 1714–1720 (2014).

393. Kim, C. *et al.* Fermi Level Pinning at Electrical Metal Contacts of Monolayer Molybdenum Dichalcogenides. *ACS Nano* **11**, 1588–1596 (2017).

394. Bardeen, J. Surface states and rectification at a metal semi-conductor contact. *Phys. Rev.* **71**, 717–727 (1947).

395. Guimarães, M. H. D. *et al.* Atomically Thin Ohmic Edge Contacts between Two-Dimensional Materials. *ACS Nano* **10**, 6392–6399 (2016).

396. Cui, X. *et al.* Lowerature Ohmic Contact to Monolayer MoS_2 by van der Waals Bonded Co/h-BN Electrodes. *Nano Lett.* **17**, 4781–4786 (2017).

397. Wu, J. *et al.* High Mobility MoS_2 Transistor with Low Schottky Barrier Contact by Using Atomic Thick h-BN as a Tunneling Layer. *Advanced Materials* vol. 28 8302–8308 (2016).

398. Kaushik, N., Karmakar, D., Nipane, A., Karande, S. & Lodha, S. Interfacial n-Doping Using an Ultrathin TiO_2 Layer for Contact Resistance Reduction in MoS_2. *ACS Appl. Mater. Interfaces* **8**, 256–263 (2016).

399. Yu, L. *et al.* Graphene/MoS_2 Hybrid technology for large-scale two-dimensional electronics. *Nano Lett.* **14**, 3055–3063 (2014).

400. Cho, K. *et al.* Contact-Engineered Electrical Properties of MoS_2 Field-Effect Transistors via Selectively Deposited Thiol-Molecules. *Advanced Materials* vol. 30 (2018).

401. Chee, S. S. *et al.* Lowering the Schottky Barrier Height by Graphene/Ag Electrodes for High-Mobility MoS_2 Field-Effect Transistors. *Adv. Mater.* **31**, 180442 (2019).

402. Xie, L. *et al.* Graphene-Contacted Ultrashort Channel Monolayer MoS_2 Transistors. *Adv. Mater.* **29**, 1702522 (2017).

403. Liu, Y. *et al.* Toward barrier free contact to molybdenum disulfide using graphene electrodes. *Nano Lett.* **15**, 3030–3034 (2015).

404. Liu, Y. *et al.* Approaching the Schottky-Mott limit in van der Waals metal-semiconductor junctions. *Nature* **557**, 696–700 (2018).

405. Liu, Y., Huang, Y. & Duan, X. Van der Waals integration before and beyond two-dimensional materials. *Nature* **567**, 323–333 (2019).

406. McDonnell, S., Smyth, C., Hinkle, C. L. & Wallace, R. M. MoS_2-Titanium Contact Interface Reactions. *ACS Appl. Mater. Interfaces* **8**, 8289–8294 (2016).

407. Wang, Y. *et al.* Van der Waals contacts between three-dimensional metals and two-dimensional semiconductors. *Nature* **568**, 70–74 (2019).

408. Smyth, C. M., Addou, R., McDonnell, S., Hinkle, C. L. & Wallace, R. M. Contact Metal–MoS_2 Interfacial Reactions and Potential Implications on MoS_2-Based Device Performance. *J. Phys. Chem. C* **120**, 14719–14729 (2016).

409. English, C. D., Shine, G., Dorgan, V. E., Saraswat, K. C. & Pop, E. Improved contacts to MoS_2 transistors by ultra-high vacuum metal deposition. *Nano Lett.* **16**, 3824–3830 (2016).

410. Gong, C. *et al.* Metal contacts on physical vapor deposited monolayer MoS_2. *ACS Nano* **7**, 11350–11357 (2013).

411. Kshirsagar, C. U. *et al.* Dynamic Memory Cells Using MoS_2 Field-Effect Transistors Demonstrating Femtoampere Leakage Currents. *ACS Nano* **10**, 8457–8464 (2016).

412. Liu, W. *et al.* High-performance few-layer-MoS_2 field-effect-transistor with

record low contact-resistance. in *IEEE Intenational Electronic Devices Meeting (IEDM) (IEEE, Piscataway, NJ, 2013)* 19.4.1-19.4.4 (2013).

413. Egerton, R. F. Electron Energy-Loss Spectroscopy. in *Electron Microscope* (Springer: New York, 2011).

414. Dadsetani, M., Nejatipour, H. & Nouri, T. First-principles study of the sulfur K and $L_{2,3}$ edges of transition metal disulfide monolayers, MS_2 (M=Mo, W and Re). *Phys. E Low-Dimensional Syst. Nanostructures* **73**, 198–206 (2015).

415. Muller, D. A. *et al.* The electronic structure at the atomic scale of ultrathin gate oxides. *Nature* **399**, 758–761 (1999).

416. Kang, J., Liu, W., Sarkar, D., Jena, D. & Banerjee, K. Computational study of metal contacts to monolayer transition-metal dichalcogenide semiconductors. *Phys. Rev. X* **4**, 1–14 (2014).

417. Popov, I., Seifert, G. & Tomanek, D. Designing electrical contacts to MoS2 Monolayers: A computational study. *Phys. Rev. Lett.* **108**, 1–5 (2012).

418. Zhong, H. *et al.* Interfacial Properties of Monolayer and Bilayer MoS_2 Contacts with Metals: Beyond the Energy Band Calculations. *Sci. Rep.* **6**, 1–16 (2016).

419. Sotthewes, K. *et al.* Universal Fermi-Level Pinning in Transition-Metal Dichalcogenides. *J. Phys. Chem. C* **123**, 5411–5420 (2019).

420. Freedy, K. M. *et al.* Titanium contacts to graphene: Process-induced variability in electronic and thermal transport. *Nanotechnology* **29**, 145201 (2018).

421. Bunshah, R. F. Handbook of deposition technologies for films and coatings: science, technology, and applications. in (William Andrew, 1994).

422. Society, A. W. *Brazing Manual*. (American Welding Society, 1976).

423. Komsa, H. P. *et al.* Two-dimensional transition metal dichalcogenides under electron irradiation: Defect production and doping. *Phys. Rev. Lett.* **109**, 1–5 (2012).

424. Dorfman, K. D. & Daoutidis, P. *Numerical Methods with Chemical Engineering Applications*. (Cambridge University Press, 2017).

425. Kirkland, E. J. *Advanced computing in electron microscopy*. (Springer: New York, 2010).

426. Wu, R. J., Mittal, A., Odlyzko, M. L. & Mkhoyan, K. A. Simplifying Electron Beam Channeling in Scanning Transmission Electron Microscopy (STEM). *Microsc. Microanal.* **23**, 794–808 (2017).

427. Feldman, J. L. & Boyer, L. L. Atomic Mean-Squared Displacements For 2H—MoS_2. *Solid State Commun.* **37**, 879–881 (1980).

428. Mittal, A., Zhang, D. B., Teresi, C., Dumitrică, T. & Mkhoyan, K. A. Routes to identification of intrinsic twist in helical MoS_2 nanotubes by electron diffraction and annular dark-field scanning transmission electron microscopy imaging. *Phys. Rev. B - Condens. Matter Mater. Phys.* **84**, 1–4 (2011).

429. Young, P. A. Lattice parameter measurements on molybdenum disulphide. *J.*

Phys. D. Appl. Phys. **1**, 936–938 (1968).

430. Puigdollers, A. R., Schlexer, P. & Pacchioni, G. Gold and Silver Custers on TiO_2 and ZrO_2 (101) Surfaces: Role of Dispersion Forces. *J. Phys. Chem. C* **119**, 15381–15389 (2015).

431. Schlexer, P. & Pacchioni, G. Anchoring Small Au Clusters on the Dehydroxylated and Hydroxylated SiO_2 α-Quartz (001) Surface via Ti-Alloying. *J. Phys. Chem. C* **121**, 14717–14724 (2017).

432. Wilson, J. A. & Yoffe, A. D. The Transition Metal Dichalcogenides Discussion and Interpretation of the Observed Optical, Electrical and Structural Properties. *Adv. Phys.* **18**, 193–335 (1969).

433. Lin, C. H., Wang, J. X. & Lunsford, J. H. Oxidative dimerization of methane over sodium-promoted calcium oxide. *J. Catal.* **111**, 302–316 (1988).

434. Shi, C., Hatano, M. & Lunsford, J. H. A kinetic model for the oxidative coupling of methane over Li /MgO catalysts. *Catal. today* **13**, 191–199 (1992).

435. Morales, E. & Lunsford, J. H. Oxidative dehydrogenation of ethane over a lithium-promoted magnesium oxide catalyst. *J.Catal.* **118**, 255–265 (1989).

436. Nelson, P. F. & Cant, N. W. C, Hydrocarbon Products during the Oxidative Coupling. **32**, 3756–3761 (1990).

437. Newhouse, T. & Baran, P. S. If C-H bonds could talk: Selective C-H bond oxidation. *Angew. Chemie - Int. Ed.* **50**, 3362–3374 (2011).

438. Nicolaou, K. C., Montagnon, T. & Baran, P. S. HIO_3 and I_2O_5: Mild and selective alternative reagents to IBX for the dehydrogenation of aldehydes and ketones. *Angew. Chemie - Int. Ed.* **41**, 1386–1389 (2002).

439. Asadi, M. *et al.* Robust carbon dioxide reduction on molybdenum disulphide edges. *Nat. Commun.* **5**, 1–8 (2014).

440. Asadi, M. *et al.* Nanostructured transition metal dichalcogenide electrocatalysts for CO_2 reduction in ionic liquid. *Science* **353**, 467–470 (2016).

441. Gao, G., O'Mullane, A. P. & Du, A. 2D MXenes: A New Family of Promising Catalysts for the Hydrogen Evolution Reaction. *ACS Catal.* **7**, 494–500 (2017).

442. Wang, A., Kadam, S., Li, H., Shi, S. & Qi, Y. Review on modeling of the anode solid electrolyte interphase (SEI) for lithium-ion batteries. *npj Comput. Mater.* **4**, (2018).

443. Kang, J., Liu, W., Sarkar, D., Jena, D. & Banerjee, K. Computational study of metal contacts to monolayer transition-metal dichalcogenide semiconductors. *Phys. Rev. X* **4**, 1–14 (2014).